

**An Experimental Investigation of
Wind Turbine Wake Evolution
and
Flow Over Complex Terrain**

by

Michael John Sherry

A Thesis submitted to Monash University
for the degree of
Doctor of Philosophy

July 2012

Department of Mechanical and Aerospace Engineering
Monash University

Notices

1. Under the Copyright Act 1968, this thesis must be used only under the normal conditions of scholarly fair dealing. In particular no results or conclusions should be extracted from it, nor should it be copied or closely paraphrased in whole or in part without the written consent of the author. Proper written acknowledgement should be made for any assistance obtained from this thesis.
2. I certify that I have made all reasonable efforts to secure copyright permissions for third-party content included in this thesis and have not knowingly added copyright content to my work without the owner's permission.

*This thesis is dedicated to my family,
without whom it would not have been possible*

Statement of Originality

I, Michael Sherry, declare that this thesis is my own work and contains no material that has been accepted for the award of a degree or diploma in this, or any other, university. To the best of my knowledge and belief, information derived from the published and unpublished work of others has been acknowledged in the text of the thesis and a list of references is provided in the bibliography.

Candidate: Michael Sherry

Submitted: 4 Jul 2012

PART A: General Declaration

Monash University
Monash Research Graduate School

Declaration for thesis based or partially based on conjointly published or unpublished work

General Declaration

In accordance with Monash University Doctorate Regulation 17/ Doctor of Philosophy and Master of Philosophy (MPhil) regulations the following declarations are made:

I hereby declare that this thesis contains no material which has been accepted for the award of any other degree or diploma at any university or equivalent institution and that, to the best of my knowledge and belief, this thesis contains no material previously published or written by another person, except where due reference is made in the text of the thesis.

This thesis includes 1 original papers published in peer reviewed journals and 2 unpublished publications. The core theme of the thesis is the near wake of a horizontal axis wind turbine. The ideas, development and writing up of all the papers in the thesis were the principal responsibility of myself, the candidate, working within the Department of Mechanical Engineering under the supervision of Prof. John Sheridan and Dr. David Lo Jacono.

The inclusion of co-authors reflects the fact that the work came from active collaboration between researchers and acknowledges input into team-based research.

In the case of chapter my contribution to the work involved the following:

Thesis chapter	Publication title	Publication status*	Nature and extent of candidate's contribution
8	An experimental investigation of the recirculation zone formed downstream of a forward facing step	published	80%. acquired and analysed data. Wrote manuscript.
8	The effect of turbulence on flow over a forward facing step	Under review	80%. acquired and analysed data. Wrote manuscript.
8	The recirculation region downstream of 2D escarpments	Prepared for submission	80%. acquired and analysed data. Wrote manuscript.

I have / have not (circle that which applies) renumbered sections of submitted or published papers in order to generate a consistent presentation within the thesis.

Signed: ... 

Date: 03/07/2012

Abstract

This thesis investigates two flow fields that a wind turbine in a wind farm might experience. The first is the near-wake of a wind turbine where the focus was on the helical tip and root vortices. Two scale model wind turbines were investigated using PIV. A geometrically scaled rotor was observed to generate a chaotic wake due to poor aerodynamic performance at the experimental Reynolds number. Flow visualisations on a static 3D wing confirmed laminar separation is likely on the geometrically scaled model.

A research orientated model was designed based on the optimum Glauert rotor to investigate the stability of the tip and root vortices. A pairing instability was observed in the tip vortices. The onset of this instability was found to be dependent on the tip speed ratio. The root vortices become unstable due to their proximity to the turbine support structures.

The influence of freestream turbulence was studied by varying the turbulence intensity using passive turbulence grids including a novel tethered sphere grid. Increased turbulence intensity was observed to hasten the breakdown of the vortices, via turbulent diffusion rather than the pairing instability which was absent in the phase-locked average velocity fields.

Tip and root vortices of both turbine models were characterised using Galilean invariant vortex identification schemes. The meander of the vortices was observed to be Gaussian at early vortex ages when interaction between vortices is minimal. Meander magnitude was shown to increase with distance absolutely. However, the magnitude of meander was found to be dependent on tip speed ratio and freestream turbulence intensity.

A secondary focus was the flow fields above complex terrain features, a common location for wind farms. The recirculation region which formed downstream of various escarpment geometries was characterised using PIV. The size of the recirculation region was found to be dependent on the escarpment angle, the boundary layer to step height thickness ratio, the Reynolds number and the freestream turbulence intensity. An application of POD phase-averaging revealed the dynamic nature of the recirculation region. The wind speed-up above the escarpment beneficial in a wind energy sense was observed to be coupled to a vertical velocity component. Further, significant turbulence generation in the separated shear was observed which questions the appropriateness of complex terrain as a wind farm location.

Acknowledgements

First of all I would like to acknowledge the support and contribution from my primary supervisor, Prof. John Sheridan. John steadfastly supported my research throughout candidature and gave me the freedom to pursue a broad range of research topics. He provided significant financial support which allowed me to attend conferences and collaborate with world leading research institutions. I consider myself very privileged to have had the opportunity to work with John and would like to extend a sincere thankyou.

Secondly, I would like to thank my co-supervisor Dr. David Lo Jacono. I have learnt a lot working with David and appreciate the time he invested in my project. There is never a dull moment when conducting research with David and I have enjoyed the banter over the years.

I would also like to thank personnel within the Department of Mechanical Engineering at the Technical University of Denmark (DTU) who made me feel welcome while I studied there.

This research would not have been possible without the financial support I received from an Australian Postgraduate Award (APA) scholarship. Further, no research institution can function without the administrative staff who maintain order, thankyou to the administration staff at Monash. I must also acknowledge the creative workmanship of the mechanical and electrical workshop staff within the department who constructed my models during candidature.

I wish to thank my colleagues at Monash for many constructive discussions over the years. Many have become close friends. I must personally thank Mr. Jisheng Zhao, Mr. Andras Nemes and Dr. Justin Leontini who provided many laughs and urged me to finish in the latter stages of candidature. For this, I am very grateful.

Thankyou to my extended family for your continual encouragement and feigning an interest in what I do:) This thesis would not have been possible without the unwavering support of my immediate family and their loved ones; Phillip, Beth, Teresa, Greg, Joanne, Peter and Damien. You have all played a significant role in this process and I could not have done it without you. To all my friends, thank you for the laughs and continual questioning as to when I would finish, this spurred me on. I look forward to catching up soon.

So I as prepare to submit this thesis, I hope the above persons will be glad that I have completed this formidable task, I know I am. Thanks.

List of Publications

Arising from the work reported in this Thesis

Journal papers

1. M. Sherry, D. Lo Jacono, and J. Sheridan, *An experimental investigation of the recirculation zone formed downstream of a forward facing step*, Journal of Wind Engineering and Industrial Aerodynamics, vol 98, pg, 888-894, 2010.
2. M. Sherry, J. Sheridan and D. Lo Jacono, *The effect of turbulence on flow over a forward facing step*, Journal of Wind Engineering and Industrial Aerodynamics, *Under review*, 2012.
3. M. Sherry, J. Sheridan and D. Lo Jacono, *Characterisation of a horizontal axis wind turbine's tip and root vortices*, Experiments in Fluids, *Submitted revised version*, 2012.
4. M. Sherry, D. Lo Jacono and J. Sheridan, *An experimental investigation of flow topography over two dimensional escarpments*, Drafted for submission to *Journal of Wind Engineering and Industrial Aerodynamics*, 2012.
5. M. Sherry, D. Lo Jacono and J. Sheridan, *The effect of turbulence on vortex interaction in the wake of a horizontal axis wind turbine*, Drafted for submission to *Physics of Fluids*, 2012.

Conference papers

1. M. Sherry, J. Sheridan, and D. Lo Jacono, *The effect of turbulence on near wake structure of a horizontal axis wind turbine wake*, In Proceedings of 15th Australasian Wind Engineering Society (AWES) Workshop, Sydney, Australia, February 23-24, 2012.
2. M. Sherry, J. Sheridan, W.Z. Shen and D. Lo Jacono, *The affect (sic) of wind turbine nacelle geometry on near wake structure*, In Proceedings of Gotland Wake Conference, Visby, Sweden, June 08-09, 2011.
3. M. Sherry, J. Sheridan, and D. Lo Jacono, *Turbulence effects on wind flow over complex terrain*, In Proceedings of 17th Australian Fluid Mechanics Conference, Auckland, New Zealand, December 05-09, 2010.

-
4. M. Sherry, J. Sheridan, and D. Lo Jacono, *An experimental study of the vortical wake evolution of the Tjæreborg wind turbine*, In Proceedings of 8th Euromech Fluid Mechanics Conference (EFMC8), Bad Reichenhall, Germany, September 13-16, 2010.
 5. M. Sherry, J. Sheridan, and D. Lo Jacono, *Horizontal axis tip and root vortex measurements*, In Proceedings of 15th International Symposium on Applied Laser Techniques to Fluid Mechanics, Lisbon, Portugal, July 05-08, 2010.
 6. M. Sherry, D. Lo Jacono, J. Sheridan, R. Mathis, and I. Marusic, *Flow separation characterisation of a forward facing step immersed in a turbulent boundary layer*. In Proceedings of 6th International Symposium on Turbulence and Shear Flow Phenomena, Seoul, Korea, June 22-24, 2009.

Conference posters

1. M. Sherry, J. Sheridan, and D. Lo Jacono, *Turbulence effects on the wake of the Tjæreborg turbine*. Presented at 'The Impact of Turbulence on Wind Energy Converters', within the 2010 iTi (interdisciplinary turbulence initiative) conference on turbulence, Bertinoro, Italy, September 23, 2010.

Arising from other work conducted during candidature

Journal papers

1. J.L. Park, M.R. Hodge, S. Al-Mulla, M. Sherry and J. Sheridan, *Air flow around the point of an arrow*, Proceedings of the Institution of Mechanical Engineers, Part P: Journal of Sports Engineering and Technology, December 13, 2011, doi: 10.1177/1754337111430569.

Nomenclature

English Symbols

Symbol	Description
1D	One-dimensional
2D	Two-dimensional
3D	Three-dimensional
A	Turbine rotor area
a	Axial interference factor due to induction
a_c	Axial interference factor loading limit
AR	Aspect ratio
a_t	Tangential interference factor due to induction
A_z	Amplification factor
b	Turbulence mesh bar width
B	number of blades
c	airfoil chord
C_l	2D lift coefficient
C_d	2D drag coefficient
C_l/C_d	lift to drag ratio
C_n	Normal force coefficient
C_t	Tangential force coefficient
C_P	turbine power coefficient
C_T	turbine thrust coefficient
$C_{P,max}$	Lanchester–Betz–Jokowski power coefficient, ~ 0.593

Continued on next page...

Continued from previous page...

Symbol	Description
D	Turbine diameter
Dx	PIV integration window width
Dy	PIV integration window height
dt	Time delay
D^*	Tethered sphere diameter/mesh width ratio
E	control volume energy
f_d	Doppler frequency
F_D	Drag force acting on a blade segment
F_L	Lift force acting on a blade segment
F_N	Normal force acting on a blade segment
F_T	Tangential force acting on a blade segment
F	Prandtl's tip loss factor
F_1	Shen et al. (2005) tip loss factor
F_s	Sloshing frequency
h	helical vortex filament pitch step height
h_{\min}	minimum step height
Hz	Hertz
I_u	Streamwise turbulence intensity
k	turbulent kinetic energy
L^*	Tether length/mesh width ratio
M	Number of pixels Turbulence mesh grid dimensions
\dot{m}	Mass flow rate
n	wind shear exponent
N	Image pair number
P, Q, R	Invariants $\nabla \mathbf{u}$
P	turbine shaft power
P_{avail}	Maximum available power ($1/2\rho AU_\infty^3$) to a turbine

Continued on next page...

Continued from previous page...

Symbol	Description
pm	Γ_1 radius vector
px	pixel
P_k	Mean turbulent kinetic energy production
p_u, p_d	Upstream and downstream pressures on the rotor
p_∞	Freestream pressure
r	Turbine radius
r_{vc}	Vortex core radius
R	Turbine tip radius
R_{cross}	PIV cross correlation function
Re_c	$Re_c = cU_\infty/\nu$
Re_h	$Re_c = hU_\infty/\nu$
Re_M	$Re_c = MU_\infty/\nu$
s_k	Threshold POD eigenvalue
t	Time
T	Rotor thrust
q	B-S induced velocity
Q	Turbine torque
u, v, w	Velocity components in the x, y and z directions respectively
U_∞	Free-stream velocity
U_D	Axial velocity in the rotor plane
U_{rel}	Relative velocity at the turbine blades
$u_{rms}, v_{rms}, w_{rms}$	axial, vertical and transverse root mean square velocities
$\overline{\mathbf{u}'\mathbf{u}'}$	Mean Reynolds longitudinal stress
$\overline{\mathbf{v}'\mathbf{v}'}$	Mean Reynolds vertical stress
$\overline{\mathbf{u}'\mathbf{v}'}$	Mean Reynolds shear stress
u_t	Induced tangential velocity component
U_W	Axial velocity in the far wake
V_θ	Vortex swirl velocity
VA	Vortex age

Continued on next page...

Continued from previous page...

Symbol	Description
\mathbf{w}	total induced velocity on blade
x, y, z	rectangular Cartesian coordinates in physical space
X_L	Mean recirculation region length
Y_1, Y_2	Shen et al. (2005) tip loss factor functions
Y_b	Mean recirculation region height
z_c	Gaussian confidence level
ABL	Atmospheric boundary layer
B–S	Biot–Savart
CAD	Computer aided design
CCD	Charge coupled device
CFD	Computational fluid dynamics
CMOS	Ceramic metal oxide sulphate
CNC	Computer numerically controlled
EMD	Empirical mode decomposition
FFS	Forward facing step
FLAIR	Fluids laboratory for aeronautical and industrial research
H ₂	Hydrogen bubble
HAWT	Horizontal axis wind turbine
IMF	Intrinsic mode function
K–J	Kutta–Joukowski theorem
LDV	Laser doppler velocimetry
LED	Light emitting diode
NACA	National advisory committee for aeronautics
PIV	Particle image velocimetry
PLIF	Planar laser induced fluorescence
POD	Proper orthogonal decomposition
rpm	Rotations per minute
WAsP	Wind atlas analysis and application program

Greek Symbols

Symbol	Description
\int	Integration
α	Angle of attack

Continued on next page...

Continued from previous page...

Symbol	Description
σ	Standard deviation Turbulence mesh solidity
$\sigma(r)$	Blade solidity ratio
δ	Boundary layer thickness
Δ	Discriminant of the characteristic equation of $\nabla \mathbf{u}$
δ/h	Boundary layer to step height ratio
ΔS	Fractional speed up
Δx	Displacement vector
ϵ	Fractional error of $\bar{\mathbf{u}}$ from PIV PIV uncertainty 0.1px Biot-Savart cut off distance
ρ	Density
ψ	Rotor yaw angle Blade coning angle
Ψ	Streamfunction
Ψ_0	Dividing streamline
ϕ	Angle of the relative wind to the rotor plane POD phase average bin number
Γ	Circulation
Γ_B	Blade bound circulation
Γ_1	Vortex identification scheme
Γ_2	Vortex identification scheme
λ	Tip speed ratio Taylor micro length scale
$\lambda(r)$	Local turbine velocity ratio
λ_{ci}^2	Swirling strength criteria
λ_{ci}^*	Threshold swirling strength criteria
λ_l	Laser wavelength
λ_n	POD eigenvalues

Continued on next page...

Continued from previous page...

Symbol Description

Λ_{u_x}	Taylor macro (integral) length scale
$\nabla \mathbf{u}$	Rate of deformation/velocity gradient tensor
$\nabla \mathbf{u}_{2D}$	2D velocity gradient tensor
\mathbf{S}^2	Rate-of-strain tensor
$\mathbf{\Omega}^2$	Rotation tensor
ω	Vorticity vector
θ	Blade twist angle Escarpment angle
θ_1^2	Normal strain rates
θ_2^2	Shear strain rates
θ_M	Angle between \mathbf{pm} and \mathbf{u}
θ_{tip}	Tip pitch angle
θ_{crit}	Critical slope angle for boundary layer separation
$\phi_{\mathbf{n}}(x)$	POD spatial modes
∂_f	LDV fringe spacing
Ω	Turbine rotational rate
η	Kolmogorov length scale
ν	Kinematic viscosity
μ	Dynamic viscosity

Subscripts

Symbol Description

i, j, k	spatial coordinate indices
max	maximum addition value
rms	root mean square value
∞	free-stream value
opt	optimum value

Superscript

Symbol Description

\prime	fluctuating value
----------	-------------------

Contents

1	Introduction	1
1.1	Scope of Thesis	2
1.2	Outline of Thesis	2
2	Literature Review	5
2.1	The near-wake of a horizontal axis wind turbine	6
2.1.1	Vortical wake of a HAWT	8
2.1.2	Helical vortex filaments	11
2.1.3	Meander of trailing vortices	18
2.1.4	Prior works characterising helical vortices in a HAWT wake	20
2.2	Flow over complex terrain	22
2.2.1	Desirable features of complex terrain	24
2.2.2	Un-desirable features of complex terrain	25
2.2.3	Prior works characterising flow over complex terrain	25
2.3	Summary and the need for further research	26
2.4	Present work	27
3	Experimental Techniques, Models and Equipment	29
3.1	Experimental Techniques	29
3.1.1	Particle Image Velocimetry (PIV)	29
3.1.1.1	Details of the PIV system used in this research	31
3.1.1.2	Data processing algorithms	33
3.1.1.3	Energy based filter	38
3.1.2	Laser Doppler Velocimetry (LDV)	43

3.1.3	Flow Visualisation Techniques	46
3.1.3.1	Hydrogen bubble (H ₂)	46
3.1.3.2	Particle streak	48
3.1.3.3	Planar laser induced fluorescence (PLIF)	48
3.2	Experimental Models	51
3.2.1	Flat plate blade sets	51
3.2.2	Airscrew blade sets	51
3.2.3	Geometrically scaled wind turbine rotor	51
3.2.4	Optimum Glauert wind turbine rotor	55
3.2.4.1	Final rotor design	58
3.2.4.2	Model imperfections	59
3.2.5	Wind turbine model components	60
3.2.6	Experimental setup	61
3.2.7	2D escarpment model	63
3.3	Experimental Facility	65
4	Flow over Airfoils at Low Reynolds Numbers	69
4.0.1	Static 3D wing at low Reynolds number	69
4.0.2	Low Reynolds number specific flow features	71
4.0.3	Mean PLIF visualisation results	73
4.0.4	Instantaneous PLIF visualisation results	75
4.0.5	Tip vortex evolution at low Reynolds number	78
4.0.6	Tip vortex properties at low Re_c	84
4.0.7	Meander of fixed wing tip vortices at low Re_c	88
4.1	Summary of the low Reynolds number airfoil study	92
5	Wake Structure of a Geometrically Scaled Rotor	95
5.0.1	H ₂ flow visualisations reveal tip vortex formation	95
5.0.2	Near-wake velocity and vorticity fields	97
5.0.3	Rotor suffers from poor aerodynamic performance at Re_c	107

5.0.4	Vortex Properties	114
5.0.5	Vortex meander	116
5.0.6	Root vortex behaviour	118
5.0.6.1	Nacelle boundary layer vorticity	120
5.0.6.2	Root vortex tower interaction	121
5.0.6.3	Central wake region	122
5.0.7	Root vortex destabilisation	122
5.1	Summary of the geometrically scaled rotor wake data	123
6 Wake Structure of an Optimum Glauert Rotor		125
6.0.1	Tip speed regulation has no effect on wake structure at runaway . . .	125
6.0.2	Phase averaged wake structure	128
6.0.3	BEM analysis of rotor	128
6.0.4	Rotor loading predictions by VST	132
6.0.5	Phase-locked averaged wake structure	134
6.0.6	Tower causes the faster breakdown of vortices in bottom half of wake	137
6.0.7	Stable helical vortex system	139
6.0.8	Near-wake vorticity field and vortex properties	145
6.0.9	Rotor blade flow structure at λ_d	149
6.0.10	Pairing instability affecting the tip vortices	156
6.0.11	The effect of tip speed ratio	159
6.1	Summary of optimum Glauert rotor wake data	163
7 The Effect of Turbulence on the Near-Wake		165
7.0.1	The wind turbine operating environment	165
7.0.2	Turbulence production by passive grids	168
7.0.3	The effect of I_u on the near-wake velocity and vorticity fields	172
7.0.4	Evolution of vortex properties with I_u	176
7.0.5	Meander of the tip and root vortices in a turbulent flow field	182
7.0.6	Momentum transfer in the wake due to turbulent processes	184

7.1	Summary of the near-wake turbulence data	186
8	Complex terrain chapter Summary	193
8.1	An experimental investigation of the recirculation zone formed downstream of a forward facing step	196
8.1.1	Abstract	196
8.1.2	Introduction	196
8.1.3	Experimental facilities	199
8.1.4	Experimental model	200
8.1.5	Results	201
8.1.5.1	Wind turbine placement	210
8.1.6	Forward facing step section summary	212
8.2	The effect of turbulence on flow over a forward facing step	213
8.2.1	Abstract	213
8.2.2	Introduction	213
8.2.3	Experimental Method	215
8.2.3.1	Turbulence Grids	216
8.2.4	Results	218
8.2.4.1	Reynolds stress generation	222
8.2.5	The effect of turbulence section summary	225
8.3	The recirculation region downstream of 2D escarpments	227
8.3.1	Abstract	227
8.3.2	Introduction	227
8.3.3	Experimental setup	230
8.3.4	Experimental model	232
8.3.5	Results	232
8.3.6	Quadrant analysis	239
8.3.7	2D escarpment studies summary	241

9 Thesis Summary	243
9.1 Recommendations for Future Work	244
10 Appendix	247
10.1 Analytical models of a HAWT	247
10.1.1 One-dimensional momentum method without wake rotation	248
10.1.2 One dimensional momentum method with wake rotation	251
10.2 Blade element theory	253
10.3 BEM method	255
10.3.1 Optimum turbine	256
10.3.2 Correction for tip losses	257
10.3.3 Corrections for heavy rotor loading	259
10.3.3.1 BEM code	259
Bibliography	261

List of Tables

2.1	Reattachment length results from previous FFS studies including important study parameters, boundary layer height to step height ratio δ/h , step length aspect ratio L/h , and Reynolds number Re_h	26
3.1	Specifications of the PIV cameras used during candidature. fps represents the maximum frames per second	32
5.1	BEM and PIV analysis of the experimental model in an upwind configuration and full-scale Tjæreborg wind turbine (bold text). $\langle \bar{a} \rangle$: average axial interference factor, $a_{\bar{\phi},PIV}$: axial interference factor from PIV results as determined from equation 5.2, $\langle \bar{a}_t \rangle$: average tangential interference factor, $a_{t,root}$: root region ($x/R = 0.21$) tangential interference factor, $\langle \Gamma_B/RU_\infty \rangle$: normalized average blade bound circulation, $\Gamma_{V,PIV} = \Gamma_T + \Gamma_R $: sum of normalised circulation in the tip and root vortices at 120° (downwind results in brackets), C_T : thrust coefficient.	113
7.1	Turbulence properties of the four flow/grid settings investigated. Grid 1: small grid; Grid 2: large grid; Grid 3: tethered sphere grid.*Note: the solidity ratio of the tethered sphere grid is based on the grid support structure, an alternate solidity ratio could be defined based on the projected area of the spheres, this value is 45%.	170
8.1	Reattachment length results from previous FFS studies including important study parameters, boundary layer height to step height ratio δ/h , step length aspect ratio L/h , and Reynolds number Re_h	198

List of Tables

8.2	Turbulence properties of the four flow/grid settings investigated. Grid 1: small grid; Grid 2: large grid; Grid 3: tethered sphere grid.*Note: the solidity ratio of the tethered sphere grid is based on the grid support structure, an alternate solidity ratio could be defined based on the projected area of the spheres, this value is 45%.	218
8.3	Summary of the recirculation region dimensions with the differing inlet turbulence intensities.	222
8.4	The Reynolds number ranges based on the various Reynolds number definitions. All values in units of thousands	231

List of Figures

2.1	Theoretical vortex wake for a three bladed wind turbine with lifting surface termination prior to the rotational axis. Modified after Ivanell et al. (2010).	10
2.2	Stability boundaries for a single helical vortex filament in an inviscid flow field using the matched asymptotic expansion method (Widnall 1972). Figure taken from Walther et al. (2007).	13
2.3	Stability boundaries for a single (left) and triple (right) helical tip vortex system evaluated using 2.5 (Gupta and Loewy 1974).	14
2.4	Numerical stability results from the simulations by Ivanell et al. (2010) showing the out of phase oscillations leading to wake breakdown for a perturbation frequency of 5.	16
2.5	Wind tunnel smoke flow visualisations by Alfredsson and Dahlberg (1979) showing vortex interaction and coalescence. Figure taken from Ivanell et al. (2010).	16
2.6	Schematic of vortex interaction leading to ‘leapfrogging’ phenomena between two vortex rings. Red arrows indicate the resultant induced velocity. Reproduced after Lim and Nickels (1995)	17
2.7	Smoke visualisation of along filament velocity component of the tip vortices in a HAWT wake (Alfredsson and Dahlberg 1979).	20
2.8	Location of wind farms in Australia indicating prevalence in coastal regions (Geoscience Australia 2010).	23
2.9	Flow features over a 2D escarpment. Left to right: upstream boundary layer profile, upstream recirculation, angled step face, recirculation region of importance to wind energy installations, reattachment point.	24

3.1	Operating principle of dual-frame single-exposure cross-correlation PIV technique illustrating the three primary steps for vector field determination. 1) Image object plane at two instants $t, t + dt$, 2) discretize image plane into interrogation windows of size Dx and Dy , 3) Determine average pixel displacements within interrogation window, dx and dy from peak of cross correlation function $R_{\text{cross,max}}$ (modified after figure 1.11 in (Adrian and Westerweel 2011)).	30
3.2	Flow field topologies based on the determinant and trace of the velocity gradient tensor, $\nabla \mathbf{u}$ (Vollmers 2001), used in the identification of vortices. . . .	35
3.3	Logarithmic decay of the normalised singular value with POD mode number of tip vortices at various vortex ages created at λ_d . s_k is a threshold based on the criteria of Epps and Techet (2010). Between 10 and 25 modes are used depending on vortex age. red triangles: $VA = 120^\circ$ (solid symbol/line) and $VA = 600^\circ$ (hollow symbol/dashed line), blue circles: $VA = 240^\circ$ and $VA = 720^\circ - 840^\circ$, black squares: $VA = 360^\circ$ and $VA = 960^\circ$, green diamonds: $VA = 480^\circ$ and $VA = 1080^\circ - 1200^\circ$	41
3.4	Induced velocity fields of the first 9 reconstructed tip vortex modes at a $VA = 240^\circ$ and λ_d . Contour lines indicate ω_z	42
3.5	Schematic of the process to characterise tip and root vortex meander at a particular vortex age for the optimum Glauert rotor. Step 1: Extract a sub PIV field containing vortex based on phase-locked average data. Step 2: Apply energy filter to instantaneous sub PIV fields and locate vortex centres. Step 3: Generate probability density function (p.d.f) of instantaneous vortex positions in each measurement axis. Fit normal curve to p.d.f and extract standard deviation as measure of meander.	43

3.6	LDV system used during candidature. Components include 1: multicolour beam separator (ColorBurst model 9201, TSI), 2: continuous wave laser (Stabilite 2017, SPECTRA-PHYSICS), 3: laser remote control (model 2670, SPECTRA-PHYSICS), 4: photo detector module (PDM 1000, TSI), 5: signal processor (FSA 3500 MultiBit digital processor, TSI), 6: LDV probe head (Model 9253-350, TSI), 7: (not shown) computer station with specialist software (Flowsizer, TSI), 8: laser shield, 9: power conditioner (SOLA 210 series, SOLA)	45
3.7	Power spectral density (PSD) function behind a passive turbulence grid evaluated by the slotted method in the Flowsizer LDV software. black: $x/M = 12.4$, red: $x/M = 30.4$	45
3.8	Side view of the experimental setup of the hydrogen bubble rig used in flow visualisations. A single blade is aligned with the tower section in the phase-locked visualisations. Freestream flow, U_∞ is from left to right aligned with positive x -axis, y and z axis follow a right handed coordinate system. Channel depth reduced in figure. Images were captured in the x - z plane.	47
3.9	Examples of H2 technique, 3D wing: $\alpha = 10^\circ$ at $x/c = 0.5, 1.0, 1.5$; Rotating turbine blades: $\lambda = 6.62$	48
3.10	Particle streak flow visualisation sequence in the x - y plane (120° progression A–D) showing blade passage, rotating cavity flow (below rc marker and white circles), root vortex (above rv1 and rv2 markers) passage and recirculation region (marker rr) behind nacelle. Bottom images, expanded view of white circle regions. Flow from left to right, $\lambda = 7, Re_c = 2900$, particle streak lengths show qualitative instantaneous velocities.	49
3.11	Suction surface flow patterns above a NACA4412 airfoil at $\alpha = 10^\circ$ (left) and $\alpha = 20^\circ$ (right) at $Re_c = 3484$. Leading edge separation is evident for $\alpha = 20^\circ$	50
3.12	Views of the fullscale Tjæreborg wind turbine. Images winddata.com	52

List of Figures

3.13 Aerodynamic properties of the NACA44XX airfoil at a Reynolds number of 6×10^6 (Oye 1990). left: lift coefficient C_l , right: drag coefficient C_d . Solid line (-): 4412, dashed line(- -): 4415, small dash(- ·): 4418, dots(· · ·): 4421 and dash dot(- ·): 4424. The effect of airfoil thickness on the lift coefficient is clearly shown in the inset. 53

3.14 The NACA4412 airfoil profile used in the tip region of the full scale Tjæreborg turbine and along the entire span of the geometrically scaled experimental model. The dashed line depicts the mean camber line. Length and thickness non-dimensionalised by the chord length. 53

3.15 Geometrically scaled model of the Tjæreborg fullscale wind turbine. left: span-wise chord and twist angle variation. Origin taken as the tip quarter chord position. The NACA4412 airfoil profile was along entire span. Length dimensions are made dimensionless by the rotor radius. Tip, root and the leading and trailing edge profiles are shown in red for clarity. right: 3D CAD model used to manufacture the blade set. 54

3.16 Fluid and body velocity vectors and the resulting forces experienced by a cross-sectional element of a wind turbine blade. Freestream flow is from bottom to top, resulting blade rotation is left in the rotor plane, α is the angle of attack, a and a_t are the axial and tangential interference factors at the blade section respectively. 56

3.17 The effect of airfoil section lift to drag ratio, L/D and tip speed ratio, λ on the maximum power coefficient, $C_{p,max}$, of an optimum three bladed turbine. Solid lines: L/D increments of 20, dotted line: Lanchester–Betz-Joukowski limit ($C_{p,L-B} = 0.593$). 56

3.18 Sectional airfoil performance of the NACA4412 at a Reynolds number of 4.21×10^4 , left: α vs. C_l shaded areas A,B and C depict the attached, pre-stall and post-stall regions respectively. right: C_d vs. C_l polar (Jacobs and Sherman 1937). 57

3.19	Left: Spanwise variation of the optimum rotor chord and twist angle. Tip, root and the leading and trailing edge profiles are shown in red for clarity. Right: Planform view of single blades.	59
3.20	Experimental setup of the water channel and PIV data acquisition configuration used in the rotor wake studies. The turbine model is placed inverted in the channel and a measurement field of view in the lower half of the wake is shown. The laser sheet is shown intersecting the vertical centre-plane (<i>i.e.</i> the x - y plane) along with a single helical vortex filament.	62
3.21	Schematic of the 2D escarpment model constructed out of polycarbonate and acrylic. The escarpment height could be varied in the range, $15 \text{ mm} \leq h \leq 45 \text{ mm}$. The escarpment angle could be varied in the range $30^\circ \leq \theta \leq 90^\circ$. $L = W = 500 \text{ mm}$. Height of end plates is 210 mm	63
3.22	The upstream boundary layer profile measured at $9h_{\min}$ upstream of the step using 2500 independent PIV images. Only every fifth data point is presented for clarity.	64
3.23	Schematic of FLAIR free surface water channel	65
3.24	Characterisation of the velocity field in the FLAIR free surface water channel by Leweke (2002) at two reference speeds. left: $U_\infty = 0.27\text{m/s}$, right: $U_\infty = 0.06\text{m/s}$. Flow uniformity is seen outside the influence of the boundary layers.	67
4.1	Time averaged flow features of a laminar separation bubble on the suction side of an airfoil. S : separation point, R : reattachment point, T : maximum vertical displacement where transition is most likely (Horton 1968).	71
4.2	PLIF visualisation schematic showing the seeding of the fluorescent substance in the application area (AA) on the pressure side (+) of the wing. Fluorescent material is transported around the trailing edge into the separation zone and reveals the separated shear layer downstream of the separation point (S).	73

List of Figures

- 4.3 PLIF mean flow visualisation results in the angle of attack range $-5^\circ < \alpha < 30^\circ$ for the NACA4412 airfoil profile at a Reynolds number of $Re_c=3484$. The movement of the separation point toward the airfoil leading edge with increasing angle of attack is clearly visible. 74
- 4.4 PLIF mean flow visualisation results showing the effect of Reynolds number for $\alpha = 10^\circ$ and $\alpha = 15^\circ$ for the NACA4412 airfoil profile at Reynolds number of $Re_c=3484$ and $Re_c=5300$ 75
- 4.5 PLIF instantaneous flow visualisation results in the angle of attack range $-5^\circ < \alpha < 30^\circ$ for the NACA4412 airfoil profile at a Reynolds number of $Re_c=3484$. The movement of the separation point toward the airfoil leading edge with increasing angle of attack is clearly visible. The formation length of a K-H instability also shortens with increasing angle of attack. 77
- 4.6 PLIF instantaneous flow visualisation results showing the effect of Reynolds number for $\alpha = 10^\circ$ and $\alpha = 15^\circ$ for the NACA4412 airfoil profile at $Re_c=3484$ and $Re_c=5300$. Also shown is the PLIF visualisation of Alam et al. for a NACA0012 airfoil at 10° and $Re_c = 5300$ 78
- 4.7 Experimental setup of H2 tip vortex visualisations. The H2 probe was fixed at $0.25c$ upstream of the image plane/light sheet. The image plane distance x/c was varied manually. 79
- 4.8 Composite hydrogen bubble flow visualisations of the tip vortex formed by the bluff tip at in the angle of attack range $0^\circ \leq \alpha \leq 20^\circ$ and streamwise planes $0.5 \leq x/c \leq 1.5$. Top: $x/c = 0.5$, Middle: $x/c = 1.0$, Bottom: $x/c = 1.5$, $Re_c = 6700$ 81
- 4.9 Velocity vector field of the tip vortex at $x/c = 0.5$ and $\alpha = 10^\circ$, $Re_c = 6400$. Every second data point is shown for clarity and the vector size has been decreased by a factor of 6. The swirling motion of the tip vortex is clearly evident in the centre of the figure. 82

4.10 Mean non-dimensional axial vorticity, $\overline{\omega_x}c/U_\infty$, contours of the tip vortex formed by a NACA4412 airfoil profile with a bluff tip shape at $Re_c = 6400$. Airfoil profile and trailing edge are depicted by the dashed and solid lines respectively. left: $x/c = 0.5$, middle: $x/c = 1.0$ right: $x/c = 1.5$. top: $\alpha = 0^\circ$, middle: $\alpha = 5^\circ$ and bottom: $\alpha = 10^\circ$	84
4.11 Description as for figure 4.10. top: $\alpha = 15^\circ$, bottom: $\alpha = 20^\circ$	85
4.12 Variation of the mean normal location on the tip vortices with angle of attack at $Re_c = 6400$. The tip vortices form in board of the tip. Red: $x/c = 0.5$, blue: $x/c = 1.0$ black: $x/c = 1.5$	85
4.13 Tip vortex circulation, $100\Gamma/cU_\infty$, variation with angle of attack at $Re_c = 6400$. Circulation increases with angle of attack until leading edge separation occurs. Red triangles: $x/c = 0.5$, blue circles: $x/c = 1.0$, black squares: $x/c = 1.5$	86
4.14 Tip vortex maximum tangential velocity, $\overline{V}_{\theta,max}/U_\infty$, variation with angle of attack at $Re_c = 6400$. Red triangles: $x/c = 0.5$, blue circles: $x/c = 1.0$, black squares: $x/c = 1.5$	87
4.15 Tip vortex maximum squared swirling strength, λ_{ci}^2 at $Re_c = 6400$. Red triangles: $x/c = 0.5$, blue circles: $x/c = 1.0$, black squares: $x/c = 1.5$	87
4.16 Tip vortex core radius, $100r_{vc}/c$, variation with angle of attack at $Re_c = 6400$. Red triangles: $x/c = 0.5$, blue circles: $x/c = 1.0$, black squares: $x/c = 1.5$	88
4.17 Instantaneous vortex position fluctuations relative to the mean location indicating tip vortex meander for $\alpha = 5^\circ$, $x/c = 0.5$, $Re_c = 6400$	89
4.18 Probability density functions (p.d.f) of the instantaneous vortex locations at $Re_c = 6400$. top: transverse, Δ_z , bottom: normal, Δ_y , left: $x/c = 0.5$, middle: $x/c = 1.0$, right: $x/c = 1.5$. red circles: $\alpha = 0^\circ$, blue squares: $\alpha = 5^\circ$, black delta: $\alpha = 10^\circ$, orange diamonds: $\alpha = 15^\circ$, green nabla: $\alpha = 20^\circ$. Symbols indicate histogram values whereas solid lines indicate normal distribution applied to data.	90

List of Figures

4.19 Tip vortex meander amplitude for different angles of attack and wake distances at $Re_c = 6400$. Solid line: tranverse meander magnitude, σ_z/c , dashed line: normal meander magnitude, σ_y/c . red lines: $x/c = 0.5$, blue lines: $x/c = 1.0$ and black lines: $x/c = 1.5$ 91

5.1 Phase-locked average H2 flow visualisations. U_∞ as shown with the H2 probe visible upstream. The first tip vortex in the visualisations is 30° old. The tip vortex shear layer trajectory (TVSLT) is indicated in the $\lambda = 8.11$ results. The front stagnation point on the hub is also visible. The helicoidal pitch reduces and wake expansion increases reducing tip speed ratio. 97

5.2 Tip vortex axial positions extracted from the phase-locked average H2 flow visualisations. $\lambda = 3.31$: red circles–solid line/symbols, $\lambda = 4.01$: blue squares–solid line/symbols, $\lambda = 5.12$: black triangles–solid line/symbols, $\lambda = 6.62$: red circles–dashed line/hollow symbols, $\lambda = 8.11$: blue squares–dashed line/hollow symbols, $\lambda = 9.61$: black triangles–dashed line/hollow symbols. 98

5.3 Cumulative mean of the fluctuating velocity components indicating convergence prior to $N = 300$ image pairs. Upwind configuration, $\lambda_{d,f-s}$, $VA = 120^\circ$, $Nx = Ny = 42$. red: $C(\langle \overline{u'u'} \rangle)$, blue: $C(\langle \overline{v'v'} \rangle)$, black: $C(\langle \overline{v'v'} \rangle)$ 99

5.4 Phase-locked average wake of the Tjæreborg wind turbine operating in an upwind configuration at $\lambda_{d,f-s}$. Left: Contours of axial velocity, \bar{u}/U_∞ , dashed line encapsulates region of mean reverse flow, velocity gradients due to tip and root vortices are visible at the tip radius and close to nacelle respectively. Right: wake velocity profiles, $x/R = 0.5$ (—), $x/R = 1.0$ (---), $x/R = 1.5$ (⋯) 100

5.5 Caption as for figure 5.4. Downwind configuration, $\lambda = 4$ 101

5.6 Caption as for figure 5.4. Downwind configuration, $\lambda = 10$ 101

5.7 Caption as for figure 5.4. Downwind configuration, $\lambda_{d,f-s}$ 102

5.8 Caption as for figure 5.4. Downwind configuration, $\lambda = 4$ 102

5.9 Caption as for figure 5.4. Downwind configuration, $\lambda = 10$ 103

5.10 Phase-locked average wake of the Tjæreborg wind turbine operating in an downwind configuration at $\lambda_{d,f-s}$ depicting the coherent vortical structures which dominate the near wake, contours of non-dimensional tangential vorticity, $\overline{\omega_z}R/U_\infty$	104
5.11 Phase-locked average wake of the Tjæreborg wind turbine operating in an upwind configuration at $\lambda_{d,f-s}$ depicting the coherent vortical structures which dominate the near wake, contours of non-dimensional tangential vorticity, $\overline{\omega_z}R/U_\infty$	104
5.12 Caption as for figure 5.10. Downwind configuration, $\lambda = 4$	105
5.13 Caption as for figure 5.11. Upwind configuration, $\lambda = 4$	105
5.14 Caption as for figure 5.10. Downwind configuration, $\lambda = 10$	106
5.15 Caption as for figure 5.11. Upwind configuration, $\lambda = 10$	106
5.16 Mean axial (left) and radial (right) position of the tip vortices with increasing vortex age. Trend lines have been applied to the axial positions only. Dashed lines and hollow symbols: downwind results; solid lines and solid symbols: upwind results.	108
5.17 Angle of attack distribution, $\alpha(r)$, as determined by a BEM analysis for the three tip speed ratios. black: $\lambda = 4$, blue: $\lambda_{d,f-s}$, red: $\lambda = 10$. The blade twist angle distribution $\theta(r)$ is also indicated by the orange dashed line. The shaded area indicates where leading edge separation is likely based on static airfoil PLIF flow visualisations.	109
5.18 Axial interference factor distributions, $\overline{a}(r)$ (solid line), $a_B(r)$ (dashed line) as determined by a BEM analysis for the three tip speed ratios. black: $\lambda = 4$, blue: $\lambda_{d,f-s}$, red: $\lambda = 10$	111
5.19 Tangential interference factor distributions, $\overline{a_t}(r)$ (solid line) and $a_{t,B}(r)$ (dashed line) as determined by a BEM analysis for the three λ . black: $\lambda = 4$, blue: $\lambda_{d,f-s}$, red: $\lambda = 10$	112

List of Figures

5.20 Dimensionless blade bound circulation distribution, $100\Gamma_B(r)/RU_\infty$ as determined by a BEM analysis and the K-J theorem for the three tip speed ratios. black: $\lambda = 4$, blue: $\lambda_{d,f-s}$, red: $\lambda = 10$ 113

5.21 Vortex induced flow field parameters of a tip vortex at a vortex age of 120° , $\lambda_{d,f-s}$, $Re_c = 2900$, $MF = 78$ px/mm, upwind configuration. **a)** $\bar{\mathbf{u}}'/U_\infty$, **b)** $\bar{\mathbf{v}}'/U_\infty$, **c)** $\bar{\omega}_z R/U_\infty$, **d)** $\bar{\mathbf{u}}'^2/U_\infty^2$, **e)** $\bar{\mathbf{v}}'^2/U_\infty^2$, **f)** $\bar{\mathbf{u}}'\bar{\mathbf{v}}'/U_\infty^2$ 115

5.22 Tip vortex circulation, Γ , (left) and vortex core radius, r_{vc} , (right) variation with vortex age. Dashed lines and hollow symbols: downwind results, solid lines and symbols: upwind results. The black circles, blue triangles and red squares represent $\lambda = 4$, $\lambda_{d,f-s}$, and $\lambda = 10$ respectively. 115

5.23 Streamwise and radial tip vortex meander increase with vortex age, dashed lines and hollow symbols - downwind results, solid lines and symbols - upwind results black lines: $\lambda = 4$, blue lines: $\lambda_{d,f-s}$, red lines: $\lambda = 10$ 117

5.24 Particle streak flow visualisation sequence in the x - y plane (120° progression A–D) showing blade passage, rotating cavity flow (below rc marker and white circles), root vortex (above rv1 and rv2 markers) passage and recirculation region (marker rr) behind nacelle. Bottom images, expanded view of white circle regions. Flow from left to right, $\lambda_{d,f-s}$, $Re_c = 2900$, particle streak lengths show qualitative instantaneous velocities. 120

6.1 Sample encoder traces for the drive (red) and free (black) cases showing the periodic variation in free case due to a sloshing motion in the water channel. 127

6.2 Near wake velocity field of a driven (top) and freely spinning (bottom) optimum Glauert rotor at a runaway tip speed ratio of $\lambda_R = 6.07$, $U_\infty = 0.2\text{m/s}$, $Re_{c(R)} = 14.187 \times 10^3$. Freestream flow is from left to right, contours of non-dimensionalised streamwise velocity, \bar{u}/U_∞ . Velocity gradients due to tip and root vortices are clearly visible and persist for some distance. 128

6.3	Vortical wake of a driven (top) and freely spinning (bottom) optimum Glauert rotor at a runaway tip speed ratio of $\lambda_R = 6.07$, $U_\infty = 0.2\text{m/s}$, $Re_{c(R)} = 14.187 \times 10^3$. Contours of non-dimensionalised out of plane vorticity, $\overline{\omega_z}R/U_\infty$. Tip and root vortices are clearly visible in the wake and persist for some distance.	129
6.4	Blade AOA variation with tip speed ratio range ($2.0 \leq \lambda \leq 6.07$) and spanwise location. blue: $\lambda_d = 3.50$, red: $\lambda_R = 6.07$, black: $\lambda = 2.00$. Dashed black lines indicate $\lambda = 0.5$ increments. The shaded area indicates region where leading edge separation likely from static flow visualisations presented in chapter 4. The black region indicates the nacelle location.	130
6.5	Axial (left) and tangential (right) interference factor variation with tip speed ratio. λ range, lines and colours as for figure 6.4.	131
6.6	Spanwise Reynolds number variation with tip speed ratio. λ range, lines and colours as for figure 6.4.	131
6.7	Blade bound circulation distributions for three tip speed ratios. blue: $\lambda_d = 3.5$, red: $\lambda_R = 6.0$, black: $\lambda = 2.0$	132
6.8	Upstream velocity profile of the optimum Glauert rotor operating at $\lambda_d = 3.5$ (blue) and $\lambda_R = 6.07$ (red). Error bars represent the rms magnitudes. The dashed blue and red lines represent the VST (Johnson 1980) predictions for $\bar{a} = 0.21$ and $\bar{a} = 0.25$. The solid line is the VST predictions for a_{opt}	133
6.9	Phase-averaged near wake axial velocity field near the design tip speed ratio, $\lambda_d = 3.55$. Wake expansion is evident by the line indicating the wake boundary, $\bar{u}/U_\infty = 1$	134
6.10	Phase-averaged near wake axial velocity profiles near the design tip speed ratio, $\lambda_d = 3.55$. left: $0.5 \leq x/R \leq 7.5$, right: $1.0 \leq x/R \leq 8.0$, $1.0R$ resolution. The red and blue lines indicate the first and last profile in the range. By $x/R = 8.0$, the wake velocity deficit reduces smoothly toward rotational axis.	135
6.11	Phase-averaged near wake turbulent kinetic energy, \bar{k}/U_∞^2 , field near the design tip speed ratio, $\lambda_d = 3.55$. Elevated \bar{k} correspond to vortex locations and regions of intense mixing in the wake.	136

List of Figures

6.12	Near wake out-of-plane vorticity, $\overline{\omega_z}R/U_\infty$, field near the design tip speed ratio, $\lambda_d = 3.55$	137
6.13	Near wake axial velocity contour plot at the design tip speed ratio, $\lambda_d = 3.5$. Contour lines indicate location of tip and root vortices.	138
6.14	Near wake radial velocity contour plot at the design tip speed ratio, $\lambda_d = 3.5$. Contour lines indicate location of tip and root vortices.	139
6.15	Near wake phase-locked axial velocity profiles at the design tip speed ratio, $\lambda_d = 3.5$. left: $0.5 \leq x/R \leq 4.5$, right: $1.0 \leq x/R \leq 5.0$, $1.0R$ resolution. Red and blue lines indicates first and last profile in the range. Jet like structures due to the lifting surface termination in the root section are clearly evident at $x/R = 0.5$	139
6.16	The affect of blade number on the attainable power coefficient attainable with an optimum Glauert rotor. red: 1 blade, blue: 2 blades and black: 3 blades. L/D ratio of 5 and ∞ shown.	140
6.17	Phase-locked average streamwise velocity field of a one-blade configuration of the optimum 3 bladed rotor at a tip speed ratio approaching runaway of $\lambda = 5.71$	141
6.18	Vortical wake of the on-bladed optimum rotor configuration at a tip speed ratio approaching runaway of $\lambda = 5.71$	141
6.19	Trajectory of the tip vortices of the single bladed optimum rotor at a tip speed ratio approaching runaway of $\lambda = 5.71$	142
6.20	Mean tip (black) and root (red) vortex property variation with vortex age for the one bladed configuration at a tip speed ratio approaching runaway of $\lambda = 5.71$. Left: non-dimensionalised circulation and right, non-dimensionalised core radius. Dashed line and hollow symbols, Γ_2 data, solid line and symbols, λ_{ci}^2 data.	143

6.21 Normalised probability density functions of the axial (left) and radial (right) instantaneous deviations from the phase-locked tip vortex mean position. One-bladed optimum rotor configuration at a tip speed ratio approaching runaway of $\lambda = 5.71$. Curves represent tip vortices at different vortex ages, ($k \times 360^\circ$). Solid red circle/line: $k = 1$, solid blue square/line: $k = 2$, solid black triangle/line: $k = 3$, solid orange diamond/line: $k = 4$, solid green nabla/line: $k = 5$, hollow/dashed red circle/line: $k = 6$, hollow/dashed blue square/line: $k = 7$, hollow/dashed black triangle/line: $k = 8$, hollow/dashed orange diamond/line: $k = 9$ 144

6.22 Tip vortex meander magnitude variation with vortex age. Left: raw results, right: results corrected for water channel sloshing (*i.e.* $\sigma_x = \sigma_x - \sigma_{x(\text{VA}=360^\circ)}$). Single bladed optimum rotor at a tip speed ratio approaching runaway of $\lambda = 5.71$ 144

6.23 Near wake vorticity contour plot at the design tip speed ratio, $\lambda_d = 3.5$. Tip vortices are seen in both the upper (red) and lower (blue) portions of the wake. Root vortices are also seen in the upper (blue) and lower (red) portions of the wake. The vortices in the lower part of the wake are 60° younger than those in the upper half of the wake. The vortices in the lower half of the wake degenerate rapidly due to the wake of the tower structure. 146

6.24 Tip vortex properties in the top (black) and bottom (red) wake halves for the three bladed optimum rotor at a tip speed ratio near the design $\lambda = 3.55$. Circulation is shown on the left whereas vortex radius is shown on the right. 147

6.25 Axial (left) and radial (right) tip (black) and root (red) vortex positions in the top half of the wake at $\lambda = 3.55$. The shaded region indicates where vortex interaction occurs. 148

List of Figures

6.26 Experimental setup to determine the tangential velocity component and the spanwise circulation distribution. U_∞ is aligned with the positive x direction and the blade rotates at an angular speed Ω . The laser sheet illuminates an x - z plane. The camera is perpendicular to the laser sheet indicated by the black circle in the middle of the image plane. 150

6.27 Plan form view of the blade with dashed lines illustrating the spanwise locations where data was captured in the x - z plane. **a)** $y/R = 1.09$, **b)** $y/R = 1.00$, **c)** $y/R = 0.91$, **d)** $y/R = 0.83$, **e)** $y/R = 0.74$, **f)** $y/R = 0.65$, **g)** $y/R = 0.57$, **h)** $y/R = 0.48$, **i)** $y/R = 0.39$, **j)** $y/R = 0.24$ 151

6.28 Axial velocity profiles generated by the rotating wind turbine blade at spanwise positions $0.65 \leq y/R \leq 1.09$. The solid black line encapsulates region of entirely negative flow. The airfoil profile is shown in white. 152

6.29 Caption as for figure 6.28 for spanwise positions $0.245 \leq y/R \leq 0.57$ 153

6.30 Azimuthal velocity profiles generated by the rotating wind turbine blade at spanwise positions $0.65 \leq y/R \leq 1.1$. Flow separation can be seen. Airfoil section is shown in white. 154

6.31 Azimuthal velocity profiles generated by the rotating wind turbine blade at spanwise positions $0.245 \leq y/R \leq 0.57$. Flow separation can be seen. Airfoil section is shown in white. 155

6.32 Dependence of blade bound circulation on the integration path length. Solid red: **b)**, solid blue: **c)**, solid black: **d)**, dashed red: **e)**, dashed red: **f)**, dashed red: **g)**. 155

6.33 Spanwise variation of the blade bound circulation calculated by experimentally (red) and by a BEM method (blue) at λ_d . Error bars indicate the circulation calculated at $y/R = 1.09$ 156

6.34 Scatter plot of tip and root vortex meander for the three bladed optimum Glauert rotor operating at $\lambda = 3.55$. Colour indicates blade number which created vortex. Meander magnitude increases with vortex age. 157

6.35	Tip and root vortex meander in the radial (hollow) and axial (filled) directions at λ_d . Left: raw results, right: results corrected for water channel sloshing (<i>i.e.</i> $\sigma_x = \sigma_x - \sigma_{x(\text{VA}=120^\circ)}$). Meander magnitude increases with vortex age.	158
6.36	Average streamwise velocity field (left) and profiles in the range $0.5 \leq x/R \leq 3.5$ with $0.5R$ resolution at the runaway tip speed ratio in the top half of the wake.	159
6.37	Vortex wake at the runaway tip speed ratio in the top half of the wake.	160
6.38	Axial (left) and radial (right) tip (black) and root (red) vortex positions in the top half of the wake at $\lambda_R = 6.07$. The shaded region indicates where vortex interaction occurs.	161
6.39	Mean tip (black) and root (red) vortex property variation with vortex age for the three bladed configuration at $\lambda_R = 6.07$. Left: non-dimensionalised circulation and right, non-dimensionalised core radius. Dashed line and hollow symbols, Γ_2 data, solid line and symbols, λ_{ci}^2 data.	162
6.40	Scatter plot of tip vortex meander for the optimum Glauert rotor operating at λ_R . Colour indicates blade number which created vortex. Meander magnitude increases with vortex age.	162
6.41	Tip (black) and root (red) vortex meander in the radial (hollow) and axial (filled) directions for the optimum Glauert rotor operating at λ_R . Left: raw results, right: results corrected for water channel sloshing (<i>i.e.</i> $\sigma_x = \sigma_x - \sigma_{x(\text{VA}=120^\circ)}$). Meander magnitude increases with vortex age.	163
7.1	The effect of inflow turbulence on the evolution of numerically generated wake vortical structures behind the Tjæreborg wind turbine at the design tip speed ratio of $\lambda_d = 7.07$ (Troldborg et al. 2007). Iso-contours of vorticity on an equivalent x - y plane through the rotational axis. Top: uniform inflow, $I_u \sim 0\%$. Bottom: turbulent inflow, $I_u = 14\%$. Scale bar represents $1R$	167

List of Figures

7.2	Passive turbulence grid geometries. Left: Grids are defined by the mesh size, M , and the bar width, b . Centre: Tethered sphere turbulence grid with sphere diameter to mesh size ratio, $D^* = 0.75$. Shade of sphere indicates tether length; light: $L^* = 1.5$, dark: $L^* = 2$. Right: isometric view of tethered sphere grid, only spheres of a single tether length are shown for clarity.	169
7.3	Streamwise and normal turbulence intensity variation with streamwise distance as measured by the LDV; black circles – grid 3, red squares – grid 2. Solid symbols, I_u , hollow symbols, I_v	170
7.4	Local turbulence intensity, $I_u(r)$, distribution at $\lambda_d = 3.5$. Dashed blue and black lines indicates BEM derived α and U_{rel} distributions. Red line: grid 1, blue line: grid 2, black line: grid 3.	171
7.5	Average streamwise velocity contours downstream of turbulence grid 3, $I_u = 6.2\%$, $\lambda = 3.73$, $x/M = 28.7$	172
7.6	Phase-locked averaged streamwise velocity contours downstream of turbulence grid 1, $I_u = 1.68\%$, $\lambda = 3.24$, $x/M = 140$	173
7.7	Phase-locked averaged streamwise velocity contours downstream of turbulence grid 2, $I_u = 2.26\%$, $\lambda = 3.26$, $x/M = 35.5$	174
7.8	Phase-locked averaged streamwise velocity contours downstream of turbulence grid 3, $I_u = 6.2\%$, $\lambda = 3.73$, $x/M = 28.7$	174
7.9	Evolution of the streamwise velocity component at two wake locations in the three turbulence intensity levels. solid lines: $x/R = 0.5$, dashed lines: $x/R = 5.5$. Red lines: grid 1, blue lines: grid 2, black lines: grid 3.	174
7.10	Phase-locked average out-of-plane vorticity field, $\overline{\omega_z}R/U_\infty$, behind turbulence grid 1, $I_u = 1.68\%$, $\lambda = 3.24$, $x/M = 140$	175
7.11	Phase-locked average out-of-plane vorticity field, $\overline{\omega_z}R/U_\infty$, behind turbulence grid 2, $I_u = 2.24\%$, $\lambda = 3.26$, $x/M = 35.5$	175
7.12	Phase-locked average out-of-plane vorticity field, $\overline{\omega_z}R/U_\infty$, behind turbulence grid 3, $I_u = 6.2\%$, $\lambda = 3.73$, $x/M = 28.7$	176

7.13 Mean axial (left) and radial (right) vortex positions for the three turbulence intensities. Solid lines and solid symbols: tip vortices, dashed lines and hollow symbols: root vortices. Red: grid 1, Blue: grid 2: Black: grid 3.	177
7.14 Mean tip (left) and root (right) vortex circulation determined by the two vortex identification mechanisms. Solid lines and solid symbols: λ_{ci}^2 , dashed lines and hollow symbols: Γ_2^* . Red: grid 1, Blue: grid 2: Black: grid 3.	179
7.15 Mean tip (left) and root (right) vortex core radius determined by the two vortex identification mechanisms. Solid lines and solid symbols: λ_{ci}^{2*} , dashed lines and hollow symbols: Γ_2^* . Red: grid 1, Blue: grid 2: Black: grid 3.	180
7.16 Mean maximum, $\overline{V_{\theta_{max}}}$, (dashed lines hollow symbols) and azimuthally averaged, $\overline{\langle V_{\theta} \rangle}$, (solid lines and solid symbols) tangential velocity of the tip (left) and root (right) vortices along Γ_2^* . Red: grid 1, Blue: grid 2: Black: grid 3.	181
7.17 Mean difference between the line integral derived tip (left) vortex circulation and that calculated by equation 7.7. Solid lines and solid symbols: λ_{ci}^{2*} , dashed lines and hollow symbols: Γ_2^* . Red: grid 1, Blue: grid 2: Black: grid 3.	181
7.18 Tip and root vortex scatter in the measurement plane behind turbulence grid 1, $I_u = 1.68\%$, $\lambda = 3.24$, $x/M = 140$	182
7.19 Tip and root vortex scatter in the measurement plane behind turbulence grid 2, $I_u = 2.26\%$, $\lambda = 3.26$, $x/M = 35.5$	183
7.20 Tip and root vortex scatter in the measurement plane behind turbulence grid 3, $I_u = 6.2\%$, $\lambda = 3.73$, $x/M = 28.7$	183
7.21 Vortex meander of the tip (left) and root (right) vortices with varying freestream turbulence intensity. Hollow symbols: radial meander, solid symbols: axial meander. Magenta: no grid, red: grid 1, blue: grid 2, black: grid 3.	184
7.22 Reynolds shear stress, $\overline{\mathbf{u}'\mathbf{v}'}$, field in a low turbulence (no grid) inflow case. $\lambda = 3.5$	185
7.23 Reynolds shear stress, $\overline{\mathbf{u}'\mathbf{v}'}$, field behind turbulence grid 1. $\lambda = 3.24$, $x/M = 140$, $I_u = 1.68\%$	186

List of Figures

7.24	Reynolds shear stress, $\overline{\mathbf{u}'\mathbf{v}'}$, field behind turbulence grid 2. $\lambda = 3.26$, $x/M = 35.5$, $I_u = 2.2\%$	187
7.25	Reynolds shear stress, $\overline{\mathbf{u}'\mathbf{v}'}$, field behind turbulence grid 3. $\lambda = 3.73$, $x/M = 28.7$, $I_u = 6.2\%$	187
8.1	Flow features over a forward facing step (FFS). Left to right: upstream boundary layer profile, upstream recirculation, step face, recirculation region of present interest, reattachment point.	197
8.2	Schematic of the polycarbonate and acrylic experimental model used in the current study. Height of end plates is 210 mm	201
8.3	The upstream boundary layer profile measured at $9h_{h=15\text{mm}}$ upstream of the step using 2500 independent PIV images. Only every fifth data point is presented for clarity.	202
8.4	General bluff body flow features of the FFS flow, contour lines of mean streamwise velocity \bar{u} ; reference value of $1.3 \bar{u}/U_\infty$ shown with line increments equal to $0.2 \bar{u}/U_\infty$; solid line is the dividing streamline Ψ_0 , dashed contour lines depict region of entirely negative flow, $\delta/h = 1.25$, $Re_h = 6741$	203
8.5	Eight phase averages from a POD analysis of the FFS shear layer dynamics for $\delta/h = 1.25$, $Re_h = 6741$. Phase progression is from top to bottom, 1–4 ($0-3\pi/4$) this page, 5–8 ($\pi-7\pi/4$) on following page, contours of mean velocity \bar{u} ; white solid streamlines indicate dynamics of recirculation region shape and size. . .	204
8.6	Streamwise perturbations within the shear layer above a FFS for $\delta/h = 1.25$; $Re_h = 6741$, contours of $\overline{u'u'}/U_\infty^2$; solid line is the dividing streamline Ψ_0 . .	206
8.7	Reynolds shear stress contours produced above a FFS for $\delta/h = 1.25$; $Re_h = 6741$, contours of $-\overline{u'v'}/U_\infty^2$; solid line is the dividing streamline Ψ_0	207
8.8	Variation of X_L with Re_h for three δ/h ratios, $0.83 < \delta/h < 2.5$, \bullet : $\delta/h = 2.5$; \blacksquare : $\delta/h = 1.25$; \blacktriangle : $\delta/h = 0.83$	208
8.9	Contours of the amplification factor, A_z above a FFS for $\delta/h = 1.25$; $Re_h = 6741$. Dashed line indicates position where A_z has a unit value	211

8.10 Schematic of the polycarbonate and acrylic experimental model used in the current study. h fixed at 30 mm, $L = W = 500$ mm. Height of end plates is 210 mm 215

8.11 Passive turbulence grid geometries. Left: Grids are defined by the mesh size, M , and the bar width, b . Centre: Tethered sphere turbulence grid with sphere diameter to mesh size ratio, $D^* = 0.75$. Shade of sphere indicates tether length; light: $L^* = 1.5$, dark: $L^* = 2$. Right: isometric view of tethered sphere grid, only spheres of a single tether length are shown for clarity. 217

8.12 Experimental setup showing the tethered sphere turbulence grid upstream of forward facing step model in the FLAIR water channel. 218

8.13 General bluff body flow features of the FFS flow in four different inlet turbulence intensities for $\delta/h = 1.25$. Isocontours of mean streamwise velocity, \bar{u}/U_∞ ; solid line is the dividing streamline Ψ_0 ; dashed white line encapsulates region of entirely negative flow. a) $I_u = 1.45\%$, $Re_h = 7371$; b) $I_u = 1.85\%$, $Re_h = 7267$; c) $I_u = 3.18\%$, $Re_h = 7250$; d) $I_u = 9.90\%$, $Re_h = 6531$ 219

8.14 Recirculation region reduction with elevated inlet turbulence intensity. Recirculation region downstream of a FFS depicted by dividing streamline (Ψ_0) for the four different inlet turbulence settings, all cases with $\delta/h = 1.25$. Dashed line: no grid $I_u = 1.45\%$, $Re_h = 7371$; long dashed line: small grid $I_u = 1.85\%$, $Re_h = 7267$; dotted line: large grid $I_u = 3.18\%$, $Re_h = 7250$; solid line: tethered sphere grid $I_u = 9.90\%$, $Re_h = 6531$ 220

8.15 Reynolds stress profiles. Top: streamwise; centre: vertical; and bottom: shear profiles above the forward facing step subjected to various inlet turbulence intensities at numerous downstream distances in the wake for $\delta/h = 1.25$. Dashed line: no grid: $I_u = 1.45\%$, $Re_h = 7371$; long dashed line: small grid $I_u = 1.85\%$, $Re_h = 7267$; dotted line: large grid $I_u = 3.18\%$, $Re_h = 7250$; solid line: tethered sphere grid $I_u = 9.9\%$, $Re_h = 6531$. a) $x = 0h$, b) $x = 1h$, c) $x = 2h$, d) $x = 3h$ 224

List of Figures

8.16 Reynolds shear stress contours above a forward facing step subjected to various inlet turbulence intensities for $\delta/h = 1.25$. Isocontours of $\overline{\mathbf{u}'\mathbf{v}'}/U_\infty^2$; solid line is the dividing streamline Ψ_0 , dashed line encapsulates region of entirely negative flow. a) $I_u = 1.45\%$, $Re_h = 7\,371$, b) $I_u = 1.85\%$, $Re_h = 7\,267$, c) $I_u = 3.18\%$, $Re_h = 7\,250$, and d) $I_u = 9.9\%$, $Re_h = 6\,531$ 225

8.17 Flow features over a 2D escarpment. Left to right: upstream boundary layer profile, upstream recirculation, angled step face, recirculation region of present interest, reattachment point. 229

8.18 Streamwise velocity, $\bar{\mathbf{u}}/U_\infty$, variation with escarpment angle, θ for the minimum Reynolds number. 233

8.19 Variation in reattachment length, X_L , with Reynolds number for various step angles 234

8.20 Variation in recirculation region height, Y_b with Reynolds number and escarpment angles 235

8.21 Variation in axial position of Y_b with Reynolds number and escarpment angle. 236

8.22 Variation of the amplification factor, A_z , with escarpment angle, θ , above a 2D escarpment for the minimum Reynolds number. Dashed lines represent a unit A_z value. Solid line represent the dividing streamline. 237

8.23 Average turbulence kinetic energy production term, P_k , variation with escarpment angle, θ , for the minimum Reynolds number. The production term is made dimensionless by the factor U_∞^3/h 238

8.24 Reynolds shear stress, $\overline{\mathbf{u}'\mathbf{v}'}/U_\infty^2$, variation with escarpment angle, θ , for the minimum Reynolds number. 239

8.25 Partition of the $\mathbf{u}'\text{-}\mathbf{v}'$ plane into quadrants. Events in the second quadrant and termed ‘ejections’, whereas events in the fourth quadrant are termed ‘sweeps’ (Emeis et al. 1995). 240

8.26 Quadrant analysis of the $\mathbf{u}'\mathbf{v}'$ field for $\theta = 90^\circ$ and $Re_h = 2.77 \times 10^3$ 241

10.1 One dimensional streamtube analysis of a wind turbine 249

10.2 One dimensional streamtube analysis of a wind turbine with wake rotation 251

10.3 Velocity diagram at the rotor plane at a given spanwise location, r . The angle ϕ is the sum of α -local blade angle of attack and θ -local blade pitch angle. . . 253

10.4 Momentum theory for wind turbines, with the axial interference factor and the thrust coefficient on the horizontal and vertical axes respectively (Eggleston and Stoddard 1987) 259

Chapter 1

Introduction

Wind energy is currently one of the fastest expanding methods of energy generation in the world. The uptake of wind energy is in response to climate change, the most significant environmental issue facing the world today. A wind turbine is a device which converts the kinetic energy of atmospheric surface winds into electricity via a generator. The first documented wind turbine was built by Charles F. Brush in Cleveland, Ohio. It had a rotor diameter of 17 m, 144 blades, a generator capacity of 12kW and operated between 1888 and 1908 (Sørensen 2011). Wind turbines are now highly complex industrial machines operating both on land and at sea around the world. They have generator capacities between 1MW and 6MW and rotor diameters in excess of 100 m.

Wind turbines are seldom placed in isolation. Rather, they are collected in groups. A wind farm is a cluster of wind turbines strategically placed in a location with a high average wind resource. The turbines collectively share required infrastructure to transport the generated electricity to load centres. In large countries such as Australia, these distances may be vast. Economies of scale has seen turbines become larger, wind farms contain more turbines spread out over a larger area.

However, a wind turbine in a wind farm produces less power than a stand alone turbine (Hansen et al. 2012). This is due to the velocity deficit created by the foremost turbine. A internal turbine in such a situation is deemed a wake affected turbine. In addition to the velocity deficit, internal turbines maybe subjected to coherent vortices shed from other turbines (Troldborg et al. 2011). These vortices are dangerous to internal turbines in a wind farm due to the large fluctuating loads they can cause. The distance between turbines in a wind farm is therefore an important wind farm design criteria. The planning and optimisation of a wind farm is known as wind farm siting.

Further, wind farms are not always placed in uniform terrain. Geomorphology may dictate

turbines must be placed in non-uniform terrain. Alternatively, wind farm planners may seek to capitalise on the wind speed-up effects non-uniform terrain produces. However, wind flow in non-uniform terrain may be highly complex with flow separation occurring. Improperly placed turbines in non-uniform terrain will experience increased fatigue and require more frequent maintenance.

Wind farm siting is therefore a balance between maximising energy yield from a given area and minimising turbine loads due to wake interaction and turbulence in non-uniform terrain.

1.1 Scope of Thesis

This thesis aims to further understanding on the flow fields which a wind turbine in a wind farm may experience.

The research has two main aspects.

1. Firstly, it focusses upon the evolution of the tip and root vortices in the near wake of a horizontal axis wind turbine. The main goal of this research is to determine the mechanisms which lead to wake instability.
2. A secondary focus is the flow fields above complex terrain features, a common location for wind farms. The main goal of this research is to determine the suitability of complex terrain as a wind farm location.

1.2 Outline of Thesis

Aside from this introduction, this thesis consists of nine additional chapters and one appendix. A brief overview of each chapter is given below.

Ch.2 presents a critical review of the existing literature concerning the two topics to be investigated. It highlights discrepancies and gaps in knowledge where further research is required.

Ch.3 outlines the experimental techniques, methodologies and models used to acquire and analyse the experimental data to be presented in future chapters.

Ch.4 presents an experimental study of flow over airfoils at low Reynolds numbers. An understanding of low speed airfoil aerodynamics is necessary to design efficient wind turbine models and allow detailed analysis of wind turbine near-wake data.

- Ch.5** details the evolution of the near-wake of a geometrically scaled rotor over the tip speed ratio range $4 \leq \lambda \leq 10$.
- Ch.6** details the evolution of the near-wake of an optimum Glauert rotor at the design and runaway tip speed ratios. The effect of the tower and the mechanisms leading to wake instability are investigated.
- Ch.7** details the evolution of the near-wake of an optimum Glauert rotor wind turbine model subjected to three levels of freestream turbulence intensity. The stability and vortex properties of the tip and root vortices are investigated.
- Ch.8** characterises the recirculation region downstream of 2D escarpments. The suitability of these features as wind farm locations is addressed.
- Ch.9** summarizes the main findings of the thesis and suggests directions for further research.
- Ch.10** details the analytical models used to design the optimum Glauert rotor and assess rotor performance.

Chapter 2

Literature Review

In this chapter a selection of the experimental, some numerical and analytical studies related to wind farm siting are reviewed. The review is split into two sections; the first is concerned with the near-wake of a horizontal axis wind turbine (HAWT) and the second reviews flow over complex terrain.

The first section begins with a discussion of HAWT wake features including the velocity deficit, increased turbulence intensity and helical tip and root vortices. In the case of the helical tip and root vortices, the state of the art will be reviewed in detail because of its relevance to this research. Unless stated a wind turbine refers to a horizontal axis wind turbine.

In the second section, the review will address flow over complex terrain, a common site for wind farms.

This literature review will highlight knowledge deficiencies in the area of wind farm siting. Finally it will propose a plan for an experimental investigation to contribute to the body of knowledge in this area.

2.1 The near-wake of a horizontal axis wind turbine

The wake is an inherent feature of flow past a wind turbine. Wind turbine wakes are important for wind farm siting as wake affected turbines produce less energy (Hansen et al. 2012) and experience greater fatigue (Frandsen and Thøgersen 1999). There have been a number of investigations of wind turbine wakes. The review by Vermeer et al. (2003) detailed the state-of-the-art of HAWT wake aerodynamics and highlighted the need for further detailed experiments in both the near-wake and far-wake regions. Sørensen (2011) also recently reviewed and analysed the state-of-the-art in wind turbine aerodynamics. Here, citations are given for specific features of wind turbine wakes. In the absence of a citation, the review papers by Snel (1998); Vermeer et al. (2003) and Sørensen (2011) can be consulted.

This review focuses on the near-wake region of a wind turbine. The near-wake is the region immediately behind the turbine where the local effect of the rotor remains discernible. However, consensus on the axial extent of the near-wake has not been reached as indicated by the varied estimates of the near-wake cessation point (Crespo et al. 1999; Vermeer et al. 2003; Sanderse 2009). Criteria for transition to the far wake range include one rotor revolution (Micallef et al. 2012), one rotor diameter (Vermeer et al. 2003; Sanderse 2009), tip vortex shear layer reaching the rotational axis (Crespo et al. 1999), absence of rotor profile (*e.g.* blade wakes) and a self similar velocity profile (Burton et al. 2001).

The near-wake is dominated by B coherent rotating helical vortex pairs, where B is the number of blades and a pair consists of a tip and root vortex. As these vortices contain significant angular momentum (Ebert and Wood 2001), they pose the greatest risk to other turbines in a wind farm. These structures require further investigation to determine their lifetime and breakdown mechanisms. Prior to reviewing works investigating the vortical wake of a HAWT, general features of the near wake are presented.

The near-wake and rotor aerodynamics are strongly coupled, the flow over the rotor blades and the blade performance determines the structure of the near-wake. This makes comparisons between experimental results obtained with different models difficult. For example, the velocity deficit magnitude and position depends on turbine operating conditions (Medici and Alfredsson 2006), blade geometry (Krogstad and Adaramola 2011) and inlet conditions (Alfredsson and Dahlberg 1979; Chamorro and Porté-Agel 2009). The velocity deficit maximum is commonly located on the wake centreline. However, a jet structure may form in the central region of the wake (Krogstad and Adaramola 2011) if the lifting surface terminates prior to the rotational axis as occurs on full-scale turbines.

Further, the velocity deficit becomes asymmetric when the turbine operates in a boundary layer inflow due to reduced kinetic energy close to the ground (Alfredsson and Dahlberg 1979; Chamorro and Porté-Agel 2009; Zhang et al. 2012). Boundary layer inflow thus causes asymmetric loading on the rotor plane. Another cause of asymmetric loading with a asymmetric wake velocity profile is yawed inflow (Krogstad and Adaramola 2011). Yawed inflow occurs when the freestream velocity vector, U_∞ , is not perpendicular to the rotor plane. Yawed inflow has been investigated extensively by Grant et al. (1997); Grant and Parkin (2000); Haans et al. (2005); Maeda et al. (2008); Medici and Alfredsson (2006); Krogstad and Adaramola (2011).

The recovery of the velocity deficit in the wake depends on inlet conditions such as turbulence intensity and length scale (Alfredsson and Dahlberg 1979) and boundary layer profile (Chamorro and Porté-Agel 2009). The streamwise turbulence intensity is defined as the ratio of the root mean square (rms) of the fluctuating streamwise velocity component to U_∞ as shown in equation 8.6.

$$I_u = u_{\text{rms}}/U_\infty. \quad (2.1)$$

The turbulence intensity is elevated in the wake by the rotating turbine blades (Chamorro and Porté-Agel 2009). Turbulence intensity levels in the wake are important as they are used as a measure of fatigue of a wind turbine (Frandsen and Thøgersen 1999). The turbulence level is not uniform throughout the wake. Peaks are found close to the tip radius associated with the tip vortices (Alfredsson and Dahlberg 1979) and in the root region (Zhang et al. 2012). After breakdown of the tip vortices, the turbulence level in the wake becomes more uniform (Alfredsson and Dahlberg 1979). The viscous wakes of individual blades also contain high levels of turbulent kinetic energy (Ebert and Wood 1999). The width and intensity of the blade wakes depends on whether flow separation over the blades occurs (Ebert and Wood 1999). Flow separation can be minimised by incorporating a high level of blade twist to ensure attached flow across the entire span (Haans et al. 2008b; Corten et al. 2004; Mikkelsen et al. 2011; Krogstad and Lund 2012). However, the twist of the blades in the root region is typically insufficient to avoid flow separation at low tip speed ratios (Ebert and Wood 1997; Whale et al. 2000). The tip speed ratio shown in equation 2.2 is the ratio between the turbine angular velocity, ΩR , and U_∞ . λ is the principal independent variable in the study of wind turbine wakes. It has a large effect on the tip and root vortices which are reviewed next.

$$\lambda = \frac{\Omega R}{U_\infty}. \quad (2.2)$$

2.1.1 Vortical wake of a HAWT

The helical tip and root vortices which dominate the near-wake region form as a by product of force generation by the blades. From Helmholtz' vortex law, a vortex cannot end in a fluid so circulation is shed into the wake where a spanwise blade bound circulation gradient exists, *i.e.* $\partial\Gamma_B(r)/\partial r \neq 0$. Lifting line theory due to Prandtl can be used to determine the strength of the trailing vortex system, Γ_W , as in equation 2.3 (Betz 1935),

$$\Gamma_W = \int_0^R \partial\Gamma_B(r)/\partial r dr. \quad (2.3)$$

With a uniform $\Gamma_B(r)$ distribution, $\partial\Gamma_B(r)/\partial r$ is largest at lifting surface discontinuities, *e.g.* the tip and root regions. In this case, the wake consists of tip and root vortices of strength equal to the mean $\Gamma_B(r)$. However, $\Gamma_B(r)$ is approximately constant only at the design tip speed ratio (Ebert and Wood 1997; Ivanell et al. 2009). In off design conditions, $\Gamma_B(r)$ varies across the span resulting in a thin vorticity sheet connecting the tip and root vortices.

The helical tip and root vortices are the most interesting and potentially dangerous feature of the near-wake of a wind turbine. They contain significant angular momentum (Ebert and Wood 2001) which poses a risk to other turbines in the wind farm. If spacing between turbines in a wind farm is too small, these coherent structures may interact with other turbines (Troldborg et al. 2011). Such interaction increases the dynamic loading of the wake affected turbines and reduces performance.

Wind turbine tip and root vortices form in an analogous manner to fixed wing tip vortices. At lifting surface discontinuities, pressure equalisation occurs. A 3D fluid flow forms between the high and low pressure surfaces. This 3D fluid flow creates swirl which forms the vortex. The tip and root vortices are of opposite sign. The tip vortices form slightly inboard of the tip due to the negative radial velocity component downstream of the rotor (Micallef et al. 2012). The tip vortex entrains vorticity from the trailing edge vorticity sheet. This process, termed vortex 'roll-up', is dependent on the Reynolds number, Re_c , and Γ_B (Green 1995). The tip chord Reynolds number, Re_c is given in equation 2.4,

$$Re_c(R) = \frac{c_{tip}U_{rel}(R)}{\nu} = \frac{c_{tip}\sqrt{(U_\infty(1 - a_b(R)))^2 + (\lambda U_\infty(1 + a_t(R)))^2}}{\nu}, \quad (2.4)$$

where c_{tip} is the blade tip chord, $a_b(R)$ and $a_t(R)$ are the axial and tangential interference factors at the tip, defined in appendix 10. The relative velocity, U_{rel} , is assumed to consist of only the freestream and blade rotation components.

Roll-up is complete when the tip vortex properties no longer vary with distance (Green 1995; Grant and Parkin 2000). The roll-up of helical vortices is similarly dependent on these parameters. As an example, tip vortex roll-up was completed by a vortex age of $VA = 174^\circ$ in the Grant and Parkin (2000) study. VA is defined as the angular travel in degrees($^\circ$) of the blade which created the helical vortex filament. The turbine yaw angle also significantly affects tip vortex formation (Grant and Parkin 2000). Further, helical tip vortex formation is highly dependent on blade tip shape (Hansen and Johansen 2004). (Haans et al. 2005) showed a symmetrical tip vortex trajectory depends on a uniform inflow.

Root vortices, on the other hand, do not always form in the near-wake of a HAWT. Root vortex formation is highly dependent on the rotor and hub geometries. Root vortices tend not to form when the lifting surface extends to the rotational axis (Grant and Parkin 2000; Dobrev et al. 2008; Hu et al. 2012; Zhang et al. 2012). An exception is the Ebert and Wood (1997, 1999, 2001) study which appears to be the only investigation to have captured a coherent root/hub vortex experimentally. The root vortices are those created by individual blades whereas a hub vortex is the cylindrical vorticity sheet centered on the wake centreline created by the nacelle/hub. When the lifting surface terminates prior to the rotational axis, Zahle and Sørensen (2011) found root vortices co-exist with the hub vortex. The axial vorticity contours revealed three counter rotating vortices per blade next to the nacelle boundary layer Zahle and Sørensen (2011). The three vortices correspond to the root vortex and the von-Kármán vortices from the cylindrical sections of the blade in the root region. The simulations highlighted the highly complex nature of the flow in the root region (Zahle and Sørensen 2011).

In the Ebert and Wood (2001) study, a horseshoe vortex structure seen in other lifting surface-body junction geometries is present in the root region of the blades (Ebert and Wood 2001). The horseshoe structure does not persist downstream due to the effects of rotation, with the negative vorticity region enveloping the positive region. The negative and positive regions of axial vorticity arise from the pressure and suction surfaces of the blades (Ebert and Wood 2001). The negative vorticity region develops into a cylindrical vorticity sheet described as a hub vortex (*i.e.* the +1 in the B+1 vortex wake models (Okulov and Sørensen 2007)). The lifting surface extended all the way to the rotational axis, limiting the formation

of a root vortex due to interaction with the hub boundary layer (Ebert and Wood 2001). The literature indicate root vortices can form when the lifting surface terminates prior to the rotational axis (Ivanell et al. 2009; Micallef et al. 2011) but are not guaranteed to (Mast et al. 2004; Haans et al. 2008a).

The lifting surface (*i.e.* airfoil section) of modern wind turbine blades terminates prior to the rotational axis due to rigidity requirements. When this occurs, coherent root vortices are likely to form at a radial distance from the rotational axis. A schematic of an idealised vortex model for a three bladed turbine is shown in figure 2.1. Assuming $\Gamma(r) = \text{const}$, the tip and root vortices have a strength of Γ . Ignoring wake expansion for simplicity, the tip and root vortex filaments have a radii of R and R_r respectively. The tip speed ratio, λ , determines the helical pitch, h , of the wake system, where h is defined as the axial distance a tip vortex travels in a single revolution. The filament length in a single revolution is $L = 2\pi h$.

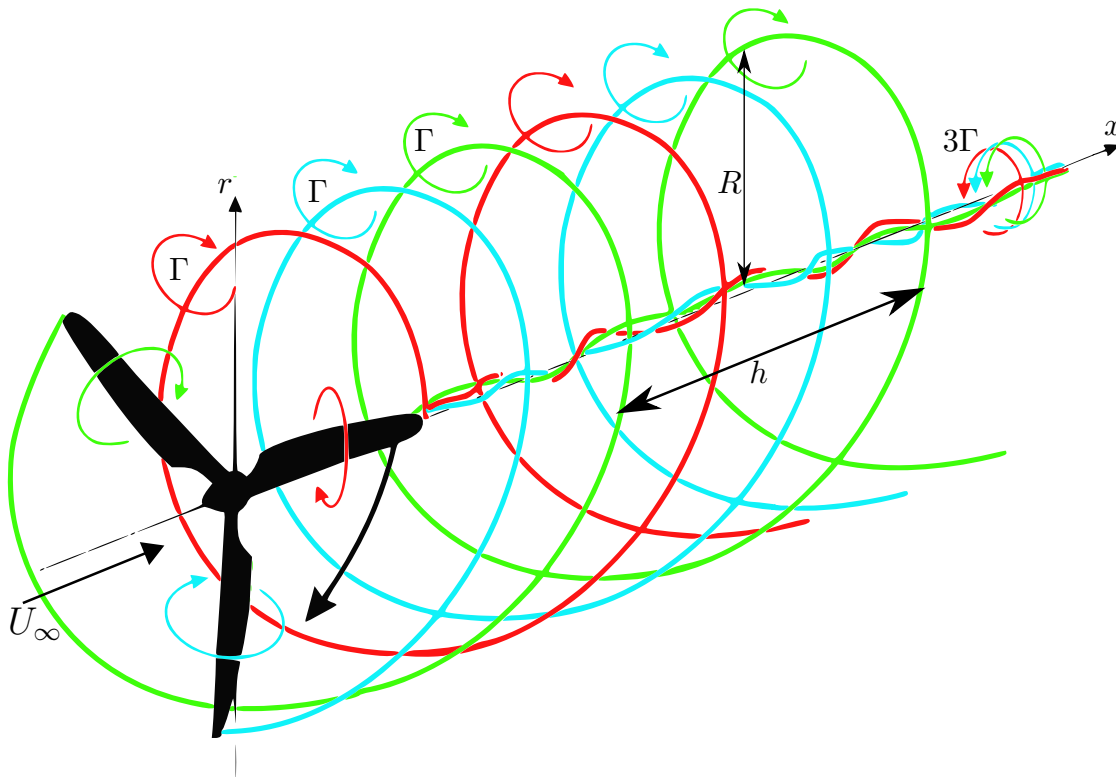


FIGURE 2.1: Theoretical vortex wake for a three bladed wind turbine with lifting surface termination prior to the rotational axis. Modified after Ivanell et al. (2010).

The investigation of this helical vortex system forms the major basis of the wind turbine wake studies conducted during candidature.

The focus of the literature review now considers helical vortex filaments and, in particular,

those in a wind turbine wake.

2.1.2 Helical vortex filaments

Helical vortex filaments have been investigated from two primary viewpoints: the induced velocity field of the helices; and the stability of the filaments themselves. The stability of helical vortex filaments is of key importance to the development of the near-wake of a HAWT. The current state of knowledge is reviewed in the next section of the literature review.

Analytical solutions via the Biot-Savart law

Analytical studies of helical vortex filament stability date from the early 20th century. Investigations perturb the filament (sinusoidal function with amplitude a , and frequency ω) and determine the perturbation growth rates. The Biot-Savart (B-S) has been used extensively in stability studies of helical vortex filaments, *e.g.* (Widnall 1972; Gupta and Loewy 1974). The B-S law can be used to investigate the self induced velocities of vortex filaments in an inviscid flow field. Adopting the notation from Widnall (1972), the Biot-Savart law is shown in equation 2.5

$$\mathbf{q}(\mathbf{y}') = \frac{\Gamma}{4\pi} \int_c \frac{(\mathbf{y} - \mathbf{y}') \times d\mathbf{y}}{|\mathbf{y} - \mathbf{y}'|^3}, \quad (2.5)$$

where \mathbf{y}' is the point on the filament where the induced velocity \mathbf{q} is desired and Γ is the vortex circulation.

The induced velocities within the vortex core cannot be determined due to the dominance of viscous forces. Thus, with a direct application of equation 2.5, vortex core form (*e.g.* Lamb-Oseen, Batchelor, Scully, Vatistas etc.) is not considered. Several methods exist to avoid the integral singularity in equation 2.5. The most common method is to use a cut-off distance, ϵ , to avoid the integral singularity and ensure applicability in an inviscid flow field (Widnall 1972; Gupta and Loewy 1974). The B-S integral has also been evaluated at a point near the filament rather than in the core itself (Levy and Forsdyke 1928). A further method uses a local induction model to approximate equation 2.5 (Betchov 1965).

The B-S law has been used to evaluate the induced velocity field of the perturbed filament. A linear stability analysis can then be performed to determine stability criteria. However, stability criteria depend on the method to determine the induced velocity field of the perturbed vortex when using the B-S law. For example, Widnall (1972) showed that the local induction model used in the analysis of (Betchov 1965) is not sufficient to describe

the total induced velocity field of the filament leading to errors in the stability analysis. The majority of stability studies have employed a cut-off method in the B-S law. An appropriate choice of ϵ is crucial to the accuracy of the calculated induced velocity field. It is often made proportional to the vortex core radius, r_{vc} (Crow 1970).

The seminal work on helical vortex stability is that of Widnall (1972). A single filament was subjected to small sinusoidal displacements in two orthogonal directions and the kinematics of the perturbed filament was calculated from the total induced velocity field. The total induced velocity, \mathbf{q}_T , consists of components due to; the self induced velocity of local segments using the local induction model, \mathbf{q}_l , and distant portions of the filament, \mathbf{q}_g , and that due to deformation of the filament structure arising from the initial perturbation, \mathbf{q}'_0 . The kinematics of the perturbed filament is thus described by equating the self-induced velocity, \mathbf{q} from equation 2.5, to the total induced velocity, \mathbf{q}_T .

Widnall (1972) employed a cut-off length, δ , and cut-off arc length distance, l . The correct choice of both cut-off length scales was made using a matched asymptotic expansion between an inner and outer solution for the self induced velocity of the filament. The inner solution included details of the swirl velocity distribution (hence vorticity) within the core.

Three instability modes were determined depending on filament (*e.g.* pitch) and perturbation (*e.g.* wavenumber) parameters. The short-wave instability arises when the perturbation wavenumber is high. Widnall (1972) state this instability mode most likely affects all curved vortex filaments. When the perturbation wavenumber is less than unity, a long-wave instability arises. The amplification rate of the long-wave instability mode is generally greater than the short-wave mode (Widnall 1972). When $h \leq 0.3R$, a mutual inductance instability mode arises. With further reductions in the pitch, the mutual inductance instability modes merge and the filament is unstable for nearly all wavenumbers. For the mutual inductance mode, decreasing core size leads to a reduction in the amplification rate.

The stability map (pitch parameter, $\tau^{-1} = \frac{h}{R}$ vs. perturbation wavenumber, γ/k') of the Widnall (1972) study for a single inviscid helical vortex filament is shown in figure 2.2. k' is equal to $\tau/R(1+\tau^2)$. This figure was taken from Walther et al. (2007). In figure 2.2, the solid lines denote the stability boundaries ($\bar{\alpha} = 0$, where $\bar{\alpha}$ is the non-dimensional perturbation growth rate) for various vortex core to filament radius, r_{vc}/R , ratios. This stability map applies for a single vortex filament where the core size is less than both the local radius of curvature and any perturbation wavelength along the filament.

Gupta and Loewy (1974) independently investigated the stability of a helical vortex fila-

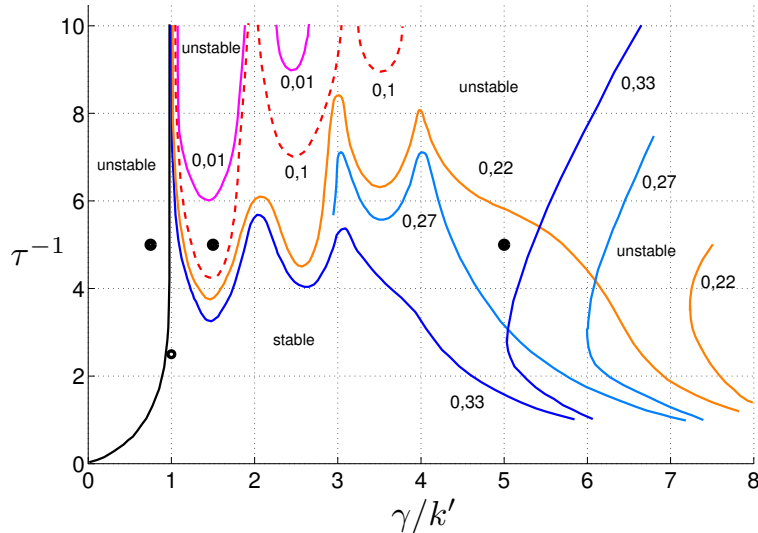


FIGURE 2.2: Stability boundaries for a single helical vortex filament in an inviscid flow field using the matched asymptotic expansion method (Widnall 1972). Figure taken from Walther et al. (2007).

ment subjected to small first order perturbations. Their analysis also considered B filaments. They found that for all wavenumbers, disturbances with positive, negative and neutrally stable growth rates existed. However, the largest unstable modes dominate the solution and determine the deformed shape of the helices (Gupta and Loewy 1974). The maximum divergence rates, λ , for a single and triple filament systems subjected to varying perturbation wavenumbers are shown in figure 2.3.

Figure 2.3 indicates an appreciable stability effect of core radius for a single helix but this effect diminishes in the triple filament system. Maximum divergence rates for multiple helices occur at wave numbers equal to half integer multiples of the number of blades. The highest perturbation growth rates are recorded when the deformation modes reduce the axial separation between adjacent helices. More generally, when the pitch of the helices reduce and/or the number of helices is increased and/or the wavenumber of the perturbation increases, the system becomes more unstable, presumably due to the increased interaction between vortices of adjacent turns (Gupta and Loewy 1974).

Although the stability studies of Widnall (1972) and Gupta and Loewy (1974) were inviscid in nature, they provide insight into the likely instability modes affecting multiple helical filaments in a wind turbine wake. The higher order interaction of the instability modes could not be deduced due to the linear nature of the stability analysis (Widnall 1972; Gupta and Loewy 1974).

The stability of multiple helical tip vortices was also investigated by Okulov (2004). The problem was formulated in helical variables for $B \leq 7$ tip vortices. A flow is helically sym-

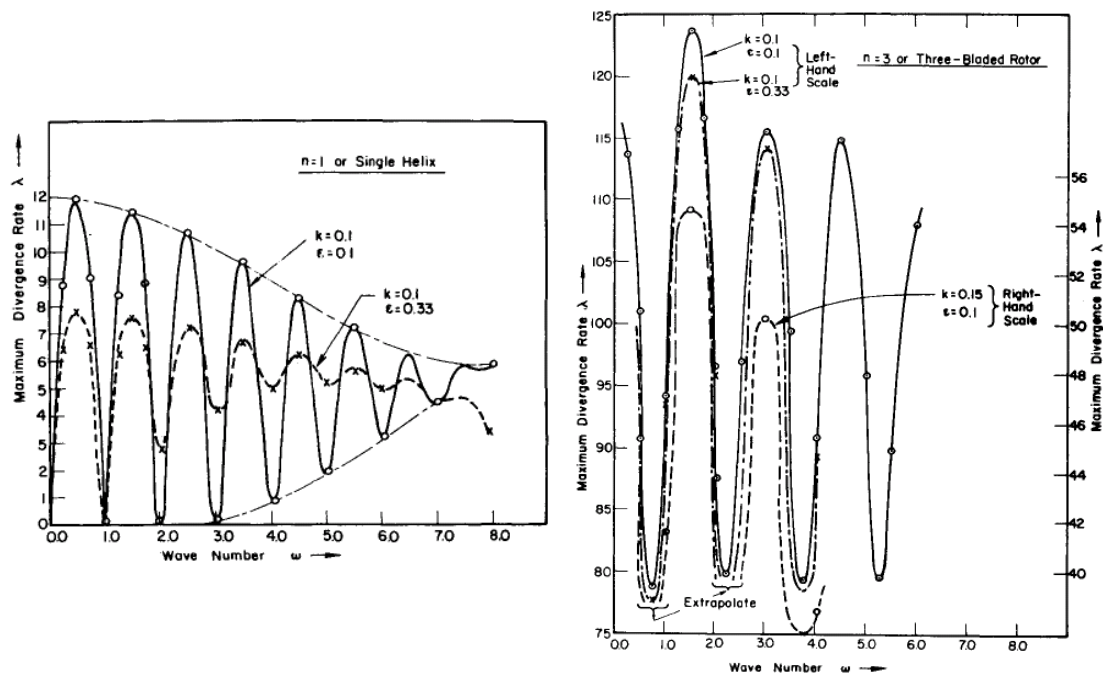


FIGURE 2.3: Stability boundaries for a single (left) and triple (right) helical tip vortex system evaluated using 2.5 (Gupta and Loewy 1974).

metric when the velocity field remains constant irrespective of an axial, Δz and angular displacement, $\Delta\theta$. For all B multiples and (fixed) core sizes, stable vortex configurations were only present for $h < 0.238$ (Okulov 2004). Okulov and Sørensen (2007) extended the earlier work by Okulov (2004) and investigated the stability of a vortex system representative of a wind turbine or propeller far wake. The tip vortices were embedded in a prescribed vortex flow field of circulation, Γ_{R+H} , created by root and hub vortices. The total velocity field of the helix thus consisted of the prescribed background flow, the induced and self induced motions. The interaction between the helices and the assigned flow field was not considered.

Constant spatial perturbations were applied in the azimuthal and axial directions (Okulov and Sørensen 2007). The vortex system was unconditionally unstable when the net circulation was zero, *i.e.* $\Gamma_{R+H} = B\Gamma$ (Okulov and Sørensen 2007). The analysis showed the propeller far wake model of Joukowski (1912) to be unconditionally unstable when a Rankine vortex flow field was assigned as the hub vortex (Okulov and Sørensen 2007). The induced velocity field predicted by the analysis compared exceptionally well to experimental data.

The analytical helical stability studies presented so far are inviscid in nature. B-S formulations have this implicitly implied. Viscous effects can be included in numerical solutions, as can higher order instability modes. Walther et al. (2007) simulated several points on the Widnall (1972) stability map (figure 2.2) using a vortex particle method. The vortex

cores were Gaussian, thus avoiding the integral singularity in equation 2.5. The Walther et al. (2007) study showed that an elliptic instability forms in the helical filaments when the radius of curvature increases beyond a limit due to changes in the core structure. This was not realisable in the linear stability studies using equation 2.5 (*e.g.* (Levy and Forsdyke 1928; Betchov 1965; Widnall 1972; Gupta and Loewy 1974)). The shortwave instability mode took less time to break down compared to the longwave and mutual induction instability modes. Walther et al. (2007) also investigated a vortex system containing three counter rotating helical vortex pairs (*i.e.* a triple doublet with $3 \times \Gamma_{tip}$ and Γ_{root}) corresponding to an idealised turbine wake. A stable configuration was only possible when the total angular velocity of the tip and root vortices are identical (Okulov 2004). The radial position of the root vortices determines the mode and time to breakdown. The simulations indicated the tip vortices in an unperturbed idealised wind turbine wake (triple doublet) filament system can maintain their shape after the root vortices become unstable (Walther et al. 2007).

The simulations presented so far were of multiple stand alone helical vortices. Full CFD simulations of a wind turbine are computationally very expensive (*e.g.* (Zahle et al. 2009)). Less computationally expensive simulations depend on the rotor discretisation method. The stability of the tip vortices in a HAWT wake has been investigated numerically (Ivanell et al. 2010) using the ‘actuator-line’ (AL) method (Sørensen and Shen 2002). In this method, the aerodynamic forces generated by the blade segments are distributed along actuator lines. The aerodynamic forces are included in the Navier-Stokes equation through the use of body forces, f_{body} . The AL method thus circumvents the excessive mesh density required to resolve the blade boundary layer. Turbulent eddies smaller than the mesh (finite volume discretisation) are modelled through an eddy viscosity using a mixed sub-grid-scale model. The AL method is thus a Large-Eddy-Simulation (LES) formulation.

Ivanell et al. (2010) introduced a time-dependent body force perturbation close to the blade tip. The (sinusoidal) perturbation was applied in the axial direction. The spatial growth of the perturbation is evaluated on the tip vortex spiral by a Fourier series constructed from eight velocity fields over a single rotational period. Ivanell et al. (2010) found that the instability growth rate depended on the perturbation frequency, ω . Maximum growth rates occurred at two distinct ω values. At these ω , adjacent filaments were out of phase with each other reducing the spacing between filaments to a minimum leading to maximum interaction. Isosurfaces of vorticity are shown on the left of figure 2.4 with these same results projected onto a 120° plane on the right of the figure. The spatial growth of the instability leads to

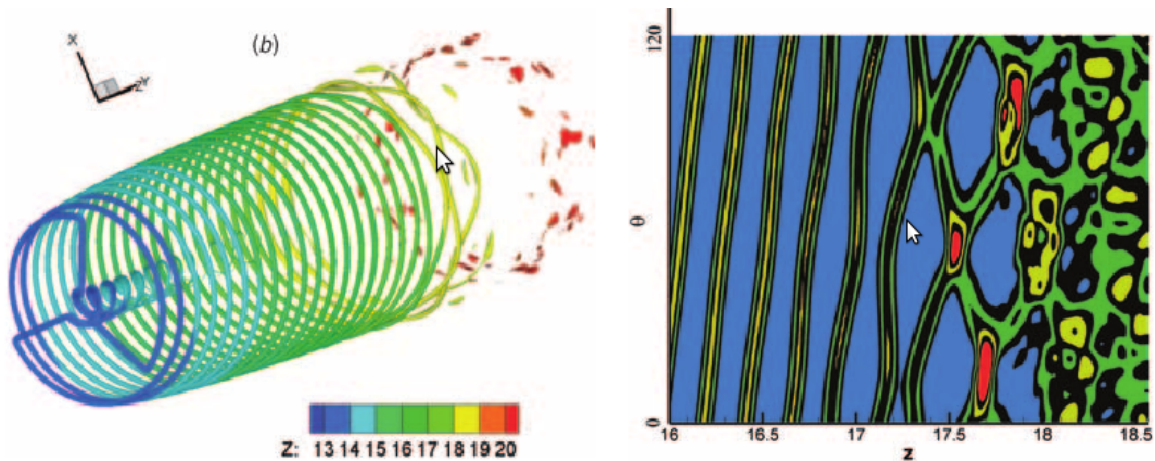


FIGURE 2.4: Numerical stability results from the simulations by Ivanell et al. (2010) showing the out of phase oscillations leading to wake breakdown for a perturbation frequency of 5.

vortex pairing and coalescence. The developing instability is evident by the out of plane oscillation of adjacent tip vortices by $Z = 16.5$. At $Z \sim 17.5$ or $x/R = 4$, adjacent tip vortices touch with wake breakdown complete by $Z \sim 18.5$ or $x/R = 5$.

The pairing instability in a HAWT wake was first seen in the smoke visualisations of Alfredsson and Dahlberg (1979), shown in figure 2.5. The tip vortices interact leading to vortex coalescence and wake breakdown. Bolnot et al. (2011) investigated the 2D pairing instability shown in figure 2.5 using a vortex ring formulation. The system of vortices was unstable when the perturbation travelled faster than the advection velocity (Bolnot et al. 2011).

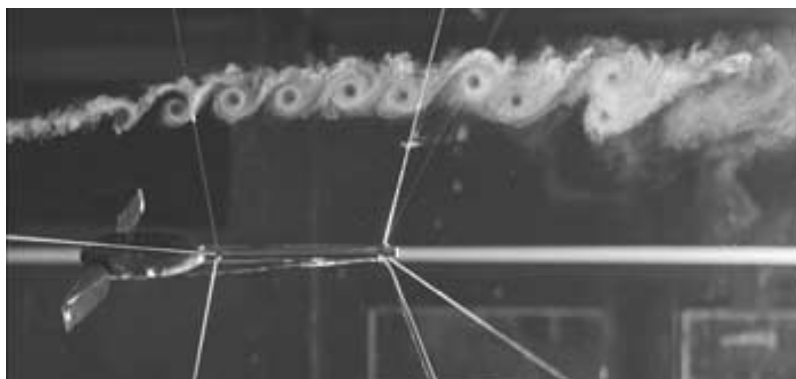


FIGURE 2.5: Wind tunnel smoke flow visualisations by Alfredsson and Dahlberg (1979) showing vortex interaction and coalescence. Figure taken from Ivanell et al. (2010).

The interaction between vortices in figure 2.5 is also seen in vortex ring pairs. However, the interaction between vortex ring pairs leads to the ‘leapfrogging’ phenomena (Lim and Nickels 1995). Leapfrogging is a striking example of Helmholtz’ vortex law. Leapfrogging, shown

schematically in figure 2.6, is the process where an aft vortex ring overtakes the foremost ring due to the resultant induced velocity between the two rings. The velocity field of the second vortex causes the first vortex ring diameter to expand. The filament is stretched in this expansion and from Helmholtz' vorticity laws requires the ring to slowdown. Conversely, the velocity field of the first ring causes the second ring to contract and accelerate. If the spacing between the vortex rings is small enough, the second ring can overtake the first ring.

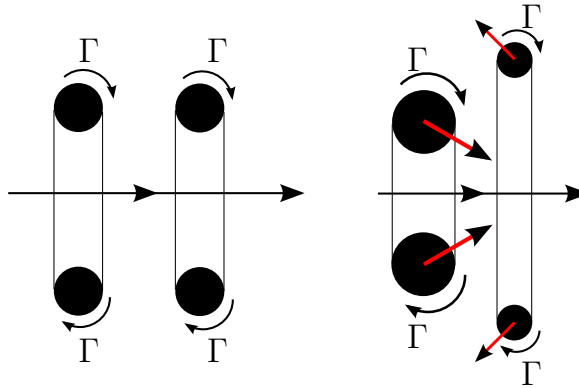


FIGURE 2.6: Schematic of vortex interaction leading to ‘leapfrogging’ phenomena between two vortex rings. Red arrows indicate the resultant induced velocity. Reproduced after Lim and Nickels (1995)

Whilst vortex interaction in helical filaments and that in vortex rings is controlled by the B–S law, it results in very different outcomes. As the helical filaments are continuous, complete positional reordering cannot occur. Vortex entanglement and the pairing instability seen in figure 2.5 occurs rather than leapfrogging.

The mutual inductance instability mode also affects the helical vortices in marine propeller wakes (Felli et al. 2011). It is important to note that the wake state in a marine propeller is different due to power addition rather than power subtraction. Further, a marine propeller wake contains $B + 1$ vortices where the ‘+1’ vortex is a rectilinear hub vortex centred on the rotational axis. This corresponds to the Joukowski vortex wake model. It is different to the $2B$ vortex wake of an idealised HAWT shown in figure 2.1.

Unlike those in a HAWT wake (Ivanell et al. 2007), the tip vortices become unstable first leading to a perturbation which causes the hub vortex to become unstable (Felli et al. 2011). Due to power addition, a jet forms on the wake centreline and the tip vortices trail the blade wakes. The trigger of an instability in the tip vortices coincides with the position where a tip vortex interacts with the wake of a prior blade (Felli et al. 2006).

The instability transition point moved downstream when the helical pitch was increased (Felli

et al. 2011). Felli et al. (2011) took this to indicate the mutual inductance instability mode as the primary cause of wake destabilisation. They propose the mutual inductance instability mode occurs due to the radial and axial deformation modes being 180° out-of-phase, in agreement with the findings of Gupta and Loewy (1974); Ivanell et al. (2010). However, unlike the simulations by Ivanell et al. (2010), the interaction/grouping of tip vortices occurs initially between a number of vortex structures depending on the number of filaments (Felli et al. 2011).

Therefore, the vortex interaction leading to the pairing instability seen in figure 2.5 requires further investigation to resolve this discrepancy.

2.1.3 Meander of trailing vortices

Stability analyses and flow visualisations highlighted the mutual inductance instability mode as a mechanism of wake breakdown. To determine if an instability exists in the helices, the instantaneous vortex positions can be compared to a temporal mean. Such an analysis will also contain the motions due to vortex meander. Vortex meander also known as wandering in fixed wing trailing vortices is the slow, seemingly random movement of the vortex core about a mean position (Green 1995). Helical vortices also meander (Dobrev et al. 2008). Vortex meander is not to be confused with wake meandering. Wake meandering is the slow movement of a wind turbines wake region about the wake centre line (Bingöl et al. 2007; Larsen et al. 2008; Medici and Alfredsson 2008). There have been many hypotheses as to the origin of vortex meander which are summarised by (Jaquin et al. 2001). They were; **1)** perturbation of the core by freestream turbulence, **2)** perturbation of the core by unsteadiness in the vorticity sheet surrounding the core, **3)** co-operative instabilities (*e.g.* Crow instability) or **4)** propagation of unsteadiness from the model (Jaquin et al. 2001).

Multiple vortex systems such as those arising in a wind turbine wake are more complex than the fixed wing case. The origins of meander in helical vortex filaments are also more numerous than the fixed wing case. For example, three instability mechanisms were shown to affect helical vortex filaments (Widnall 1972). Propagation of unsteadiness from the model is more likely due to the rotating lifting surface. Further, the existence of bluff body vortex shedding (*e.g.* see Medici and Alfredsson (2006)) seen in some wind turbine wake studies may also affect vortex meander.

Point measurements are affected by vortex meander as the probe is stationary in space. The meandering motion causes a spatial smoothing of vortex properties and introduces tur-

bulent kinetic energy into the core. Using the vorticity transport theorem, *i.e.* the vortices are treated as solid (Devenport et al. 1996; Vandernoot et al. 2008), vortex properties can be corrected for the meandering motions. Devenport et al. (1996) assumed a Gaussian bi-variate probability distribution of the meandering motion of the tip vortices formed by a NACA0012 wing. In the Devenport et al. (1996) vortex model, a Gaussian vorticity and axial velocity deficit were also assumed. The measured velocity profiles were thus the convolution of the true velocity profile and the bi-variate normal probability distribution function.

Velocity field measurement techniques such as particle image velocimetry (PIV) alleviate the need to assume a meandering motion distribution. The instantaneous vortex cores can be determined and the entire field re-centered onto a common grid (Heyes et al. 2004). The interpolation can however introduce errors. Heyes et al. (2004) showed the assumption of a Gaussian distribution for the meandering motions of a NACA0012 tip vortex was a valid one. They found that without correction for meandering, the vortex core radius was over predicted by 12.5% and the maximum tangential velocity was underpredicted by 6% (Heyes et al. 2004). They postulated the meandering motion was due to external circumstances such as freestream turbulence rather than self induced motions but no firm conclusions were drawn.

There are fewer investigations of meander in helical vortices. In helicopter wakes (Heineck et al. 2000; van der Wall and Richard 2006), the smoothing effects of vortex meander were avoided in a similar to the method to Heyes et al. (2004). Vortex meander also affects the helical vortices in a HAWT wake. Conditional sampling based on vortex position (Grant and Parkin 2000; Dobrev et al. 2008) allowed the smoothing effects of vortex meander to be avoided. Dobrev et al. (2008) and Yang et al. (2011) qualitatively noted that meander amplitudes increased with axial distance. Dobrev et al. (2008) noted the magnitude was larger than the fixed wing case and they attributed the increase (without supporting evidence) to a helical vortex instability (Dobrev et al. 2008). Very little comment was provided as to the origins of vortex meander in helicopter (Heineck et al. 2000; van der Wall and Richard 2006) or wind turbine (Dobrev et al. 2008; Yang et al. 2011) studies.

Therefore the origins of vortex meander in helical vortex filaments still require significant research to deduce its origin. Further characterisation under a range of operating conditions will increase understanding in this area.

2.1.4 Prior works characterising helical vortices in a HAWT wake

Studies which have investigated the tip and root vortices in the near-wake of a wind turbine wake will now be reviewed to determine the state-of-the-art in the area. However, it should be noted that the inherent coupling of the blade and near-wake aerodynamics make comparisons between prior studies difficult. Further, the tip vortices are almost exclusively studied due to the dependence of root vortex formation on reasons previously outlined.

The tip vortices have been investigated by both qualitative and quantitative techniques. On the qualitative side, flow visualisations have revealed much about the structure of the near-wake, an example of which was shown in figure 2.5. A further example from this investigation are shown in figure 2.7, indicates an along filament velocity component as the smoke trace is sucked into the filament trace. Swirling flow at the core boundaries is evident in certain filament traces. This phenomena was also seen more recently in the experimental campaign of Mikkelsen et al. (2011). Smoke visualisations also showed tip vortex formation is impeded by freestream turbulence (Alfredsson and Dahlberg 1979). Further tip vortex visualisation studies are by Vermeer (2001); Montgomerie and Dahlberg (2003); Haans et al. (2005); Grant et al. (1997, 2000). Montgomerie and Dahlberg (2003) noted vortex pairing occurred 'a little before 2D downstream'.

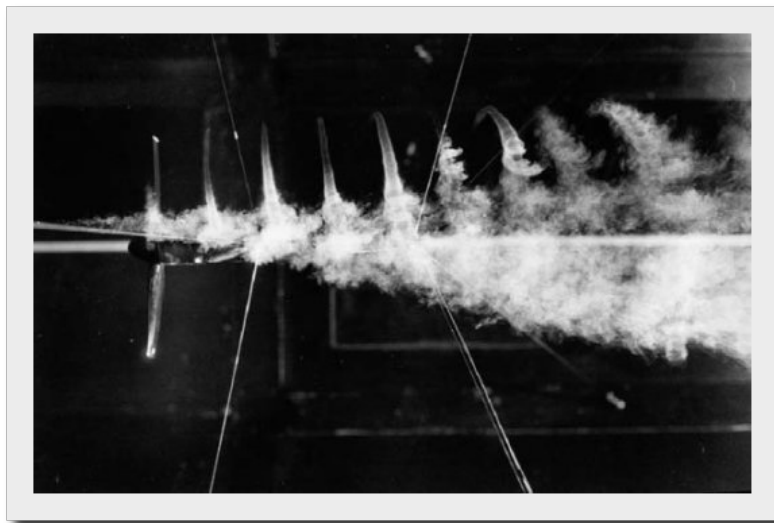


FIGURE 2.7: Smoke visualisation of along filament velocity component of the tip vortices in a HAWT wake (Alfredsson and Dahlberg 1979).

To investigate the vortices within a wind turbine wake quantitatively, requires a phase averaging technique. The experiments of (Ebert and Wood 1997, 1999, 2001) revealed the structure of the very near-wake ($0.167 \leq x/c \leq 1.667$) of a two bladed turbine. They showed

the tip vortices contain significant turbulent kinetic energy (Ebert and Wood 2001). Further, although the tip vortices form due to momentum extraction and more specifically bound circulation generation by the blades, they contain angular momentum and power, which ideally would be extracted by the blades (Ebert and Wood 1997). The level of the angular momentum in the tip vortices increases with tip speed ratio (Ebert and Wood 1999) until the ‘runaway’ state (no net power is produced by the turbine), where the tip vortices absorb all the angular momentum extracted from the wake (Ebert and Wood 2002).

Grant et al. (1991) were the first to investigate tip vortex properties using PIV. They computed blade bound circulation and tip vortex circulation in the near wake (Grant et al. 1991). Whale (1996) was the first to employ PIV on a wind turbine in a water channel. Evidence of tip vortex coalescence appeared at $1.0D$ for a flat plate blade set operating at $\lambda = 6$ and $\lambda = 8$ (Whale et al. 2000). Whale et al. (2000) showed root vortex formation with a vortex lattice method. However, poor agreement was found between the simulation and experimental results due to flow separation over the untwisted flat plate experimental model (Whale et al. 2000). Dobrev et al. (2008) and Zhang et al. (2012) on the other hand, found a signature of vorticity consistent with a hub vortex in the root region.

Akay et al. (2011) used Stereo PIV (SPIV) to investigate blade aerodynamics on a two meter diameter turbine. Micallef et al. (2011) used an inviscid panel code to show root vortices formed on the same model. The root vortices persisted over their measurement domain ($x/R \leq 0.6$) adjacent to the nacelle section but no vortex characteristics were presented (Micallef et al. 2011). The experimental field of view did not extend far enough into the wake to allow imaging of the tip and root vortices (Micallef et al. 2011).

On a larger scale still, the ‘model experiments in controlled conditions’ (MEXICO) project allows investigation of tip vortex evolution at $Re_c = 0.8 \times 10^6$. The three bladed 4.5 m diameter turbine was tested in the 9.5×9.5 m DNW wind tunnel (Micallef et al. 2012). The near-wake measurements extended to $x/R \sim 1$ downstream of the rotor. The program produced interesting results with the necessity for a uniform blade profile apparent. An overview of the MEXICO project is given by Schepers and H.Snel (2007). Tip vortex locations were determined using several independent fields of view in both yawed and non-yawed cases at several tip speed ratios (Nilsson et al. 2011). The vortex locations were compared to AL simulations achieving excellent agreement in the yawed flow case with agreements reduced in the non-yawed case (Nilsson et al. 2011).

Interaction between tip and root vortices depends on blade geometry and operating con-

ditions, principally λ . When λ is low, the pitch, h , of the helical vortices is large. Interaction between tip vortices is minimal in these cases and the vortices advect at a constant velocity (Grant and Parkin 2000). Grant and Parkin (2000) was one of the first to characterise the evolution of tip vortex properties with vortex age. They found that after vortex roll-up is complete, the tip vortex shrinks with a reduction in circulation and vortex radius. The core then expands by viscous diffusion (Grant and Parkin 2000). Dobrev et al. (2008) also characterised the tip vortices and found the Vatistas model exponent α was less than that in helicopter wakes. This suggests tangential velocity decay occurs slower in wind turbine wakes compared to helicopter tip vortices (Dobrev et al. 2008).

The tip vortices have also been investigated in boundary layer flows using PIV (Hu et al. 2012). The meander of the tip vortices in the top half of the wake increased with axial distance (Hu et al. 2012). The absence of tip vortices in the bottom half of the wake suggest the boundary layer shear and turbulence impede vortex formation.

The body of literature regarding the vortices in the near wake of a wind turbine has now been critically reviewed. Although numerous works have been conducted, this literature review highlighted unanswered questions requiring further investigation. The flow over complex terrain will now be reviewed in the following section.

2.2 Flow over complex terrain

The majority of Australian wind farms are located in coastal regions possibly close to coastal cliffs as shown in figure 2.8. This image was created using Google maps and information collated by Geoscience Australia (2010). The terrain may induce desirable flow effects like an increase in wind speed. The physics of flow over complex terrain is presented in this section.

Complex terrain is defined here as any local topographical feature that alters the undisturbed wind speed and causes flow separation. Such terrain include hills, escarpments, embankments and cliffs. Two dimensional isolated hills of smooth curved profiles have received considerable attention in the past. The flow over shallow hills can be described using a linearized boundary layer theory (Jackson and Hunt 1975; Hunt et al. 1988). However, flow separation cannot be predicted by these linear theories. Review papers of experimental and numerical studies of flow over hills are presented in Taylor (1998) and Bitsuamlak et al. (2004).

Wind farms in coastal regions of Australia are likely to be placed in the vicinity of coastal cliffs. Cliffs can be modelled by 2D escarpments. A 2D escarpment is defined as an angled



FIGURE 2.8: Location of wind farms in Australia indicating prevalence in coastal regions (Geoscience Australia 2010).

surface connecting two elevations as shown in figure 8.17. Similar linear theories to those for shallow hills are not available for the flow over embankments; a cliff corresponds to an escarpment with 90° slope angle. The main flow features in a mean sense are shown in figure 8.17. The boundary layer flow approaches the terrain feature. A deceleration occurs as the flow approaches the slope of the hill due to the blockage created by the terrain. If the terrain is steep enough, the flow can separate upstream and form a recirculation region. This recirculation region acts as an effective slope angle. The flow accelerates up the slope face to the apex where a pressure minimum and corresponding maximum velocity occurs. In the case of an isolated hill, the flow decelerates and separates in the lee side of the hill if the slope is too large (Ayotte and Hughes 2004). For 2D escarpment flow, the flow will separate close to the apex if the boundary layer flow encounters an adverse pressure gradient. This can be related to a large divergence of the streamlines downstream of the apex. The slope angle of the escarpment, θ , determines whether separation occurs. The flow reattaches in the lee side of the hill or on the top surface of the escarpment at the mean reattachment position, X_L . The recirculation region exists in a quasi-steady state such that reattachment occurs in a zone.

A prospective wind farm site may contain many complex terrain features where interaction between several topographical features creates a very turbulent and challenging modelling environment. Wind farm planning tools such as WAsP (Mortensen et al. 1993) were developed using linearised boundary layer models and as a result can break down in complex terrain (where the slope > 0.3) (Petersen et al. 1998b). These one-dimensional models are unable

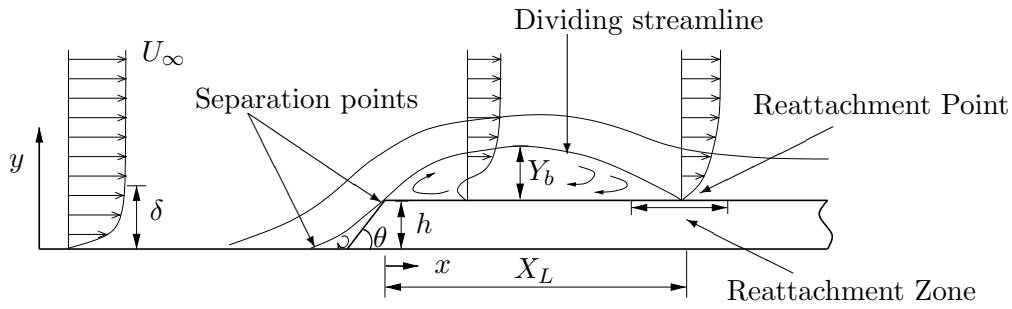


FIGURE 2.9: Flow features over a 2D escarpment. Left to right: upstream boundary layer profile, upstream recirculation, angled step face, recirculation region of importance to wind energy installations, reattachment point.

to predict where flow separation occurs. Recently, wind engineers have used 3D CFD models to investigate the wind flow over prospective wind farm sites. Whilst requiring significant computing power, the models are likely to increase the accuracy of wind energy predictions but clearly need to be properly validated. A blind comparison of numerical micro-scale model predictions highlighted the variability of results of flow over complex terrain Berg et al. (2011); Bechmann et al. (2011).

2.2.1 Desirable features of complex terrain

An isolated cliff, hill or escarpment provides a simplified complex terrain topology. Focus is given to 2D escarpments due to their prevalence in Australian coastal regions. Complex terrain induces both desirable and un-desirable flow effects. The desirable flow effects are presented first.

The terrain induces a region of elevated wind speed above the apex. This speed up is beneficial in a wind energy sense. The speed up effect generated by the topology can be characterised by the *amplification factor*, A_z (Bowen and Lindley 1977), defined this as the ratio of the wind speed above the topology to that at the same height above flat ground as shown in equation 2.6. An alternative characterisation is by the *fractional speed-up ratio*, ΔS (Taylor 1998), calculated as shown in equation 2.7. Kondo et al. (2002) present a scalar equivalent to equation 2.6, which they term the *topographic multiplier*, TM.

$$A_z = \frac{u(x, z)}{u(x_o, z)}, \quad (2.6)$$

$$\Delta S = \frac{u(z) - u_0(z)}{u_0(z)} = A_z - 1, \quad (2.7)$$

where (\mathbf{z}) is the velocity profile above the topographical feature and $\mathbf{u}_0(\mathbf{z})$ is the reference

velocity profile above flat land.

The fractional speed-up ratio is highly dependent on a number of flow properties, including boundary layer to cliff height ratio, δ/h , boundary layer shear exponent, n , escarpment angle and turbulence intensity and atmospheric stability. The only known full scale investigation of 2D escarpment flow is by Emeis et al. (1995) over the Hjärdemål site. The site had a escarpment 16 m high with a slope of 28° (Emeis et al. 1995). In small scale experimental studies, A_z reaches a unit value at approximately 1/3 of the way up the slope (Bowen and Lindley 1977; Kondo et al. 2002). At full scale, a unit value is reached between halfway up the slope and the crest, depending on atmospheric stability (Emeis et al. 1995). Values of A_z downstream of the apex range from 1.3–1.8 (Berg et al. 2011; Bowen and Lindley 1977; Kondo et al. 2002; Emeis et al. 1995). Maximum speed-up occurs under stably stratified conditions (Emeis et al. 1995). The region of speed-up extends further above the step with increasing atmospheric instability (Emeis et al. 1995). It is maximum at the apex where the pressure minimum and velocity maximum occurs.

2.2.2 Un-desirable features of complex terrain

Complex terrain is however not an ideal wind energy installation location. If the terrain slope angle is greater than a critical angle, $\theta_{crit} = 17^\circ$ (Oke 1987), boundary layer separation occurs at the apex. However, full scale experimental data reveal flow separation also depends on U_∞ (Emeis et al. 1995). The recirculation region which forms downstream of the separation point is an undesirable and unavoidable feature of flow in complex terrain. The flow within this region is lower than the freestream such that the speed up ratio reduces below unity. Therefore, a turbine placed in the recirculation region will produce less power compared to a turbine in uniform terrain. In addition to the reduced velocities (less power) in the recirculation regions, the turbulence level is also elevated (Bowen and Lindley 1977; Kondo et al. 2002). The turbulence level is highest in the separated shear layer. It is thus important from a wind energy perspective to determine if flow separation occurs. This is required to critically determine whether complex terrain is a suitable wind farm location.

2.2.3 Prior works characterising flow over complex terrain

There have been few studies investigating the separating and reattaching flows over 2D escarpments. The mean recirculation region is characterised by a length, X_L and height, Y_b as shown in figure 8.17. Table 8.1 highlights the sensitivity of X_L to δ/h , model aspect ratios and the Reynolds number, Re_h for a forward facing step (FFS) where a reattachment length

TABLE 2.1: Reattachment length results from previous FFS studies including important study parameters, boundary layer height to step height ratio δ/h , step length aspect ratio L/h , and Reynolds number Re_h .

Study	δ/h	L/h	Re_h	X_L
Largeau and Moriniere (2007)	≤ 0.3	≥ 9	$2.88-12.82 \cdot 10^4$	3.5-5
Hattori and Nagano (2010)	0.33-0.66	23.3	$0.9-3 \cdot 10^3$	1.82-2.04
Bergeles and Athanassiadis (1983)	0.48	4	$2.7 \cdot 10^4$	3.75
Moss and Baker (1980)	0.7	12.7	$5 \cdot 10^4$	4.7
Gasset et al. (2005)	~ 0.7	> 6	$5 \cdot 10^4$	5.0
Zhang (1994)	0.7	32	-	4.02
Leclercq et al. (2001)	0.7	10	$1.7 \cdot 10^5$	3.2
Arie et al. (1975)	1.96	4	-	2.5
Farabee and Casarella (1986)	2.4	> 10	$2.1 \cdot 10^4$	~ 3
Camussi et al. (2008)	5	> 8	$8.8-26.3 \cdot 10^3$	1.5-2.1
Castro and Dianat (1983)	5.2	2	$5 \cdot 10^4$	1.4
Agelinchaab and Tachie (2008)	9.3	6	$1.92 \cdot 10^3$	4.1

was stated. The Reynolds number definition for flow 2D escarpments is based on U_∞ and the step height as shown in equation 8.1,

$$Re_h = \frac{U_\infty h}{\nu}. \quad (2.8)$$

The recirculation region downstream of 2D escarpments does not appear to have been characterised extensively. In addition, the sensitivity of this flow to freestream turbulence has not been investigated.

2.3 Summary and the need for further research

From the literature survey it is apparent that a considerable body of research exists on the near-wake of a wind turbine and flow over complex terrain. However, several questions remain as highlighted by the following summary:

- 1. The tip vortices are the dominant structures in the near wake of a wind turbine. How far do they persist into the wake?
- 2. Formation of root vortices appears highly dependent on turbine geometry and operating conditions with very few studies capturing the root vortex. Under what conditions does root vortex formation occur?
- 3. The tip/root vortices breakdown in the near-wake due to instabilities which grow on the filament. A pairing instability was shown in both flow visualisations and numerical

simulations. Is the mutual inductance instability mode the dominant mechanism leading to wake breakdown?

- 4. Freestream conditions such as turbulence intensity have little effect on rotor performance. What effect do the freestream conditions have on tip vortex formation and subsequent evolution in the wake?
- 5. Complex terrain is beneficial in a wind energy yield sense due to the speed up the terrain produces. However, the flow in these areas is turbulent and difficult to model. Is complex terrain a suitable wind farm location?

Thus an experimental study of several aspects of wind farm siting is required to expand understanding to answer these questions. The first aspect requiring investigation is the evolution of the tip and root vortices in the near-wake of a horizontal axis wind turbine. Secondly, the flow over complex terrain needs to be characterised further. This thesis provides experimental data to add to the expanding body of work in these areas.

2.4 Present work

The questions which arose from the literature review are investigated using particle image velocimetry (PIV) in a water channel facility. The non-intrusive nature of PIV make this technique very suitable for the current work. PIV and other experimental techniques used during candidature are outlined in chapter 3.

The vortices in the near-wake are investigated using two small scale three bladed wind turbine models. As the near-wake experiments are conducted at low Reynolds numbers, a static 3D wing is first investigated to determine airfoil flow states at very low Reynolds numbers. The wind turbine models employ very different design criteria. The literature review revealed root vortex formation is more likely to occur when the lifting surface terminates prior to the rotational axis. Therefore, the first wind turbine model is a geometrically scaled version of the Tjæreborg wind turbine. The second model is based on an optimum Glauert rotor. The lifting surface of this model also terminates prior to the rotational axis. The optimum Glauert rotor was designed to achieve dynamic similarity between model and full scale. The models are outlined in chapter 3

The turbines are tested at numerous tip speed ratios, as the literature review indicated this parameter to have an appreciable affect on wake stability. The tip speed ratio is the principal independent variable in the near-wake studies due to the coupling between the

blade and near-wake aerodynamics. It controls the dependent variables in the problem, the helical pitch, h , the Reynolds number, Re_c and the blade bound circulation, Γ_B . The results of the near-wake studies in a uniform inflow are presented in chapters 5 and 6.

The effect on wake stability of an additional independent variable, the freestream turbulence intensity, I_u was investigated by implementing passive turbulence grids. The turbulence intensity was characterised using a laser doppler velocimeter (LDV). Three turbulence grids were used to generate turbulence intensity values in the range $1.68\% \leq I_u \leq 6.2\%$. The water channel facility has a residual turbulence intensity of $I_u \sim 1.2\%$. The effect of turbulence effect on wake structure is presented in chapter 7.

The suitability of complex terrain as a wind farm location is investigated using a versatile 2D escarpment model. Of specific interest is the recirculation region dimensions and turbulence generation above the terrain 2D escarpment. The literature review revealed the flow over 2D escarpments depends on inlet flow parameters such as the boundary layer to step height ratio, δ/h , in addition to feature specific parameters like the escarpment angle, θ , and the Reynolds number Re_h . The effect of the δ/h ratio on the recirculation region is investigated by varying the step height, h , for the forward facing step (FFS) geometry. Whereas, the escarpment angle is varied in the range $30^\circ \leq \theta \leq 90^\circ$ for $\delta/h = 1.25$. The effect of I_u on the recirculation region is also investigated using passive turbulence grids at $\delta/h = 1.25$. To determine the suitability of complex terrain as a wind farm location, the amplification factor, A_z , and turbulent quantities such as the Reynolds shear stress, $\overline{\mathbf{u}'\mathbf{v}'}$ and turbulent production, P_k are evaluated. The results of the complex terrain investigations are presented in chapter 7.

Further independent variables which affect both wind turbine wake evolution and flow over complex terrain at full-scale include are the boundary layer shear exponent, n , and turbulence length scales such as the Taylor macro (integral) length scale, Λ_{u_x} . These variables will not be investigated here.

Chapter 3

Experimental Techniques, Models and Equipment

The literature review revealed a dearth of quality experimental data investigating fluid dynamics problems concerned with wind farm siting. In this chapter I discuss the techniques, equipment and models used to obtain the experimental data which I analyse in future chapters. This data is presented in a succinct chapter to avoid repetition in future chapters.

3.1 Experimental Techniques

The quantitative experimental techniques used during candidature were laser doppler velocimetry (LDV) and particle image velocimetry (PIV). Also, the flow was visualised using the following techniques: hydrogen bubble, planar laser induced fluorescence (PLIF), and particle streaklines. How the data was processed is presented at the end of each section describing each experimental technique.

3.1.1 Particle Image Velocimetry (PIV)

Particle image velocimetry (PIV) is a non-intrusive optical experimental technique that resolves a fluid's displacement by imaging neutrally buoyant reflective particles placed in the fluid. PIV's non-intrusive nature and its ability to measure instantaneous velocity fields make it an attractive experimental technique to capture wake vortex structures. It has become the method of choice to capture instantaneous velocity fields. The technique will be briefly described here, more in-depth analyses of the technique are available in Adrian and Westerweel (2011) and Raffel et al. (1998).

The form of PIV used depends on the region being investigated. PIV can measure velocities in a plane, or more recently a volume, of interest. Planar particle image velocimetry (2D2C) resolves the two in-plane velocity components. The three principle stages of single-

exposure planar PIV are shown in figure 3.1. In step one, the region of interest (object plane) is seeded with particles having a high reflective index. Ideally, the seed particles are fine neutrally buoyant spheres that act as a proxy for the surrounding fluid. A laser illuminates the region of interest in the flow field. A digital camera captures the position of the seed particles on an image plane at two time instants t and $t + dt$. The time delay, dt , determines the seed particle displacement.

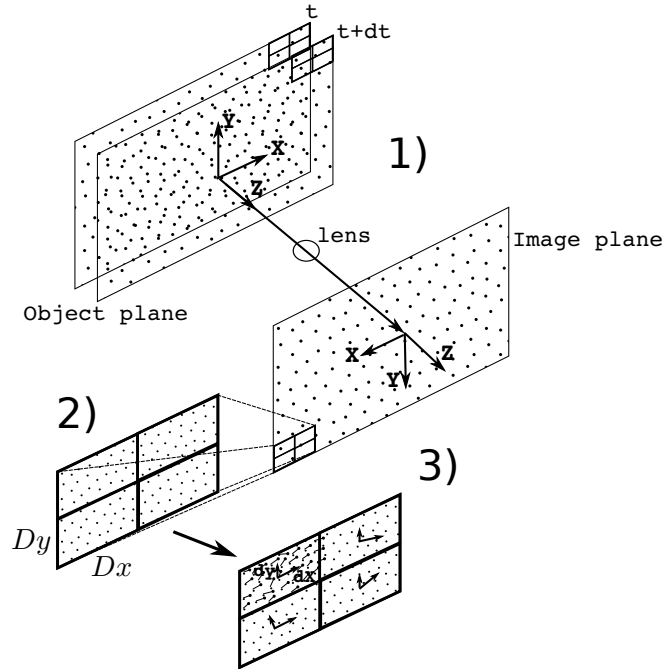


FIGURE 3.1: Operating principle of dual-frame single-exposure cross-correlation PIV technique illustrating the three primary steps for vector field determination. 1) Image object plane at two instants t , $t + dt$, 2) discretize image plane into interrogation windows of size Dx and Dy , 3) Determine average pixel displacements within interrogation window, dx and dy from peak of cross correlation function $R_{cross,max}$ (modified after figure 1.11 in (Adrian and Westerweel 2011)).

In step two, the first post processing stage, individual images at times t and dt are linked to become a single image pair. Seed particles appear as bright spots as they reflect the laser illuminating the field of interest. The intensity map is discretized into interrogation windows of size, Dx by Dy pixels to speed up processing and localise flow physics.

In step three, particle motion is determined by statistical algorithms. For single exposure images, the cross-correlation function, $R_{cross}(s)$ is calculated in frequency space (FFT) using the correlation theorem (Raffel et al. 1998). The FFT peak provides the estimate of the average pixel displacements, $\Delta x = (\Delta x, \Delta y)$ within the interrogation window. The displacement vector is assigned to the mid-point of the interrogation window. The process is repeated for all interrogation windows resulting in a displacement field, $\Delta x(x, y)$. The velocity field,

$\mathbf{u}(x, y)$ is then determined from equation 3.1:

$$\mathbf{u} = \frac{\Delta x}{MFdt}, \quad (3.1)$$

where MF (pixels/mm) is the magnification factor.

The magnification factor determines the length dimension ratio between the object and image planes. The magnification factor is a critical parameter to ensure the desired flow features are resolved with sufficient resolution. This is particularly important for flow fields containing vortices where centrifugal forces push particles out of the core region resulting in regions void of particles and higher uncertainty (Ramasamy et al. 2011). The low circulation of the tip and root vortices of the experimental model mean this problem is not encountered here.

3.1.1.1 Details of the PIV system used in this research

A PIV system has four principal components; a fluid seeded with tracer particles; a coherent light source, such as a laser with optics to condition and direct the light source to the field of interest; a timing box and; a recording device. The sections below describe the components used here.

Seed Particles

The tracer particle size and density must such that the seed particles act as an accurate proxy for the surrounding fluid's trajectories.

Two types of seed particles were used; polyamide particles (Vestosint, Degussa AG) and hollow glass spheres (Spherical 110P8, Potters Industries Inc.). The polyamide particles have a high reflective index making them suitable as PIV tracer particles but they are opaque. As a result the reflected light has to pass through a field of opaque particles prior to reaching the recording plane. These particles had nominal diameters ranging from $11\mu\text{m} \leq p_d \leq 50\mu\text{m}$ and were used depending on the flow of interest. Their density was 1.016 g/cm^3 .

The second type of particles were hollow glass spheres (Spherical 110P8, Potters Industries Inc.). They are preferable to the polyamide particles because they are transparent and because they don't agglomerate. Hollow glass spheres scatter light efficiently due to the multiple internal reflections at the solid wall-trapped air interface (Adrian and Westerweel 2011). The hollow glass spheres have a nominal diameter of $13\mu\text{m}$ and a density of $1.1 \pm 0.05 \text{ g/cm}^3$.

Light Source

A pulsed laser was used as the coherent light source to illuminate the region of interest. A pair of neodymium-doped yttrium aluminium garnet (Nd:YAG) lasers (Minilite PIV, Continuum) of wavelength 532 nm produced a laser sheet of 2 mm thickness. The laser delivers 25mJ of energy per pulse. The lasers were triggered by a transistor-transistor logic (TTL) signal sent from a timing box.

Timing Box

A timing box controlled the image acquisition sequence. The sequence was initiated by a TTL input that arrived from either a secondary timing box or the experimental model. The time gaps were set manually on the timing box or via a terminal prompt on a personal computer. The time gaps were shown on the box's display. The timing boxes were internally manufactured.

Imaging Media

There are two most widely used media to record the light intensity maps of the flow fields are charge-coupled device (CCD) chips or the complementary metal-oxide semiconductor (CMOS) chips. Both use semiconductor technology to capture photons from incident light, which is converted to an analog signal and recorded by specialist software (Camware, PCO AG).

Here a CCD camera was mainly used to capture the single-exposure PIV images. A CCD camera chip contains a prescribed maximum number of pixels, where a pixel is defined as a photon accumulation area (μm^2). The sensitivity of the semiconductor material dictates the size of a pixel. The specifications of the cameras used during candidature are shown in table 3.1.

Number	Model	chip	resolution(px)	px size(μm^2)	fps
1	pco.4000 (PCO AG)	CCD	4 008×2 672	9.0	5.0
2	pco.2000 (PCO AG)	CCD	2 048×2 048	7.4	14.7
3	MotionPro X3 (IDT REDLAKE)	CMOS	1 280×1 024	12.0	1000

TABLE 3.1: Specifications of the PIV cameras used during candidature. fps represents the maximum frames per second

PIV Software

A validated in-house PIV code was used in the current work (Fouras and Soria 1998; Fouras et al. 2008). The code, written in the C programming language is controlled via the command line prompt. It uses single exposure images as an input and FFT based cross correlation algorithms to determine particle displacements. The PIV software used mesh refinement and image overlap. These methods improve accuracy using multiple passes through the image fields. The details of the method used is available from Raffel et al. (1998). Here, an image overlap of 50% was used to balance computational time and minimise correlation between adjacent displacement estimates. However, during candidature, the standard image overlap moved from 50 to 75%. An image overlap of 50% was maintained throughout candidature. As a consequence, the spatial resolution of the vector map was typically 16 by 16 pixels. Knowing the time delay between image pairs, the velocity fields can then be calculated from equation 3.1. The following section discusses the secondary variables that are used to analyse flow features of interest.

3.1.1.2 Data processing algorithms

The velocity fields were analysed using scripts written in the octave and fortran programming languages. Secondary flow variables such as vorticity and circulation are calculated from the equi-spaced velocity fields. The vorticity vector, ω , is defined as the curl of the velocity vector as shown in equation 3.2 where \mathbf{i} , \mathbf{j} and \mathbf{k} represent a cartesian coordinate system:

$$\omega \equiv \nabla \times \mathbf{u} = \left(\frac{\partial w}{\partial y} - \frac{\partial v}{\partial z} \right) \mathbf{i} + \left(\frac{\partial u}{\partial z} - \frac{\partial w}{\partial x} \right) \mathbf{j} + \left(\frac{\partial v}{\partial x} - \frac{\partial u}{\partial y} \right) \mathbf{k}, \quad (3.2)$$

With planar PIV oriented in the x - y plane, the out-of-plane vorticity component, $\omega_{\mathbf{z}}$, can be calculated using equation 3.3. $\omega_{\mathbf{z}}$ is calculated by differentiating a polynomial fitted to the surrounding 21 points (Fouras et al. 2008). This method has been shown to reduce random and bias errors (Fouras and Soria 1998). The vorticity vector reveals the rotational and shearing motions within the flow field.

$$\omega_{\mathbf{z}} = \left(\frac{\partial v}{\partial x} - \frac{\partial u}{\partial y} \right) \mathbf{k}. \quad (3.3)$$

The velocity gradient or rate-of-deformation tensor, $\nabla \mathbf{u}$, is an important tensor quantity in fluid mechanics. It can be separated into symmetric and anti-symmetric parts, $\nabla \mathbf{u} = \mathbf{S} + \mathbf{\Omega}$, where \mathbf{S} is the rate-of-stain tensor and $\mathbf{\Omega}$ is the rotation tensor. The vorticity vector equates to the rotation tensor. For planar PIV the velocity gradient tensor reduces to a 2

by 2 matrix, as shown in equation 3.4. As planar PIV was used exclusively here Δx and \mathbf{u} will refer to the 2 dimensional vectors $\Delta x(\Delta x, \Delta y)$ and $\mathbf{u}(u, v)$ from hereon, unless otherwise indicated. In addition, $\nabla \mathbf{u}$ will refer to $\nabla \mathbf{u}_{2D}$ from hereon. From $\nabla \mathbf{u}$, the rotational motion of the vortices can be resolved.

$$\nabla \mathbf{u}_{2D} = \begin{bmatrix} \frac{\partial u}{\partial x} & \frac{\partial u}{\partial y} \\ \frac{\partial v}{\partial x} & \frac{\partial v}{\partial y} \end{bmatrix}. \quad (3.4)$$

Circulation is the vorticity in a unit area. It can be calculated either by a line integral of the velocity vector around a closed path, c , as shown in equation 3.5 or integrating the vorticity vector over a surface whose boundary demarcates the vortex tube, using Stokes theorem as in equation 3.6.

$$\Gamma = \oint_c \mathbf{u} \cdot d\mathbf{l}. \quad (3.5)$$

$$\Gamma = \iint_A (\nabla \times \mathbf{u}) \cdot \mathbf{n} \, d\mathbf{A}. \quad (3.6)$$

Vortices can be located by the maxima/minima in either the circulation or vorticity fields. Vortex identification based on the vorticity vector alone is not feasible as vorticity does not necessarily correspond to a vortex. The following section outlines the vortex identification algorithms that were used to locate and analyse the tip and root vortices in a wind turbine wake.

A single definition of a vortex that the entire fluid dynamics community accepts has proved difficult to achieve (Jeong and Hussain 1995; Chong et al. 1990; Green 1995). A common definition states a 'fluid vortex as any region of concentrated vorticity' (Green 1995). Vortex structures can then be located by distinct vorticity signatures within the flow field. In a flow field relatively free of shear, maxima/minima of the vorticity field can be used to locate vortices. However, if the flow field contains an appreciable amount of strain as is the case in a wind turbine wake, shear generated vorticity will mask the eddying motion of the vortex structures. An additional concern is how to determine the boundary of the vortex core, as this requires a nominated threshold criteria.

In the case of a laminar vortex, a region of solid body rotation can be used to locate the vortex core. The vortex centre is then the mid-way point between the maxima and minima of the tangential velocity profile. For PIV data, where orthogonal velocity components are measured, the vortex centre can be located where both velocity components (say u and v)

are zero (Heyes et al. 2004). However, for turbulent wind turbine tip vortices, the solid body rotation region is distorted due to the skew angle in the wake (Dobrev et al. 2008).

Lugt (1979) in Jeong and Hussain (1995) on the other hand state that vortex cores should have closed pathlines. However, this is not a Galilean invariant definition. An axisymmetric vortex core also has a pressure minima at its centre due to the balance of the centrifugal force (swirling flow) and the pressure force (Green 1995). Isosurfaces of local pressure minima intuitively can then be used to locate a vortex. Jeong and Hussain (1995) indicate that this definition alone is problematic due to the length scale difference between the vortex core (vorticity definition) and that of the low pressure region of a vortex core. They state that a vortex core should be both a region of net vorticity and a Galilean invariant description.

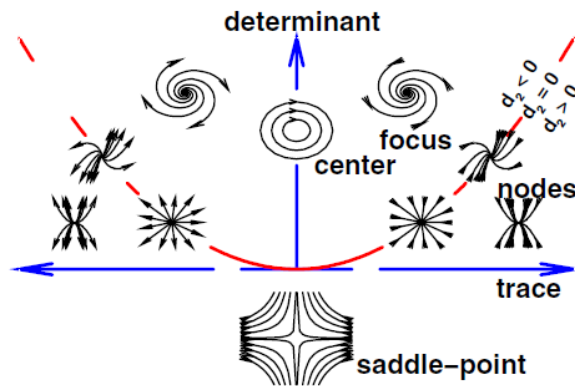


FIGURE 3.2: Flow field topologies based on the determinant and trace of the velocity gradient tensor, $\nabla\mathbf{u}$ (Vollmers 2001), used in the identification of vortices.

In turbulent flow fields, such as the near wake of a HAWT, vortex identification schemes can be based on invariants of the full velocity gradient tensor, $\nabla\mathbf{u}_{3D}$. Various flow topologies are shown in figure 3.2. A brief review of such schemes is presented in the following. For further information see text in Jeong and Hussain (1995), Chakraborty et al. (2005) and vonCarmer et al. (2008). Chong et al. (1990) used a critical point analysis to determine the instantaneous flow topologies based on, $\nabla\mathbf{u}_{3D}$. They state that ‘a vortex core is a region of space where the vorticity is sufficiently strong to cause the rate-of-strain tensor to be dominated by the rotation tensor, *i.e.* the rate of deformation tensor has complex eigenvalues’ (Chong et al. 1990). The eigenvalues of $\nabla\mathbf{u}_{3D}$ are found by solving the system characteristic equation 3.7,

$$\lambda^3 - \mathbf{P}\lambda^2 + \mathbf{Q}\lambda - \mathbf{R} = 0, \quad (3.7)$$

where the invariants $\mathbf{P}, \mathbf{Q}, \mathbf{R}$ are given in (Jeong and Hussain 1995). For the rate of defor-

mation tensor to have complex eigenvalues, the discriminant of the characteristic equation is positive. *i.e.* $\Delta = (1/3\mathbf{Q})^3 + (1/2\mathbf{R})^2 > 0$. The method is known as the Δ criterion.

Hunt et al. (1988) on the other hand, define an eddy as a region where the second invariant of $\nabla\mathbf{u}_{3D}$ is positive, *i.e.* $Q > 0$ and the pressure is lower than the surrounding fluid. This methodology is known as the Q criterion. The realisation of a positive Q value does not explicitly correspond to a local pressure minima but it is often implicitly realised (Jeong and Hussain 1995). For predominantly 2 dimensional flow fields another formulation based on the Q criteria is that of Weiss (1991), which is shown in equation 3.9:

$$\begin{aligned} Q_w &\equiv \left(\frac{\delta u}{\delta x} - \frac{\delta v}{\delta y}\right)^2 + \left(\frac{\delta v}{\delta x} + \frac{\delta u}{\delta y}\right)^2 - \left(\frac{\delta v}{\delta x} - \frac{\delta u}{\delta y}\right)^2, \\ &= \theta_1^2 + \theta_2^2 - \omega_z^2, \end{aligned} \quad (3.8)$$

where θ_1^2 represents normal strain rates, θ_2^2 represents shear strain rates and ω_z^2 is the squared out of plane vorticity. Vortical structures are identified as regions with a negative Weiss value as the magnitude of vorticity in equation 3.9, exceeds that of the strain terms. Conversely regions with a positive Weiss value indicate strain dominated regions.

Jeong and Hussain (1995) realising the inadequacy of intuitive vortex definitions (*e.g.* pressure minimum and vorticity) proposed a new velocity gradient tensor based criterion. The λ_2 criterion requires a connected region with two negative eigenvalues of the symmetric tensor $\mathbf{S}^2 + \mathbf{\Omega}^2$. Since $\lambda_1 \geq \lambda_2 \geq \lambda_3$, this requires the second largest eigenvalue to be negative, *i.e.* $\lambda_2 < 0$ (Jeong and Hussain 1995). The λ_2 method locates swirling flow regions with a pressure minima aligned with the vortex axis within the flow field (Jeong and Hussain 1995).

More recently, Zhou et al. (1999) extended the earlier critical point analysis of Chong et al. (1990) to develop the squared swirling strength λ_{ci}^2 , criterion. Zhou et al. (1999) noted that vortices correspond to regions with $\lambda_{ci}^2 > 0$, as particle trajectories about the real eigenvector axis have a finite time period of revolution $2\pi/\lambda_{ci}^2$. Regions of shear in a fluid field have infinite revolution time periods corresponding to $\lambda_{ci}^2 = 0$. The method is thus able to discern between regions of shear and vortical motions and λ_{ci}^2 is a measure of the ‘swirling strength’ of a vortex (Zhou et al. 1999).

In planar flows or two dimensional velocity fields (*e.g.* 2D PIV data), the velocity gradient tensor invariants are all proportional, *i.e.* $\Delta \propto Q \propto \lambda_2 \propto \lambda_{ci}^2$ (vonCarmer et al. 2008). However, the vortex identification schemes based on the velocity gradient tensor, ω_z , Δ , Q ,

Q_w , λ_2 and λ_{ci}^2 all require determination of velocity gradients introducing dependence on the differentiation method. The velocity gradient terms are here calculated by a central difference scheme ensuring second order accuracy.

The λ_{ci}^2 method was chosen to locate the tip and root vortices in the near wake of the geometrically scaled HAWT model turbine presented in chapter 5. λ_{ci}^2 is a more robust method to locate vortical structures than the vorticity component, ω_z , as it distinguishes between rotational and shearing motions. This is particularly important in the root region where large velocity gradients exist next to the nacelle. The λ_{ci}^2 method gives no indication of the direction of rotation of the identified vortical structures. The vorticity, ω_z , in the fluid regions where the swirling strength parameter identifies a vortex is thus checked to determine the rotation of the vortex. The background level of λ_{ci}^2 is determined from the freestream flow measurements to account for turbulent structures within the freestream flow and measurement noise. An absolute definition of the threshold value $\lambda_{ci}^* = \overline{\lambda_{ci}^2} + 2\overline{\sigma_{\lambda_{ci}^2}}$ is used as a base value to determine the presence of vortical structures.

In both the phase-locked average and instantaneous velocity fields, the vortex core location is defined as the centroid of area of the minimum threshold λ_{ci}^* contour encapsulating the λ_{ci}^2 maximum (Vollmers 2001). Once a vortex has been identified, the circulation Γ , is calculated using equation 3.5. The line integral path, c , is the threshold contour, λ_{ci}^* . The vortex radius, r_{vc} , is designated as the radius of a circle with equivalent area to the area that the threshold contour encompasses.

However, the near wake of a HAWT is turbulent. The λ_{ci}^2 method's reliance on velocity differentials produces noisy results. Small scale turbulent eddies were often (correctly) located based on the maximum λ_{ci}^2 value, which did not necessarily correspond to the large scale tip/root vortices. Locating these turbulent eddies biased the distribution of instantaneous vortex results away from the large scale tip/root vortices of interest. The vortex extraction methodology, while robust, was strengthened when analysing the optimum Glauert blade results in chapter 6. A vortex identification scheme that characterises the flow topologies based on the velocity field alone was used.

The $\mathbf{\Gamma}_1$ method calculates in-plane rotation directly from the velocity field (Graftieaux et al. 2001). The discretized version of the $\mathbf{\Gamma}_1$ function, readily calculable on equi-spaced PIV data, is shown in equation 3.9. The $\mathbf{\Gamma}_1$ function, is evaluated at a number, n , of points, m , in a rectangular subspace of points, s , surrounding the evaluation point, p . $\mathbf{\Gamma}_1$ determines the angle between the velocity vector, \mathbf{u} , and the radius vector, \mathbf{pm} , of all m points within

s . The size of the subspace, s , acts as a spatial filter, which has minimal affect on vortex position (Graftieaux et al. 2001). The vortex centre is determined by peak detection with typical Γ_1 values between $\pm 0.9 - \pm 1$ for axisymmetric vortices. The sign of the function gives indicates the vortex orientation, an added benefit over the λ_{ci}^2 method.

$$\Gamma_1(p) = \frac{1}{n} \sum_s \frac{(\mathbf{pm} \wedge \mathbf{u}(m)) \cdot \mathbf{z}}{\|\mathbf{pm}\| \cdot \|\mathbf{u}(m)\|} = \frac{1}{n} \sum_s \sin(\theta_m), \quad (3.9)$$

where n are a number of points m in s , \mathbf{pm} is the vector between the evaluation point p and m , $\mathbf{u}(m)$ is the velocity vector at m , \mathbf{z} is the unit normal vector from the 2D plane and θ_M is the angle between $\mathbf{u}(m)$ and \mathbf{pm} (Graftieaux et al. 2001).

The vortex core boundary is evaluated by an adaptation of the Γ_1 function. The Γ_2 function subtracts the local convection velocity, $\tilde{\mathbf{u}}_P = (1/s) \int_s \mathbf{u} ds$, within the subspace s , making the technique Galilean invariant (Graftieaux et al. 2001). The discretized version of the Γ_2 function, suitable for equi-spaced PIV data is shown in equation 3.10:

$$\Gamma_2(p) = \frac{1}{n} \sum_s \frac{[\mathbf{pm} \wedge (\mathbf{u}(m) - \tilde{\mathbf{u}}_P)] \cdot \mathbf{z}}{\|\mathbf{pm}\| \cdot \|\mathbf{u}(m) - \tilde{\mathbf{u}}_P\|}. \quad (3.10)$$

A threshold Γ_2 value, $\Gamma_{2*} = |2/\pi|$, is used to determine the vortex core boundary within which solid body rotation occurs. The threshold value was largely independent of s and thus n (Graftieaux et al. 2001). Unlike the λ_{ci}^2 method, which determined regions where eddying motion occurs, the Γ_2 determines the core boundaries based on regions of solid body rotation.

The Γ_1 and Γ_2 functions improved vortex detection when using the instantaneous frames but small scale turbulent eddies were still located preferentially over the large scale tip/root vortices. An energy based filter based on the snapshot proper orthogonal decomposition (POD) technique (Sirovich 1987) was implemented to ensure detection of the vortices of interest. It is outlined below.

3.1.1.3 Energy based filter

In a turbulent flow field such as a HAWT wake, the instantaneous velocity field can be separated into mean, $\bar{\mathbf{u}}(\mathbf{x})$, and fluctuating, $\mathbf{u}'(\mathbf{x}, t)$, components as in equation 3.11:

$$\mathbf{u}(\mathbf{x}, t) = \bar{\mathbf{u}}(\mathbf{x}) + \mathbf{u}'(\mathbf{x}, t). \quad (3.11)$$

Turbulent eddies, which contribute to the fluctuating component, are often smaller than the vortex of interest and can contain a large component of vorticity. Energy and/or scale

based filtering techniques can be used to remove smaller eddy structures. One such technique is proper orthogonal decomposition (POD) (Lumley 1987; Berkooz et al. 1993). For an in depth analysis of the POD technique see Berkooz et al. (1993) and chapter 22 in Tropea et al. (2007). POD has been applied to PIV data to evaluate topologies in a variety of flow fields (Graftieaux et al. 2001; Kostas et al. 2005; van Oudheusden et al. 2005). POD provides an optimal energy based orthonormal approximation of a continuous function, $\mathbf{u}(\mathbf{x}, t)$, using a number of basis functions, $\phi_n(x)$, or ‘mode shapes’ (Chatterjee 2000). POD is optimal from an energy point of view, any other decomposition technique with the same number of modes will contain less of the systems energy (Tropea et al. 2007; Graftieaux et al. 2001). POD is concerned with the choice of the spatial modes, $\phi_n(x)$ which best represent the function $\mathbf{u}(\mathbf{x}, t)$ whilst minimising the residual error between the approximation and the true function.

The method of snapshots (Sirovich and Kirby 1987) is used if the order of temporal realisations is much less than that of the spatial realisations, *i.e.* $N \ll M$. Common CCD arrays contains thousands of pixels, *i.e.* order of M is $\mathcal{O}(10^3)$, meaning the method of snapshots is the preferred decomposition method when dealing with PIV data. As the velocity snapshots are uncorrelated in time, no temporal information is available. The variable t represents an average spatial quantity. For N PIV realisations, a cross-correlation (snapshot) matrix is constructed which contains the temporal/spatial fluctuating kinetic energy information of the series,

$$R_{mn} = \sum_{m=1}^N \sum_{n=1}^N \mathbf{u}'(\mathbf{x}, t_n) \mathbf{u}'(\mathbf{x}', t_m). \quad (3.12)$$

The cross-correlation matrix then presents an eigenvalue problem of the form,

$$R_{mn} \phi_n = \lambda_n \phi_n. \quad (3.13)$$

The orthonormal eigenvectors, ϕ_n , and eigenvalues, λ_n , are determined using the singular value decomposition (SVD). The eigenvalue matrix contains the squared singular values, s , of $\mathbf{u}'(\mathbf{x}, t)$ (Epps and Techet 2010). The SVD ensures an ordered nature (in terms of magnitude) of the eigenvalues, *i.e.*

$$\lambda_1 > \lambda_2 > \lambda_3 > \dots > \lambda_N,$$

with the n th eigenvalue, λ_n , quantifying the kinetic energy of the n th, ϕ_n , mode. The first modes contain the most energy, and in the case of velocity realisations are usually associated

with large scale flow structures. The technique thus allows filtering based on energy content and implicitly on scale.

The orthonormal eigenvectors from equation 3.13, form a basis to construct the spatial POD modes, $\phi_n(\mathbf{x})$. Following Sirovich (1987), the spatial modes are reconstructed by a linear combination of the eigenvectors and the velocity field and normalised as in equation 3.14,

$$\phi_n(\mathbf{x}) = \frac{\sum_{n=1}^N \phi_n \mathbf{u}'(\mathbf{x}, t)}{\|\sum_{n=1}^N \phi_n \mathbf{u}'(\mathbf{x}, t)\|}, \quad t = 1, 2, \dots, N, \quad (3.14)$$

where ϕ_n is the n-th component of the eigenvector corresponding to the eigenvalue λ_n and the $\|\dots\|$ represents the L_2 -norm.

An instantaneous velocity snapshot can be approximated in a series of POD modes with spatial coefficients, a_n for each POD mode n . The spatial mode coefficients, a_n , are determined by projecting the velocity field, $\mathbf{u}'(\mathbf{x}, t)$, onto the POD basis, ϕ_n as in equation 3.15. The $\langle \cdot \rangle$ represents an inner product.

$$a_n(t) = \langle \mathbf{u}'(\mathbf{x}, t), \phi_n \rangle \quad (3.15)$$

The normalised POD basis functions, $\phi_n(\mathbf{x})$, are spatially orthogonal, *i.e.* $\langle \phi_i \phi_j \rangle = \delta_{ij}$. The mode coefficients a_n are also uncorrelated in time, *i.e.* $\overline{a_i a_j} = \lambda_i \delta_{ij}$.

The POD based approximation of the instantaneous snapshot $\hat{\mathbf{u}}'(\mathbf{x}, t)$, equation 3.16, thus comprises spatial mode coefficients, $a_n(t)$, and spatial modes, $\phi_n(\mathbf{x})$, where n is the order of the approximation.

$$\hat{\mathbf{u}}'(\mathbf{x}, t) \sim \sum_{n=1}^{N_{POD}} a_n(t) \phi_n(\mathbf{x}). \quad (3.16)$$

The number of modes is an important parameter in the reconstruction of the instantaneous velocity realisations. The initial modes represent the large scale flow structures with higher order modes describing small scale fluctuations. The small scale turbulent eddies should be filtered, so vortex detection algorithms find the large scale vortices generated by the blade sections. Epps and Techet (2010) recently provided a guideline for the threshold singular value (eigenvalue) magnitude. The basis of the threshold criteria is that the root-mean-square (rms) error of the reconstructed velocity field should be less than the rms of the original data. The threshold eigenvalue, s_k , shown in equation 3.17, states the highest singular value and hence POD mode number where the velocity fluctuations are due to flow features rather than measurement noise (Epps and Techet 2010).

$$s_k > \sqrt{MN} \cdot \epsilon, \quad (3.17)$$

where s_k is the threshold eigenvalue with acceptable signal to noise ratio (SNR), M is the number of sample points (for PIV fields, $M = m \times n$) and ϵ is the measurement uncertainty. A PIV measurement uncertainty, $\epsilon = 0.1$ (px/dt), achievable with sub-pixel accurate peak detection schemes (Raffel et al. 1998) is used in the threshold definition. The threshold method of (Epps and Techet 2010) thus provides a physical mechanism to determine the maximum number of usable POD modes. It must be noted that modes with $s < s_k$, may still contain important information but are hampered by a higher uncertainty due to lower signal to noise ratio. The required number of modes for several tip vortex ages is shown in figure 3.3. This data was produced by the optimum Glauert rotor operating at its design tip speed ratio, λ_d . This figure indicates between 10 and 25 modes can be used in the POD reconstruction depending on tip vortex age. At earlier vortex ages, the large scale structures dominate as can be seen by the abrupt drop off of energy.

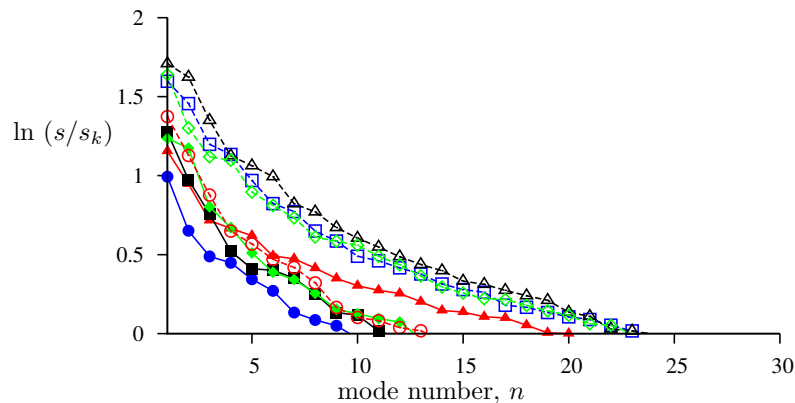


FIGURE 3.3: Logarithmic decay of the normalised singular value with POD mode number of tip vortices at various vortex ages created at λ_d . s_k is a threshold based on the criteria of Epps and Techet (2010). Between 10 and 25 modes are used depending on vortex age. red triangles: $VA = 120^\circ$ (solid symbol/line) and $VA = 600^\circ$ (hollow symbol/dashed line), blue circles: $VA = 240^\circ$ and $VA = 720^\circ - 840^\circ$, black squares: $VA = 360^\circ$ and $VA = 960^\circ$, green diamonds: $VA = 480^\circ$ and $VA = 1080^\circ - 1200^\circ$

The beauty of the POD is the organised nature of the modes in terms of energy content and implicitly scale of the structures the modes reveal. Large scale structures are associated with higher order modes as they contain the most energy. As an example, the first nine modes of a tip vortex at a vortex age of 240° are presented in figure 3.4. These structures correspond to the filled blue circles in figure 3.3. The contour levels illustrate the induced velocity field whereas the lines represent out-of-plane vorticity, ω_z . The contour lines illustrate vortices. It is clear the first mode corresponds to the large scale tip vortex of interest. With

increasing mode number the scale of the structures reduces along with its energy content. The nine modes depicted in figure 3.4 contain 40% of the fluctuating kinetic energy. These higher order modes will contribute to the fluctuations about the mean vortex position, *i.e.* meandering motion.

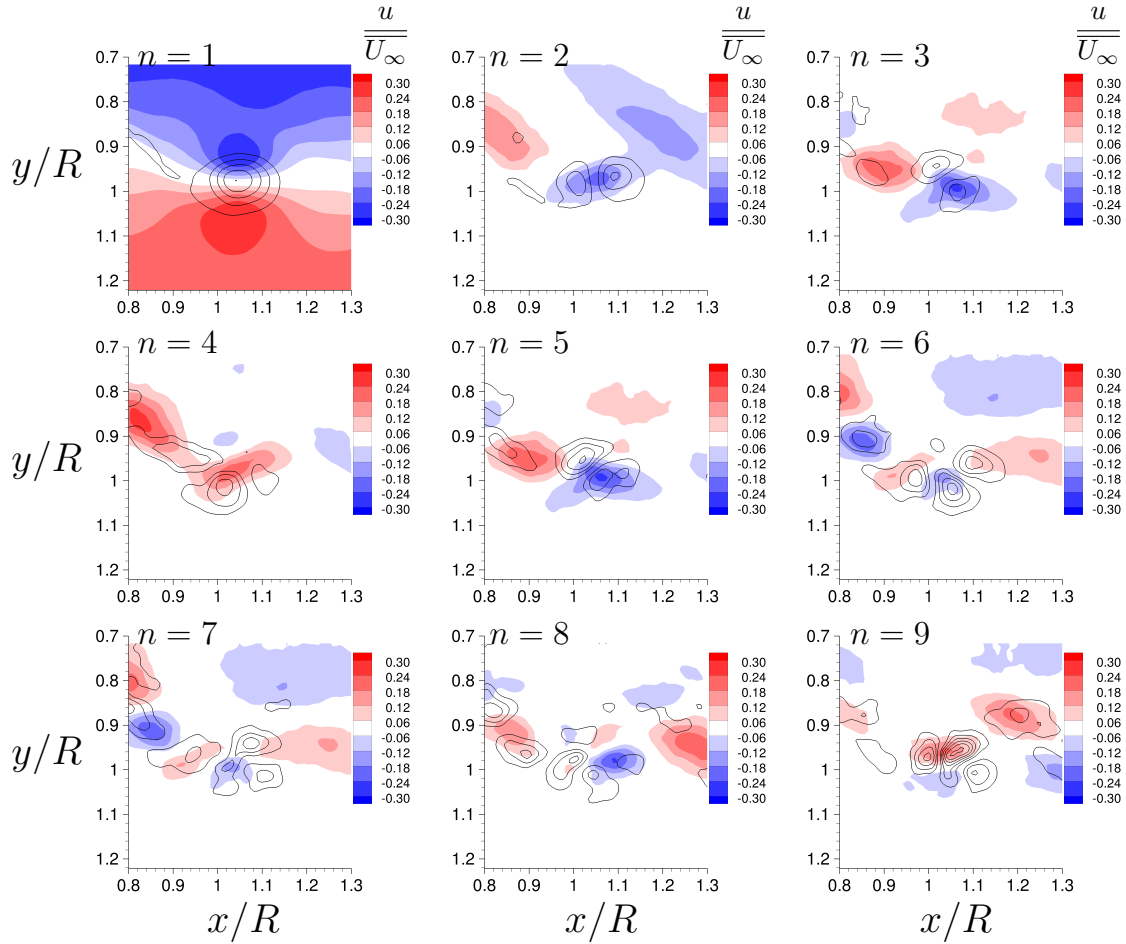


FIGURE 3.4: Induced velocity fields of the first 9 reconstructed tip vortex modes at a $VA = 240^\circ$ and λ_d . Contour lines indicate ω_z .

The purpose of the energy based filter was to evaluate the dynamics of the tip and root vortices in the plane of measurement. An alternative to an energy based filter is ensemble averaging based on vortex location (Grant and Parkin 2000; Dobrev et al. 2008). However, ensemble averages still contain undesired small scale turbulent motions. The energy based filter is thus preferable to ensemble averaging.

Figure 3.5 illustrates the automated process used to characterise tip and root vortex meander in chapter 6. The process contained the following steps,

- 1 The average phase-locked tip/root vortex positions were located based on the λ_{ci}^2 method. A sub PIV field around the phase-locked average vortex position was then

extracted.

- 2 The energy based filter was implemented to filter out small scale eddies due to turbulent motions. The number of modes used in the reconstruction was based on the threshold criteria of Epps and Techet (2010). The instantaneous vortex locations were evaluated using both the Γ_1 and λ_{ci}^2 methods creating a scatter plot.
- 3 A probability density function (p.d.f) was created based on the vortex core locations in each measurement axis. A normal distribution was then fit to the p.d.f, with the standard deviation extracted as a measure of the meander magnitude in each measurement axis.

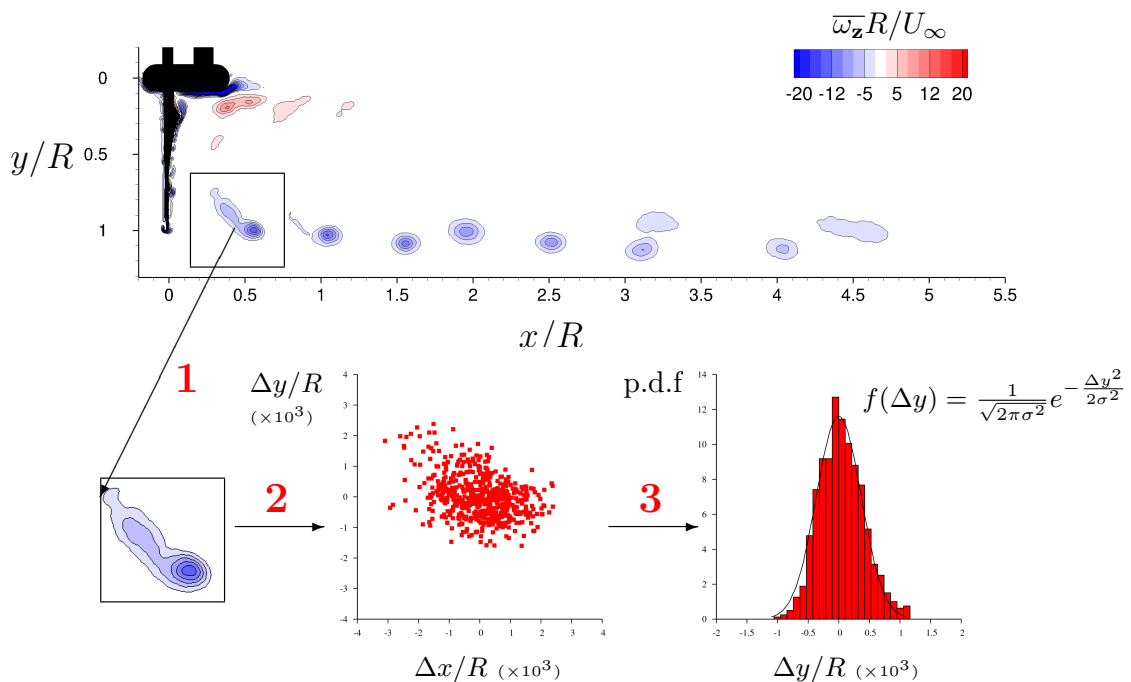


FIGURE 3.5: Schematic of the process to characterise tip and root vortex meander at a particular vortex age for the optimum Glauert rotor. Step 1: Extract a sub PIV field containing vortex based on phase-locked average data. Step 2: Apply energy filter to instantaneous sub PIV fields and locate vortex centres. Step 3: Generate probability density function (p.d.f) of instantaneous vortex positions in each measurement axis. Fit normal curve to p.d.f and extract standard deviation as measure of meander.

3.1.2 Laser Doppler Velocimetry (LDV)

Laser Doppler velocimetry (LDV) is a non-intrusive optical technique that makes point velocity measurements in a flow field. It permits a high sample frequency making it suitable for measuring turbulence. It was used in this capacity here. Sample frequencies achieved in

the water channel were of the order of 100Hz, two orders of magnitude higher than those achievable with the high resolution CCD PIV cameras.

The technique measures the doppler effect created by particles passing through a measurement volume formed by the intersection of two coherent laser beams. A pair of laser beams are required for each velocity component. The intersection of the two beams results in a fringe pattern with alternating dark and light bands with spacing ∂_f , determined from equation 3.18. As the fringe pattern depends on the laser wavelength, λ_l , multiple beams of different wavelength can intersect at a measurement point and be used to determine multiple velocity components.

$$\partial_f = \frac{\lambda_l}{2 \sin \kappa}, \quad (3.18)$$

where ∂_f is the fringe spacing (μm), λ is the laser wavelength (μm), and κ is the half angle of the two intersecting beams.

When a particle moves through the measurement volume the fringe pattern is altered. The particle reflects light when it crosses a bright fringe and no light when it crosses a dark fringe. The frequency of the fluctuating light intensity signal (Doppler frequency, f_d) is thus proportional to the particles velocity. The reflected light from the particle passing through the measurement volume is collected by optics in the probe head. The velocity is then determined with knowledge of the fringe spacing, equation 3.19:

$$\mathbf{u} = \partial_f f_d. \quad (3.19)$$

To determine the direction of the particles moving through the measurement volume, one of the intersecting laser beams is frequency shifted by a 40MHz Bragg cell. This technique allows reverse flow to be determined (TSI 2006).

The two colour, four beam LDV system used here is shown in figure 3.6. The system is operated in burst mode (irregular arrival of particles) and the back scatter configuration. The LDV system was mounted on a computer-controlled three axis traverse (IMC-S8 controller, ISEL) which allowed accurate positioning of the measurement volume and long automated runs.

The LDV (Flowsizer) software used a slotted method to determine the power spectral density (PSD) function. In this method (Bell in (TSI 2006)), the auto-correlation function is binned to equispaced data and then the power spectral density function is calculated. The sample frequency, n_i , is based on the average data rate over the entire series, *i.e.* $n_i =$

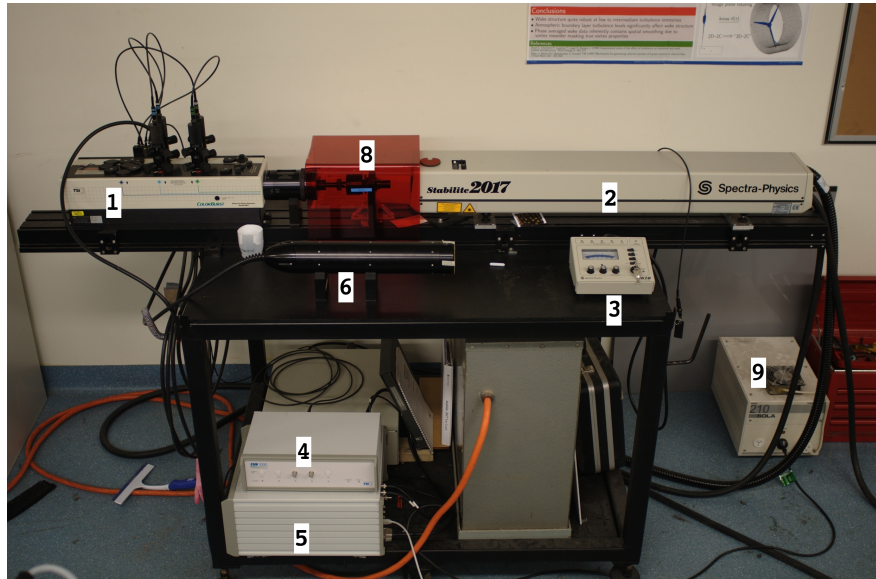


FIGURE 3.6: LDV system used during candidature. Components include 1: multicolour beam separator (ColorBurst model 9201, TSI), 2: continuous wave laser (Stabilite 2017, SPECTRA-PHYSICS), 3: laser remote control (model 2670, SPECTRA-PHYSICS), 4: photo detector module (PDM 1000, TSI), 5: signal processor (FSA 3500 MultiBit digital processor, TSI), 6: LDV probe head (Model 9253-350, TSI), 7: (not shown) computer station with specialist software (Flowsizer, TSI), 8: laser shield, 9: power conditioner (SOLA 210 series, SOLA)

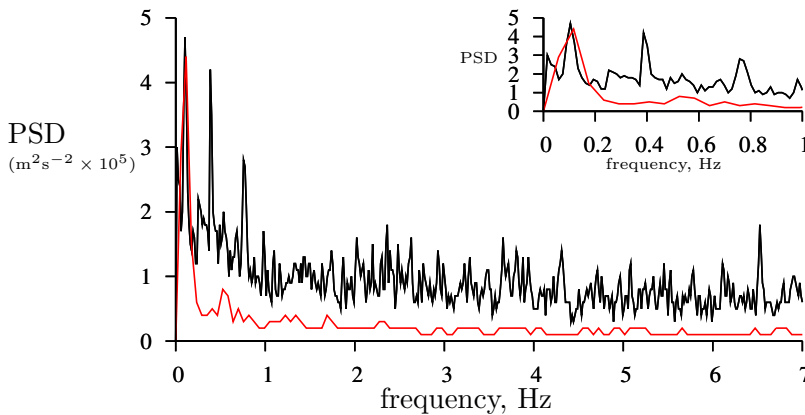


FIGURE 3.7: Power spectral density (PSD) function behind a passive turbulence grid evaluated by the slotted method in the Flowsizer LDV software. black: $x/M = 12.4$, red: $x/M = 30.4$.

N_s/t_{end} . The PSD functions evaluated by the Flowsizer software at two distances from a passive turbulence grid are shown in figure 3.7. The black line indicates the PSD at a distance $x/M = 12.4$ whereas the red line is for $x/M = 30.4$. A clear peak at $\sim 0.1\text{Hz}$ is evident in both PSD functions as highlighted by the inset. This is caused by a sloshing motion within the water channel. However, we are only interested in fluctuating velocities at higher frequencies than this, *i.e.* turbulent motions.

The low-frequency oscillations due to sloshing were filtered out using the empirical mode decomposition (EMD) technique (Huang et al. 1998). The time series was first interpolated

to an equispaced time domain. A slotted method was employed. The sample frequency, n_i , was chosen to minimise number of bins with no data. Bins with no data were discarded and the remaining smoothed data were interpolated to the original specified sample frequency. The time series could then be filtered using the EMD technique.

The EMD technique uses the Hilbert spectrum to decompose a data set into a number of intrinsic mode functions (IMF) (Huang et al. 1998). The IMF's represent fluctuating signals in the data set. As the frequency of the sloshing was known, all IMF's with frequencies lower than the sloshing frequency were discarded and the remaining IMF's reconstructed into a filtered signal. The filtering process confirmed the sloshing motion was not the source of the velocity fluctuations which control the turbulence intensity. The turbulence generated by passive turbulence grids was characterised using the LDV over a broad spatial range in the water channel. The evolution of the generated turbulence is presented in chapter 7.

3.1.3 Flow Visualisation Techniques

Flow visualisation techniques were used here to gain rapid understanding of the flow topology in cases of interest. Often these focused the quantitative experiments. The following section briefly describes the flow visualisation techniques used. A comprehensive review of flow visualisation techniques can be found in Smits and Lim (2000).

3.1.3.1 Hydrogen bubble (H2)

A widely used visualisation technique employed in low speed water channels is the hydrogen bubble (H2) technique. The H2 technique provides a fast and effective way to seed the flow domain with a tracer particle that minimises disruption to the flow. A brief review of the technique is provided below with a more comprehensive summary provided in Schraub et al. (1965).

The H2 technique works by the process of electrolysis whereby an electrical charge is passed through a negatively charged electrode (cathode) placed in a body of water. A Hydrogen gas bubble is created on cathode until U_∞ sweeps it off the cathode surface. However, the hydrogen bubbles are not neutrally buoyant due to their smaller density compared to the surrounding fluid (hydrogen 0.0838kg/m^3 compared to water 998kg/m^3 at 20°C). The hydrogen bubbles thus rise at a rate dependent on their diameter after detaching from the cathode. The rise rate was negligible over the field of view employed in the current studies. Further, the freestream speed was limited to $U_\infty \leq 0.11\text{m/s}$ to minimise flow induced vibrations of the H2 probe.

The H2 technique produces timelines, *i.e.* streaklines of a set of particles. The flow is marked at a particular instant in time with subsequent times revealing the timelines of the injected bubbles. A schematic of the H2 system used in wind turbine wake visualisations is shown in figure 3.8. A laser sheet passing through the rotational axis was used to illuminate a 2D (x - z) plane containing the tip and root vortices. The hydrogen bubble (H2) probe was fixed in space, not the coordinate system of the rotating blades. The H2 technique seeded a 2D plane that was illuminated by the laser sheet.

The system consists of a number of d.c. power supplies (MP-3086, POWERTECH) connected in series ($V_{total} = 64$), a probe holder, a cathode typically made from platinum wire of 25-50 μm diameter and a streamlined anode. The body of water acts as the electrical conduit to complete the circuit between the anode and cathode. The H2 system could be triggered at known time spacing creating pulsed output allowing quantitative data acquisition. Triggering of the hydrogen bubble system was controlled via a control box made in-house.

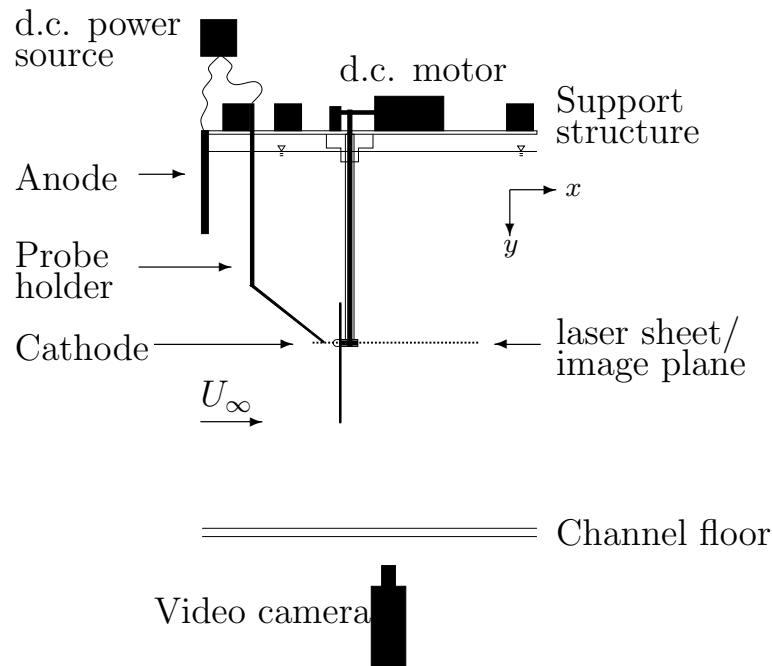


FIGURE 3.8: Side view of the experimental setup of the hydrogen bubble rig used in flow visualisations. A single blade is aligned with the tower section in the phase-locked visualisations. Freestream flow, U_∞ is from left to right aligned with positive x -axis, y and z axis follow a right handed coordinate system. Channel depth reduced in figure. Images were captured in the x - z plane.

Either studio lighting or a continuous wave laser (Model 85-GHS-309, MELLES GRIOT) was used to produce a light sheet to illuminate the plane of interest. Generally speaking, a more powerful and coherent light source improved image contrast and allowed better imaging.

H2 visualisations are valuable because they minimise flow disturbances whilst seeding the

flow over a wide area of interest. Two examples of how the H2 technique were used during candidature are presented in figure 3.9. This figure illustrates tip vortex formation behind a static 3D wing (left) at $\alpha = 10^\circ$ and several wake ages $x/c = 0.5, 1.0, 1.5$, and behind the geometrically scaled rotating wind turbine blades (right) at a tip speed ratio of $\lambda = 6.62$.

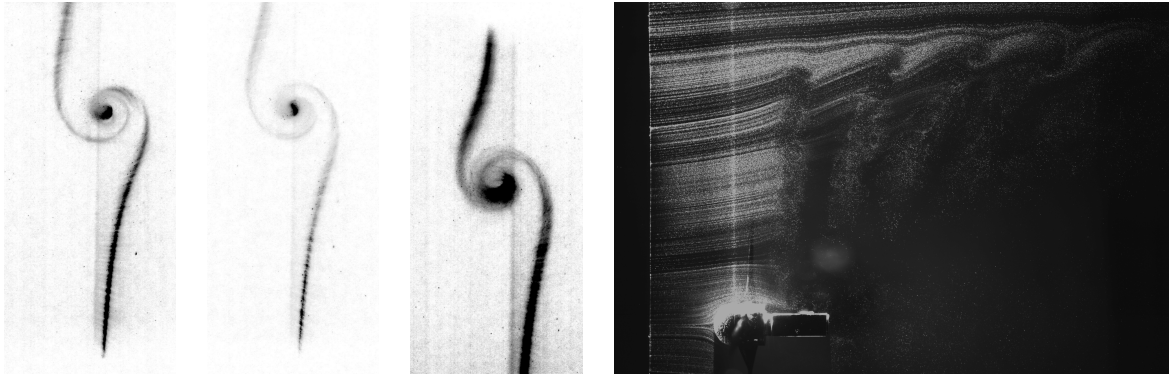


FIGURE 3.9: Examples of H2 technique, 3D wing: $\alpha = 10^\circ$ at $x/c = 0.5, 1.0, 1.5$; Rotating turbine blades: $\lambda = 6.62$

The H2 technique was used to visualise the flow tip vortex formation at low Reynolds numbers behind a planar wing in chapter 4 and the near wake of a wind turbine in chapter 5.

3.1.3.2 Particle streak

Particle streak flow visualisation is an optical technique similar in form to PIV. The equipment used in particle streak flow visualisations is the same as that used for PIV. Unlike PIV however, the flow visualisations provide largely qualitative rather than quantitative information. The image exposure is increased so that particles appear streaked in the images revealing the pathlines of the particles. The velocity of the particles can be determined from the length of the particle streaks. The streak length also indicates areas where three dimensional particle movement occurs.

Particle streak flow visualisations were used to determine the three dimensionality of the flow behind the nacelle and also the dynamics of the root vortices. Some example particle streak images are shown in figure 5.24. These images show the three-dimensionality of the flow in the root region of a wind turbine. Further analysis is presented in chapter 5.

3.1.3.3 Planar laser induced fluorescence (PLIF)

If visualisations with a high image contrast and minimal flow disturbance were required, planar laser induced fluorescence (PLIF) was used. In PLIF a light source causes a material in the flow to fluoresce which is then imaged by a digital camera. A digital SLR camera

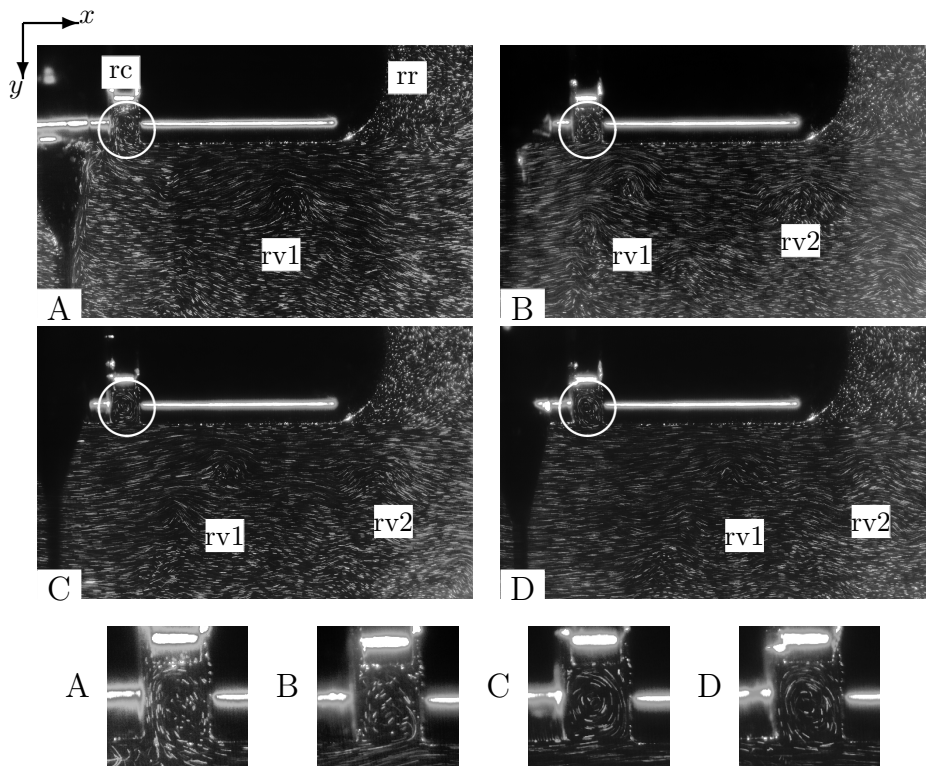


FIGURE 3.10: Particle streak flow visualisation sequence in the x - y plane (120° progression A–D) showing blade passage, rotating cavity flow (below rc marker and white circles), root vortex (above rv1 and rv2 markers) passage and recirculation region (marker rr) behind nacelle. Bottom images, expanded view of white circle regions. Flow from left to right, $\lambda = 7$, $Re_c = 2900$, particle streak lengths show qualitative instantaneous velocities.

(D7000, NIKON) with a 105 mm (AF105, NIKKOR) lens and a computer controlled shutter was typically employed to acquire the image. A computer controlled traverse (IMC-S8 controller, ISEL) was used to position the camera. The PLIF visualisation technique produces streaklines.

The wavelength and energy of the light source determines whether fluorescence occurs in the fluorescent material. Several light sources were used based on the desired field of interest. Ultra-violet (UV or black) lights emit diffuse light in the ultra violet wavelength range allowing imaging of a volume of interest. For planar visualisations, two continuous lasers models were used; a green laser with wavelength $\lambda_l = 514.5\text{nm}$, (85-GHS-309, MELLES GRIOT) and a blue laser with wavelength $\lambda_l = 488\text{nm}$, (85-BCD-030-230, MELLES GRIOT). These lasers produced a coherent light sheet well-suited to visualise flow features in a plane of interest.

Fluorescein and Rhodamine B were used here. The fluorescent material can be mixed to a desired concentration with water and injected into the flow. Care was taken to ensure the injection does not disturb the flow and alter the flow physics of interest. Alternatively,

Chapter 3. Experimental Techniques, Models and Equipment

the fluorescent material can be mixed with a soluble substance which dissolves, 'leaching' the fluorescent material into the flow when placed in water. Soluble substances that were found to work well in the water channel were honey and maple syrup. The latter technique minimises flow disturbances but may change the surface roughness profile of the application surface. An example of how the PLIF technique was used during candidature is shown in figure 3.11. Here, the suction surface flow patterns over a NACA4412 airfoil at a Reynolds number of $Re_c = 3484$ are shown. These flow visualisations were undertaken to determine the applicability of a BEM method to the low Reynolds number wind turbine models. More analysis is presented in chapter 4.

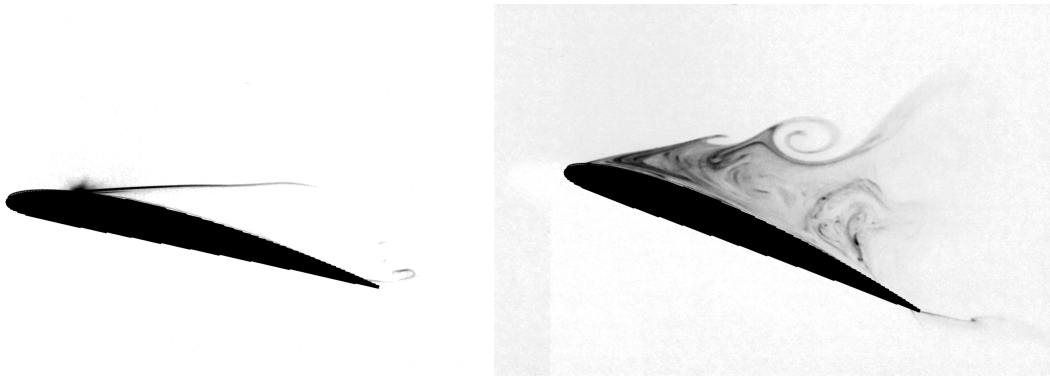


FIGURE 3.11: Suction surface flow patterns above a NACA4412 airfoil at $\alpha = 10^\circ$ (left) and $\alpha = 20^\circ$ (right) at $Re_c = 3484$. Leading edge separation is evident for $\alpha = 20^\circ$.

The experimental techniques and data processing methodologies have now been presented. The experimental models and equipment used to test the hypotheses presented at the end of the literature review are presented in the following sections.

3.2 Experimental Models

3.2.1 Flat plate blade sets

As a first approximation to wind turbine blades, flat plate blade sets were designed and investigated. These blade sets were quick to manufacture and were useful for the initial optimisation of the experimental parameters. The flat plate blade sets revealed both a tip and root vortex signal could be measured experimentally. However, the vortices were weak due to minimal blade bound circulation generation. Further, a large proportion of the blade in the root region experienced separation. No flat plate experimental data will be presented in the results chapters.

3.2.2 Airscrew blade sets

To overcome the poor aerodynamic performance (minimum circulation production, separated flow) of the flat plate blade profiles, a commercial ‘master airscrew’ type propeller was investigated. The blade uses a cambered airfoil profile and contains significant twist with minimal taper. The airfoil profile and twist and chord distribution were not available from the manufacturer. The high level of twist on the blades promoted attached flow and hence a strong tip vortex signal. The propeller blade set indicated that an airfoil profile produced a stronger tip vortex signal, allowing investigation and characterisation.

However, the propeller blades are designed to operate in the rpm range 17.5×10^3 to 20×10^3 . This rotational speed is far in excess of the rpm used in the wind turbine wake studies. The difference in rotational speeds introduces airfoil inefficiencies. No propeller experimental data will be presented in the results chapters.

3.2.3 Geometrically scaled wind turbine rotor

A geometrically scaled rotor design was a natural progression in the model evolution. Full scale turbines contain both twist and taper in addition to lifting surface termination prior to the rotational axis. The results of the two preliminary blade designs suggested a geometrically scaled turbine would produce a strong tip and root vortex signal. The Tjæreborg wind turbine was chosen as a suitable full scale turbine for scaling. The turbine geometric data was readily available (Oye 1990), has been investigated at fullscale in the past (Oye 1991) and has recently seen interest from the CFD community (*e.g.* (Ivanell et al. 2010, 2009; Troldborg et al. 2007)). A brief introduction to the Tjæreborg wind turbine follows and is largely taken from CADDET (1998).

Chapter 3. Experimental Techniques, Models and Equipment

The Tjæreborg wind turbine was a pitch regulated turbine. The 3 bladed turbine had a rotor diameter of $D = 61.1$ m. The rotor was positioned at a hub height of 61 m on a conical concrete tower. The three blades contained both linear taper (0.1 m/m) and twist ($1^\circ/3$ m) (Oye 1990). The rotor tip speed was 70m/s at a freestream velocity of 10m/s giving a full scale design tip speed ratio of $\lambda_{d,fs} = 7.07$. The tip chord Reynolds number was $Re_c = 5.3 \times 10^6$. Several views of the full scale turbine are shown in figure 3.12.



FIGURE 3.12: Views of the fullscale Tjæreborg wind turbine. Images winddata.com

Airfoil profiles with a high lift to drag ratio (C_l/C_d), a stable Cl_{max} at stall, and which are insensitive to blade fouling are desired in a wind turbine application (Spera 1994). The Tjæreborg turbine was constructed of NACA44XX family airfoils. The amount of camber and position of maximum camber was constant along the span. The airfoil thickness increased from 12% at the tip to 24% in the root section for blade stiffness (Oye 1990). The airfoil performance of the NACA44XX family at a Reynolds number of $Re = 6 \times 10^6$, are shown in figure 3.13. The airfoil family has a large C_l/C_d ratio with a minimal reduction in performance in the early stall region. The inset of figure 3.13 clearly shows a reduction in performance with increasing airfoil thickness. The thickness shows little effect on the drag properties of the airfoil at high Reynolds numbers due to the thin boundary layer present.

The geometrically scaled model has the same twist and taper as the full scale turbine. The model turbine used the NACA4412 airfoil profile along the entire span for ease of construction and better performance at the low experimental Reynolds number. Thick airfoils perform poorly at low Reynolds number due to the large viscous drag experienced (Kunz and Kroo 2002). The NACA4412 airfoil is shown in figure 3.14 with the cambered nature of the airfoil clearly evident. The dashed line indicates the mean camber line.

To design the geometrically scaled blade set, a program was written in the GNU-octave

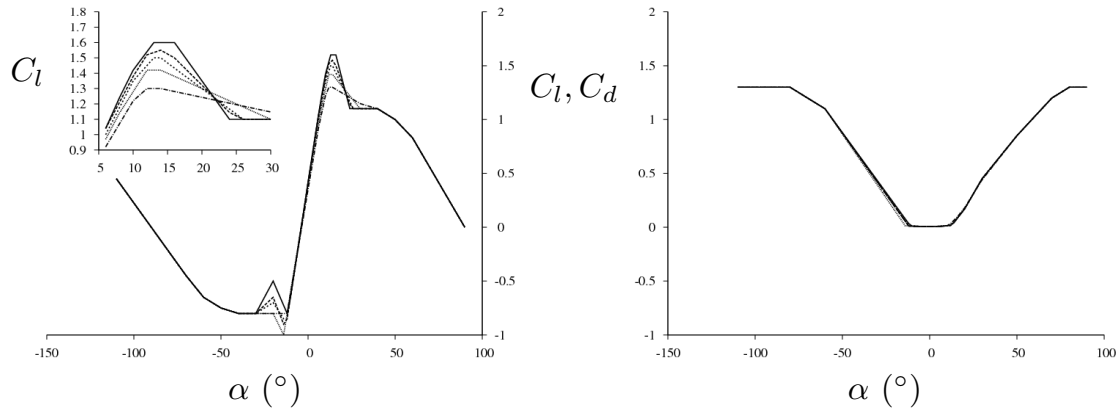


FIGURE 3.13: Aerodynamic properties of the NACA44XX airfoil at a Reynolds number of 6×10^6 (Oye 1990). left: lift coefficient C_l , right: drag coefficient C_d . Solid line (-): 4412, dashed line(- -): 4415, small dash(- · -): 4418, dots(· · ·): 4421 and dash dot(- · ·): 4424. The effect of airfoil thickness on the lift coefficient is clearly shown in the inset.

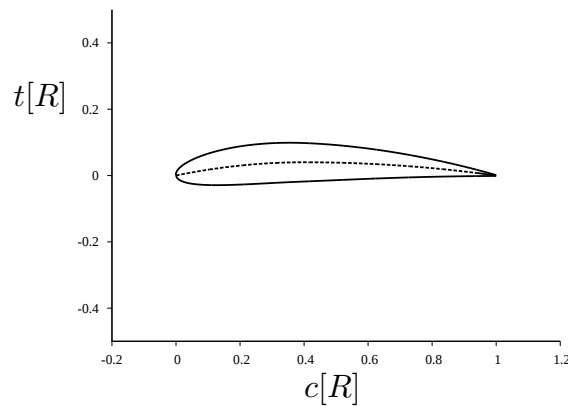


FIGURE 3.14: The NACA4412 airfoil profile used in the tip region of the full scale Tjæreborg turbine and along the entire span of the geometrically scaled experimental model. The dashed line depicts the mean camber line. Length and thickness non-dimensionalised by the chord length.

mathematical language. The program determined the surface coordinates of the airfoil sections at various spanwise blade locations. A 3D model of blade was created based on the surface coordinates in a computer aided design (CAD) software (NX-5 and later NX-7, SIEMENS) software. The 3D CAD model was manufactured out of stainless steel by a computer numerically controlled (CNC) milling machine. The model was constructed from stainless steel to avoid oxidation in the water channel.

The rotor assembly was created as a solid structure to avoid issues with blade alignment. The tip pitch angle was thus fixed at a single angle, $\theta = 0^\circ$. The blade twist and taper are shown on the left in figure 3.15. The origin is taken at the quarter chord position. The leading and trailing edges in addition to the tip and root chord profiles are shown in red for clarity. A plan-view of the entire rotor assembly is shown on the right. The model diameter of 230 mm ensured the blade swept area blockage ratio (8.65%) remained less than 10%,

Chapter 3. Experimental Techniques, Models and Equipment

thus minimising wake contraction effects (Vermeer et al. 2003). The model was operated in a freestream speed of $U_\infty = 0.092\text{m/s}$. Three tip speed ratios $\lambda = 4, 7, 10$, were investigated by varying the blade rotational rate. The tip speed ratio range corresponds to a lightly and heavily loaded rotor around the full scale design condition. The Reynolds number range of the tests was thus, $1\,385 < Re_c < 3\,369$.

The Reynolds number of wind turbines in atmospheric conditions are several orders of magnitude larger than those in the experiments. The primary differences the Reynolds number dissimilarity will cause are; a reduction in both the C_l/C_d ratio and $C_{l,\text{max}}$, stall of the blades at an earlier angle of attack, possible formation of a laminar separation bubble, and enhanced diffusion of vortical structures. The flow over airfoils at low Reynolds numbers is investigated in chapter 4. However, as turbulence levels in the atmospheric boundary layer are much greater than those simulated in the experimental conditions, the difference in vortex diffusion rates may be reduced because of the higher levels of turbulent diffusion of the coherent structures. The discrepancy between model and full scale is discussed in chapter 5.

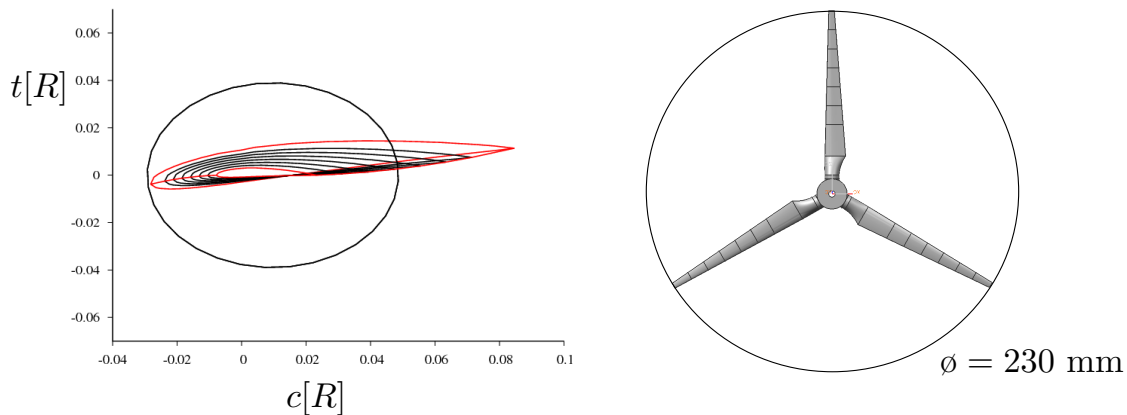


FIGURE 3.15: Geometrically scaled model of the Tjæreborg fullscale wind turbine. left: spanwise chord and twist angle variation. Origin taken as the tip quarter chord position. The NACA4412 airfoil profile was along entire span. Length dimensions are made dimensionless by the rotor radius. Tip, root and the leading and trailing edge profiles are shown in red for clarity. right: 3D CAD model used to manufacture the blade set.

The geometrically scaled rotor was used extensively to characterise the near wake of a wind turbine. The vortex extraction methodologies and algorithms were developed using experimental data taken with this rotor. The geometrically scaled rotor results are presented in chapter 5. The data reveal the wake structures suffer from reduced aerodynamic performance at the experimental Reynolds number.

3.2.4 Optimum Glauert wind turbine rotor

The geometrically scaled rotor results revealed geometric scaling alone was not sufficient to generate a clean vortex wake. A custom rotor design optimised for the low experimental Reynolds number was required. Several issues which arose from the geometrically scaled rotor were used as design criteria for an optimised rotor design. These included,

- 1 Difficulty in comparing model and full scale wake profiles due to differences in rotor loading
- 2 Inability to change blade loading through pitch angle alteration
- 3 Low tip Reynolds number due to small tip chord arising from geometric scaling
- 4 Separated flow along a large proportion of blade span due to minimum twist of blade
- 5 Vortex interaction difficult to characterise due to stalled flow and presence of blade wakes
- 6 Tip vortices very small due to small tip chord
- 7 Low C_l/C_d value due to low Reynolds number, leading to tip vortices of low strength

A new model was thus required to overcome the above issues. Particular attention was given to increasing the strength of the wake vortices. Further, attempts were made to achieve dynamic similarity between full and model scale turbines. The optimum rotor analysis of Glauert (1935) was used as the base turbine design. This analysis was presented in chapter 2. A BEM method was used to optimise each annular segment of the rotating wing. The fluid forces acting on a generic airfoil section are again shown in figure 3.16.

The optimum rotor analysis is applicable when $C_l/C_d = \infty$. However, the C_l/C_d is finite at the experimental Reynolds number, Re_c . Therefore, an appropriate λ must be selected based on the C_l/C_d ratio of the NACA4412 at Re_c . Wilson and Lissaman (1974) investigated the effect of C_l/C_d ratio and number of blades on the maximum C_p achievable by an optimum rotor. They developed an empirical relationship, shown in equation 3.20 for the optimisation of a wind turbine rotor considering sectional airfoil performance and number of blades ((Wilson and Lissaman 1974) in (Spera 1994)).

$$C_{p,max} = \frac{16}{27} \lambda \left[\frac{B^{2/3}}{1.48 + (B^{2/3} - 0.04)\lambda + 0.0025\lambda^2} - \frac{C_d}{C_l} \frac{1.92B\lambda}{1 + 2\lambda B} \right]. \quad (3.20)$$

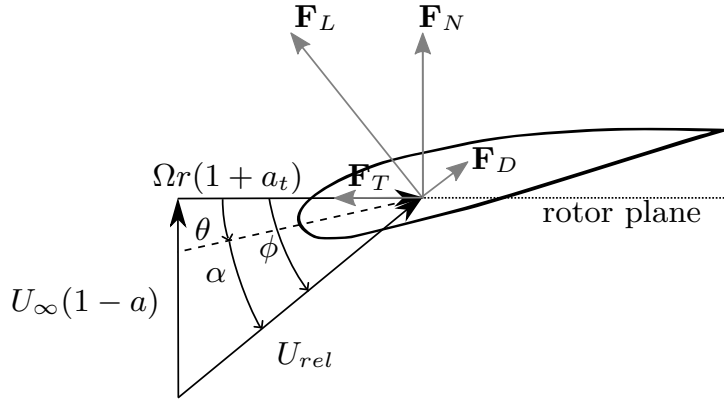


FIGURE 3.16: Fluid and body velocity vectors and the resulting forces experienced by a cross-sectional element of a wind turbine blade. Freestream flow is from bottom to top, resulting blade rotation is left in the rotor plane, α is the angle of attack, a and a_t are the axial and tangential interference factors at the blade section respectively.

Equation 3.20 is represented graphically in figure 3.17. Also shown on figure 3.17 is the Lanchester–Betz–Joukowski limit of $C_{p,L-B} = 16/27$. To determine the tip speed ratio that produces a maximum power coefficient for a given number of blades and sectional airfoil properties, the design C_l/C_d ratio of an airfoil is substituted into equation 3.20. The maximum C_l/C_d ratio of the NACA4412 at a Reynolds number in the order of the full scale turbine is 130 at an angle of attack of $\alpha = 6^\circ$ (Oye 1990) corresponding well to the design tip speed ratio of $\lambda_{d,fs} = 7.07$.

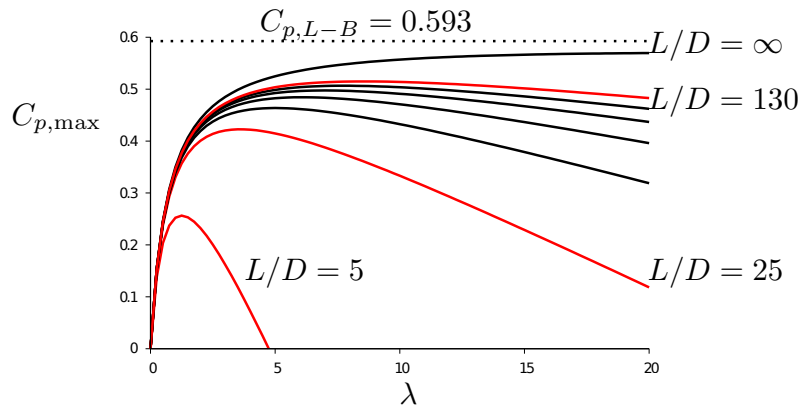


FIGURE 3.17: The effect of airfoil section lift to drag ratio, L/D and tip speed ratio, λ on the maximum power coefficient, $C_{p,max}$, of an optimum three bladed turbine. Solid lines: L/D increments of 20, dotted line: Lanchester–Betz–Joukowski limit ($C_{p,L-B} = 0.593$).

The sectional airfoil performance is however reduced at the experimental Reynolds number. The NACA4412 was also used for the optimum Glauert rotor. Comparison is thus possible purely on rotor design. However, airfoil performance data is scarce at low experimental Reynolds numbers. The airfoil performance data of Jacobs and Sherman (1937) at

a Reynolds number of $Re_c = 4.21 \times 10^4$ was used in the blade optimisation process. This Reynolds number is larger than that of the rotating model so the data act as an upper limit on performance. Importantly, Re_c of the Jacobs and Sherman data is below the threshold for laminar separation bubbles to form (5×10^4) as stipulated by (Mueller and J.D.Delaurier 2003). It will thus provide quality airfoil performance data for the rotating model design process. This airfoil data is shown in figure 3.18.

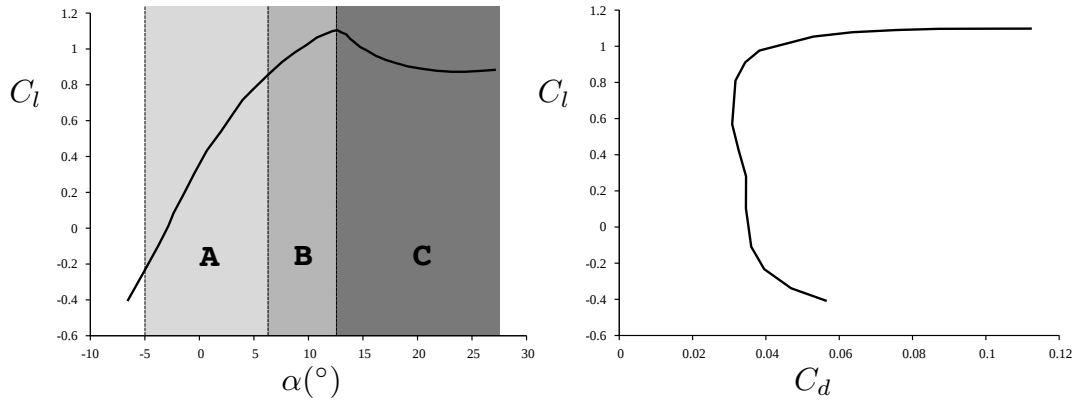


FIGURE 3.18: Sectional airfoil performance of the NACA4412 at a Reynolds number of 4.21×10^4 , left: α vs. C_l shaded areas A,B and C depict the attached, pre-stall and post-stall regions respectively. right: C_d vs. C_l polar (Jacobs and Sherman 1937).

The regions of attached (approximately linear C_l vs. α), pre-stall, and post-stall regions are shaded and labelled on the left in 3.18 as A,B and C respectively. The lift and drag polar shown on the right of figure 3.18 indicates that the drag increases dramatically approaching the stall angle as the flow separates close to the leading edge. Due to the low Reynolds number, the airfoil deviates from the linear regime at an earlier angle of attack compared to figure 3.13. Also importantly, no 'drag-bucket' is evident in the polar of figure 3.18 indicating laminar separation bubble is absent at this Reynolds number.

The maximum C_l/C_d ratio at this $Re_c = 4.2 \times 10^4$ is 26.75 and occurs at $\alpha = 7.3^\circ$. Substituting these values into equation 3.20 resulted in an optimum tip speed ratio of $\lambda = 3.75$. However, this angle of attack is in the early pre-stall region as shown in figure 3.18. A more conservative design angle of attack was chosen as $\alpha_d = 6^\circ$, located on the border of the attached regime of the C_l vs. α performance curve. The optimum lift and drag coefficients at α_d are thus $C_{l,opt} = 0.8382$ and $C_{d,opt} = 0.033$. At this prescribed angle of attack, $C_l/C_d \sim 25$. This value was substituted into equation 3.20 to determine the optimum tip speed ratio for the three bladed model. Figure 3.17 shows that for $C_l/C_d = 25$, the optimum tip speed ratio is $\lambda_d = 3.5$.

The design parameters for the optimum Glauert rotor were thus $U_\infty = 0.2\text{m/s}$, $N = 3$, $\alpha_{opt} = 6^\circ$, $C_{l,opt} = 0.8382$, $C_{d,opt} = 0.033$ and $\lambda(r) = 3.5$ from figure 3.17. The chord distribution (ignoring tip losses) is determined from equation 3.21 (Hansen 2008).

$$\frac{c(\lambda(r))}{R} = \frac{8\pi a \lambda(r) \sin^2 \phi}{(1-a)BC_n \lambda} \quad (3.21)$$

where $c(\lambda(r))$ is the chord at a radius r rotating at a local tip speed ratio $\lambda(r)$ and C_n is the normal force coefficient.

Tip loss and heavy loading formulae of Shen et al. (2005) outlined in chapter 2 were used. The BEM method detailed in chapter 2 was used to calculate the optimum rotor design based on the input parameters.

The detailed design process led to the final rotor design which will be presented in the following section.

3.2.4.1 Final rotor design

Figure 3.19 displays the spanwise chord and twist distribution of the optimum rotor. The origin was taken as the tip quarter chord position and the length dimensions were made dimensionless by the rotor radius. The NACA4412 airfoil profile was exclusively used. The optimum rotor has a much larger twist variation compared to the geometrically scaled rotor. The angle of the relative velocity, U_{rel} , (vector sum of the freestream and blade rotational velocities) increases from tip to the root section of the blade. The increase in twist angle toward the blade root attempts to maintain the prescribed angle of attack. The large blade twist reflects a research based approach to the rotor design. In a full scale turbine, it becomes prohibitively expensive to include significant blade twist in the root section to avoid blade stall. Thicker airfoil profiles are also used in the root section to increase blade rigidity where the blade bending moments are greatest. These requirements are avoided in a research setting.

The blade was manufactured by a 3-axis CNC milling machine. The accuracy of the milling machine was $\pm 0.1\text{mm}$. The optimum rotor was constructed of 6061 Aluminium and hard anodised post production. A single optimum blade was also constructed out of polycarbonate for the blade bound circulation measurements. The transparent nature of the polycarbonate improves light intensity aft of the blade.

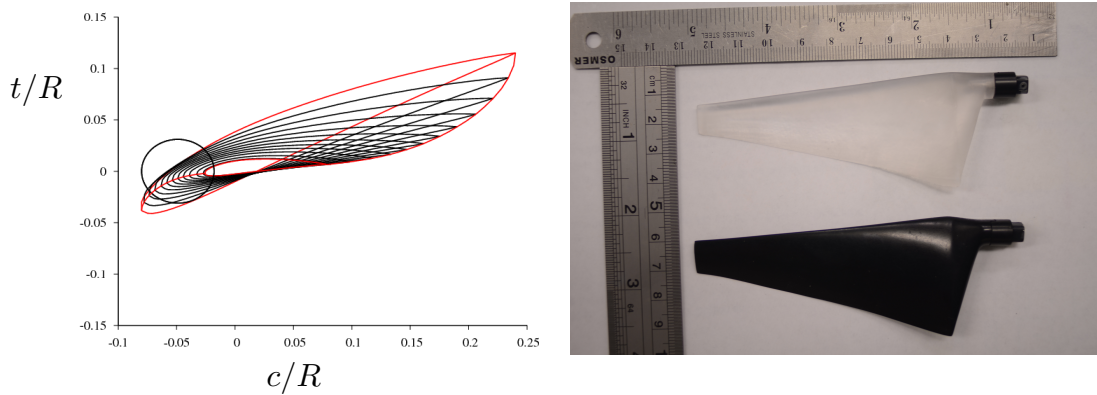


FIGURE 3.19: Left: Spanwise variation of the optimum rotor chord and twist angle. Tip, root and the leading and trailing edge profiles are shown in red for clarity. Right: Planform view of single blades.

3.2.4.2 Model imperfections

The blade pitch angle, $\theta(r)$, is critical for uniform tip vortex formation. The tip pitch angle was equivalent to $\pm 0.5^\circ$. Every precaution was taken to ensure equally loaded blades. Due to the model size and the achievable tolerances of the CNC milling machine, one blade housing contained larger uncertainty. This led to a coning angle variability between the blades. The coning angle variability was measured as $\psi = 0.5^\circ$ downstream. Only the normal force coefficient is altered in a coned rotor (Wilson et al. 1976). The thrust acting on the coned blade will be less than the un-coned blades.

The loading difference due to coning angle variability was calculated using the BEM method. Due to the axi-symmetry of the BEM method, a single blade cannot be varied. Instead, the two blade coning angle configurations ($\psi = 0^\circ$ and $\psi = 0.5^\circ$) were investigated. The coning angle variation created a non-dimensional difference in blade loading of the order of 1×10^{-5} . This loading difference is an inherent perturbation to the vortex system.

The coning angle variation also causes a change in pitch, h , between filaments. The coned blade in the three-blade configuration, reduces the pitch between two tip/root vortices. Interaction will be enhanced between the two closely spaced vortices. Vortex interaction is one avenue to wake instability. This pitch variability is inherent in the wake vortex system.

3.2.5 Wind turbine model components

The auxiliary components which complete the wind turbine model will now be presented. These components include motors and their controllers used to drive the turbine, and optical encoders to determine blade azimuthal position. The evolution of the model components is presented to highlight improvements and the quality of the final model design.

dc motor and controllers

To achieve truly controlled conditions, the wind turbine tip speed was regulated by an external motor. A comparison between a freely spinning and driven turbine is presented in chapter 6.

The geometrically scaled model was driven by an 18V d.c. motor. The d.c. motor was chosen to provide high torque at the low model rotational speeds. The rotational speed accuracy of the d.c. motor was $\pm 1rpm$.

The optimum Glauert rotor was driven by a stepper motor (50800 counts/rev) with micro stepping drive (OEM350-650, Parker) and controller (Parker 6K2, Parker). A beam coupler was used to connect the stepper motor shaft and the turbine upper shaft. The beam coupler allowed provision for small shaft mis-alignment without backlash. The rotational speed was highly accurate with the new drive system.

Optical encoders

To allow phase-locked averaging of the wake, a device which measures the blade rotational rate is required. Optical encoders were used to determine the blade rotational rate and set the data acquisition sequence at a prescribed blade azimuthal position.

The first generation optical encoder (HEDS 5645 G13, AVAGO) was connected to a signal box with an LED display screen which indicated the angular speed. The angular speed was determined by continuously averaging the time taken to travel 8° . The control box allowed phase averaging of angular increments ranging from 1° (quasi time resolved) to 360° (phase-locked averaged data). The optical encoder sent a TTL signal via BNC cable to the laser timing box to start the image acquisition sequence.

An additional optical encoder (HBM5-1250, US DIGITAL) was mounted on the shaft of the stepper motor to monitor the rotational speed prior to the beam coupler. The optical encoder output was sampled for each data set via a labview program at 25-50Hz. The optical encoder setup was sufficiently accurate for all measurements and has been used for all experimental campaigns bar the initial flat plate and airscrew data sets.

A custom optical encoder was used to measure the rotational rate of the freely spinning turbine. The optical encoder system was developed with electrical workshop personnel in the department. It consisted of a reflective sensor (HOA2498, HONEYWELL) and required circuitry. The reflective sensor consists of two components, an infra-red emitting diode (IRED) and a photo-transistor positioned on converging optical axes. The photo-transistor responds to the IRED when a reflective object passes within its field of view. The frequency of the sensor was calibrated using a micro-controller and internal amplifier producing an analog voltage output. The analog output was calibrated as $1V/25rpm$ and sampled using labview.

The encoder outputs were recorded on a computer with a data acquisition (DAQ) board (PCI-6221(37pin), NATIONAL INSTRUMENTS) connected to a BNC adapter (BNC2110, NATIONAL INSTRUMENTS). A labview program received an analog input via the DAQ board and performed simple data manipulation to calculate λ based on two user inputs, U_∞ and R .

3.2.6 Experimental setup

With all components introduced, the entire experimental setup is shown in figure 3.20. The turbine is placed in an inverted position in the channel. U_∞ is from left to right with the wind turbine model rotating in a counter-clockwise direction when viewed from upstream. The motor drive shaft is connected to the turbine main shaft by a timing belt. The timing belt runs through the turbine tower. The optical encoder is attached aft of the upper shaft bearing. The laser is situated under the channel on a movable trolley. The camera is placed perpendicular to the laser sheet on a computer controlled three axis traverse (IMC-S8 controller, ISEL) (not shown) allowing accurate positioning.

The experimental models used to investigate the near wake of a horizontal axis wind turbine have now been presented. The wind turbine wake data are presented in chapters 5, 6, and 7. The experimental model used to investigate the flow over complex terrain will now be presented.

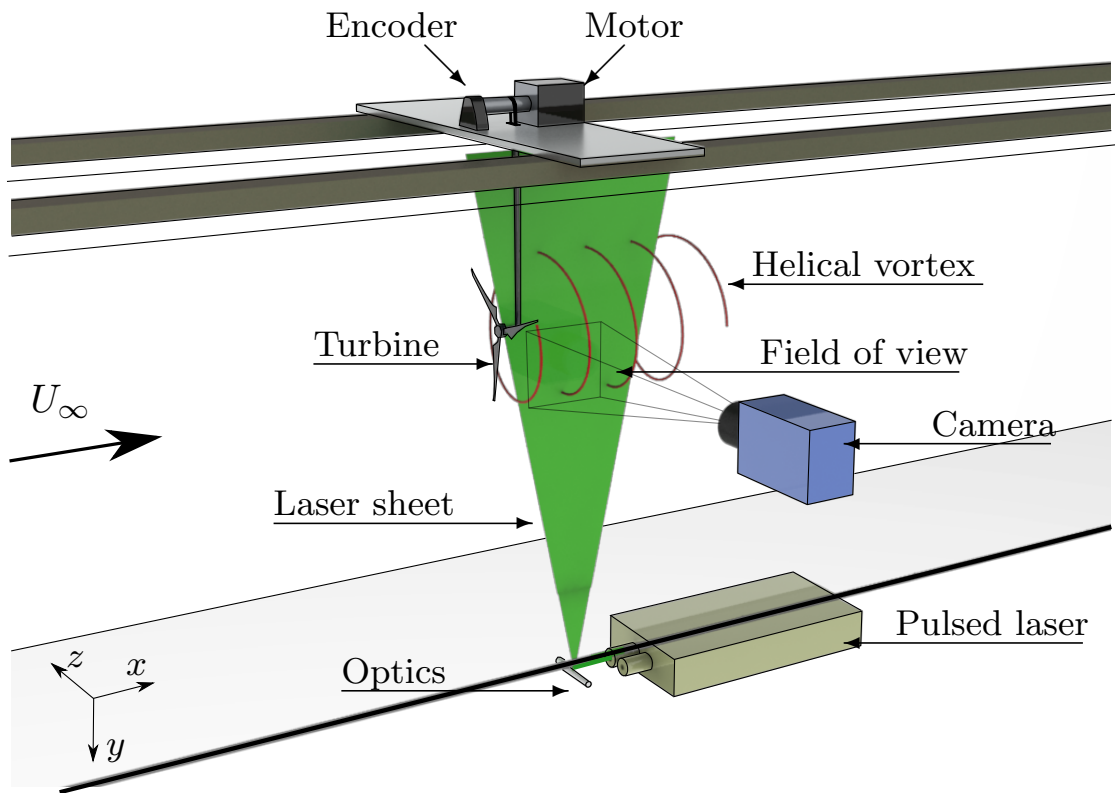


FIGURE 3.20: Experimental setup of the water channel and PIV data acquisition configuration used in the rotor wake studies. The turbine model is placed inverted in the channel and a measurement field of view in the lower half of the wake is shown. The laser sheet is shown intersecting the vertical centre-plane (*i.e.* the x - y plane) along with a single helical vortex filament.

3.2.7 2D escarpment model

To investigate the flow patterns in the vicinity of complex terrain, a 2D escarpment model was manufactured out of polycarbonate and acrylic. The transparent nature of the materials allowed the use of the optical based experimental techniques presented in section 3.1. The step height h , could be varied in the range, $5 \leq h(\text{mm}) \leq 45$, through the use of perspex spacers. The model length and width aspect ratios $AR_L = L/h$ and $AR_W = W/h$, ranged between $11.1 \leq AR_L, AR_W \leq 100$. The minimum aspect ratio was above the threshold to ensure flow reattachment to the top surface ($AR_L > 10$) (Castro and Dianat 1983) and that the flow is nominally 2D at mid span ($AR_W > 10$) (de Brederode and Bradshaw 1972). The model is thus representative of an isolated 2D step in every flow setting. The escarpment angle, θ , was varied by inserting perspex wedges. Wedges of $\theta = 30^\circ, 45^\circ, 60^\circ$ were used.

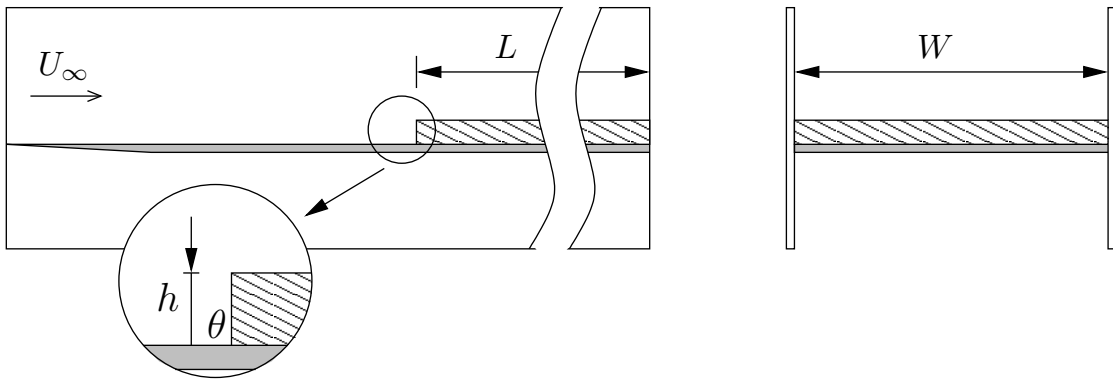


FIGURE 3.21: Schematic of the 2D escarpment model constructed out of polycarbonate and acrylic. The escarpment height could be varied in the range, $15 \text{ mm} \leq h \leq 45 \text{ mm}$. The escarpment angle could be varied in the range $30^\circ \leq \theta \leq 90^\circ$. $L = W = 500 \text{ mm}$. Height of end plates is 210 mm

The model was fitted with end plates of a modified design after Kubo et al. (1989) to minimise 3D edge effects. Further, all edges bar the escarpment leading edge were formed into an asymmetric 5° taper to minimise blockage effects. The maximum blockage ratio ($h = 45 \text{ mm}$) was 9.73%. No corrections were made to adjust the results due to blockage affects. A schematic of the 2D escarpment model ($\theta = 90^\circ$) is shown in figure 3.21. The model was suspended within the channel in an inverted position. In this configuration, free surface effects of the water channel were minimised. The experimental arrangement thus more closely resembles a closed channel flow rather than the typical open channel flow obtained from water channels. The model was painted black at mid span (measurement position) to minimise unwanted reflections and biasing of results close to the model surface.

A boundary layer naturally formed on the 600 mm plate upstream of the step with the

Chapter 3. Experimental Techniques, Models and Equipment

profile as shown in figure 8.3. The boundary layer had a thickness $\delta = 2.7h_{\min}$ measured at a distance $9h_{\min}$ upstream of the step, where $h_{\min} = 15$ mm. The different step heights gave a δ/h range of $0.9 < \delta/h < 2.7$. A total of 2500 image pairs were utilised for convergence of the boundary layer profile results. The results captured with the 2D escarpment are presented in chapter 8.

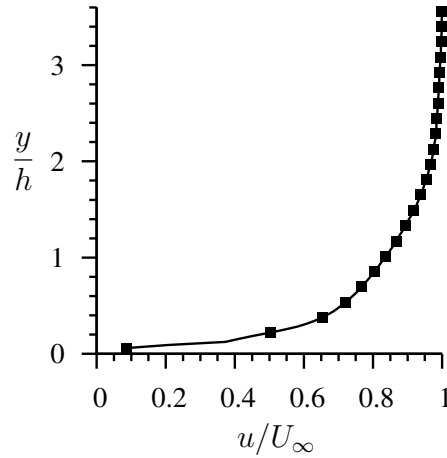


FIGURE 3.22: The upstream boundary layer profile measured at $9h_{\min}$ upstream of the step using 2500 independent PIV images. Only every fifth data point is presented for clarity.

The experimental models which will be used to gather data to test the hypotheses presented at the end of chapter 2 have now been presented. The models are tested in a water channel facility which will now be outlined.

3.3 Experimental Facility

The fluids laboratory for aeronautical and industrial research (FLAIR) free surface water channel was used during candidature. This facility has test section dimensions of $4000 \times 600 \times 800$ mm and a freestream speed that can be varied between 60 mm/s and 460 mm/s. A recirculating pump delivers water via guide vanes and a perforated metal plate to an upstream settling chamber. The perforated plate is included to equalise the pressure drop across the entire cross section. The water then passes through a 50 mm honeycomb section to remove large scale turbulent structures from the flow. A fine mesh is placed downstream of the honeycomb to remove small scale turbulent structures. The flow then moves through a $3:1$ contraction to increase the speed. After the contraction, the flow enters the test section.

The test section walls are constructed of glass allowing unhindered optical access from three sides. The free surface is accessible along the entire length of the water channel from the fourth side. The test section is separated into three working sections by cross member supports providing lateral stiffness. Aft of the test section the water enters the downstream settling tank where it passes through an outlet pipe. A centrifugal pump returns the flow to the upstream settling chamber once more. A schematic of the water channel facility is shown in figure 3.23.

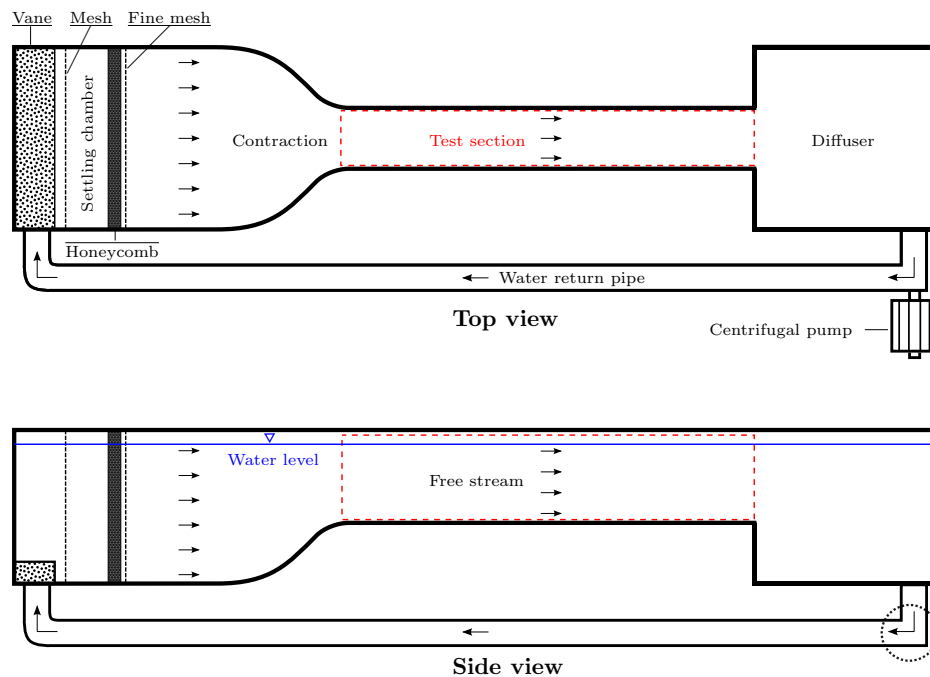


FIGURE 3.23: Schematic of FLAIR free surface water channel

The water channel flow is characterised in an internal report by Leweke (2002). The

coordinate axis for the channel characterisation was orientated as x, U -downstream, y, V -cross stream and z, W -vertical. The origin is located in the lower right corner of the test section when looking downstream (Lewke 2002). The measurements were captured at a downstream distance $x = 2140$ mm. Two reference speeds are shown in figure 3.24, $U_\infty = 0.27$ m/s on the left and $U_\infty = 0.06$ m/s on the right. The boundary layers on the channel floor are evident in the vertical profiles of U_∞ taken in the middle of the channel (*i.e.* $y = 300$ mm). Flow is uniform outside the influence of the boundary layers. The boundary layers on the side walls of the channel can also be seen in the horizontal profiles of U_∞ taken in the middle of the channel (*i.e.* $z = 400$ mm)

The water channel speed is calibrated against the pump operating frequency. Equation 3.22 indicates the linear relationship between the pump frequency, P_f and the water channel freestream velocity, U_∞ . Equation 3.22 thus allows determination of the freestream channel velocity based on any pump frequency. The water temperature is constantly monitored by resistance temperature detector (RTD) (Model: P-M-1/10-1/8-6-1/8-P-3, OMEGA ENGINEERING LIMITED). The temperature is accurate to $\pm 0.03^\circ\text{C}$ and recorded using lab-view.

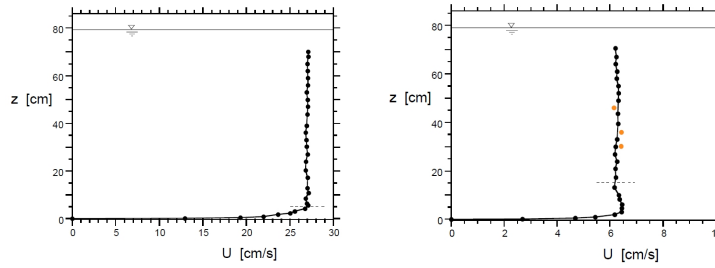
$$U_\infty = 0.00910763 * P_f + 0.00176369 \quad (3.22)$$

The water channel facility contains a sloshing motion with a characteristic frequency of 0.1 Hz. During candidature, several methods were tried to minimise the effects of sloshing. These included, a porous wedge in the downstream settling chamber to minimise traveling waves in the channel. Cylinders placed on the surface at the entrance to the downstream settling chamber to minimise surface waves. Extending the channel walls into the settling chamber to minimise the end effects the rotational flow in the settling chamber has on the test sections. After addition of each body, the channel velocity profile was characterised using the LDV. The inserted bodies were capable of reducing or lengthening the period of the fluctuations rather than removing them entirely. The sloshing motion was also intermittent, meaning it could not be low pass filtered out.

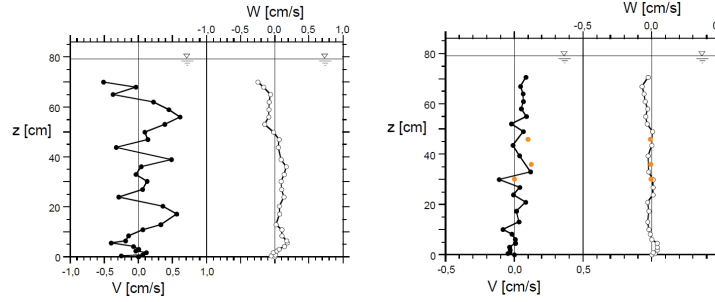
To minimise the effects of the sloshing motion the following steps were taken. Firstly, it was noted that the magnitude of the sloshing was largest after a velocity change. Therefore, a waiting period was employed to allow the channel velocity to reach an equilibrium level.

To correct for the effect of sloshing, the meander data in chapter 6 and 7 were normalised against the meander of the youngest vortex realisation. The earliest vortex realisation will

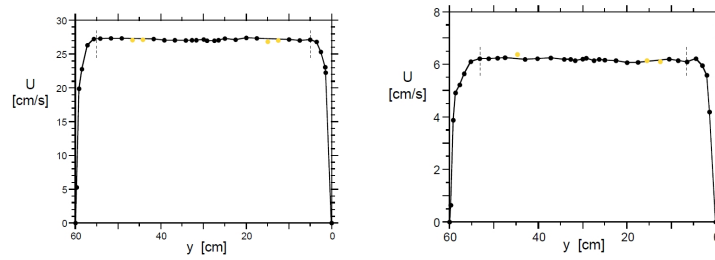
– Vertical profile of U_∞ taken at $y = 300$ mm



– Vertical profile of W and V taken at $y = 300$ mm



– Horizontal profile of U_∞ taken at $z = 400$ mm



– Horizontal profile of W and V taken at $z = 400$ mm

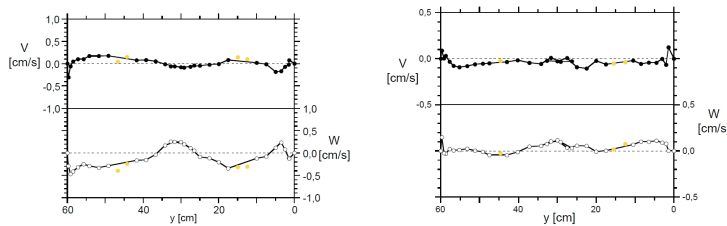


FIGURE 3.24: Characterisation of the velocity field in the FLAIR free surface water channel by Leweke (2002) at two reference speeds. left: $U_\infty = 0.27$ m/s, right: $U_\infty = 0.06$ m/s. Flow uniformity is seen outside the influence of the boundary layers.

primarily contain meandering motions due to the water channel sloshing, as vortex meander will be minimal Green (1995).

Chapter 4

Flow over Airfoils at Low Reynolds Numbers

This chapter investigates the flow over a static, low aspect 3D ratio wing at low Reynolds numbers. Flow over an airfoil at high Reynolds numbers is well-studied for many airfoil profiles. However, the flow over an airfoil at low Reynolds number differs from this because viscous effects dominate. Mueller and J.D.Delaurier (2003) note that airfoil performance is not well understood at low Reynolds numbers (*e.g.* $Re_c \leq 5 \times 10^4$). Here airfoil properties at low Reynolds numbers were measured to determine their effect on the flow in the wake of rotating turbines. Once the airfoil performance is understood at the experimental Reynolds number, it can be modified for rotational effects and used in the BEM method to assess rotor performance when no direct force measurements are available.

Here, the research focusses on two areas of low Reynolds number airfoil flow that affect tip vortex formation on a rotating wind turbine. Firstly, the airfoil's susceptibility to transient flow features, such as laminar separation bubbles, is determined. Secondly, tip vortex formation and evolution at low Re_c behind a static wing is investigated.

The chapter is divided into two sections analysing the two research areas. The NACA4412 airfoil profile investigated is the same as that used on the rotating wind turbine blades. The current data appears to be the first experimental study to investigate the flow over a NACA4412 airfoil profile at a very low chordwise Reynolds number.

4.0.1 Static 3D wing at low Reynolds number

The wind turbine models outlined in chapter 3 operate in a very low Reynolds number regime. The Reynolds number range for the geometrically scaled turbine (see chapter 5) is $1 \times 10^3 \leq Re_c \leq 3 \times 10^3$, whereas the optimum Glauert rotor (see chapter 6) operates at $Re_c \sim 1 \times 10^4$. The Reynolds number of the optimum Glauert rotor is larger due to the

higher freestream velocity and larger chord. The Re_c ranges are determined by the range of tip speed ratios. As the aerodynamics of the blades and near wake are strongly coupled, it is critical to understand the flow over airfoils at low Re_c .

Little research appears to have been undertaken at $Re_c \leq 4 \times 10^4$. Excellent reviews of airfoil aerodynamics at this and higher Reynolds number can be found in Lissaman (1983) and Mueller and J.D.Delaurier (2003). Recently, flow over airfoils at low Reynolds numbers has attracted interest because of the interest in bio-mimetic flows. The wings of many bird and insect species operate in the Re_c range 1×10^3 to 1×10^5 . Micro air vehicles (MAV) designed to mimic natural flying animals also operate within this low Reynolds number range (Mueller and J.D.Delaurier 2003). At these Reynolds numbers viscous effects become important. Laminar separation becomes common, which reduces their performance because of increased pressure drag. Reduced airfoil performance is inherent in low Reynolds number airfoil flows. The investigations of airfoil performance at a $Re_c \leq 1 \times 10^4$, *i.e.* comparable to that experienced by the rotating wind turbines appear to be limited to Sunada et al. (1997); Sunada and Kawachi (2002); Alam et al. (2010) and Zhou et al. (2011). A summary of the main findings of these works is provided in the following.

Sunada et al. (1997) and later Sunada and Kawachi (2002) investigated 3D wing properties of several airfoil and flat plate geometries in a towing tank at $Re_c = 4 \times 10^3$. They found increasing airfoil thickness reduced the maximum achievable C_l/C_d ratio, presumably due to increases in the profile drag component. A 5% camber was shown to maximise performance (Sunada et al. 1997). The maximum lift to drag ratio achieved for a cambered airfoil was 4.9 at $\alpha = 7^\circ$ (Sunada and Kawachi 2002). The maximum lift to drag ratio is important for wind turbine airfoils as described in chapter 3.

Alam et al. (2010) and Zhou et al. (2011) investigated performance and the near wake of a NACA0012 airfoil over the Reynolds number range $5.3 \times 10^3 \leq Re_c \leq 5.1 \times 10^4$. They found stall and a corresponding decrease in performance was absent at $Re_c = 5.3 \times 10^3$ but present for $1.05 \times 10^4 \leq Re_c \leq 5.1 \times 10^4$ Zhou et al. (2011). Laminar separation occurred for $\alpha \geq 8^\circ$ at $Re_c = 5.3 \times 10^3$, with no transition occurring in the separated shear layer (Alam et al. 2010). Transition did occur in the separated shear layer at $Re_c = 1.05 \times 10^4$ (Zhou et al. 2011). The implications of this transition is discussed in section 4.0.2.

No data appears to be available for NACA cambered airfoils at very low Reynolds numbers. An attempt was made to measure the aerodynamic forces generated by the NACA4412 profile with a custom force balance. The large uncertainty associated with the small lift

($0.003 \leq F_L(N) \leq 0.1$) and drag ($0.009 \leq F_D(N) \leq 0.06$) forces over the angle of attack range $-2^\circ \leq \alpha \leq 20^\circ$ at $Re_c = 5300$ rendered this data unusable. The force measurements will not be presented. Instead, the focus of this chapter is the flow states over the airfoil in the low Re_c range seen by the rotating wind turbine models. The flow over the airfoil is investigated in the following section.

4.0.2 Low Reynolds number specific flow features

In addition to reduced aerodynamic performance at low Reynolds number, airfoils become susceptible to adverse flow features such as laminar separation bubbles (LSB). A LSB forms when the initially laminar flow around the airfoil encounters an adverse pressure gradient and separates forming a separated shear layer. The separated shear layer can entrain sufficient energy to reattach to the airfoil surface prior to the trailing edge thus forming a 'bubble' in a time averaged sense. Transition to a turbulent state prior to the airfoil trailing edge is required for reattachment to occur. When a LSB forms, the recirculating flow causes an increase in pressure drag. This can be visualised in some performance polar diagrams as the cessation of the 'drag bucket', *i.e.* a sharp increase in drag at particular angles of attack (Selig et al. 1996). Laminar separation bubbles also cause undesirable hysteresis effects in airfoil performance. Relatively thick (6% and above) airfoils at low Reynolds numbers are particularly susceptible to hysteresis effects (Mueller and J.D.Delaurier 2003). The 12% thick NACA4412 is thus susceptible to hysteresis effects if a LSB forms. The average flow features of a laminar separation bubble are shown in figure 4.1.

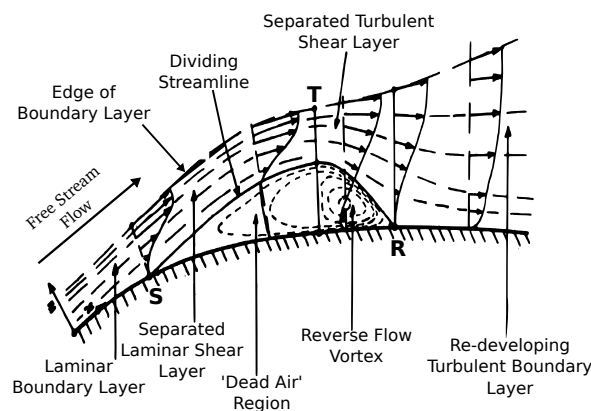


FIGURE 4.1: Time averaged flow features of a laminar separation bubble on the suction side of an airfoil. **S**: separation point, **R**: reattachment point, **T**: maximum vertical displacement where transition is most likely (Horton 1968).

If Re_c is low enough, transition in the separated shear layer will not occur and thus no laminar separation bubble forms. Several estimates exist for the critical Reynolds numbers for

LSB's to form. Lissaman (1983) state a minimum distance from separation to reattachment can be expressed as a Reynolds number of 50 000. This corresponds to a critical chord Reynolds number of $Re_c^* = 7 \times 10^4$ Lissaman (1983). Mueller and J.D.Delaunier (2003) on the other hand, state $Re_c^* = 5 \times 10^4$. Huang and Lin (1995) showed shear layer reattachment and hence laminar separation bubble formation for a NACA0012 airfoil does not occur for $Re_c \leq 1 \times 10^4$. Zhou et al. (2011) confirmed the absence of a laminar separation bubble at a Reynolds number of $Re_c = 5.3 \times 10^3$ but a LSB was present at $Re_c = 1.05 \times 10^4$. An equivalent study of cambered airfoils at such low Reynolds numbers appears not to have been previously undertaken. Intuitively, a cambered and relatively thick airfoil, such as the NACA4412 will be susceptible to boundary layer separation due to the increased surface curvature on the suction side of the airfoil. Earlier separation permits more time for transition to occur prior to the trailing edge. It is thus desirable to determine whether a LSB forms on the NACA4412 in the rotating wind turbine model Reynolds number range.

To determine the flow states over the model wind turbine lifting surfaces, the flow over a static 3D wing was visualised. The wing has a chord length of $c = 120$ mm and a length $L = 480$ mm giving a geometric aspect ratio, $AR = 4$. The immersed length aspect ratio was maintained at $AR_i = 3.8$. Here, the wing was placed in a 'mini-channel' to reduce the order of Re_c to that of the geometrically scaled blade. The chord Reynolds number of the visualisations, $Re_c = 3484$, corresponded to that experienced by the model experimental wind turbine at $\lambda = 10$. Planar laser induced fluorescence (PLIF) was used to visualise the flow states on the suction surface of the airfoil. The investigations focused on the suction side of the airfoil where separation may occur for $\alpha \geq 0^\circ$. Flow states were investigated with 2.5° resolution in the angle of attack over the range $-7.5^\circ < \alpha < 20^\circ$ and at 5° resolution in the range $20^\circ < \alpha < 30^\circ$. The angle of attack could be set with a precision of $\pm 0.5^\circ$ with a digital protractor. The Reynolds number was changed by varying U_∞ .

The laser (85-BCD-030-230, MELLES GRIOT) was formed into a sheet by a lens illuminating the region of interest on the suction side of the wing from the leading to trailing edge. A blue laser ($\lambda_l = 488$ nm) was chosen as the light source over the more fluorescein receptive wavelength of a green laser as the blue light can be filtered out by using properties of the camera CCD chips. A digital SLR camera (D7000, NIKON) with a 105 mm (105AF, NIKKOR) lens was used to acquire the images.

The fluorescein was mixed with a soluble substance (honey or maple syrup) and applied to the pressure side (+) of the wing in an application area (AA). The mixture was applied to the

pressure side of the wing to avoid affecting the separation point (S) on the suction side of the airfoil. This method allows non-intrusive seeding of the flow within the wing boundary layer and to visualise the separated shear layer. The chemical is transported around the trailing edge into the separated region as shown in figure 4.0.2. The laser causes the fluoroscein to fluoresce allowing imaging of the flow physics.

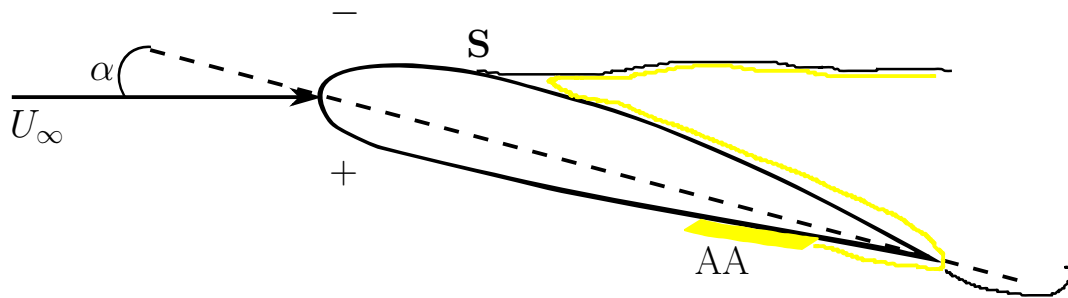


FIGURE 4.2: PLIF visualisation schematic showing the seeding of the fluorescent substance in the application area (AA) on the pressure side (+) of the wing. Fluorescent material is transported around the trailing edge into the separation zone and reveals the separated shear layer downstream of the separation point (S).

4.0.3 Mean PLIF visualisation results

To create the time averaged visualisation images, ~ 10 instantaneous images were averaged after low pass filtering to remove background noise (ambient light) from the individual frames. The mean flow visualisation images provide information on the separation point and trajectory of the separated shear for a wide angle of attack range. The mean flow regimes of the NACA4412 airfoil are presented in figure 4.3. The visualisation images are saturated at the separation point as the fluoroscein had to change direction before being entrained in the separated shear layer. Laminar separation is apparent for the angle of attack range presented in figure 4.3. The $\alpha = -7.5^\circ$ is not shown due to the absence of separated flow on the suction side. The separation point progresses from the trailing to leading edges with increasing angle of attack. At $\alpha = 20^\circ$, laminar separation occurs from the leading edge and the wing is in a fully separated state. This knowledge is important when evaluating the quantitative data taken on the rotating wind turbine model in chapters 5 and 6 and also the 3D wing in section 4.0.5.

Trailing edge separation is also evident from the dye trace emanating from the trailing edge. This dye trace implicitly reveals the vorticity sheet shed from the trailing edge. The roll up of this vorticity sheet forms one arm of the von-Kármán vortex street. The current field of view did not allow the imaging of the von-Kármán vortex street.

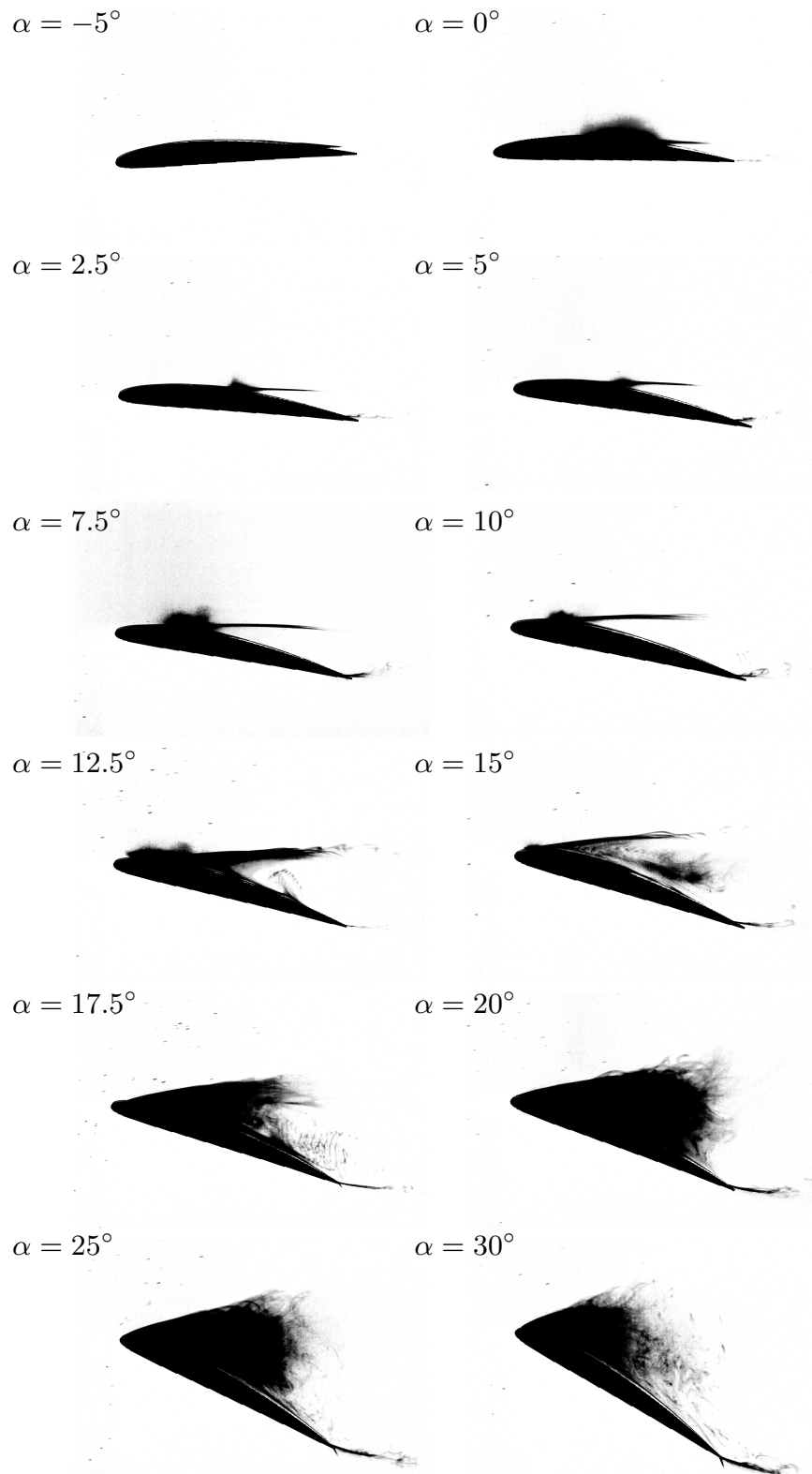


FIGURE 4.3: PLIF mean flow visualisation results in the angle of attack range $-5^\circ < \alpha < 30^\circ$ for the NACA4412 airfoil profile at a Reynolds number of $Re_c = 3484$. The movement of the separation point toward the airfoil leading edge with increasing angle of attack is clearly visible.

To investigate the effect of Reynolds number, Re_c was increased to $Re_c \sim 5\,300$ by varying U_∞ . This Reynolds number was chosen to match that of Zhou et al. (2011) who confirmed the absence of a LSB for the NACA0012 profile. As a LSB did not form at the initial Re_c , only two angles of attack ($\alpha = 10^\circ$ and $\alpha = 15^\circ$) were investigated at the higher Re_c . The effect of Re_c for the two angles of attack is shown in figure 4.4. The flow at the two Re_c appear very similar. The separation point as estimated from the saturated dye region, appears to vary minimally. However, mixing in the separated zone is greater in the higher Re_c results.

$Re_c = 3\,484$

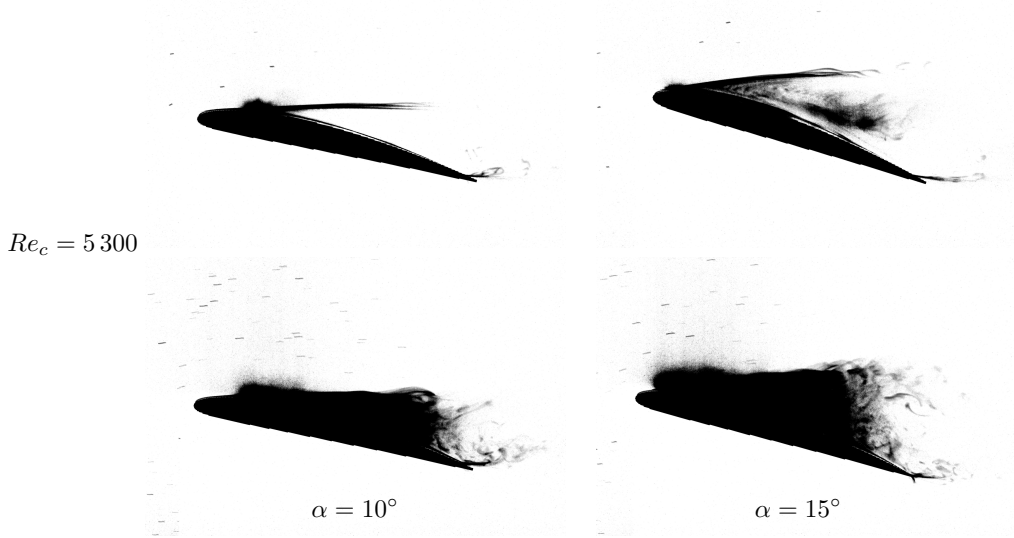


FIGURE 4.4: PLIF mean flow visualisation results showing the effect of Reynolds number for $\alpha = 10^\circ$ and $\alpha = 15^\circ$ for the NACA4412 airfoil profile at Reynolds number of $Re_c=3\,484$ and $Re_c=5\,300$.

The mean PLIF visualisation results revealed laminar separation is present but transition and thus turbulent reattachment is absent in the α and Re_c ranges investigated. The dynamics of the separated shear layer will be investigated in the following section.

4.0.4 Instantaneous PLIF visualisation results

The mean visualisation images showed the average separation point and shear layer trajectory. Instantaneous images are now presented in figure 4.5 to highlight the dynamics of the separated shear layer. The primary research interest was the existence of a laminar separation bubble.

The instantaneous visualisations reveal the presence of a Kelvin–Helmholtz (K–H) instability mode between the recirculating flow in the separated zone and the higher velocity freestream flow. The oscillations of the separated shear layer for $\alpha \geq 10^\circ$ in figure 4.5 is evidence of a K–H instability mode. With increasing α , the velocity differential between

the freestream and recirculation zone increases. The K–H mode thus appears earlier with increasing α as shown in figure 4.5. The results agree with prior visualisation studies at low Reynolds number where the leading edge separation occurred at $\alpha \geq 20^\circ$ (Alam et al. 2010). Further, shear layer transition does not occur at this Reynolds number. Although this was not measured explicitly, the absence of a laminar separation bubble is used as a proxy for shear layer transition. It is known at low Reynolds numbers that shear layer transition must occur prior to the trailing edge for a laminar separation bubble to form (Zhou et al. 2011).

The influence of Re_c is presented in figure 4.6 for $\alpha = 10^\circ$ and $\alpha = 15^\circ$. These α were chosen based on the initial formation of the K–H instability in the field of view from the $Re_c = 3\,484$ results. K–H vortices form earlier with increasing Re_c . Figure 4.6 also presents a PLIF visualisation of the symmetrical NACA0012 airfoil at $\alpha = 10^\circ$ and $Re_c = 5\,300$ (Alam et al. 2010). The separation point appears closer to the leading edge in the Alam et al. (2010) study. The vortex formation length is also shorter despite the lower turbulence level (0.4%–0.5%) (Alam et al. 2010) than the present tests ($\sim 2.4\%$). The earlier separation and appearance of the K–H instability mode in the Alam et al. (2010) study is most probably due to the dye injection point at the leading edge. Whilst every precaution can be taken to avoid introducing disturbances into the separated shear layer (*i.e.* with a regulator valve (Alam et al. 2010)), it is inevitable a disturbance will be introduced. The current results are free from such disturbances as the visualisation dye was placed on the pressure side of the wing (figure 4.0.2). Dye is transported to the suction side visualising the separated shear layers as shown in figures 4.3 through to 4.6.

To this point, the flow states above the airfoil have been investigated. Laminar separation was present for $\alpha > -5^\circ$. The absence of a laminar separation bubble on the NACA4412 profile at low Re_c was confirmed. A BEM method can thus be used to determine rotor performance with airfoil data at the wind turbine model Reynolds numbers. BEM analyses for the geometrically scaled turbine model is presented in chapter 5 and for the optimum Glauert rotor in chapter 6. Wing tip vortices are another important airfoil flow phenomena. Tip vortex formation at low Reynolds number is investigated in the next section.

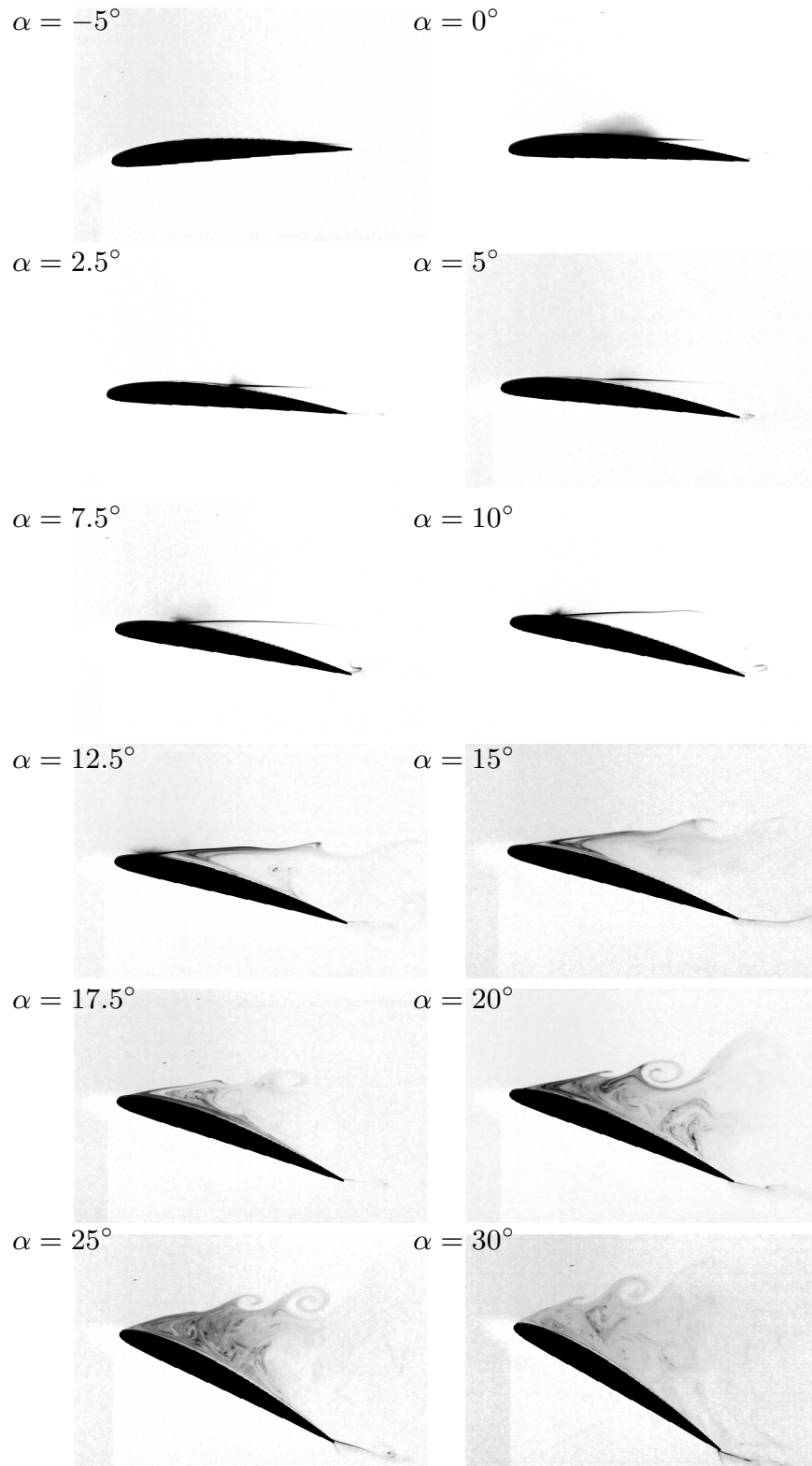


FIGURE 4.5: PLIF instantaneous flow visualisation results in the angle of attack range $-5^\circ < \alpha < 30^\circ$ for the NACA4412 airfoil profile at a Reynolds number of $Re_c=3484$. The movement of the separation point toward the airfoil leading edge with increasing angle of attack is clearly visible. The formation length of a K-H instability also shortens with increasing angle of attack.

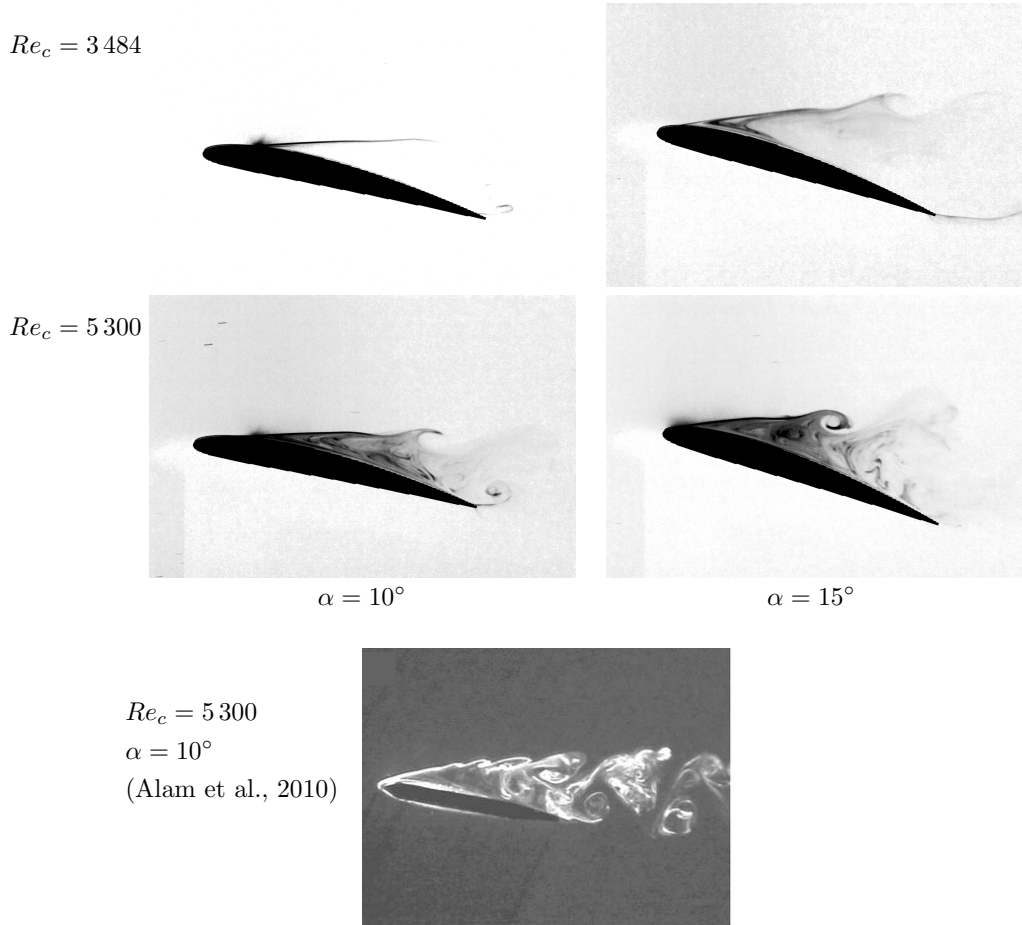


FIGURE 4.6: PLIF instantaneous flow visualisation results showing the effect of Reynolds number for $\alpha = 10^\circ$ and $\alpha = 15^\circ$ for the NACA4412 airfoil profile at $Re_c=3484$ and $Re_c=5300$. Also shown is the PLIF visualisation of Alam et al. for a NACA0012 airfoil at 10° and $Re_c = 5300$.

4.0.5 Tip vortex evolution at low Reynolds number

The tip vortices generated by a static 3D wing are the ‘simplest’ trailing tip vortices produced by a lifting surface. They result from the bound circulation generation by the wing and form due to the termination of a lifting surface in a fluid. Wing tip vortex formation is well studied at high Reynolds numbers (Green 1995) but there is little data available at low Reynolds numbers. Further, the airfoil shape at the tip plays an important role in determining the loading and hence strength of the tip vortex structure which forms downstream of a wind turbine (Hansen and Johansen 2004). The rotating wind turbine models presented in chapter 3 have a bluff tip shape like the static 3D wing. Characterising vortex formation and evolution of trailing wing tip vortices at the Reynolds number seen by the rotating model could allow us to compare the vortex evolution of straight and curved vortex filaments. Tip vortex formation was investigated using H₂ flow visualisations and PIV. The H₂ flow visualisations

are presented first in the following section.

The H2 flow visualisations were undertaken on the 3D NACA4412 wing at $Re_c = 6700$. The H2 visualisation Re_c value was an approximate mean of the tip chord Reynolds numbers of the two wind turbine models outlined in chapter 3. The visualisation results should therefore be applicable to both wind turbine models. Specifics of the H2 technique were detailed in chapter 3. A schematic of the H2 flow visualisation setup is shown in figure 4.7. The angle of attack range investigated was $0^\circ \leq \alpha \leq 20^\circ$, with 5° resolution. This range encompasses the expected angles of attack at the tip for the two turbine models (see chapters 5 and 6). The upper limit of this range corresponds to where leading edge separation occurs based on the PLIF visualisations in section 4.0.2. The effect this separation on tip vortex formation will be investigated. Studio lights were used to create a light sheet of approximately 5 mm thickness to illuminate the image plane. The effect this separation on tip vortex formation will be investigated. Studio lights were used to create a light sheet of approximately 5 mm thickness to illuminate the image plane.

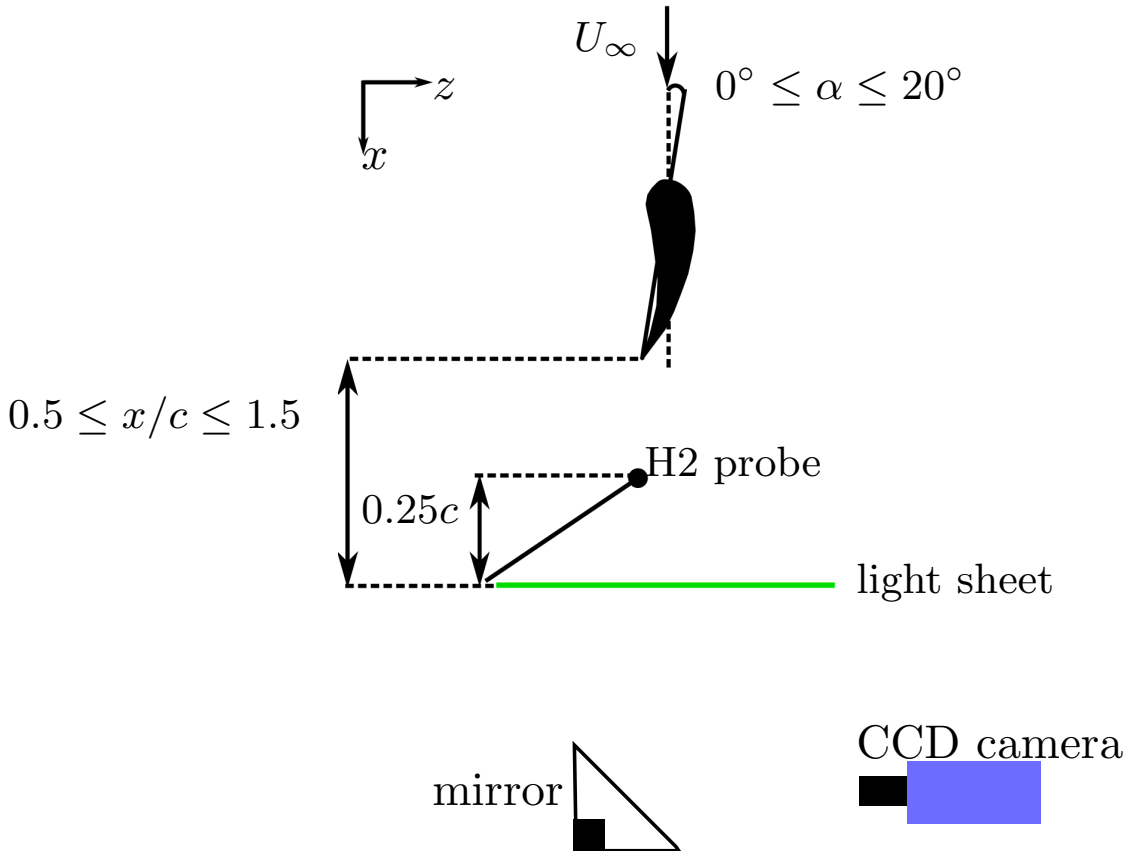


FIGURE 4.7: Experimental setup of H2 tip vortex visualisations. The H2 probe was fixed at $0.25c$ upstream of the image plane/light sheet. The image plane distance x/c was varied manually.

Vortex age was investigated by varying the streamwise distance between the wing trailing edge and the visualisation plane. The H2 probe and image plane were fixed in space. The H2 probe was fixed at $0.25c$ upstream of the image plane to maintain concentration of the

hydrogen bubbles seeding the tip vortex. Several images were averaged to increase the signal to noise ratio of the H2 trace. The wing position was varied using a manual traverse. The axial range of measurements was $0.5 \leq x/c \leq 1.5$ in $0.5c$ resolution, where the x origin is the wing trailing edge. The H2 probe was set at $\theta \sim 45^\circ$ to the freestream flow to avoid any disturbances created by the probe holder. A 45° mirror was placed in the water channel sufficiently downstream of the trailing edge.

The results of the tip region H2 flow visualisations are shown in figure 4.8. The bubble traces demarcate the area where swirling flow exists. At $\alpha = 0^\circ$ the flow affected area is quite small due to minimal lift force production for all vortex ages. The characteristic swirling flow pattern of a vortex is present for $\alpha = 5^\circ$ at $x/c = 0.5$ in figure 4.8. The area of swirling flow increases with angle of attack. The vortex pattern is strong for $\alpha = 10^\circ$ and $\alpha = 15^\circ$ at $x/c = 0.5$. At subsequent vortex ages in figure 4.8, the vortex spreads by viscous diffusion. The coherence of the tip vortex is reduced at $\alpha = 20^\circ$. Referring to the PLIF flow visualisations in section 4.0.2, leading edge separation occurs for $\alpha \geq 20^\circ$. The formation of a coherent tip vortex is therefore affected by the separated flow over the wing. Based on the results in figure 4.8, the most coherent tip vortex appears to be generated at $\alpha = 10^\circ$ in the streamwise planes investigated.

The H2 tip vortex visualisations provided a quick and simple way to evaluate the coherence of the developing vortex. A correlation was found between tip vortex coherence and leading edge separation. However, the visualisations are purely qualitative. To characterise the developing tip vortices, quantitative data was captured using PIV. This data is presented next.

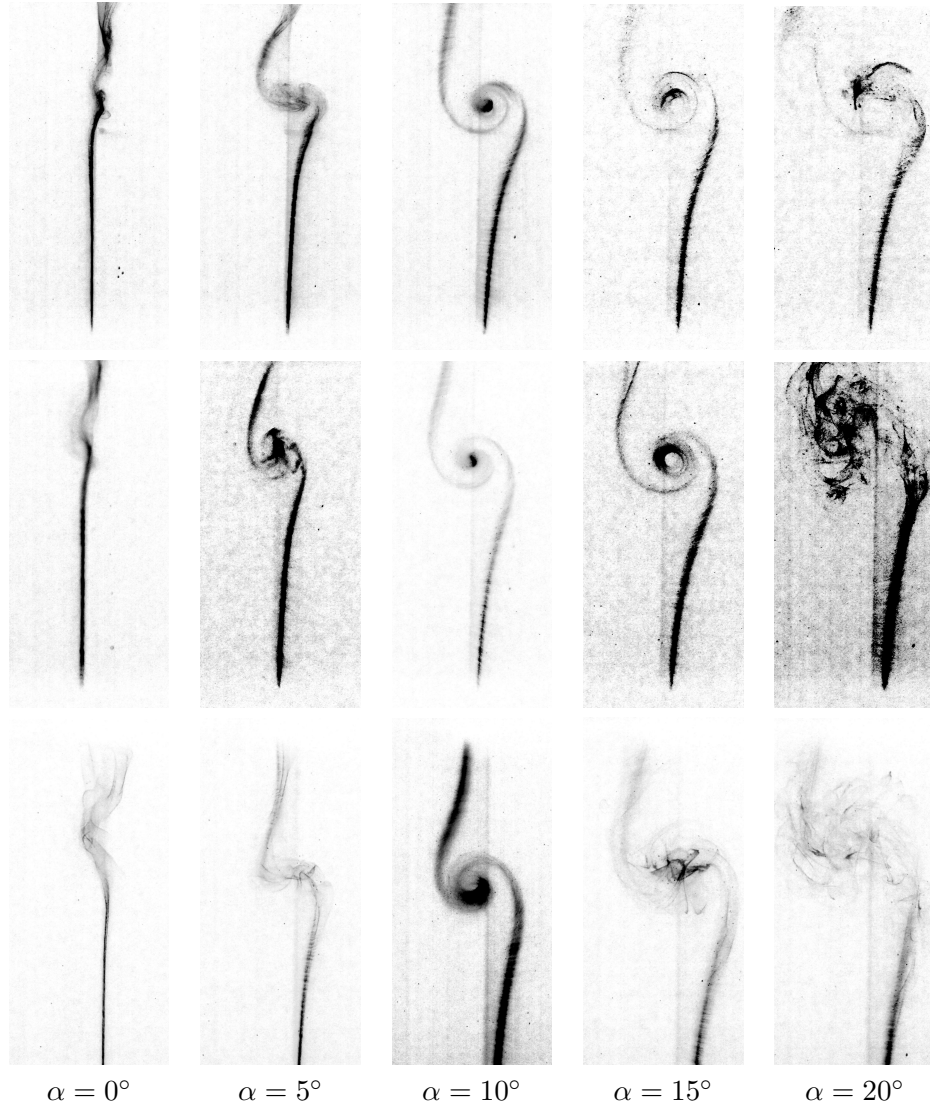


FIGURE 4.8: Composite hydrogen bubble flow visualisations of the tip vortex formed by the bluff tip at in the angle of attack range $0^\circ \leq \alpha \leq 20^\circ$ and streamwise planes $0.5 \leq x/c \leq 1.5$. Top: $x/c = 0.5$, Middle: $x/c = 1.0$, Bottom: $x/c = 1.5$, $Re_c = 6700$.

To characterise the 3D wing tip vortex in the low Reynolds number regime, quantitative data was captured using PIV. This technique was outlined in chapter 3. The experimental setup was similar to that shown in figure 4.7. Camera 1 from table 3.1 was used with a 105 mm lens (AF105, NIKKOR), allowing a large field of view. A region of interest of 1248 by 1536 pixels was implemented to reduce data file size. A total of 600 image pairs were captured at each spanwise location and α combination. Data was captured over the same α and x/c ranges of the H₂ flow visualisations. However, the Reynolds number, $Re_c = 6400$, was slightly less.

The tip vortices of the 3D wing have their axes aligned with the measurement plane. The

3D velocity fields thus contain the rotational motion of the vortex. The vortices can thus be characterised using the velocity gradient tensor methods presented in chapter 3. There have been few studies of tip vortex evolution at low Reynolds numbers. A notable study is that by Heyes et al. (2004) who investigated the trailing tip vortices of a NACA0012 wing at two Reynolds numbers, $Re_c = 1.0 \times 10^5$ and $Re_c = 2.2 \times 10^5$. Heyes et al. (2004) found tip vortices meander and can be described in a similar fashion to those at higher Re_c which were thoroughly investigated by Devenport et al. (1996). It is important to determine whether tip vortices in the wind turbine Reynolds number range also meander in a similar fashion. Thus, by investigating the meander of the simplest trailing tip vortices at a low Reynolds number, ones understanding of the more complex helical vortices found in a HAWT wake can improve.

The PIV image plane (y - z) is normal to the freestream velocity component, U_∞ , as shown in figure 4.7. The \mathbf{v} and \mathbf{w} , velocity components resolved in the PIV realisations are thus completely due to the induced velocities of the tip vortex. The time delay is chosen to ensure adequate particle displacements while minimising loss of particles from the field of view. With a light sheet thickness of ≈ 2 mm, and $U_\infty = 0.0558$ m/s, the maximum time delay is thus 0.0358 s.

A temporal average of the velocity field at $x/c = 0.5$ and $\alpha = 10^\circ$ is shown in figure 4.9. The length and velocity scales in this section are made dimensionless by c and U_∞ . The vector field has been cropped to focus on the tip vortex. Every second data point is shown for clarity with the vector size decreased by a factor of 6. The tip vortex induced velocities are clearly evident by the swirling flow pattern.

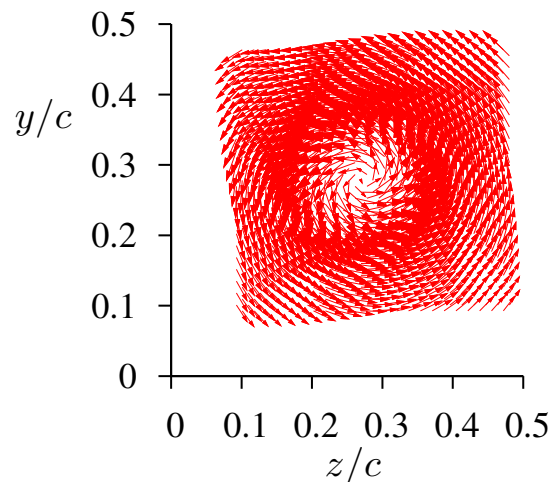


FIGURE 4.9: Velocity vector field of the tip vortex at $x/c = 0.5$ and $\alpha = 10^\circ$, $Re_c = 6400$. Every second data point is shown for clarity and the vector size has been decreased by a factor of 6. The swirling motion of the tip vortex is clearly evident in the centre of the figure.

The velocity field presented in figure 4.9 indicated swirling motion consistent with the presence of a vortex. The topology of the vortex is revealed by calculating the out-of-plane vorticity component, $\overline{\omega_{\mathbf{x}}}$ shown in equation 4.1. $\overline{\omega_{\mathbf{x}}}$ is approximately aligned with the tip vortex axis.

$$\omega_{\mathbf{x}} = \left(\frac{\partial w}{\partial y} - \frac{\partial v}{\partial z} \right) \mathbf{i}. \quad (4.1)$$

Mean axial vorticity contour plots, $\overline{\omega_{\mathbf{x}}}$, for the three streamwise locations and the various angles of attack are shown in figures 4.10 and 4.11. The coordinate system is aligned with the wing trailing edge irrespective of the angle of attack. The boundary of the wing profile is indicated by the dashed lines and the trailing edge by the solid line. The wake of the wing and the developing tip vortex is clearly evident from iso-contours of $\overline{\omega_{\mathbf{x}}}$.

The vorticity iso-contours at $\alpha = 0^\circ$ depicts a vortex sheet rather than a single coherent vortex. The pressure differential between the pressure and suction surfaces is not strong enough for tip vortex formation. Figures 4.10 and 4.11 quantify the H2 visualisations of figure 4.8. A coherent tip vortex forms for $\alpha \geq 5^\circ$. The trailing edge vorticity sheet arising from changes in the blade bound circulation is visible as the ‘tail’ attached to the tip vortex core. The 3D flow at the tip entrains this trailing edge vorticity sheet (Green 1995) forming a tip vortex with axial distance. The entire vorticity field is rotating as evident by the rotation of the tail structure for $5^\circ \leq \alpha \leq 15^\circ$ at consecutive wake distances. The tip vortices over the entire angle of attack range $0^\circ \leq \alpha \leq 20^\circ$ form inboard of the tip. The average tip vortex locations in the normal axis are shown in figure 4.12.

The vorticity magnitude in the tip vortex at $x/c = 0.5$ increases until $\alpha = 15^\circ$ as more bound circulation is created about the wing. At $\alpha = 20^\circ$, the tip vortex structure loses coherence due to separation from the leading edge as shown in figures 4.5 and 4.8. The separation region on the wing suction surface inhibits a uniform vorticity sheet which the tip vortex can entrain. This dynamic inflow to the tip vortex causes a less coherent vortex to form at $\alpha = 20^\circ$ compared to those at $5^\circ \leq \alpha \leq 15^\circ$ as shown in figures 4.10 and 4.11. The K–H vortices which form in the separated shear layer at 20° also affect the coherence of the tip vortex. This phenomena has been visualised in delta wing vortices by Lawson (1991).

The axial vorticity plots reveal the change in tip vortex topology with angle of attack and distance in the wake. In the spatial range of the measurements, the trailing edge vorticity sheet is still present which reveals the global rotation of the flow field. The coherence of the tip vortex depends on whether K–H vortices exist in the separated shear layer. To gain

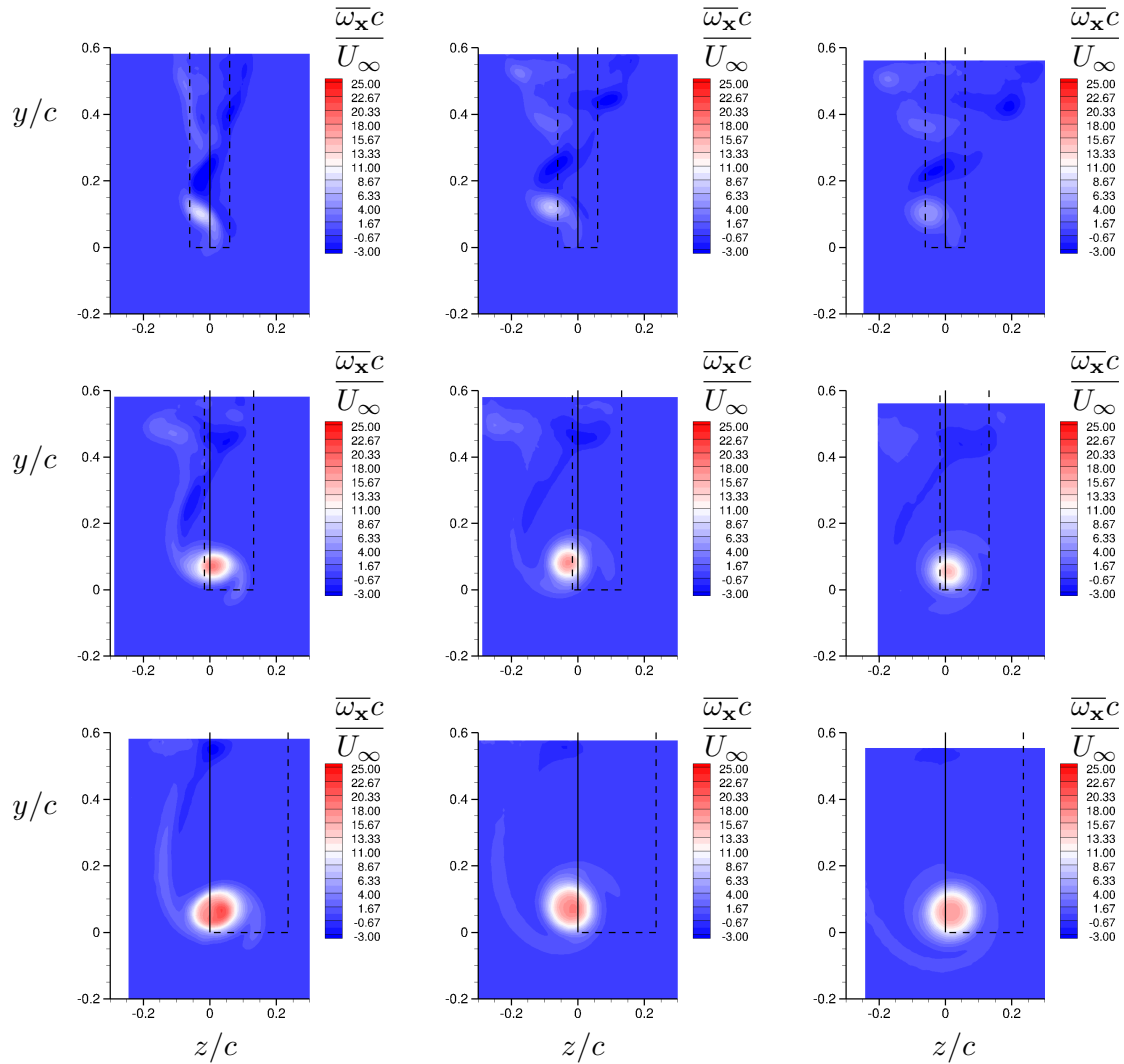


FIGURE 4.10: Mean non-dimensional axial vorticity, $\overline{\omega_x}c/U_\infty$, contours of the tip vortex formed by a NACA4412 airfoil profile with a bluff tip shape at $Re_c = 6400$. Airfoil profile and trailing edge are depicted by the dashed and solid lines respectively. left: $x/c = 0.5$, middle: $x/c = 1.0$ right: $x/c = 1.5$. top: $\alpha = 0^\circ$, middle: $\alpha = 5^\circ$ and bottom: $\alpha = 10^\circ$

a deeper understanding of tip vortex evolution at low Re_c individual vortex properties are evaluated in the following section.

4.0.6 Tip vortex properties at low Re_c

Individual vortex properties were extracted from the instantaneous PIV fields using the data analysis methodologies outlined in chapter 3. Properties such as the vortex radius, r_{vc} , strength (circulation), Γ , maximum squared swirling strength, λ_{ci}^2 and maximum tangential velocity, $V_{\theta,max}$, were determined at each wake position and angle of attack. The instantaneous frames were investigated as vortex meander is known to affect properties such as r_{vc} and $\overline{V}_{\theta,max}$ (Heyes et al. 2004). The meander of the tip vortices is investigated in section 4.0.7.

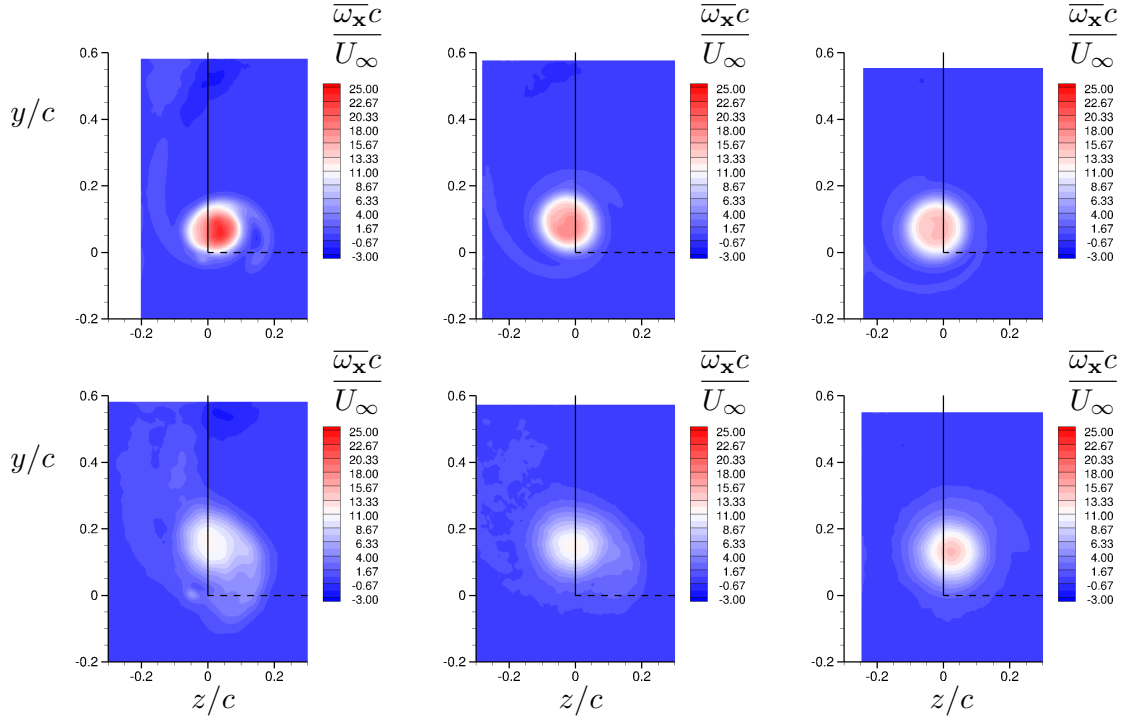


FIGURE 4.11: Description as for figure 4.10. top: $\alpha = 15^\circ$, bottom: $\alpha = 20^\circ$.

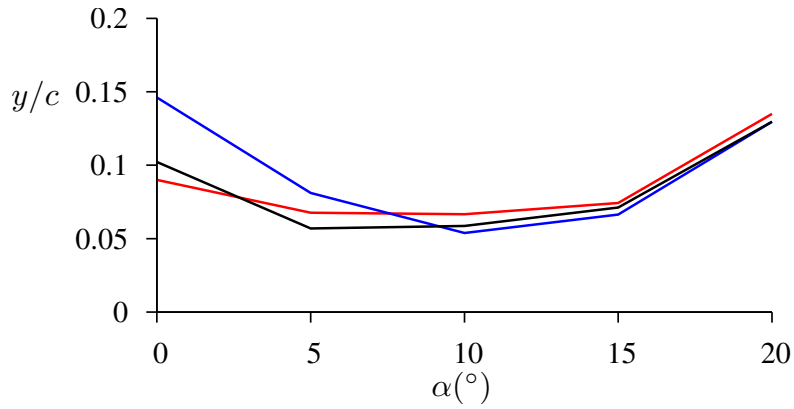


FIGURE 4.12: Variation of the mean normal location on the tip vortices with angle of attack at $Re_c = 6400$. The tip vortices form in board of the tip. Red: $x/c = 0.5$, blue: $x/c = 1.0$ black: $x/c = 1.5$.

The mean value of the vortex property distributions are presented in this section.

The mean non-dimensional circulation is presented in figure 4.13. Circulation is conserved in the wake for the angles of attack where attached flow occurs. The minimal spread of the circulation values indicates time invariant vortex production for $0^\circ \leq \alpha \leq 15^\circ$. The unsteadiness of the wake at $\alpha = 20^\circ$, as seen in the PLIF and H2 visualisations, is indicated by the larger spread of the circulation values. The linear increase in circulation of the tip vortex is representative of the increased lift production on the wing. Using lifting line theory,

the tip vortex is assumed to contain all the blade bound circulation, Γ_B (Betz 1935). The $C_l(\alpha)$ relationship can be determined using the Kutta–Joukowski (K–J) theorem as shown in equation 4.2. The lift coefficient is thus twice the tip vortex circulation magnitude shown in figure 4.13.

$$\frac{\Gamma}{U_\infty c} = \frac{1}{2}C_l. \quad (4.2)$$

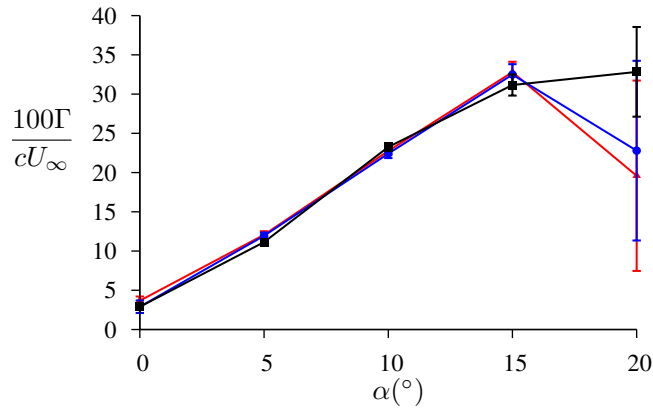


FIGURE 4.13: Tip vortex circulation, $100\Gamma/cU_\infty$, variation with angle of attack at $Re_c = 6400$. Circulation increases with angle of attack until leading edge separation occurs. Red triangles: $x/c = 0.5$, blue circles: $x/c = 1.0$, black squares: $x/c = 1.5$.

The K–J theorem implies separation from the trailing edge. The flow visualisations in section 4.0.2 indicated the separation point moves toward the leading edge with increasing angle of attack. The higher angle of attack results will thus contain larger uncertainty. Furthermore, the axial vorticity plots of figures 4.10 and 4.11 reveal the trailing edge vorticity sheet connected to the tip vortex at $x/c = 0.5$. The vorticity in this ‘tail’ was created by the blade bound circulation which will contribute to the tip vortex strength once vortex roll-up is complete. However, the invariance of tip vortex circulation with wake distance in figure 4.13 suggests vortex roll-up is complete (Green 1995) by $x/c = 0.5$.

The average maximum tangential velocity, $V_{\theta,\max}$, on the vortex core boundary is shown in figure 4.14. The core boundary is designated as the λ_{ci}^2 * contour level. The maximum tangential velocity increases in a similar fashion to the circulation with angle of attack. The tangential velocity is largest at $x/c = 0.5$ for all α and decreases with wake distance due to the effects of viscosity.

The squared swirling strength criteria, λ_{ci}^2 , is used to determine regions of local rotation. The variation of λ_{ci}^2 with position and α is shown in figure 4.15. λ_{ci}^2 increases with angle of attack in accordance with the larger $\overline{V}_{\theta,\max}$ in figure 4.14 and Γ in figure 4.13. $\overline{\lambda_{ci}^2}$ decreases

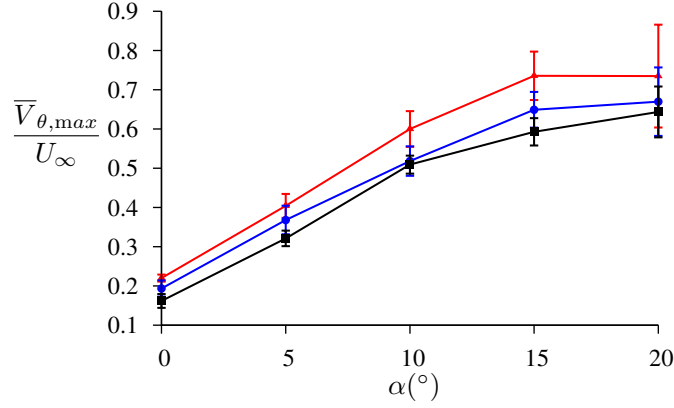


FIGURE 4.14: Tip vortex maximum tangential velocity, $\bar{V}_{\theta, \max}/U_{\infty}$, variation with angle of attack at $Re_c = 6400$. Red triangles: $x/c = 0.5$, blue circles: $x/c = 1.0$, black squares: $x/c = 1.5$.

with wake distance in a similar fashion to the average maximum tangential velocity.

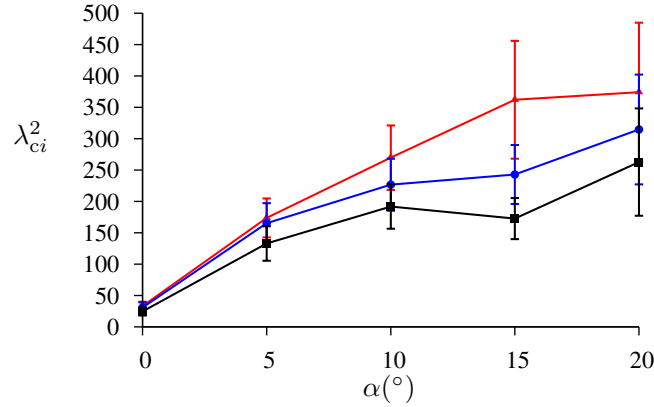


FIGURE 4.15: Tip vortex maximum squared swirling strength, λ_{ci}^2 at $Re_c = 6400$. Red triangles: $x/c = 0.5$, blue circles: $x/c = 1.0$, black squares: $x/c = 1.5$.

The vortex core radius, r_{vc} , is determined from the methodology in chapter 3. r_{vc} represents the radius of a circle of equal area to that of the λ_{ci}^2 contour. The variation of r_{vc} with angle of attack is shown in figure 4.16. r_{vc} increases with downstream distance due to the effects of viscosity. The decrease in r_{vc} for the $\alpha = 20^\circ$ results at $x/c = 0.5$ and $x/c = 1$ is an indication of the turbulent nature of the wake. The airfoil operates in a fully separated state at $\alpha = 20^\circ$ as shown by the PLIF visualisations in section 4.0.2. A range of vortex sizes will be produced due to flow separation. The large scatter in the $x/c = 0.5$ and $x/c = 1$ results is a reflection of this. The energy based filter outlined in chapter 3 was developed to focus data analysis on the large scale vortices of interest. The energy based filter is applied to investigate tip vortex meander in section 4.0.7 and in chapters 6 and 7.

Tip vortex properties were characterised at Re_c for all α and x/c combinations. The conservation of tip vortex circulation validates the data methodologies presented in chapter 3.

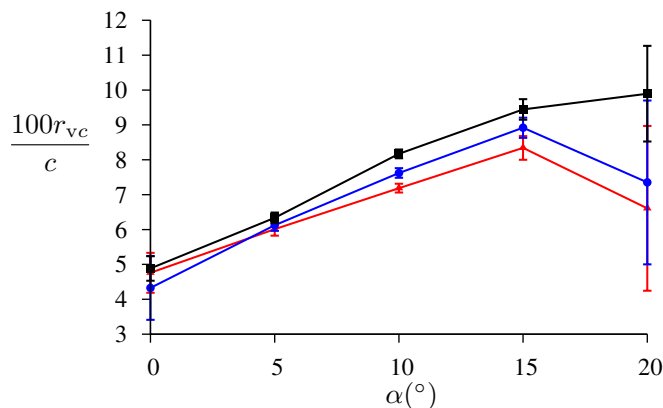


FIGURE 4.16: Tip vortex core radius, $100r_{vc}/c$, variation with angle of attack at $Re_c = 6400$. Red triangles: $x/c = 0.5$, blue circles: $x/c = 1.0$, black squares: $x/c = 1.5$.

Maximum vortex properties such as $\overline{V}_{\theta, \max}$ and λ_{ci}^2 decrease with wake distance due to viscous effects. Tip vortex meander over the α and x/c range at Re_c is characterised in the following section.

4.0.7 Meander of fixed wing tip vortices at low Re_c

The slow seemingly random oscillations of wing tip vortices about a mean position is known as meandering or wandering. Vortex meander masks the true vortex properties when instantaneous measurements are temporally averaged. It causes a reduction in peak vorticity and tangential velocity, an increase in vortex radius and introduces Reynolds stresses within the vortex core (Heyes et al. 2004). Devenport et al. (1996) assumed vortex meander was normally distributed to allow recovery of the true vortex properties from their velocity point measurements. PIV fields allow the instantaneous vortex core locations to be determined. The instantaneous frames can then be re-centered on the vortex location and interpolated to a common grid. This process corrects the data for meandering motions without specifying the form of the distribution describing the meandering motions, as in the Devenport et al. (1996) model. It has been used for both fixed (Heyes et al. 2004) and rotary wing (Heinck et al. 2000) tip vortices. Heyes et al. (2004) found that without correction, the vortex core radius was over predicted by 12.5% and the maximum tangential velocity was under predicted by 6% (Heyes et al. 2004). They postulated the meandering motion was due to external disturbances, such as freestream turbulence rather than self induced motions but no firm conclusions were drawn.

Meander of the tip vortices behind the static 3D wing was investigated here to determine if the motions were normally distributed at the low Reynolds number range at which the wind

turbine models operate. If confirmed, a similar model could then be used to characterise meander of the helical vortex filaments created in the near wake of a HAWT. Helical vortex filaments in HAWT wakes are investigated in chapters 5, 6 and 7. Further, as the tip vortices of the static 3D are the ‘simplest’ trailing vortices a lifting surface can generate, the results will be used as a reference case for the more complex helical vortex filaments in a HAWT wake.

The instantaneous frames were first passed through the energy based filter outlined in chapter 3 to remove influence of small scale turbulent eddies. The instantaneous vortex core locations were deduced using the Γ_1 (Graftieaux et al. 2001) function presented in chapter 3. An integration radius, S , of 8 data points was used in the analysis. To achieve sub-grid scale accuracy, the barycentric centre of the Γ_1 field shown in equation 4.3 was used to determine the instantaneous vortex location.

$$R = \frac{1}{\sum_{i=1}^N \sum_{j=1}^N \Gamma_1(i, j)} \sum \Gamma_1(i, j) r_{i, j} \quad (4.3)$$

The mean and standard deviations of the core position distributions in each axis were then calculated. Outlying data (3σ) based on position (\bar{x}, \bar{y}) and circulation $(\bar{\Gamma})$ were removed. This typically resulted in 5% of the data being removed. The meander of a wing tip vortex at wake distance $x/c = 0.5$ and $\alpha = 5^\circ$ is shown in figure 4.17. The red line represents the transverse deviations, Δ_z , whereas the blue line represents the normal deviations, Δ_y . As the data was sampled at 1Hz, no frequency information can be extracted from the distributions. The instantaneous positions are also shown as a scatter plot in figure 4.17.

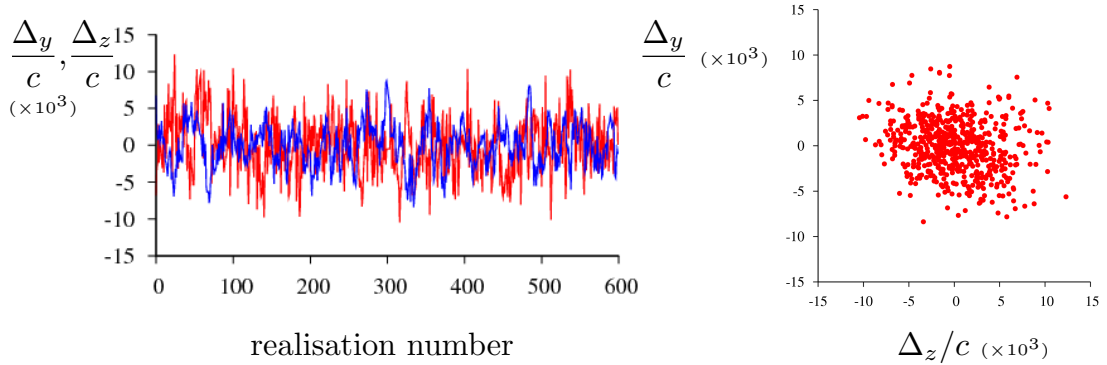


FIGURE 4.17: Instantaneous vortex position fluctuations relative to the mean location indicating tip vortex meander for $\alpha = 5^\circ$, $x/c = 0.5$, $Re_c = 6400$.

The probability density functions of the meandering motions in each measurement axis were then calculated. The results are shown in figure 4.18. The top row of figures represents

meander in the transverse direction, Δ_z , and the bottom row of figures represents meander in the normal direction, Δ_y . The left, middle and right columns represent non-dimensional wake distances, x/c , of 0.5, 1.0 and 1.5 respectively. The colour indicates the airfoil angle of attack where red, blue, black, orange and green represent $\alpha = 0^\circ$, $\alpha = 5^\circ$, $\alpha = 10^\circ$, $\alpha = 15^\circ$, and $\alpha = 20^\circ$ respectively. The raw histogram values are indicated by the points whereas the solid lines represent the normal distribution applied to the data.

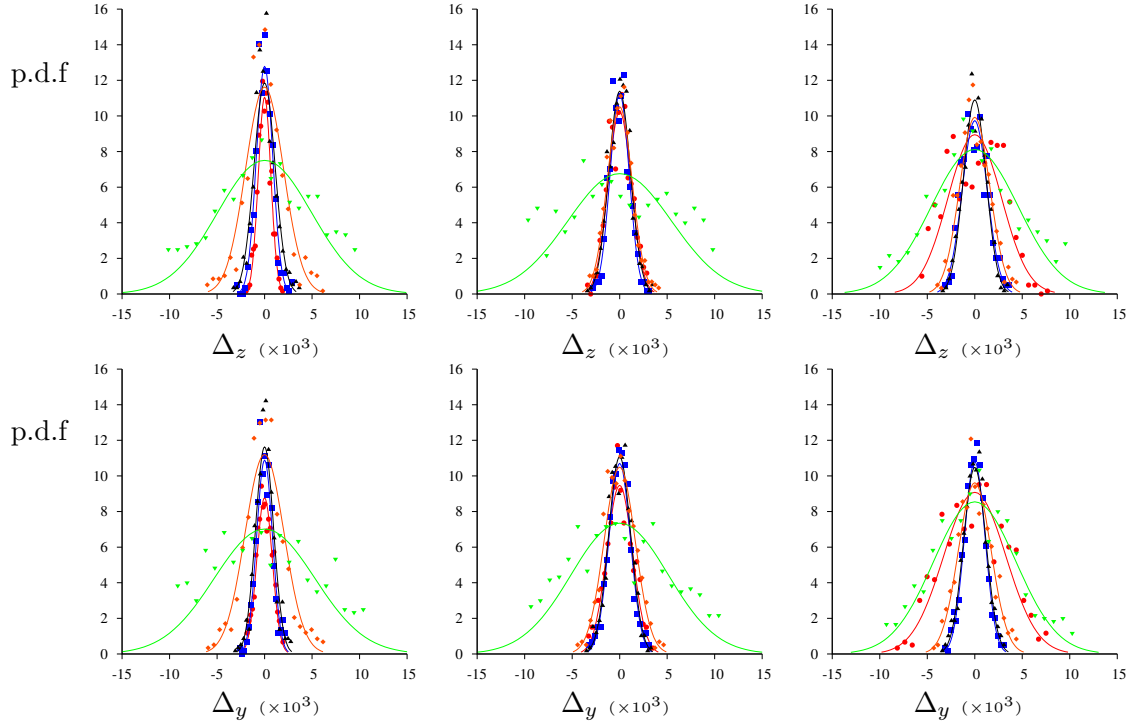


FIGURE 4.18: Probability density functions (p.d.f) of the instantaneous vortex locations at $Re_c = 6400$. top: transverse, Δ_z , bottom: normal, Δ_y , left: $x/c = 0.5$, middle: $x/c = 1.0$, right: $x/c = 1.5$. red circles: $\alpha = 0^\circ$, blue squares: $\alpha = 5^\circ$, black delta: $\alpha = 10^\circ$, orange diamonds: $\alpha = 15^\circ$, green nabla: $\alpha = 20^\circ$. Symbols indicate histogram values whereas solid lines indicate normal distribution applied to data.

Figure 4.18 shows that the meandering motions can be described by a normal distribution exceptionally well for certain conditions. The flow visualisation results of section 4.0.2 are recalled to explain these results. The angle of attack equal to 20° data are affected by the bounds of the measurement area. However, it was shown in figure 4.11 that when leading edge separation occurs tip vortex formation is adversely affected. At the measurement distances closest to the trailing edge, *i.e.* $x/c = 0.5, 1.0$, a vortex of low coherence is present. The vortex position's distribution exhibits a broad peak in these cases. As the vortex forms further, the position distribution approaches a normal distribution. Based on the p.d.f's presented in figure 4.18, meander is most accurately represented by a normal distribution when a large

proportion of the flow is attached and sufficient distance has passed for tip vortex formation. This can be said to occur when $5^\circ \leq \alpha \leq 10^\circ$ for wake distances $x/c \geq 1.0$. The standard deviation of the normal distribution will be most accurate for these cases. The standard deviation of each normal distribution is extracted and used as a measure to characterise vortex meander.

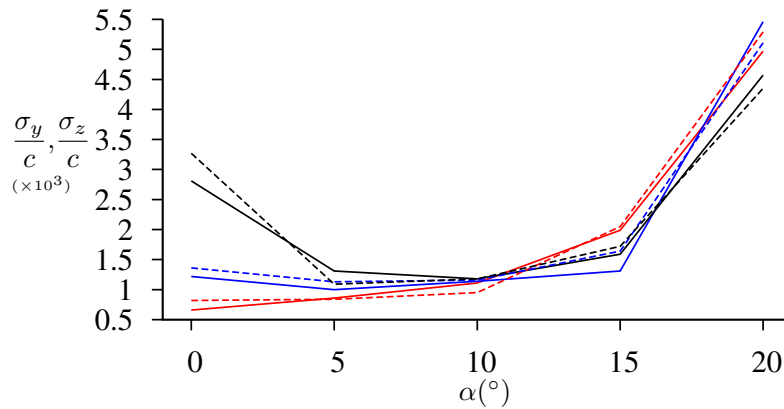


FIGURE 4.19: Tip vortex meander amplitude for different angles of attack and wake distances at $Re_c = 6400$. Solid line: transverse meander magnitude, σ_z/c , dashed line: normal meander magnitude, σ_y/c . red lines: $x/c = 0.5$, blue lines: $x/c = 1.0$ and black lines: $x/c = 1.5$

The meander results, presented in figure 4.19, show how the meander magnitude varies with both angle of attack and wake distance. The meander magnitudes are at all times less than those at higher Re_c reported by (Heyes et al. 2004). Prior studies have indicated that meander both increases (Rokhsaz et al. 2000) and decreases (Devenport et al. 1996; Heyes et al. 2004) with vortex strength. Comparing figures 4.19 and 4.13 suggests a weak relationship between increasing vortex strength and meander amplitude when a coherent vortex forms, *e.g.* in the range $5^\circ \leq \alpha \leq 15^\circ$. Heyes et al. (2004) found a linear reduction in meander magnitude with vortex strength from which he proposed the origins of meander was external rather than self induced.

There is still no consensus regarding the origins of meander. Jaquin et al. (2001) summarised four possible causes of meander in fixed wing trailing vortices which were outlined in chapter 2. The results of Heyes et al. (2004) showed the freestream turbulence intensity influences meander magnitude close to the vortex source but that this influence reduces with distance (Heyes et al. 2004). Jaquin et al. (2001) also reached a similar conclusion which suggests meander magnitude was insensitive to increasing I_u . While the freestream turbulence intensity in the present experiments ($I_u = 1 - 2.4\%$) cannot be disregarded as a source of meander, it is not believed to be the dominant mechanism.

The origins of meander in the current study are thus proposed as causes 2) and 4), *i.e.* perturbation of the core by unsteadiness in the vorticity sheet surrounding the core and propagation of unsteadiness from the model Jaquin et al. (2001). For cause 4, variation in the initial vortex trajectory will appear as a meandering motion. Such fluctuations can occur due to unsteadiness of the model. Here, the wing was mounted on a force balance sting designed to measure the small forces being generated by the wing. Using beam element theory, the maximum contribution of vortex displacement from the mean, *i.e.* meander, due to unsteadiness of the model is at worst 20% of the meander magnitude at $\alpha = 20^\circ$.

Therefore, the dominant cause for the increase in meander shown in figure 4.19 at the low experimental Re_c , is proposed to be cause 2. There is a clear correlation between an increase in meander and presence of K–H vortices in the separated shear layer. The change in flow topology above the wing was shown in section 4.0.2. At the angles of attack where K–H vortices form in the separated shear layer ($10^\circ \leq \alpha \leq 20^\circ$) meander amplitude increases. The results are consistent with those of Gursul and Xie (2000) who investigated delta wing trailing vortices. Vortex meander increased when K–H vortices existed in the separated shear layer which rolls-up into the trailing vortices (Gursul and Xie 2000). They proposed the meander of the large scale primary vortex is caused by the induced velocity fields of the small scale K–H vortices (Gursul and Xie 2000). This phenomena over delta wings was visualised by (Lowson 1991). The rapid increase in meander amplitude at $\alpha = 20^\circ$ will also be influenced by unsteadiness arising from separation from the leading edge.

4.1 Summary of the low Reynolds number airfoil study

In this chapter the flow over a static 3D wing at low Reynolds numbers has been investigated. The findings characterised the salient features of flow over a static 3D wing in the Reynolds number range the rotating wind turbine models experience. The NACA4412 airfoil profile was investigated to match that used in both rotating wind turbine models. The work was required to investigate the flow topologies on the airfoil suction surface and in the wake at the low experimental Reynolds number. The current investigation appears to be the first to examine the NACA4412 in this depth.

PLIF flow visualisations showed that laminar separation occurs over a broad α range. The wing experiences leading edge separation at $\alpha \geq 20^\circ$. Kelvin–Helmholtz disturbances form in the separated shear layer for $\alpha \geq 10^\circ$ with vortices forming prior to the trailing edge for $\alpha \geq 15^\circ$. Importantly, transition in the separated shear layer was qualitatively shown

4.1. Summary of the low Reynolds number airfoil study

not to occur. Laminar separation bubbles, and the detrimental effects on airfoil performance they cause are thus absent at the visualisation Reynolds numbers of $Re_c = 3.5 \times 10^3$ and $Re_c = 5.3 \times 10^3$. With knowledge of the flow topologies the 3D wing experiences, the airfoil performance data of Sunada and Kawachi (2002) can be used with confidence in a BEM method to evaluate the geometrically scaled turbines performance. The BEM analysis is presented in chapter 5.

Finally, tip vortex formation was investigated by both qualitative H2 flow visualisations and quantitative PIV fields. The rectilinear tip vortices a static 3D wing generates are the ‘simplest’ trailing vortices. The tangential velocity, swirling strength parameter and circulation all increased with angle of attack until leading edge separation occurred. The meander of the wing tip vortices were found to have a normal distribution when attached flow occurs over the wing. Therefore, a normal distribution will also be used to characterise the meander of the helical vortices in the HAWT wake. Meander drastically increased when leading edge separation occurred. Understanding of how these ‘simple’ vortices evolve will be used as a base case to analyze how the more complex helical vortices in a HAWT wake evolve. This data is presented in chapters 5, 6 and 7. The results obtained with the geometrically scaled wind turbine are presented in the following chapter.

Chapter 5

Wake Structure of a Geometrically Scaled Rotor

This chapter investigates wake evolution of the geometrically scaled wind turbine model presented in chapter 3 at several tip speed ratios. It does this using both flow visualisations and PIV. The results focus on the tip vortices in the top half of the wake as these vortices are most likely to interact with other turbines in a wind farm setting. Root vortices are also generated and found to cease much closer to the rotor plane. Reasons for the rapid cessation of the root vortices are presented. The model was investigated in both an upwind and downwind turbine configuration. The downwind turbine configuration was investigated to determine the effect on the root vortices of the vortex structures shed from the turbine support geometries. The results highlight the poor aerodynamic performance of the geometrically scaled blade at the experimental Reynolds number.

The chapter proceeds by first presenting the flow visualisations taken with the hydrogen bubble technique. Quantitative velocity and vorticity fields obtained using PIV are then presented followed by characterisation of the tip and root vortices using the vortex identification methodologies outlined in chapter 3.

5.0.1 H₂ flow visualisations reveal tip vortex formation

Hydrogen bubble (H₂) flow visualisations were initially captured to show tip and root vortex formation. The visualisations replicated those of Brown (1971), who investigated near wake structure of a propeller using smoke visualisations. The H₂ setup was shown in figure 3.8. The visualisations were captured as both movies and phase-locked images that show the formation and interaction (where present) of the tip vortices as they advect downstream. Due to the diffusion of the H₂ bubbles back into the water and buoyancy effects removing the bubbles from the laser sheet, only the near wake is imaged.

The visualisations provide a quick estimation of wake geometry over a range of operating conditions. They allow the more labour intensive quantitative data investigations to target regions of interest. The H2 flow visualisations were captured at numerous tip speed ratios $3.31 \leq \lambda \leq 9.61$ corresponding to a Reynolds number range of $0.75 \times 10^3 \leq Re_c \leq 1.967 \times 10^3$. In the phase-locked data, several images were averaged to increase the signal to noise ratio of the bubble trace.

The phase-locked average H2 flow visualisations at several tip speed ratios are shown in figure 5.1. U_∞ is from left to right with the blade rotating in a counter-clockwise direction when viewed from upstream. The H2 probe is clearly seen upstream of the model. The freestream flow laden with hydrogen bubbles interacts with the model such that a stagnation point is visible on the hub in line with the rotational axis. Figure 5.1 shows that the flow contracts after passing over the hub and through the blades. Based on this finding, prior to the PIV data acquisition, a cylindrical shroud of equal diameter to the hub was constructed and fitted to the nacelle.

The induced flow of the tip vortices is shown in figure 5.1 adjacent to the freestream. The first vortex which appears in the visualisation plane is 30° old. An example of the tip vortex shear layer trajectory (TVSLT) is shown by the white line in the $\lambda = 8.11$ results. Flow expansion increases with tip speed ratio. Because of the energy extraction and blockage at the rotor plane, continuity requires that the flow expands in the wake. There is evidence of root vortex formation only in the minimum tip speed ratio investigated, $\lambda = 3.31$. The absence of a root vortex indicates the 3D nature of the flow adjacent to the nacelle. The regions adjacent to the nacelle, close to the wake centerline axis and behind the nacelle geometry are devoid of tracer bubbles due to the 3D flow caused by the nacelle and blades in the root region. Three-dimensionality in these regions removes the tracer bubbles from the image plane and hence they no longer reflect the laser light, creating the dark region seen in the images.

The geometrical pitch of the tip vortices at the various tip speed ratios has been extracted from figure 5.1. The mean tip vortex position was estimated as the maximum height of the area devoid of particles. The rationale being that the vortex core location is in-line with this point. The variation in the axial position with vortex age and tip speed ratio is shown in figure 5.2. ‘Vortex age’ is defined as the angular travel in degrees($^\circ$) of the blade which created the helical vortex filament. The data points represent tip vortex locations from figure 5.1 whereas the trend lines indicate the linear lines of best fit applied to the data. The advection speed of the tip vortices is linear and the helicoidal pitch reduces with tip speed ratio.

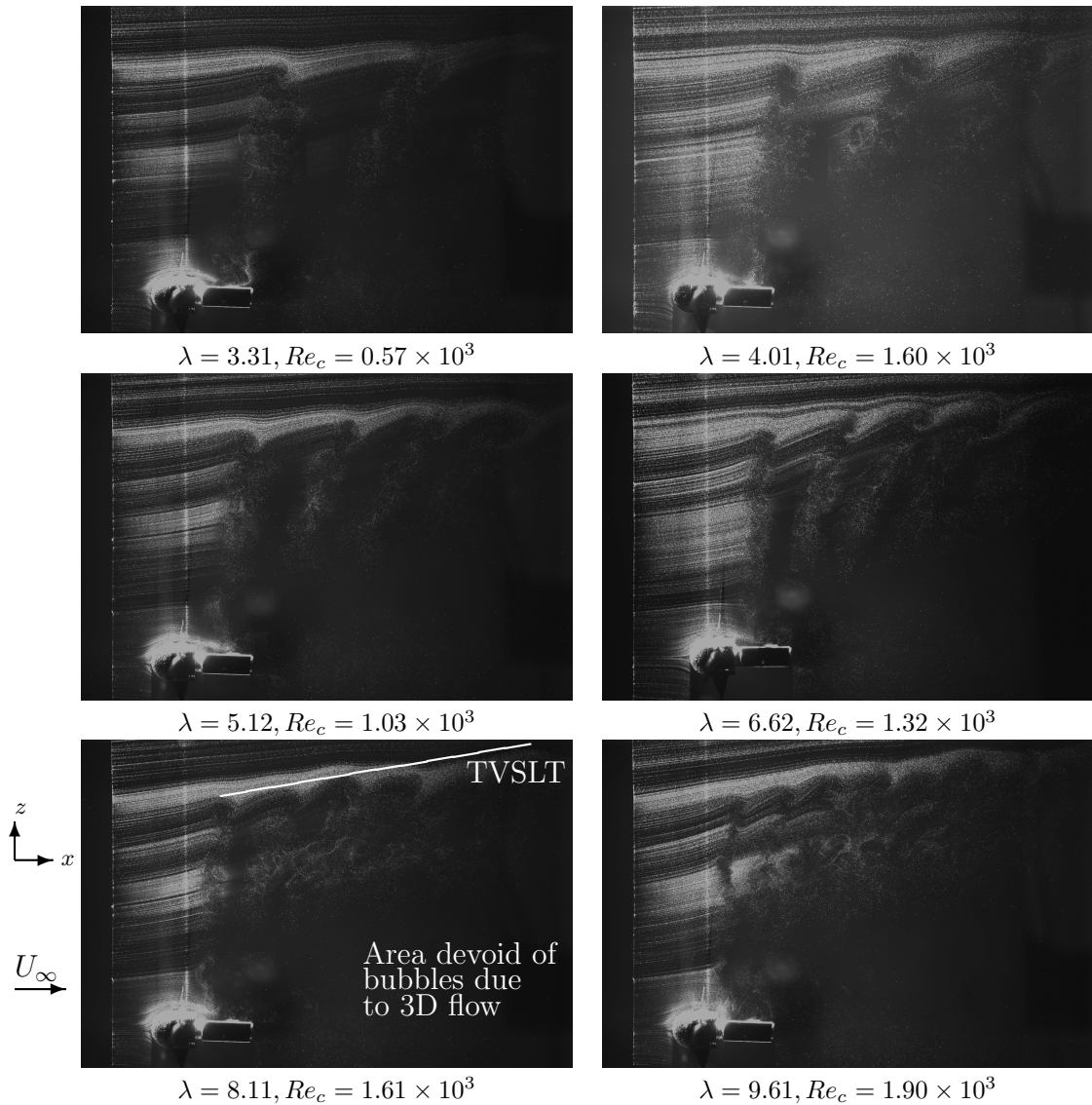


FIGURE 5.1: Phase-locked average H₂ flow visualisations. U_∞ as shown with the H₂ probe visible upstream. The first tip vortex in the visualisations is 30° old. The tip vortex shear layer trajectory (TVSLT) is indicated in the $\lambda = 8.11$ results. The front stagnation point on the hub is also visible. The helicoidal pitch reduces and wake expansion increases reducing tip speed ratio.

The visualisations provided a basis to focus the quantitative investigation of the tip and root vortices in the wake using PIV. The PIV data is presented in the following section.

5.0.2 Near-wake velocity and vorticity fields

The PIV investigation of the near wake of the geometrically scaled turbine will be investigated in this section. The model was investigated in both an upwind and downwind turbine configuration. Three tip speed ratios, $\lambda = 4, 7, 10 \pm 0.14$, were investigated, providing insight into both a lightly loaded rotor and heavily loaded rotor around the full-scale design

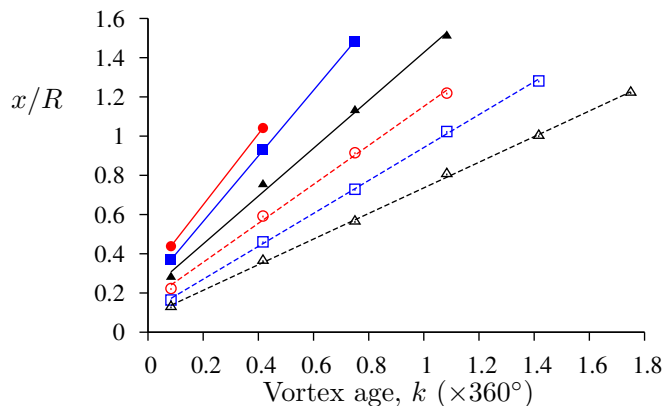


FIGURE 5.2: Tip vortex axial positions extracted from the phase-locked average H2 flow visualisations. $\lambda = 3.31$: red circles–solid line/symbols, $\lambda = 4.01$: blue squares–solid line/symbols, $\lambda = 5.12$: black triangles–solid line/symbols, $\lambda = 6.62$: red circles–dashed line/hollow symbols, $\lambda = 8.11$: blue squares–dashed line/hollow symbols, $\lambda = 9.61$: black triangles–dashed line/hollow symbols.

condition, here rounded to $\lambda_{d,f-s} = 7$. The free stream velocity was set to $U_\infty = 0.092$ m/s, giving a Reynolds number range of $1385 \leq Re_c \leq 3369$ for the investigated tip speed ratios.

The experimental setup was shown in figure 3.20 and the experimental technique outlined in chapter 3. Due to the axial advection of the tip vortices and the corresponding skew angle of the wake, a measurement plane orthogonal to multiple tip vortex axes at any one instant is not possible. The skew angle at which the vortex axis intersects the measurement plane is deduced with a-priori knowledge of the helicoidal pitch. This angle reduces with an increase in tip speed ratio.

The axial, u , and radial, v , velocity components in the wake were captured, allowing characterisation of the rotational motion in the image plane. From the sectional velocity data, vortical wake properties such as vortex radius and the circulation for both the tip and root vortices were deduced. Measurements were phase-locked with a blade aligned with the tower structure and thus within the measurement plane. To avoid the vortical structures in the tower wake contaminating the phase-locked averaged data (see chapter 6), only the top half of the wake ($y/R \geq 0$) was measured here.

Camera number 2 in table 3.1 with a 105 mm AF micro lens (Nikkor, Japan) acquired the images for the phase-locked averaged measurements. The aperture of the lens was set to f5.6. A maximum magnification factor of 17 pixels/mm was employed giving a field of view (FOV) of $2.05R \times 1.37R$ in the axial and radial directions respectively. The vector fields contained 249 by 166 vectors at a resolution of $8.2 \times 10^{-3}R$. A total of 300, *i.e.* $N = 300$, image pairs were captured for each tip speed ratio and turbine configuration. Mask files of the wind turbine geometry were used to avoid erroneous vectors.

Convergence of the PIV fields occurs when the cumulative mean of the fluctuating cross velocity product $C(\langle \overline{u'v'} \rangle)$ reaches a stable value. The $\langle \cdot \rangle$ represents a spatial average. Convergence is determined in a sub PIV field ($Nx \times Ny$) containing a tip vortex. Figure 5.3 shows the data converges prior to the $N = 300$ image pairs.

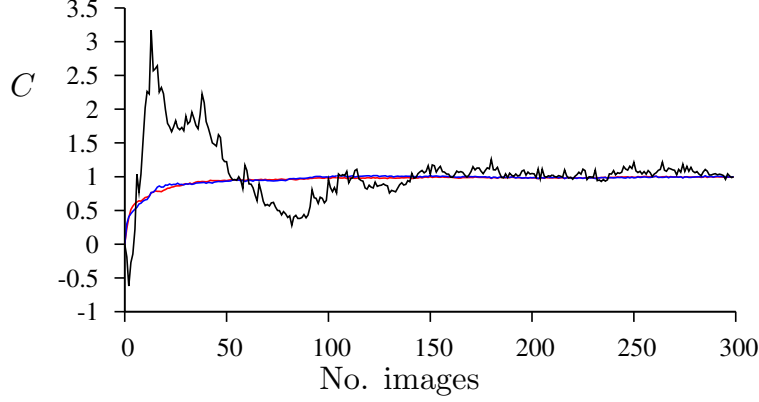


FIGURE 5.3: Cumulative mean of the fluctuating velocity components indicating convergence prior to $N = 300$ image pairs. Upwind configuration, $\lambda_{d,f-s}$, $VA = 120^\circ$, $Nx = Ny = 42$. red: $C(\langle \overline{u'u'} \rangle)$, blue: $C(\langle \overline{v'v'} \rangle)$, black: $C(\langle \overline{u'v'} \rangle)$

Uncertainty in the PIV data can arise from random and bias components. The effect of the random components reduces with image number. The random error due to turbulence in the flow field was evaluated using equation 8.11 (Grant and Owens 1990). The freestream turbulence intensity was $I_u \sim 1\%$. The fractional error estimation, ϵ , of the mean velocity is 0.135% of U_∞ , with a 98% ($z_c = 2.326$) confidence level.

$$\epsilon = \frac{z_c I_u}{\sqrt{N}} \quad (5.1)$$

The calculated vorticity also has an uncertainty that arises from random and bias errors. Here, the vorticity was calculated using an algorithm that fits it with a 2D polynomial to minimise random and bias errors (Fouras and Soria 1998). A conservative estimate of the uncertainty in the derivative terms is ± 1 pixel.

The phase-locked averaged wake axial velocity field for the full-scale design tip speed ratio, $\lambda_{d,f-s}$ is shown in figure 5.4. The flow is from left to right with the blade rotating in a counter clockwise direction when viewed from upstream. The blade is thus travelling out of the page in the negative z -direction. The effect of the wind turbine on the freestream velocity is clearly evident from the phase averaged velocity gradients present in the wake. To highlight these wake velocity gradients, velocity profiles at three axial locations, $x/R = 0.5, 1.0, 1.5$, are also shown on the right of figure 5.4. The velocity deficit increases as one moves near the wake centreline. A recirculation region forms immediately downstream of the nacelle with the

mean region of reverse flow depicted by the dashed line in figure 5.4. This recirculation region was seen in numerical simulations of a number of nacelle geometries (Ameur et al. 2011). The H2 visualisations in section 5.0.1 and particle streak flow visualisations in the root region (see figure 5.24 and text discussing this region in section 5.0.6) indicate this flow is highly 3D. This restricts how definitively one can analyse this region of the wake when using the current planar experimental technique however a qualitative argument is made and supported. The nacelle geometry sheds vorticity which can in the very near wake form into a cylindrical vortex sheet centered on the wake centerline (Ebert and Wood 2001). In the present experimental setup, the shedding process is complicated by the presence of the tower section and the pulsatile inflow created by the rotating blades. Beyond the nacelle recirculation zone a central wake region of low velocity and high turbulence forms. Momentum recovery occurs downstream by viscous diffusion and turbulent mixing.

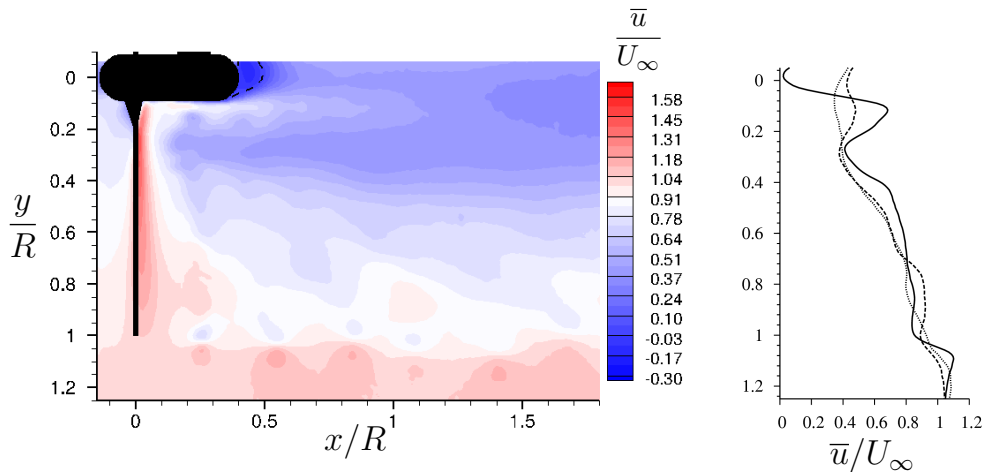


FIGURE 5.4: Phase-locked average wake of the Tjæreborg wind turbine operating in an upwind configuration at $\lambda_{d,f-s}$. Left: Contours of axial velocity, \bar{u}/U_∞ , dashed line encapsulates region of mean reverse flow, velocity gradients due to tip and root vortices are visible at the tip radius and close to nacelle respectively. Right: wake velocity profiles, $x/R = 0.5$ (—), $x/R = 1.0$ (---), $x/R = 1.5$ (···)

With increasing tip speed ratio, the model turbine acts like a solid disk which decreases the wake centreline velocity. Conversely, with a reduction in tip speed ratio, there is a corresponding increase in the wake centreline velocity. Momentum recovery thus occurs faster with reducing tip speed ratio. This is evident in figure 5.5 by the higher velocities and reduced spatial extent in the central wake region (for illustrative purposes, this is taken as $0.5U_\infty$). The wake velocity profile trends are however similar between the $\lambda_{d,f-s}$ and $\lambda = 4$ cases.

As expected $\lambda = 10$, (shown in figure 5.6) sees an increase in spatial extent of the central

wake region and a decrease in velocity within this region with an increase in the tip speed ratio. This is clearly evident in the wake velocity profiles of figure 5.6. Despite the changes in central wake region structure with tip speed ratio, the maximum mean reverse flow in the nacelle recirculation zone remains largely independent of tip speed ratio. This maximum reached approximately $0.14U_\infty$ in the tip speed ratios investigated. The recirculation zone extends furthest into the wake in the $\lambda = 4$ case, with reversed flow evident at $x/R = 0.5$ in figure 5.5.

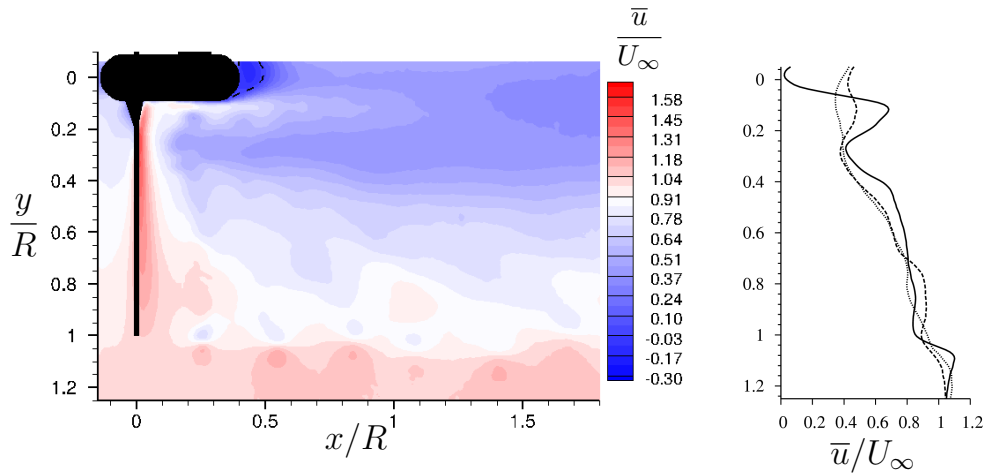


FIGURE 5.5: Caption as for figure 5.4. Downwind configuration, $\lambda = 4$.

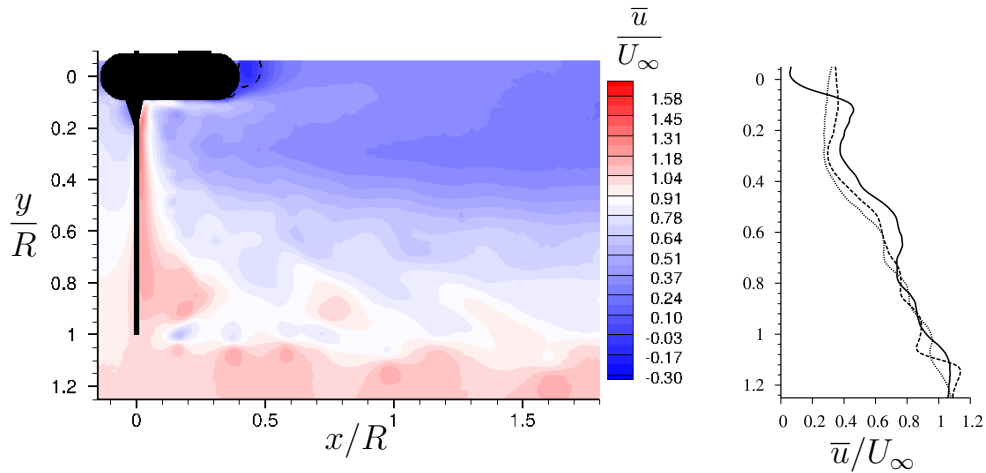


FIGURE 5.6: Caption as for figure 5.4. Downwind configuration, $\lambda = 10$.

The Tjæreborg wind turbine was designed as an upwind turbine, however at the model scale, the turbine could be easily tested in a downwind configuration. The phase-locked average wake axial velocity field for the three tip speed ratios investigated are shown in figures 5.7, 5.8 and 5.9. The region of reverse flow immediately downstream of the nacelle

extends much less into the wake. This is due to the different trajectory of the shear layer which forms off the nacelle body in the downwind case. Further, the maximum velocity deficit does not occur on the wake centreline. It occurs at approximately $0.15 \leq y/R \leq 0.3$ depending on λ . The wake velocity deficit is less than the upwind configuration due to the reduction of the recirculation region size. The tip vortex shear layer is again visible close to the unit radius.

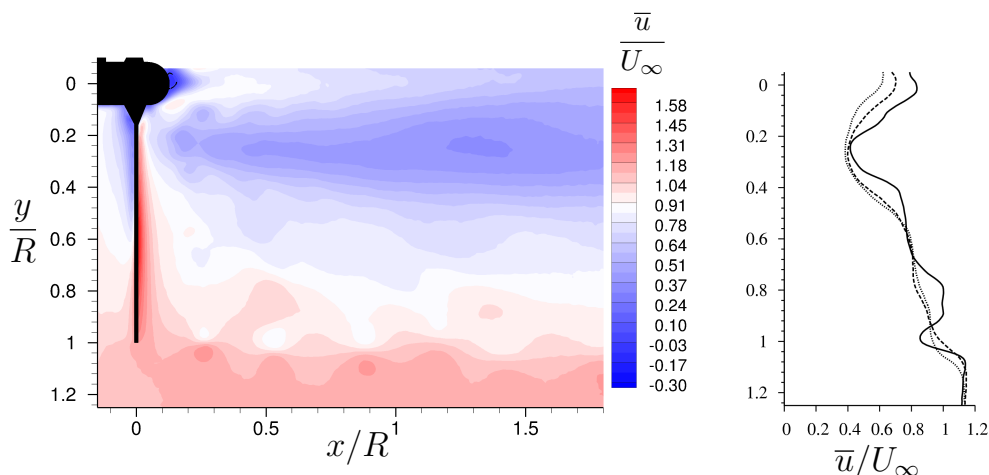


FIGURE 5.7: Caption as for figure 5.4. Downwind configuration, $\lambda_{d,f-s}$.

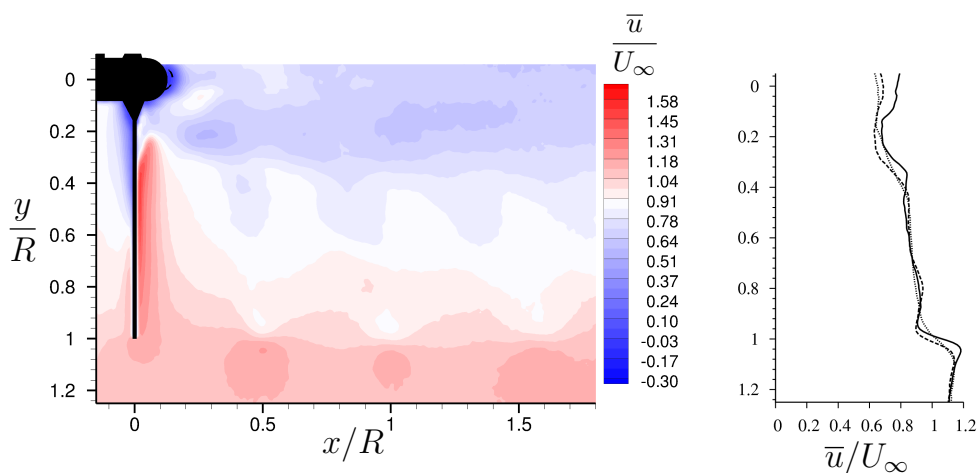


FIGURE 5.8: Caption as for figure 5.4. Downwind configuration, $\lambda = 4$.

Velocity gradients indicative of vortical structures can also be seen in figures 5.4, through to figure 5.9 at the unit radius and adjacent to the nacelle body, at $y/R \sim 0.2$ depending on λ . The tip and root vortices induce velocity components both in the direction of and opposing the mean streamwise flow. The tip vortices are located in the shear layer which forms between the freestream and retarded wake flow. The induced velocity components

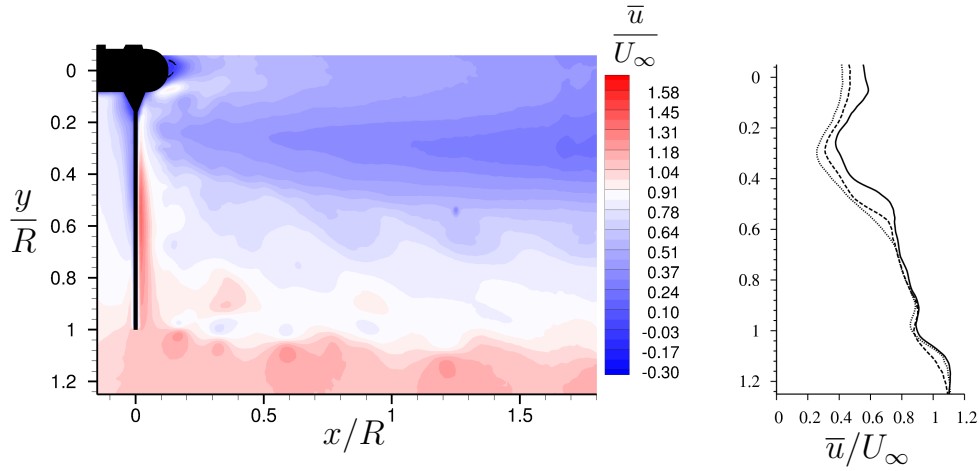


FIGURE 5.9: Caption as for figure 5.4. Downwind configuration, $\lambda = 10$.

are most easily recognisable in the tip vortex shear layer when a wake velocity trace passes through a tip vortex. In this case, the axial velocity is both larger and smaller than the mean freestream velocity. These velocity gradients become weaker with axial distance at the experimental Reynolds number, primarily due to viscous diffusion, turbulent mixing and secondarily possibly due to instabilities arising in the vortices.

The velocity profiles change little between $x/R = 1$ and $x/R = 1.5$ for all tip speed ratios suggesting the wake velocity profile is close to a fully developed state. This alone would indicate a cessation of the near wake. However, as will be shown, tip vortices are present throughout the measurement domain indicating the transition to the far wake has not occurred.

The phase-locked average vortical wakes for the full-scale design tip speed ratio $\lambda_{d,f-s}$, are shown in figure 5.10 and 5.11 for a downwind and upwind turbine configuration respectively. These figures show the out of plane vorticity, $\bar{\omega}_z$, within the near wake. In both figure 5.10 and 5.11, six tip vortices ($\bar{\omega}_z < 0$) are visible in the shear layer around the unit radius. In addition, several root vortices ($\bar{\omega}_z > 0$) are also present at small vortex ages (VA), close to the nacelle surface ($y/R = 0.15$). The root vortex is designated as the coherent region of vorticity of opposite sign (positive) to the tip vortex closest to the rotational axis.

It is evident from figures 5.10 and 5.11 that the top half of the wake ($y/R \geq 0$) is affected little by the configuration of the model turbine at $\lambda_{d,f-s}$. The most noticeable change between the two configurations occurs in the radial position of the root vortices, *i.e.* the root vortex filament radius, R_r . The root vortex filament radius at a vortex age of 120° reduces by 70% between the downwind and upwind configurations. R_r reduces due to a net radial inward

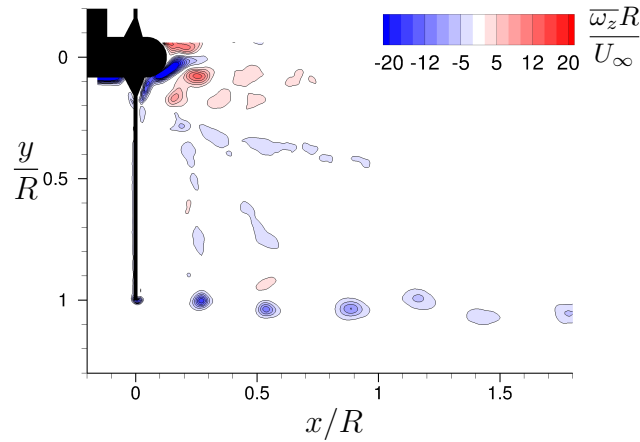


FIGURE 5.10: Phase-locked average wake of the Tjæreborg wind turbine operating in an downwind configuration at $\lambda_{d,f-s}$ depicting the coherent vortical structures which dominate the near wake, contours of non-dimensional tangential vorticity, $\bar{\omega}_z R / U_\infty$.

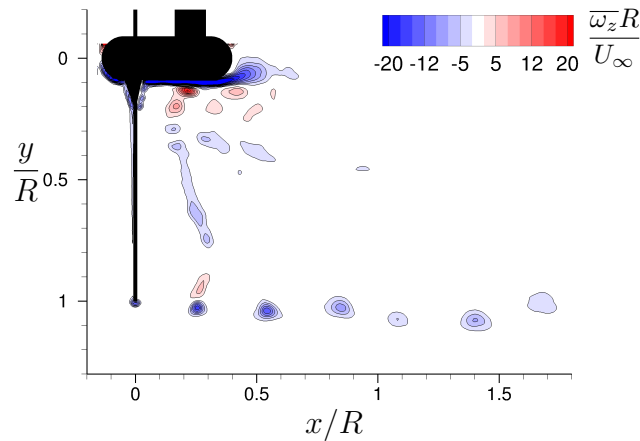


FIGURE 5.11: Phase-locked average wake of the Tjæreborg wind turbine operating in an upwind configuration at $\lambda_{d,f-s}$ depicting the coherent vortical structures which dominate the near wake, contours of non-dimensional tangential vorticity, $\bar{\omega}_z R / U_\infty$.

velocity which is impeded in an upstream configuration (Micallef et al. 2011). The bottom half ($y/R \leq 0$) of the wake will however display more pronounced differences due to the effects of tower shadow. The effect of tower shadow is investigated in chapter 6. Testing in a downwind configuration allowed investigation of the effect that vorticity within the nacelle boundary layer has on the root vortices. This effect is discussed in further detail in section 5.0.6.

The wake structure of an upwind and downwind turbine operating below $\lambda_{d,f-s}$ are shown in figures 5.12 and 5.13. Fewer tip vortices are visible in the field of view due to the increase in pitch.

The wake structure of a downwind and upwind turbine operating above $\lambda_{d,f-s}$ are shown

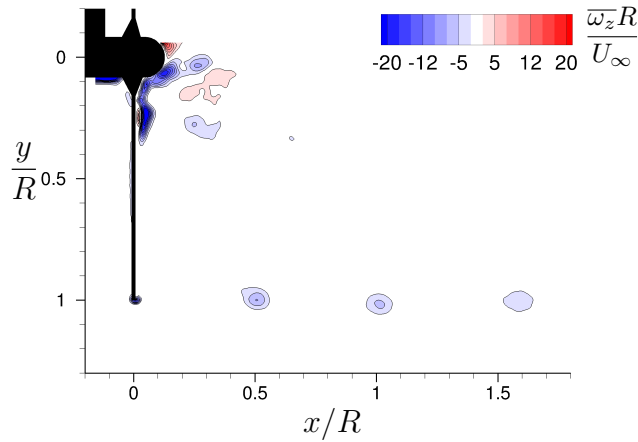


FIGURE 5.12: Caption as for figure 5.10. Downwind configuration, $\lambda = 4$.

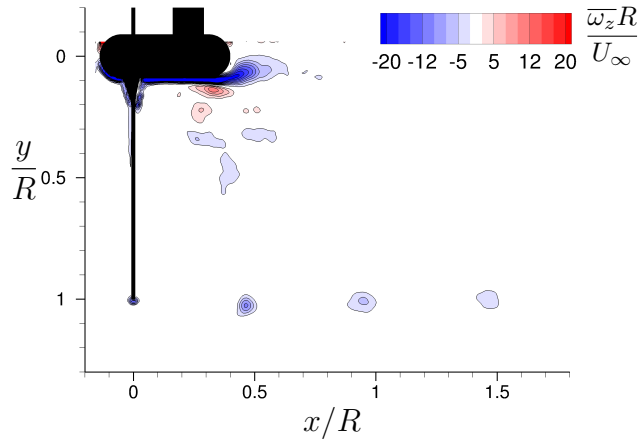


FIGURE 5.13: Caption as for figure 5.11. Upwind configuration, $\lambda = 4$.

in figures 5.14 and 5.15. The number of tip vortices visible in the field of view increase due to the reduction in pitch.

The phase-locked vorticity fields allow investigation of vortex interaction in the wake. A *single* inviscid helical vortex filament is affected by the mutual inductance instability mode when the helicoidal pitch reduces below $0.3R$ (Widnall 1972). An ideal 3 bladed wind turbine wake consists of three counter rotating helical vortex pairs. In reality however, extra sources of vorticity are present in the form of the blade wakes and those shed from the turbine support structures. Thus, extrapolating the results of (Widnall 1972), the mutual inductance mode will act when the helicoidal pitch reduces below $0.9R$. Thus, the $\lambda_{d,f-s}$ (figures 5.11 and 5.10) and $\lambda = 10$ (figure 5.15 and 5.14) results are likely to be affected by this instability mechanism. As the helicoidal pitch reduces further below the critical pitch at which the

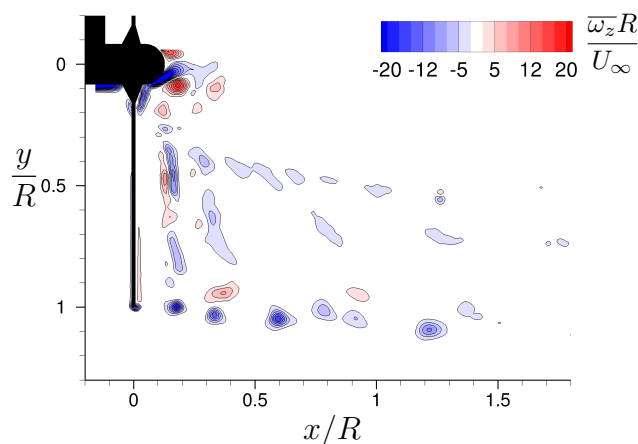


FIGURE 5.14: Caption as for figure 5.10. Downwind configuration, $\lambda = 10$.

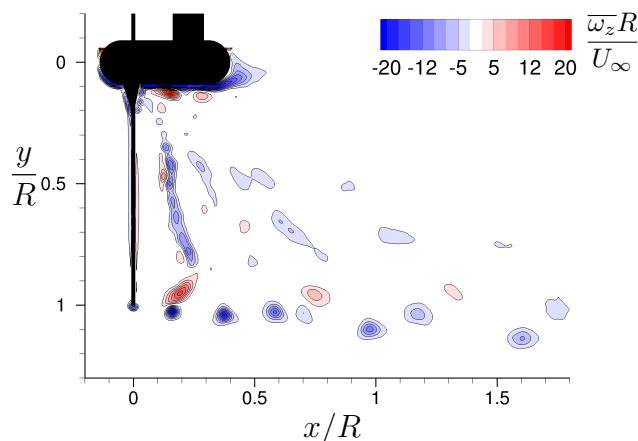


FIGURE 5.15: Caption as for figure 5.11. Upwind configuration, $\lambda = 10$.

instability mode first acts the transition to instability occurs closer to the rotor plane (Felli et al. 2011). Felli et al. (2011) showed the mutual inductance instability mode was responsible for tip vortex entanglement. Qualitative evidence of the mutual inductance instability mode between adjacent tip vortices is evident at $x/R \sim 1$ in figure 5.11 and at $x/R \sim 0.7$ in figure 5.15. The non-uniform spacing in the axial and radial directions and the change in relative strength (vorticity) of the vortices at this location indicate the presence of the mutual inductance instability mode. The instability mode causes the instantaneous vortex positions to vary about the mean shown in the temporal averages. These deviations result in a spatial smoothing of vorticity.

Vorticity signatures of individual blade wakes can be seen in the region between the root and tip vortices in figures 5.10 to 5.15. The blade wakes are the remnants of the vorticity

sheet shed from each blade into the wake which has not yet rolled up into the coherent tip and root vortices. The induced velocities of the tip vortices cause the roll up process such that with a vortex of low circulation, as in the present study, this process can be expected to take some time. The intensities of the blade wakes increase with tip speed ratio.

The blade wakes also reveal the wake radial velocity gradient ($\partial u/\partial r$). The tip and root vortices become progressively less well-aligned in the axial direction as they convect further downstream. It is apparent from equation 2.4 that the relative velocity at the tip radius is much larger than that at the root radius. As a result, the initial tip vortex advects away from the blade faster than its equivalent root vortex. Post vortex roll up, the tip vortices are adjacent to the higher velocity freestream fluid, in contrast to the root vortices, which are situated within the low velocity central wake region. Although the mechanism for the difference in axial alignment is readily explainable, one cannot draw too many conclusions regarding trends of the growth of this differential due to the limited number of root vortex realisations. The speed of the root vortex diffusion is discussed further in section 5.0.6.

A slight wake expansion is also seen in figure 5.11 and 5.15 immediately downstream of the rotor, as evidenced by the outward radial movement of the tip vortices. Wake expansion depends on the rotor loading and results from the pressure increase that takes place due to the energy extraction by the blades, which is clear here from the axial velocity slow down. The axial position of the tip vortices follows a linear trend, as shown on the left in figure 5.16, whereas the radial core positions shown on the right in figure 5.16 vary more with vortex age. There is good agreement between the downwind and upwind axial positions of the tip vortices in the top half of the wake ($y/R \geq 0$), with the pitch of the upwind results slightly less than that of the downwind results. This difference probably arises due to variation in tip speed ratios. It is slightly larger than the bounds of uncertainty in the measurements at $\lambda = 4$. The difference generally decreases with increasing tip speed ratio, as the vortices are more likely to interact.

5.0.3 Rotor suffers from poor aerodynamic performance at Re_c

The near wake velocity and vorticity fields revealed the rotor operates at a reduced efficiency at the model scale. In addition to reduced aerodynamic performance at low Reynolds number, airfoils become susceptible to adverse flow features, such as laminar separation bubbles. The PLIF flow visualisations of chapter 4 indicated LSB's do not form at the experimental Reynolds number.

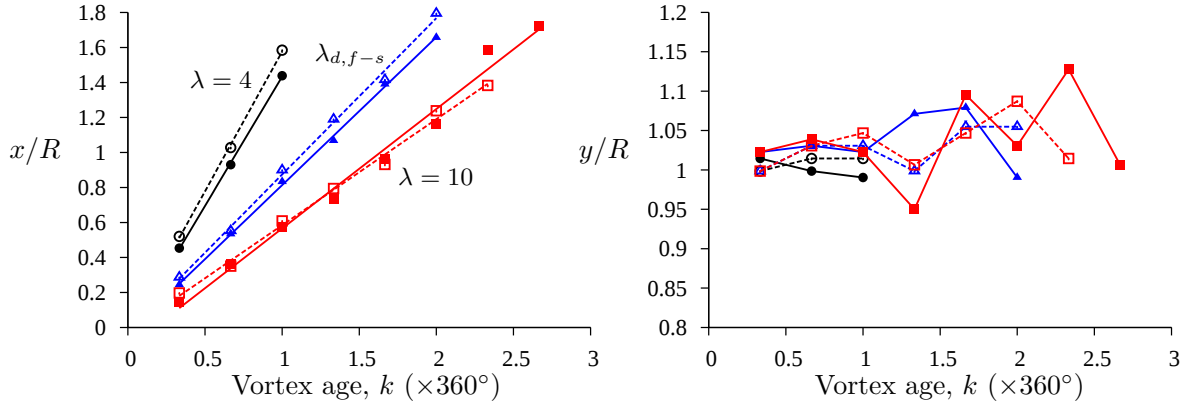


FIGURE 5.16: Mean axial (left) and radial (right) position of the tip vortices with increasing vortex age. Trend lines have been applied to the axial positions only. Dashed lines and hollow symbols: downwind results; solid lines and solid symbols: upwind results.

To gain further insight into the flow states over the rotor, a BEM analysis was undertaken. Further, as the experimental model was not fitted with a force transducer, the thrust coefficient for the different flow cases was estimated using the BEM method. The BEM method was introduced in section 2. The results of the BEM method are presented in the following section.

The near wake vorticity fields indicated the blade wakes contain significant vorticity. A source of this vorticity is separated flow over the rotating airfoil. The angle of attack (AOA) distribution, $\alpha(r)$ with tip speed ratio is shown in figure 5.17. The twist distribution, $\theta(r)$, is also shown by the orange dashed line. $\alpha(r)$ increases toward the blade root due to a reductions in the relative velocity, U_{rel} . The range of $\alpha(r)$ reduces with increasing tip speed ratio. It is largest at $\lambda = 4$, $13^\circ \leq \alpha_{\lambda=4} \leq 37^\circ$, decreases for $\lambda_{d,f-s}$, $7^\circ \leq \alpha_{\lambda_{d,f-s}} \leq 19^\circ$, and is the smallest at $\lambda = 10$, $4.8^\circ \leq \alpha_{\lambda=10} \leq 9.2^\circ$. The PLIF flow visualisations presented in chapter 4 indicated leading edge separation occurs for $\alpha \geq 20^\circ$. The grey shaded area in figure 5.17 indicates where leading edge separation is likely (ignoring 3D boundary layer effects). At $\lambda = 4$, the inner 47% of the blade will be in a fully separated state. For $\lambda_{d,f-s}$, the inner 20% of the blade will experience leading edge separation. The inner 20% of the blade has a cylindrical cross section for rigidity (as per geometric scaling), such that the fully separated flow will mostly affect the $\lambda = 4$ case.

It is important to recognise where flow separation occurs as rotational effects on airfoil performance become important in these regions. Rotational augmentation of the blade boundary layer flow leads to an increase in airfoil performance especially in separated regions. At very high Reynolds numbers, stall is delayed to higher angles of attack (Shreck et al. 2010) due to centrifugal pumping occurring on the rotating blades. The boundary layer

is therefore thinner due to spanwise gradients of the separated flow leading to higher force coefficients (Lindenburg 2004). Modification of airfoil properties due to rotational augmentation have primarily been investigated for high Reynolds number flows. However, Gross et al. (2012) investigated rotational augmentation of airfoil properties numerically at $Re_c = 1 \times 10^5$. They argued the increase in performance was due to crossflow instabilities which cause earlier transition leading to stall delay. This study is at a much higher Re_c than the presents experiments. Further, it was shown qualitatively via PLIF visualisations in chapter 4 that shear layer transition does not occur at the experimental Re_c . As such, the rotational effects on airfoil performance at the experimental Re_c are difficult to estimate. As this was outside the scope of the current study, no corrections to the airfoil data were made and it is likely the BEM predictions will under predict true rotor performance.

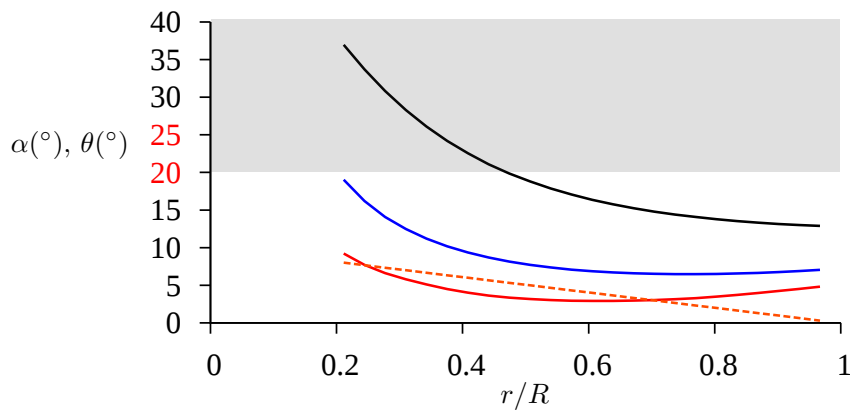


FIGURE 5.17: Angle of attack distribution, $\alpha(r)$, as determined by a BEM analysis for the three tip speed ratios. black: $\lambda = 4$, blue: $\lambda_{d,f-s}$, red: $\lambda = 10$. The blade twist angle distribution $\theta(r)$ is also indicated by the orange dashed line. The shaded area indicates where leading edge separation is likely based on static airfoil PLIF flow visualisations.

One drawback of the BEM method is the necessity for airfoil performance data at the experimental Reynolds number. As pointed out in chapter 4, airfoil data is scarce at very low Reynolds numbers. However, Sunada and Kawachi (2002) investigated the lift and drag properties of a number of airfoil profiles including the Wortmann FX63-137 cambered airfoil, at a Reynolds number of $Re_c = 4 \times 10^3$. They found the maximum C_l/C_d ratio to be equal to 4.9 at $\alpha = 7^\circ$. At very low Reynolds numbers, mean thickness ratio and camber ratio are the most important airfoil characteristics for airfoil performance (Sunada and Kawachi 2002). The mean thickness ratio of the Wortmann FX63-137 (7%) and the NACA4412 (7.2%) are very similar such that the drag coefficient will be similar. Further, the Wortmann FX63-137 has a larger camber ratio (6%) than the NACA4412 (4%) so the maximum lift will be slightly larger in the former profile.

However, the position of maximum camber is closer to the leading edge in the NACA4412, which produces a larger maximum C_l/C_d ratio (Sunada and Kawachi 2002). The NACA4412 and Wortmann FX63-137 airfoil profiles have similar performance at high Reynolds numbers and their geometric similarity suggests their performance at low Reynolds numbers could also be similar. Based on this assumption, the cambered airfoil data of Sunada and Kawachi (2002) for $-20^\circ \leq \alpha \leq 20^\circ$ was used in conjunction with modified flat plate data of Blevins (1984) for $\alpha \leq -40^\circ$ and $\alpha \geq 40^\circ$. Airfoil performance becomes less dependent of airfoil shape in the fully stalled region, permitting the use of flat plate performance data. The magnitude of the Blevins (1984) flat plate data was reduced by 20% to match the Sunada and Kawachi (2002) flat plate data at $Re_c = 4 \times 10^3$. Linear interpolation was performed between the two data sets. The modified airfoil data set was used with a standard BEM method (Hansen 2008), in conjunction with the tip and heavily loaded rotor correction formulas of Shen et al. (2005), to predict the model turbine loading.

Selected results of the BEM analysis on the model wind turbine are shown in table 5.1. Results from a BEM analysis of the full-scale Tjæreborg wind turbine are also shown in the table 5.1 in bold text, for comparison. $\langle \cdot \rangle$ indicates a spatial average taken in the radial direction. The subscript \bullet_{PIV} indicates results from the PIV data. Table 5.1 indicates that the full-scale turbine operates close to $\langle \bar{a}_{opt} \rangle$ at $\lambda_{d,f-s} = 7.07$. The average axial interference factor, $\langle \bar{a} \rangle$, for the experimental model increases with tip speed ratio whilst at all times remaining less than $\langle \bar{a}_{opt} \rangle$ and the full-scale values. In the absence of direct load measurements on the experimental model, the average value of the thrust coefficient along the blades, $C_T = \langle C_T(r) \rangle$ was used to give an indication of the loading of the model turbine. The thrust coefficient was evaluated using the axial interference factor and the BEM relations, $C_T(r) = 4\bar{a}(r)(1 - \bar{a}(r))$ where the rotor was treated as an actuator disk. As expected, the thrust coefficient increases with tip speed. As expected the full-scale turbine operates more efficiently than the model turbine due to the larger lift force produced by the blade segments.

The axial interference factor, \bar{a} , indicates the velocity slowdown in the rotor plane. It can be used to deduce the operating wake state as shown in figure 10.4. An optimal turbine operates at the Lanchester–Betz–Joukowski (L–B–J) limit which occurs when $\bar{a} \equiv \bar{a}_{opt} \equiv 0.33$. To compare the BEM \bar{a} value to the experimental data, it must be corrected for the B blades using Prandtl’s tip loss factor, *i.e.* $\bar{a} = F \cdot a_B$ (Hansen 2008). The tip loss correction factor tends to zero at the tip (Shen et al. 2005).

Geometric scaling and reduced aerodynamic performance at the experimental Reynolds

number limit the achievable interference factor. The axial interference factor distributions, \bar{a} and a_B for the λ are shown in figure 5.18. The solid line represents \bar{a} whereas the dotted line represents a_B . The L-B-J limit is also shown in figure 5.18 indicating sub-optimal performance for all tip speed ratios investigated. The axial interference factor variation with radial position increases with tip speed ratio. Whilst the spanwise interference factor variation is minimal for the lowest tip speed ratio of $\lambda = 4$, the rotor at this λ has little influence on the flow. The rotor thrust coefficient can be estimated from equation 10.13. The rotor loading for the three tip speed ratios are summarised in table 5.1.

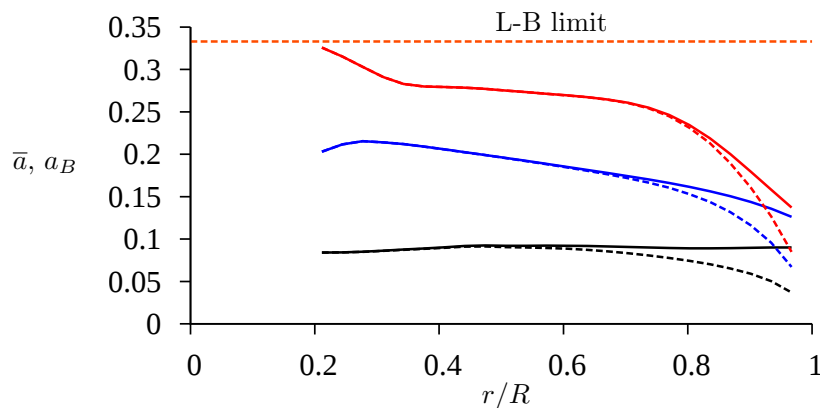


FIGURE 5.18: Axial interference factor distributions, $\bar{a}(r)$ (solid line), $a_B(r)$ (dashed line) as determined by a BEM analysis for the three tip speed ratios. black: $\lambda = 4$, blue: $\lambda_{d,f-s}$, red: $\lambda = 10$.

The full field PIV results can be compared against the BEM predictions. However, as data was only captured in the near wake, the velocity profile in the far wake is not available. Thus, the axial interference factor in the wake cannot be calculated directly from 1D momentum theory. Likewise, velocity measurements in the rotor plane are complicated due to the presence of the rotating blades. An alternate method to calculate the axial interference factor in the rotor plane is to assume the wake rotation and hence tangential interference factor is small. As the tip vortex advects downstream at the velocity at the blade trailing edge, the axial interference factor can be calculated from a velocity diagram of the blade crossing the plane of rotation, as shown in figure 10.3. The helix skew angle is equated to the angle the relative velocity, U_{rel} , makes with the plane of rotation, ϕ , as shown in equation 5.2.

$$\tan \phi = \frac{h}{2\pi r} = \frac{U_\infty(1 - \bar{a})}{\Omega R(1 + \bar{a}_t)} \quad (5.2)$$

Due to the pressure recovery occurring in the near wake, the pitch and vortex filament radius vary with vortex age. The upwind phase-locked averaged results at a vortex age of 120° were used in the analysis. Equation 5.2 can be simplified to produce a relation for the

axial interference factor at the tip, $\bar{a}(R) = 1 - \lambda \frac{h}{2\pi R}$. The pitch of the tip vortices determined from the PIV results was used to calculate the axial interference factor, $\overline{a_{\phi, \text{PIV}}}$ at the tip. The phase averaged axial interference factor from the PIV results, $\overline{a_{\phi, \text{PIV}}}$, compares acceptably well with the BEM results. The largest discrepancy arises at the lowest tip speed ratio, where the assumption of negligible tangential induction is hard to justify.

The tangential interference factor provides an estimate of the wake rotation immediately downstream of the rotor. Wake rotation is viewed as an energy loss as the inlet kinetic energy is converted to an azimuthal velocity component rather than mechanical energy. The azimuthal velocity component ceases closer to the rotor plane compared to the axial velocity deficit (Aubrun et al. 2010).

The average tangential interference factor distribution, $\bar{a}_t(r)$ and that corrected for a finite number of blades is shown in figure 5.19. $\bar{a}_t(r)$ increases with a reduction in λ . This is due to the increase in tangential force production (more energy lost to wake rotation) with reducing tip speed ratio. As the freestream contains no rotation, the tangential interference factor implicitly indicates the amount of wake rotation. $\bar{a}_t < 0$ for the largest tip speed ratio ($\lambda = 10$) indicating energy is added to the wake at some spanwise locations.

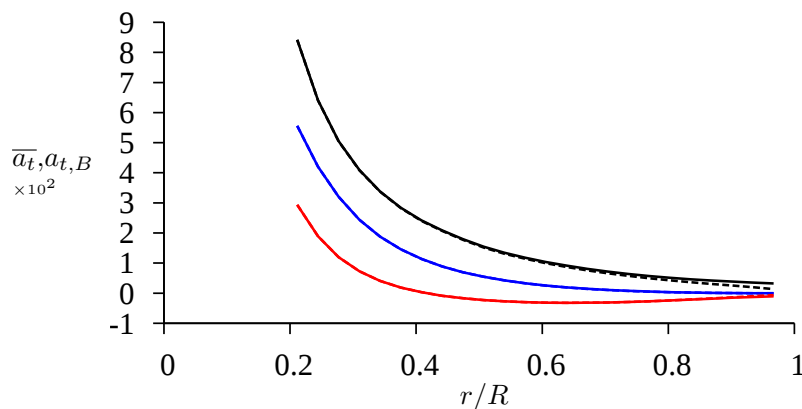


FIGURE 5.19: Tangential interference factor distributions, $\bar{a}_t(r)$ (solid line) and $a_{t,B}(r)$ (dashed line) as determined by a BEM analysis for the three λ . black: $\lambda = 4$, blue: $\lambda_{d,f-s}$, red: $\lambda = 10$.

The rotating blades generate a lift force and hence circulation which is shed into the wake to form the tip and root vortices. The trailing vortex system of a planar wing can be determined by lifting-line theory due to Prandtl and described in (Betz 1935). $\Gamma_B(r)$, is determined by applying the Kutta–Joukowski (K-J) theorem, shown in equation 4.2 to each annular segment. The K-J theorem enforces trailing edge separation such that the results will contain increasingly larger uncertainty with the advancing separation point toward the leading edge.

λ	$\langle \bar{a} \rangle$	$a_{\bar{\phi},PIV}^-$	$\langle \bar{a}_t \rangle$	$a_{t,root}$	$\langle \Gamma_B/RU_\infty \rangle$	$\Gamma_{V,PIV}/RU_\infty$	C_T
4	0.080	0.14	0.019	0.084	0.068	0.073 (0.064)	0.293
4	0.131	-	0.030	0.103	0.108	-	0.452
7	0.175	0.176	0.010	0.056	0.079	0.044 (0.073)	0.571
7.07	0.343	-	0.023	0.010	0.122	-	0.890
10	0.251	0.293	0.001	0.029	0.076	0.079 (0.089)	0.739
10	0.473	-	0.012	0.051	0.100	-	1.071

TABLE 5.1: BEM and PIV analysis of the experimental model in an upwind configuration and full-scale Tjæreborg wind turbine (**bold text**). $\langle \bar{a} \rangle$: average axial interference factor, $a_{\bar{\phi},PIV}^-$: axial interference factor from PIV results as determined from equation 5.2, $\langle \bar{a}_t \rangle$: average tangential interference factor, $a_{t,root}$: root region ($x/R = 0.21$) tangential interference factor, $\langle \Gamma_B/RU_\infty \rangle$: normalized average blade bound circulation, $\Gamma_{V,PIV} = |\Gamma_T| + |\Gamma_R|$: sum of normalised circulation in the tip and root vortices at 120° (downwind results in brackets), C_T : thrust coefficient.

$\Gamma_B(r)$ is important as its gradient, $\partial\Gamma_B(r)/\partial r$, determines the strength of the trailing vortex system (Betz 1935). The uniformity of the wake can thus be determined from $\Gamma_B(r)$ as shown in figure 5.20. With a uniform distribution of blade bound circulation and applying a zero loading ($\Gamma_B = 0$) condition at the tip and root, the strength of the tip and root vortices are the mean of the blade bound circulation (Ivanell et al. 2009). However, figure 5.20 shows $\Gamma_B(r)$ varies across the span for each λ investigated. $\Gamma_B(r)$ is maximum at the design tip speed ratio for both the full-scale and experimental model. The full-scale circulation values correspond well to LES computations of the Tjæreborg wind turbine (Ivanell et al. 2009).

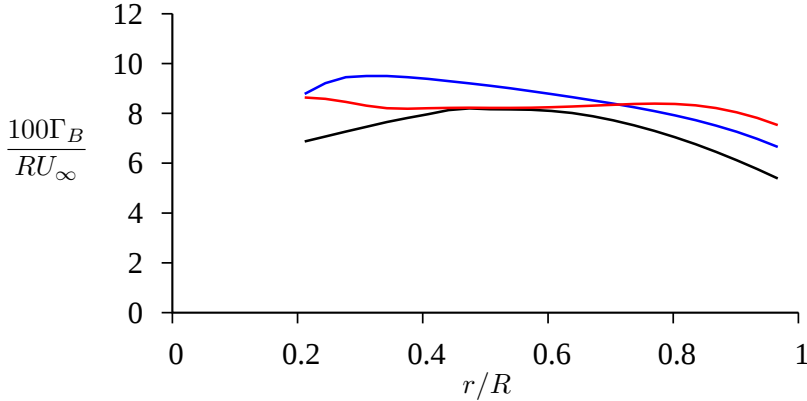


FIGURE 5.20: Dimensionless blade bound circulation distribution, $100\Gamma_B(r)/RU_\infty$ as determined by a BEM analysis and the K-J theorem for the three tip speed ratios. black: $\lambda = 4$, blue: $\lambda_{d,f-s}$, red: $\lambda = 10$.

Table 5.1 shows the sub optimum performance of the experimental model compared to the full-scale turbine. It is clear that the NACA4412 airfoil at this Reynolds number does not operate efficiently (low C_l/C_d ratio), which should be considered when devising low Reynolds number experiments to investigate wind turbine performance.

5.0.4 Vortex Properties

Here the tip and root vortices shed into the wake by the three bladed model wind turbine are characterised in an attempt to gain a deeper knowledge into their structure.

Figure 5.21 shows several high resolution ($MF = 78$ px/mm) phase-locked average field quantities created by a tip vortex at a vortex age of 120° generated at $\lambda_{d,f-s}$. The average induced axial ($\overline{\mathbf{u}'}$) and radial ($\overline{\mathbf{v}'}$) velocity fields are shown in figures 5.21a) and 5.21b). The contour lines in figure 5.21 represent ω_z which is also shown individually in figure 5.21c). The contour levels are the same as those in figure 5.11.

The vorticity and the Reynolds stress fields shown in figures 5.21d),e) and f) reveal a tail attached to the tip vortex in a similar fashion to the fixed wing results presented in chapter 4. This is the remnants of the trailing edge vorticity sheet which has not yet been entrained by the tip vortex. The longitudinal $\overline{u'^2}/U_\infty^2$ and vertical $\overline{v'^2}/U_\infty^2$ components are largest in the vortex core. A laminar axi-symmetric vortex has zero Reynolds stresses at the vortex centre. The Reynolds stress components at the vortex centre are evidence of vortex meander. The Reynolds stress fields are consistent with those of meandering fixed wing trailing vortices measured by Heyes et al. (2004). Vortex meander is investigated in section 5.0.5. The vorticity contour lines reveal there is some gradient quantity dependence on the magnification factor. However, it is important to note that vortex locations are accurately determined irrespective of magnification factor. As the focus of the research here was the interaction between the tip and root vortices, a large field of view is required. Vortex properties therefore are determined from the phase-locked average fields presented in figures 5.11 through to 5.14.

Using the data processing schemes outlined in chapter 3, the circulations of the phase-locked average tip and root vortices were calculated. The variation of the tip vortex circulation is shown on the left in figure 5.22. The root vortices are not shown due to the small number of realisations. The rapid cessation of the root vortex signal is addressed in section 5.0.6. There is considerable scatter in the tip vortex circulation values which is an indication of the turbulent nature of the wake. The $\lambda = 4$ results are the most consistent as vortex interaction appeared absent in the vorticity fields shown in figures 5.12 and 5.13.

Optimally in a uniformly loaded wing, *e.g.* in the Prandtl wing or Joukowski rotor, the circulation deduced from the integral, $\Gamma = \int_0^R \partial\Gamma_B(r)/\partial r$ should be completely contained within the tip and root vortices (Betz 1935). The average blade bound circulation, $\langle\Gamma_B(r)\rangle$, generated on the blades from a BEM analysis is indicated in table 5.1. The sum of the tip and root vortex circulation ($\Gamma_{V,PIV} = |\Gamma_T| + |\Gamma_R|$) at a vortex age of 120° is shown in table 5.1.

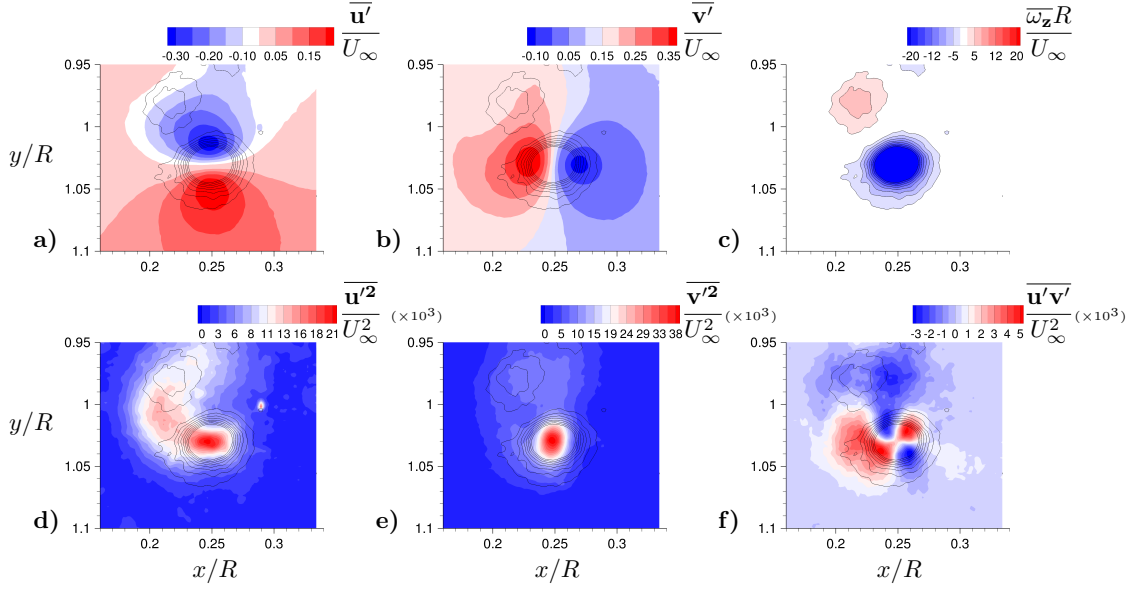


FIGURE 5.21: Vortex induced flow field parameters of a tip vortex at a vortex age of 120° , $\lambda_{d,f-s}$, $Re_c = 2900$, $MF = 78$ px/mm, upwind configuration. **a)** \bar{u}'/U_∞ , **b)** \bar{v}'/U_∞ , **c)** $\bar{w}_z R/U_\infty$, **d)** \bar{u}'^2/U_∞^2 , **e)** \bar{v}'^2/U_∞^2 , **f)** $\bar{u}'\bar{v}'/U_\infty^2$.

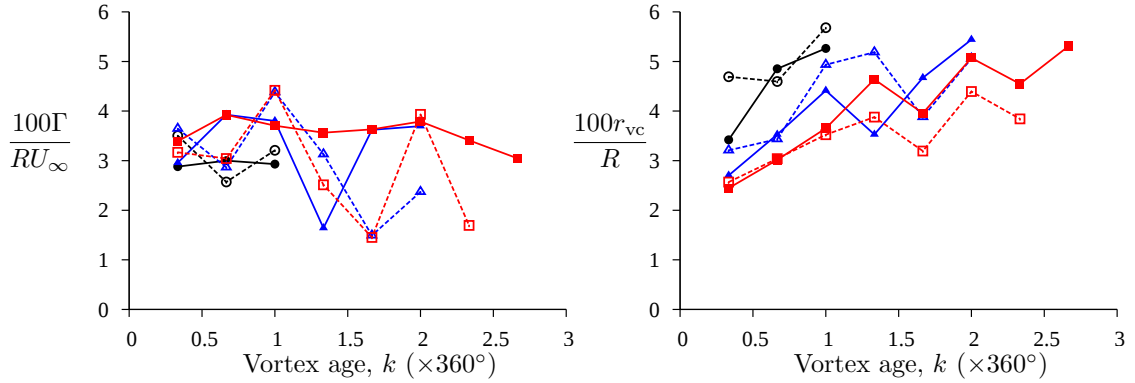


FIGURE 5.22: Tip vortex circulation, Γ , (left) and vortex core radius, r_{vc} , (right) variation with vortex age. Dashed lines and hollow symbols: downwind results, solid lines and symbols: upwind results. The black circles, blue triangles and red squares represent $\lambda = 4$, $\lambda_{d,f-s}$, and $\lambda = 10$ respectively.

The experimental results are approximately half that predicted by the BEM method and the LES computations of Ivanell et al. (2009) at $\lambda_{d,f-s}$ and $Re_c = 1.6 \times 10^3$. The difference between the BEM predictions and the experimental results arises from $\partial\Gamma_B(r)/\partial r$, shown implicitly in figure 5.20. The blade wakes visualised in figures 5.10 to 5.15 are also evidence of the continual shedding of vorticity into the wake. With downstream distance the blade wakes will be entrained by the tip and root vortices or diffused to the background flow.

There could also be an affect due to differences between the low Reynolds number performance of the current airfoil profile (NACA4412) and that used in the Sunada and Kawachi

study (Wortmann FX63-137). In addition, the airfoil properties used in the BEM analysis are not corrected for 3D effects (Sørensen 2011) and it is known that airfoil performance increases with 3D effects especially in stalled regions. Figure 5.17 indicated the percentage of the blade experiencing stall in the root region increases from $0.15R$ to $0.47R$ when λ reduces from 10 to 4. Ivanell et al.'s (2009) results indicated the wake circulation derived from the velocity field agreed well with blade bound circulation when the circulation integral was performed on a plane perpendicular to the freestream, *i.e.* a y - z plane. This analysis technique could not be used here due to the orientation of the measurement plane, *i.e.* x - y as in figure 8.12.

At the low experimental Reynolds numbers, the vortex core radius, r_{vc} , increases by viscous and turbulent diffusion. The right of figure 5.22 shows the variation in r_{vc} with vortex age. The vortex core radius increases quite linearly prior to the onset of vortex interaction. Figure 5.22 also suggests the vortex core radius reduces with increasing tip speed ratio. This can be partially explained by figure 5.17. As λ increases, $\alpha(R)$ decreases. The blades are thus more likely to operate in the attached regime minimising separation over the blades. The vorticity sheet shed into the wake will be more uniform allowing it to roll up into a tight vortex with a smaller core radius.

The results in this section showed how the tip and root vortex properties evolved in the wake. The following section investigates the meandering motions of the tip and root vortices.

5.0.5 Vortex meander

The results in chapter 4 showed fixed wing tip vortices also meander at low Reynolds numbers. The instantaneous vortex positions were shown to be accurately described by a normal distribution in a similar fashion at high Reynolds numbers (Devenport et al. 1996; Heyes et al. 2004; Roy 2008). Meander was shown to increase with blade angle of attack. Vortex meander in a multiple vortex system such as that in a wind turbine wake is more complex due to the helical nature of the vortex filaments and interaction between vortices. Vortex meander has been noted in wind turbine wake studies (Grant and Parkin 2000; Dobrev et al. 2008; Hu et al. 2012). Dobrev et al. (2008) proposed the increase in meander with vortex age is due to a helical vortex instability. However, meander of helical tip vortices in a wind turbine wake have not been characterised in a systematic fashion like fixed wing vortices to the authors knowledge. This section performs such a characterisation.

The vortex locations from each instantaneous PIV frame were extracted and compared to the temporal mean. Uncertainty in the instantaneous vortex identification using λ_{ci}^2 and the

centroid of area method is estimated as ± 4 pixels. A normal distribution is applied to the pdf of instantaneous positions in each measurement axis. Vortex meander is characterised by the normal distribution standard deviation, σ_i , at a given vortex age. The total uncertainty on the meander magnitude is then $\pm 6\%$.

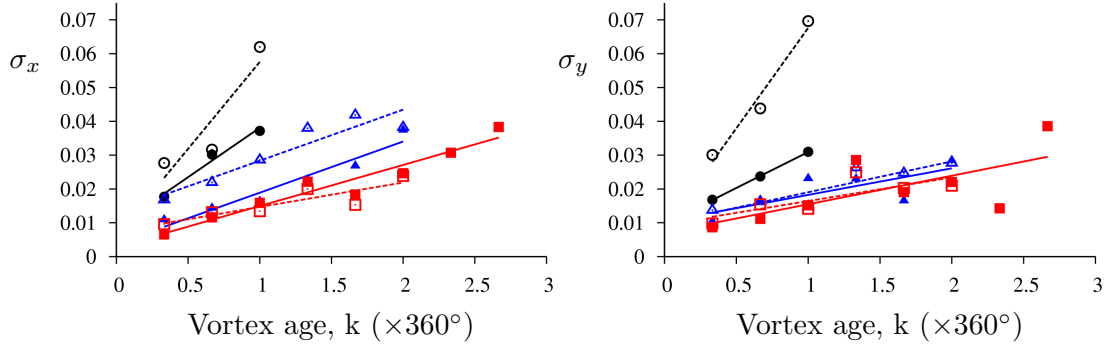


FIGURE 5.23: Streamwise and radial tip vortex meander increase with vortex age, dashed lines and hollow symbols - downwind results, solid lines and symbols - upwind results black lines: $\lambda = 4$, blue lines: $\lambda_{d,f-s}$, red lines: $\lambda = 10$

Vortex meander results for the 300 PIV realisations are presented in figure 5.23. The trendlines in figure 5.23 indicate that tip vortex meander increases with vortex age. Physically, increased vortex meander is a possible indication of instabilities which arise along the helix. The large deviations from the trend particularly evident in the $\lambda = 10$ case can be attributed to the wake becoming unstable past $VA > 360^\circ$. The trend lines indicate that a helical filament with a short helicoidal pitch is capable of resisting meander at early vortex ages. In a similar fashion to the vortex core radius results in figure 5.22, this can partially be attributed to the angle of attack in the tip region which reduces with increasing tip speed ratio. Figure 5.17 showed the angle of attack at the tip reduces from 13° to 5° when the tip speed ratio increases from 4 to 10. Attached flow in the tip region at higher tip speed ratios permits a more uniform (time invariant) pressure gradient between the pressure and suction airfoil surfaces to form. The PLIF visualisations in chapter 5 indicated K–H vortices form in the separated shear layer. These K–H vortices affect the tip vortex roll up process (vorticity entrainment) and will be a cause of meander as seen in the case of delta wing vortices (Gursul and Xie 2000). Thus in the absence of flow separation on the airfoil, tip vortex formation will be steady at early vortex ages and meander arising during the roll-up process will be minimised.

It should be noted that at early vortex ages, a gaussian distribution is a good fit to the pdf of the tip vortex position deviations. The method of Devenport et al. (1996) was

formulated for a single fixed-wing tip vortex. Such a vortex will only meander under its own influence or the aforementioned external influences. In a multi-vortex system such as a wind turbine wake, vortex meander is more complex due to the helical nature of the vortex filaments and the interaction between vortices within the wake. The induced velocity field of a single vortex acts as a perturbation to all other vortices in the field (via Biot-Savart law). Figure 5.20 indicated $\partial\Gamma_B(r)/\partial r \neq 0$ across the entire span resulting in creation of a continuous vorticity sheet between the tip and root vortices. The blade wakes complicate the interaction of the large scale vortices further. Thus, it is not surprising that as the vortex age increases, the gaussian fit becomes less robust due to the likelihood of vortex interaction. The blade wake occur due to the geometrical scaling and minimum blade twist. On the other hand, the optimum Glauert rotor was designed to minimise $\partial\Gamma_B(r)/\partial r$. Further analysis of tip and root vortex meander in a wind turbine wake is presented in chapter 6.

5.0.6 Root vortex behaviour

This section outlines the influences that lead to the rapid diffusion/destruction of the root vortex. The interaction of the rotating blades and the turbine support structures with the fluid make the flow in the root region of a wind turbine highly complex (Zahle and Sørensen 2011). The approaching flow interacts with the rotating nose cone and a 3D boundary layer forms. In an upwind turbine configuration the boundary layer is then stretched around the root section of the blades with an analogy to a fixed cylinder on a ground plate. A horseshoe vortex system progresses downstream with helical symmetry. Ebert and Wood, however, showed this vortex structure is cancelled by the root vortex quickly due to the angular momentum imparted by the rotating blades (Ebert and Wood 2001). In addition, on most full-scale turbines (the Enercon E-126 is an exception), the blade lifting surface terminates prior to the rotational axis to ensure they remain rigid. Zahle and Sørensen (2011) showed that cylindrical blade sections generate a von-Kármán vortex street.

Particle streak flow visualisations also highlighted a flow feature of the experimental model that may not feature on full-scale turbines. The visualisations were captured at a sample rate of 100 Hz with camera 3 in table 3.1 in conjunction with a green continuous wave laser of wavelength 532 nm. As found on a number of full-scale turbine models, the experimental model had a small gap between the rotor assembly and the nacelle. This is typically disregarded in numerical simulations (Masson and Smaïli 2006; Ameer et al. 2011; Zahle and Sørensen 2011). However, this gap produced a rotating cavity flow that was periodically

expelled when a root vortex passed the gap. Figure 5.24 shows the advection of a root vortex downstream in a 120° segment of the wake. The flow is from left to right with the blade rotation in a counter-clockwise direction when viewed from upstream. The labels ‘rv1’ and ‘rv2’ indicate the position of root vortices within the field of view. The streaklines of the root vortices do not form closed loops as the vortex axis is not aligned with the image plane due to the skew angle of the wake. Furthermore, the root vortex advects at a different velocity to the flow field due to the axial induction produced by the blades. The label ‘rc’ and the white circles denote the rotating cavity flow which is expelled with a passage of a root vortex. Expanded views of the cavity region are shown in the views below the main images. The rotating cavity flow is most visible in images C and D when the phase of the blade is not aligned with the measurement plane. The cavity flow rotation is of opposite orientation to that of the root vortex, which will destabilise the root vortex. The label ‘rr’ indicates the recirculation region downstream of the nacelle as indicated by the dashed contour line in figures 5.4, 5.5 and 5.6.

Coherent root vortices can be seen in figures 5.10, through to 5.15 at early vortex ages depending on tip speed ratio ($VA \leq 360^\circ$), but the signal weakens soon after. The root vortex core to filament radius ratio, r_{vc}/R_r , is larger than the tip vortex value which causes an increase in the amplification rate of the mutual inductance instability mode leading to earlier breakdown (Widnall 1972). The numerical study by Ivanell et al. (2009) indicated that the small radius of curvature of the root vortex helix and the close proximity of adjacent helix turns are the primary reasons for instabilities arising in the root vortex signal. As in the current results, the root vortices became unstable prior to the tip vortices (Ivanell et al. 2009). Felli et al. (2011), however, showed using flow visualisations, that for a propeller wake, the root vortex transitions to instability due to a perturbation caused by an unstable tip vortex (*i.e.* after the tip vortex). In addition to the previously mentioned causes of the early onset of instabilities arising in the root vortex, helical vortex filaments emanating from field turbines and scale experimental models will also be affected by the turbine support structures.

The rapid destabilisation of the root vortices in an upwind turbine wake is postulated to be primarily due to three phenomena. Firstly, the root vortices are in close proximity to the nacelle boundary layer, secondly, the root vortex must interact with the tower section and lastly the root vortices envelope the low velocity fluid in the central wake region immediately downstream of the nacelle. Operating the model turbine in a downwind configuration allowed decoupling of the root vortex tower interaction phenomena, hence the root vortices shed

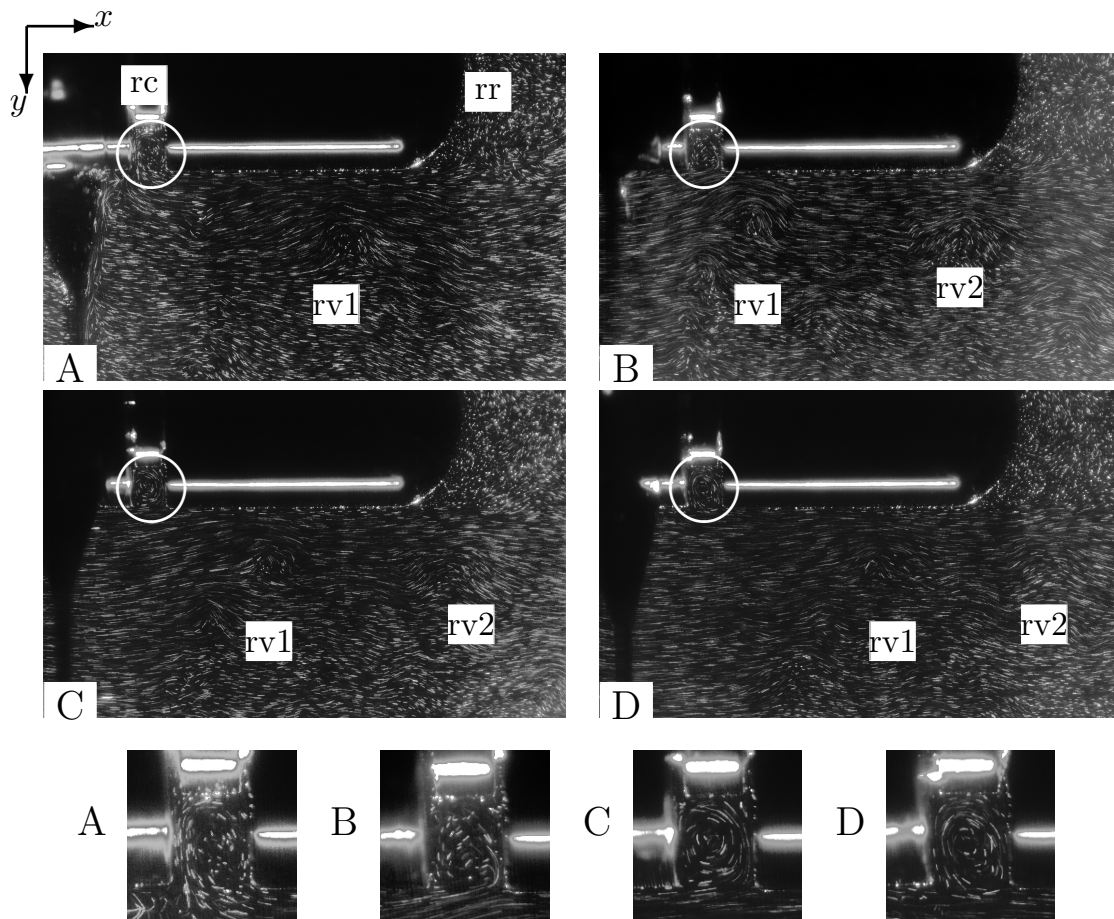


FIGURE 5.24: Particle streak flow visualisation sequence in the x - y plane (120° progression A–D) showing blade passage, rotating cavity flow (below rc marker and white circles), root vortex (above rv1 and rv2 markers) passage and recirculation region (marker rr) behind nacelle. Bottom images, expanded view of white circle regions. Flow from left to right, $\lambda_{d,f-s}, Re_c = 2900$, particle streak lengths show qualitative instantaneous velocities.

in a downwind turbine configuration are subjected to the first and third phenomena only. As upwind turbines are the most prevalent installed turbine, the three effects will now be discussed further in terms of an upwind turbine configuration.

5.0.6.1 Nacelle boundary layer vorticity

The vorticity created within the nacelle boundary layer is shown immediately adjacent to the nacelle in figures 5.10, through to 5.15. It is of the same order of magnitude and opposite in sign to the coherent root vortices, meaning there will be cross-annihilation of vorticity at the vortex core boundaries. Ebert and Wood (2001) showed through axial vorticity contours in the very near wake, that the root vortices of their experimental model merged into a single columnar ‘hub’ vortex centered on the rotational axis. The merging occurred in a shorter distance with increasing tip speed ratio. Zahle and Sørensen (2011) on the other hand, found

the flow in the nacelle region to be highly complex and dependent on the flow speed and yaw angle. In their simulations of a full-scale turbine, axial vorticity contours at the end of the nacelle ($x/R = 0.36$) showed the nacelle boundary layer and three counter rotating vortices per blade. The three vortices correspond to the root vortex and the von-Kármán vortices from the cylindrical sections of the blade in the root region. The lifting surface terminated prior to the rotational axis in the Zahle and Sørensen (2011) study, which was not the case in the model of Ebert and Wood (2001). Zahle and Sørensen (2011) noted the three vortices interact causing high velocity gradients in the root region. However, no information was presented on how they evolve. The presence of an equivalent ‘hub’ vortex to the Ebert and Wood (2001) study cannot be realised here due to the orientation of the planar experimental technique.

5.0.6.2 Root vortex tower interaction

Due to the small radius of curvature of the helix of the root vortex, the root vortices will be affected by their interaction with the tower section, here denoted as root vortex-tower interaction (RVTI). The root vortex cannot pass the tower section unaltered. This interaction will create a perturbation in the root vortex possibly leading to an instability and early breakdown. The onset of RVTI can be estimated by simulating the theoretical helical pathline (simple helix) of the root vortex core location using parameters obtained from the experimental data, namely h and R_r .

With counter clockwise rotation of the blades, the helical vortical filaments follow a clockwise pathline, thus creating a right-handed helix. The parametric equation of such a helix (single line vortex) is shown in equation 5.3,

$$\mathbf{r}(t) = R_r \cos(t - \psi)\mathbf{i} + R_r \sin(t - \psi)\mathbf{j} + h_r t/2\pi\mathbf{k} \quad (5.3)$$

where $t \in [0, 2\pi)$, ψ is the phase angle of the blade, h_r is the helicoidal pitch of the root vortex helix and the unit vector \mathbf{k} (part of a right handed coordinate system) is aligned with the positive x -axis consistent with figure 8.12. The blade phase angle ψ is relative to the y -axis. Letting d be the axial distance between the blade trailing edge and tower section geometry, the phase angle of the blade, ψ_o , at which the root vortex first interacts with the tower section can be determined from equation 5.4,

$$\psi_o = \pi(1 - m) + C, \quad m \subset 0, 2, 4 \dots \quad (5.4)$$

where the constant $C = 2\pi d/h_r$ depends on the turbine and helix geometries.

The R_r and h_r values were taken at a vortex age of 120° as they varied with vortex age. R_r generally increased and h_r decreased with vortex age. The vortical wake of a B bladed turbine contains B root vortices out of phase by $2N_b\pi/B$, where N_b is the blade number (*i.e.* $N_b \in \{0, 1, \dots, B\}$). Therefore RVTI effects will be first seen in the image plane (x - y axis) for the phase angle where $\psi_f = \psi_o - 2b\pi/n$ is a minimum positive number.

However, this analysis assumes the perturbation is transported at the rate of the rotating blades (ΩR_r). From the BEM results shown in table 5.1, the local tangential interference factor in the root section of the blades, $a_t(0.21)$, is small with $0.029 < a_{t,\text{root}} < 0.084$. Therefore, the effects of RVTI are unlikely to be seen in the current data.

5.0.6.3 Central wake region

At axial locations greater than the length of the nacelle, the root vortices are subjected to the low velocity fluid immediately downstream of the nacelle section. This region is visible in figure 5.24, indicated by ‘rr’. Flow visualisations indicated this region is highly turbulent and 3D due to the pulsatile inflow created by the rotating blades. There is also momentum transfer occurring between the outer regions of the wake and the central wake region. The three dimensionality and the turbulent nature of the fluid in this region promotes instabilities leading to breakdown of the coherent root vortex structures.

5.0.7 Root vortex destabilisation

It has been shown that the root vortex lies in close proximity to numerous factors which could cause its destabilisation. In addition to the instability modes affecting helical vortex filaments (Widnall 1972), three additional mechanisms for their rapid destabilisation were proposed. Root vortex tower interaction (RVTI) will occur in the bottom half of the wake ($y/R \leq 0$) causing rapid vortex destabilisation. RVTI effects were not imaged in the current field of view due to the small tangential induction created by the blades. The effect of RVTI is investigated further in chapter 6.

The rapid destruction of the root vortices seen in figures 5.10, 5.11, 5.13 and 5.15 can thus be attributed to the presence of vorticity of opposite sign within the nacelle boundary layer and the turbulent central wake region. The turbine was tested in downwind configuration to displace the effect of cross-annihilation of root vortex vorticity by the nacelle boundary layer vorticity. However, the root vortices in the downwind (figure 5.10) and upwind (figure 5.11) configurations persist to a similar axial extent ($x/R \sim 0.6$) suggesting that cross-annihilation of vorticity is of secondary importance to the central wake region fluid. Panel-code simulations

by Micallef et al. (2011) showed the root vortex exists across their entire domain ($x/D \leq 0.6R$). The fluid within the central wake region had no effect on the root vortices because the length of the nacelle was greater than $x/D \leq 0.6R$.

The root vortices in a wind turbine wake are destabilised by a multitude of mechanisms possibly including the three instability modes affecting helical vortex filaments (Widnall 1972) and the three additional mechanisms outlined in this section. Results from the present experimental model suggest that the central wake region is a dominant mechanism leading to root vortex destabilisation.

5.1 Summary of the geometrically scaled rotor wake data

In this chapter, the wake structure of a model horizontal axis wind turbine based on the Tjæreborg field turbine has been investigated. Three tip speed ratios were investigated corresponding to a lightly loaded, design load and heavily loaded full scale rotor condition. However, a BEM analysis revealed the sub-optimal performance of the experimental model compared to that of the fullscale turbine. This is due to the reduced aerodynamic performance of the blade airfoil section at the experimental Reynolds number. Further, geometric scaling leads to a very small tip chord which consequently resulted in small weak tip and root vortices. In addition to the weak strength of the vortices, the minimal blade twist created large regions of separated flow leading to a wake containing many regions of vorticity. It may be concluded that geometrically scaled rotors are unsuitable for vortex stability studies in the wake of HAWTs.

The current chapter highlighted the coupling between blade aerodynamics and near wake structure. It is thus advisable to consider airfoil performance when designing low Reynolds number rotary or fixed wing experiments. In the following chapter a purposely designed wind turbine rotor for the low Reynolds number experimental conditions is tested. The results highlight necessary rotor design considerations to allow investigation of the stability of helical vortices in a HAWT wake accurately. These include minimal spanwise circulation gradient and minimal separated flow regions.

Chapter 6

Wake Structure of an Optimum Glauert Rotor

This chapter investigates the near wake evolution of an optimum Glauert rotor at two tip speed ratios. The wake is more uniform compared to the geometrically scaled rotor. The three-blade turbine wake is found to be unstable for the tip speed ratios investigated. The mechanisms leading to wake instability are discussed. Breakdown of the vortices is beneficial in a wind farm siting sense but turbines should not be placed near where breakdown occurs. A stable helical vortex filament configuration is achieved by removing two blades. The evolution of the tip and root vortices is determined by evaluating vortex properties such as maximum swirl velocity, meander magnitude, circulation and vortex radius.

6.0.1 Tip speed regulation has no effect on wake structure at runaway

The tip speed regulation method is first investigated to justify driving the turbine. Full scale wind turbines rotate by the aerodynamic forces generated along the blade span. Model wind turbines in wind tunnel facilities regulate λ in an analogous manner to full scale. A pneumatic (Ebert and Wood 2002) or electrical load (Medici and Alfredsson 2006) on the generator attached to the drive shaft reduces the turbine rotation rate. The control of wind turbines in water channel facilities by an electrical load is difficult due to the conductivity of the working fluid. To overcome this issue, the models were driven by an external motor to regulate λ . This method of λ regulation is commonly employed in water channel facilities (Whale 1996; Mikkelsen et al. 2011). The major benefit of regulating the tip speed ratio is direct control of h . It will be shown the near wake is insensitive to the driving mechanism.

The rotor was allowed to freely rotate (free case) at its runaway tip speed ratio, denoted λ_R . Turbine runaway occurs at full scale when the load on the main shaft ceases often with catastrophic but spectacular consequences. Turbine runaway is a balance between the

aerodynamic forces generated by the blades and friction within the turbine system. In the runaway state, net power (after friction) transferred to the blades by the fluid is balanced the angular momentum contained in the tip and root vortices (Ebert and Wood 2002). Turbine thrust loading, C_T , and wake expansion are maximum at turbine runaway (Ebert and Wood 2002). Friction was minimised in the model by using a teflon sleeve bearing.

Despite the low friction value of teflon, the fluid layer between the main shaft and teflon sleeve bearing creates a braking torque limiting λ_R . The static braking torque was estimated in air by a mass-pulley system and equation 6.1,

$$\frac{F_A}{F_R} = e^{\mu_f \theta_l}, \quad (6.1)$$

where the applied and resistive forces are F_A and F_R respectively (N), the coefficient of friction, μ_f , between the pulley and fishing line was assumed to be 0.04 and the lap angle, θ_l , about the pulley was 90° .

The maximum weight the blade could sustain was 1.4g giving $F_R = 12.897 \times 10^{-3}$ N. The static breaking torque with a blade radius of 0.115 m was thus $T_s = 1.48 \times 10^{-3}$ Nm. The dynamic friction torque, T_f , was estimated using Petroff's equation and Raimondi–Boyd charts (Shigley et al. 2004). The dynamic friction torque for the current experimental model was determined to be $T_f = 2.67 \times 10^{-6}$ Nm.

The model rotational speeds in the free and drive cases were measured by the optical encoders outlined in chapter 3. The optical encoder in the free case was placed in the turbine tower. The flow between the two cases is thus entirely dependent on the flow over the airfoil.

The tip speed ratio variation is larger in the free case due to a sloshing motion in the water channel facility. An example of the tip speed ratio fluctuations behind the two cases is shown in figure 6.1. The frequency of the λ variability is approximately equal to the channel sloshing frequency. The water channel sloshing has a direct impact on the rotational rate of the turbine as it reacts to the U_∞ fluctuations, like a full-scale turbine. The small T_s and T_f values highlight the difficulty to regulate the tip speed ratio of a freely spinning turbine with a mechanical brake.

The U_∞ variation causes the blades of the driven turbine to operate over a greater angle of attack range. Force generation by the blades thus varies per rotation. Ignoring the induced velocities for simplicity, the angle of attack range due to freestream velocity variations can be calculated from equation 6.2,

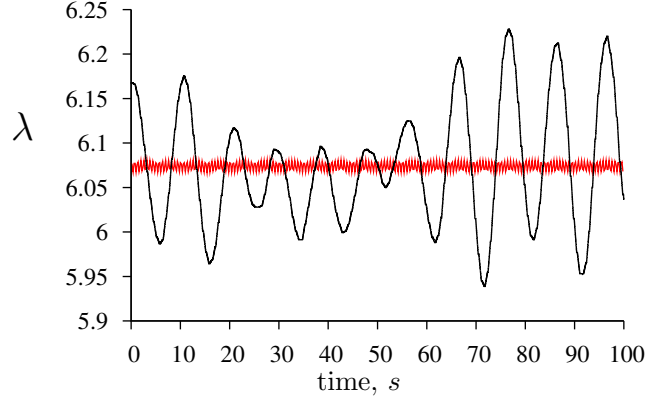


FIGURE 6.1: Sample encoder traces for the drive (red) and free (black) cases showing the periodic variation in free case due to a sloshing motion in the water channel.

$$\alpha(r) = \tan^{-1} \left[(\lambda(r) \pm \sigma_\lambda)^{-1} \right] - \theta(r), \quad (6.2)$$

where σ_λ is the measured tip speed ratio standard deviation in the free case. An example α range for the drive case is $\alpha = \alpha_d \pm 0.13^\circ$, so its effect on load production will be minimal. Blade bound circulation will be approximately equal but greater spatial smoothing will arise due to tip speed ratio variability.

The phase-locked average near wake velocity fields for the drive and free cases are shown on the top and bottom of figure 6.2. U_∞ is from left to right with the turbine spinning in a counter-clockwise direction when viewed from upstream. The contour levels have been kept consistent with chapter 5. The tip speed regulation can be said to have no effect on the wake structure.

The vortical wake of the drive and free cases at λ_R are shown in figure 6.3. The dominant vortical structures, *i.e.* tip and root vortices in the near wake are clearly evident. Importantly, with careful model design, a counter rotating helical vortex pair consisting of a tip and root vortex can co-exist in a wind turbine wake prior to onset of instabilities and vortex degeneration. The similarity between the two cases is clearly evident.

This short investigation revealed the tip speed regulation method has no effect on near wake structure at λ_R . With proper analysis of the fluid forces acting on the rotating blades, driving the turbine to regulate the tip speed ratio allows direct control over the helicoidal pitch, a key parameter in the stability of the vortices in a HAWT wake. In addition, counter rotating helical vortex pairs are produced at λ_R . The tip and root vortices at λ_R are characterised in section 6.0.11. First though, the general wake structure of the optimum Glauert turbine operating at its design tip speed ratio is presented in the following section.

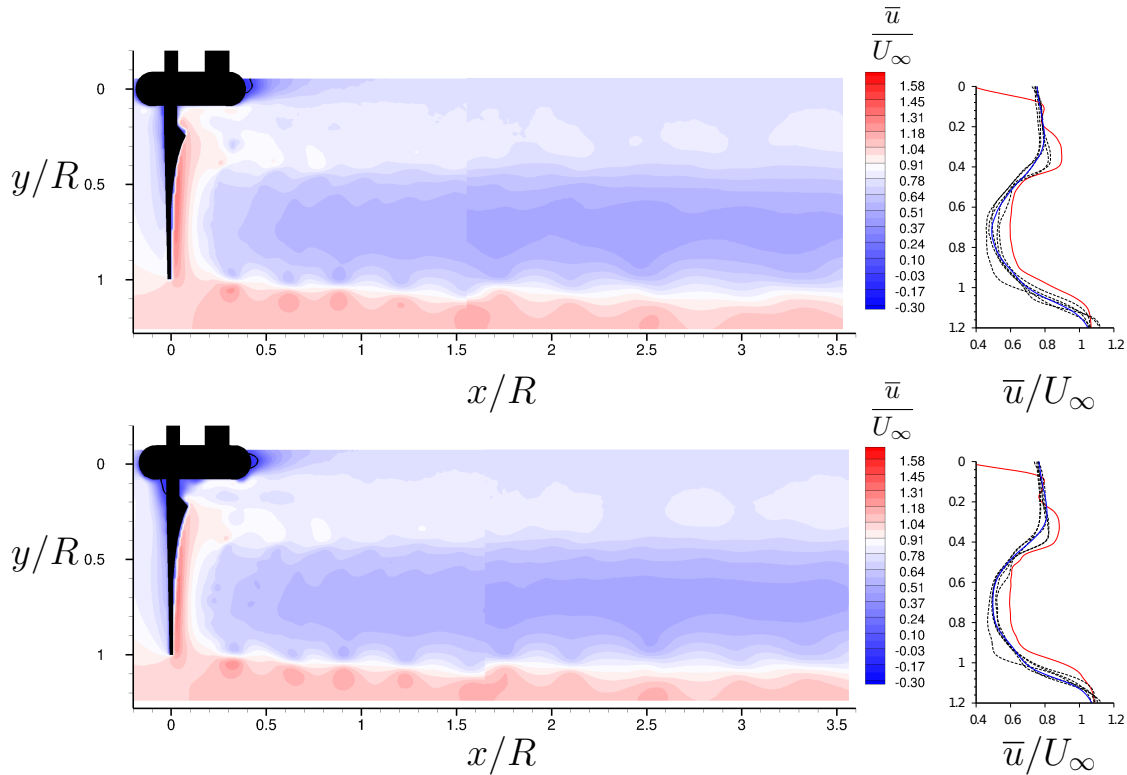


FIGURE 6.2: Near wake velocity field of a driven (top) and freely spinning (bottom) optimum Glauert rotor at a runaway tip speed ratio of $\lambda_R = 6.07$, $U_\infty = 0.2\text{m/s}$, $Re_{c(R)} = 14.187 \times 10^3$. Freestream flow is from left to right, contours of non-dimensionalised streamwise velocity, \bar{u}/U_∞ . Velocity gradients due to tip and root vortices are clearly visible and persist for some distance.

6.0.2 Phase averaged wake structure

The detailed design process for the optimum Glauert rotor was presented in chapter 3. The rotor attempts to achieve dynamic similarity between model and full scale. The average wake structure is investigated and compared against the design criteria. In the absence of direct force measurements, rotor loading is estimated using vortex sheet theory (VST) (Johnson 1980) and 1D momentum theory. Rotor loading at several investigated tip speed ratios is compared to a BEM analysis in the following section.

6.0.3 BEM analysis of rotor

The lift to drag properties of the Jacobs and Sherman (1937) airfoil data at $Re_c = 42.1 \times 10^3$, $C_l/C_d \sim 25$, recommended $\lambda_d = 3.75$ based on figure 3.17. The optimum Glauert rotor was designed using this tip speed ratio. However, it will be shown the chord Reynolds number is always less than the airfoil performance data. As a conservative estimate, the turbine was tested primarily at or near $\lambda = 3.5$. $\lambda = 3.5$ is thus referred to the design tip speed ratio, λ_d . The BEM analysis was undertaken over the tip speed ratio range $2.0 \leq \lambda \leq 6.0$.

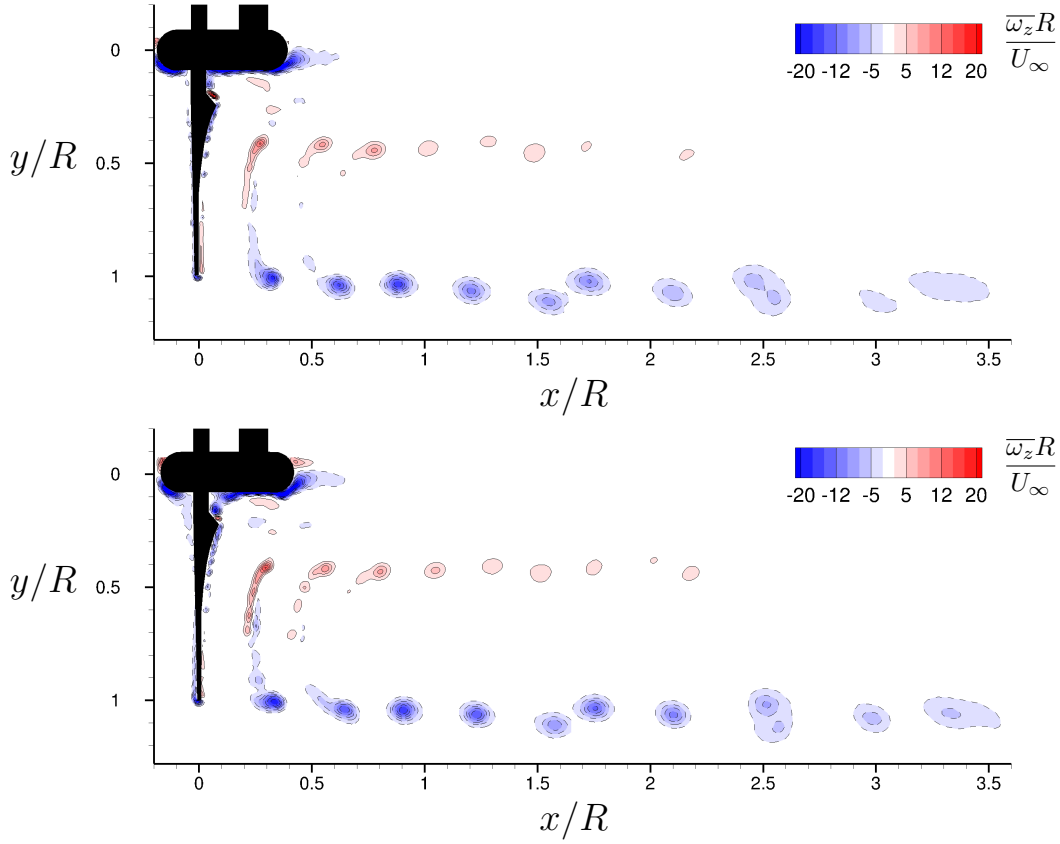


FIGURE 6.3: Vortical wake of a driven (top) and freely spinning (bottom) optimum Glauert rotor at a runaway tip speed ratio of $\lambda_R = 6.07$, $U_\infty = 0.2\text{m/s}$, $Re_{c(R)} = 14.187 \times 10^3$. Contours of non-dimensionalised out of plane vorticity, $\overline{\omega_z}R/U_\infty$. Tip and root vortices are clearly visible in the wake and persist for some distance.

The geometrically scaled blade suffered from separation due to the minimal blade twist. The design angle of attack of the Glauert rotor was $\alpha = 6^\circ$. The angle of attack (AOA) distribution, $\alpha(r)$ is shown in figure 6.4. The solid blue, red and black lines represent the design, λ_d , the runaway, $\lambda_R = 6.0$ and a low $\lambda = 2.0$ tip speed ratio. The black region indicates the location of the nacelle. Although no PIV data was taken at $\lambda = 2.0$, this case is included to illustrate rotor performance of a stall regulated turbine in high winds. The black dashed lines represent 0.5 increments in λ . The orange dashed line represents the blade twist angle, $\theta(r)$. The design tip speed ratio maintains an angle of attack of $\bar{\alpha} = 7.5^\circ$. This α is on the border of the linear and early stall regimes as shown in figure 3.18 in chapter 3.

For $\lambda < \lambda_d$, the blade operates in the early stall and post-stall regions reducing applicability of the optimum blade assumptions (*i.e.* $\mathbf{w} \perp \mathbf{U}_{\text{rel}}$, see appendix 10). The plateau of the $\lambda = 2.0$ results for $r/R \leq 0.5$, arises due to the range of available airfoil performance data, $-6.6^\circ \leq \alpha \leq 27.2^\circ$ (Jacobs and Sherman 1937). Conversely, α reduces for $\lambda > \lambda_d$ as U_{rel}

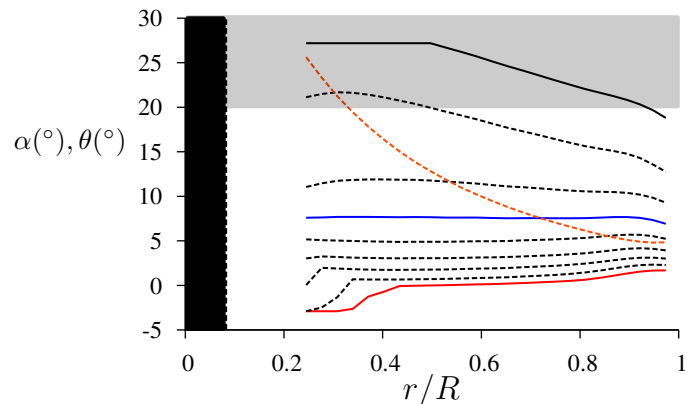


FIGURE 6.4: Blade AOA variation with tip speed ratio range ($2.0 \leq \lambda \leq 6.07$) and spanwise location. blue: $\lambda_d = 3.50$, red: $\lambda_R = 6.07$, black: $\lambda = 2.00$. Dashed black lines indicate $\lambda = 0.5$ increments. The shaded area indicates region where leading edge separation likely from static flow visualisations presented in chapter 4. The black region indicates the nacelle location.

increases. The NACA4412 airfoil profile maintains a positive lift coefficient for $\alpha \geq -2.9^\circ$ at $Re_c = 42.1 \times 10^3$ (Jacobs and Sherman 1937) due to camber (see figure 3.18). When $\alpha \leq \alpha_{Cl=0}$, the BEM analysis breaks down. An unsteady BEM would be more robust in these areas but was not used here. For $\lambda \geq 5$, $\alpha < 0^\circ$ in the root region. To achieve convergence of the BEM method, when $\alpha < -2.9^\circ$ the angle of attack is assigned the value of $\alpha_{Cl=0} = -2.9^\circ$. This modification is required only at λ_R shown in red in figure 6.4.

In addition to minimising separated flow which affects the trailing vortex system, the optimum Glauert rotor design sort to achieve dynamic similarity with full scale turbines by operating at a_{opt} . The axial interference factor distribution $a(r)$ is shown on the left of figure 6.5. The L–B–J limit is shown by the orange dashed line. $a(r) \sim a_{opt}$ at λ_d for a large proportion of the span before reducing in the tip region. The reduction in the tip region is due to a reduction in blade solidity. A tip speed ratio of 4 operates closer to the L–B–J limit. Above a tip speed ratio of 4, the outer 50% operates in the heavily loaded regime where the heavy rotor formulae of Glauert in Shen et al. (2005) have been applied.

Losses due to wake rotation can be estimated via the tangential interference factor distribution, $a_t(r)$, shown on the right of figure 6.5. Wake losses reduce with increasing tip speed ratio as expected. Further, at λ_R , internal sections of the blade operate in a propeller state ($a_t < 0$ and hence $C_T < 0$). In such instances, energy may be added to the central wake region reducing the wake centreline velocity deficit.

The Reynolds number also varies across the blade span due to both $U_{rel}(r)$ and $c(r)$. It is important to realise the Reynolds number variation as large deviations from the tabulated airfoil data introduce uncertainty in BEM predictions. The Reynolds number variation is

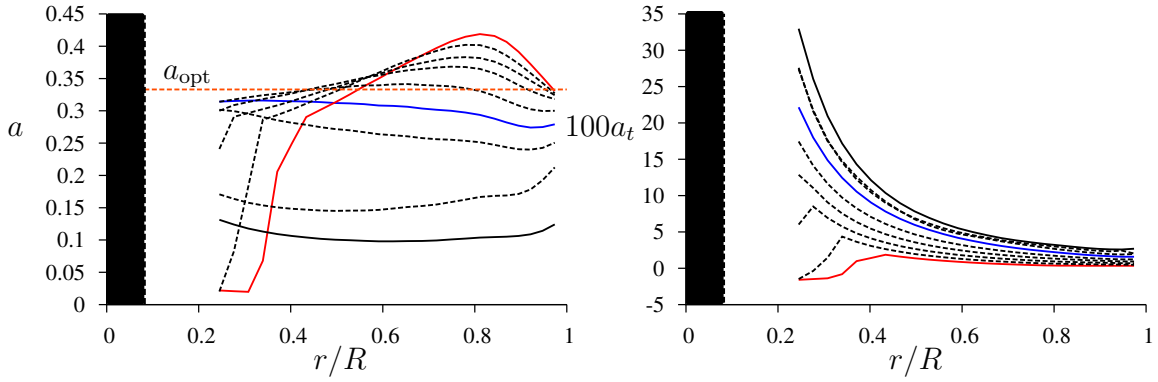


FIGURE 6.5: Axial (left) and tangential (right) interference factor variation with tip speed ratio. λ range, lines and colours as for figure 6.4.

shown in figure 6.6. The Reynolds number increases with λ as U_{rel} increases. However, it is at all times less than the airfoil performance data of Jacobs and Sherman (1937). The BEM analysis will thus overestimate the performance of the rotor at the various tip speed ratios. Due to a lack of airfoil data at low Reynolds numbers and difficulty in accurately measuring C_l and C_d at low Re_c as indicated in chapter 4, this is un-avoidable.

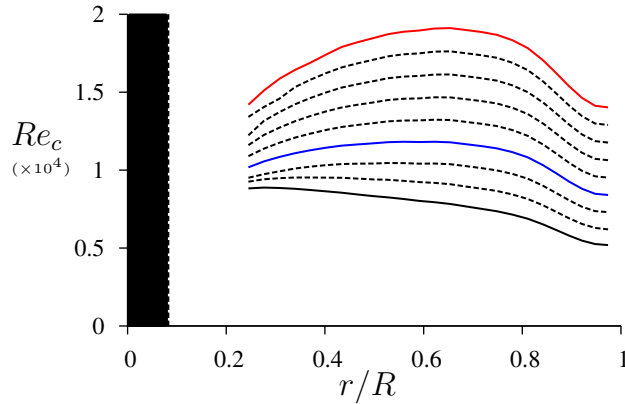


FIGURE 6.6: Spanwise Reynolds number variation with tip speed ratio. λ range, lines and colours as for figure 6.4.

The rotating blades generate blade bound circulation which is shed into the wake to form the tip and root vortices. The blade bound circulation distribution, $\Gamma_B(r)$, for three tip speed ratios is shown in figure 6.7. Figure 6.7 implicitly reveals the $\delta\Gamma_B/\delta r$ distribution. Although not shown, $\Gamma_B(r)$ is zero at the lifting surface discontinuities, *i.e.* $r/R = 0.24$ and $r/R = 1$, due to pressure equalisation. $\delta\Gamma_B/\delta r$ is thus largest in the tip and root region at λ_d resulting in the formation of coherent tip and root vortices. However, $\Gamma_B(r)$ varies over the entire span indicating a thin vortex sheet will connect the tip and root vortices. Figure 6.4 revealed attached flow is expected across a large portion of the blade. The vorticity in the wake will thus be due to $\delta\Gamma_B/\delta r$ unlike the geometrically scaled blade results of chapter 5.

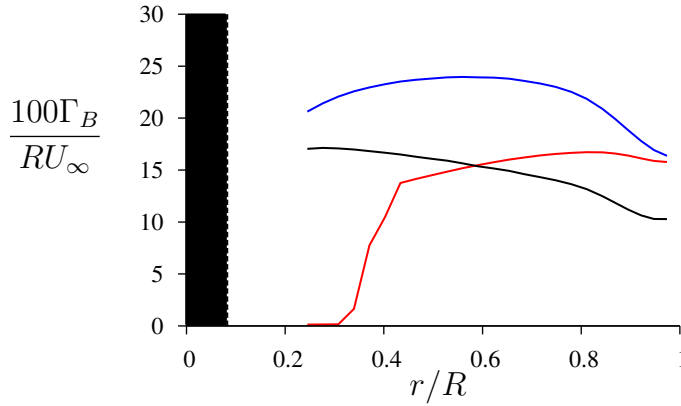


FIGURE 6.7: Blade bound circulation distributions for three tip speed ratios. blue: $\lambda_d = 3.5$, red: $\lambda_R = 6.0$, black: $\lambda = 2.0$.

The formation and radial location of the tip and root vortices at λ_R shown in figure 6.3 is clearly explained by figures 6.7 and 6.4. $\delta\Gamma_B/\delta r$ is very large at $r/R \sim 0.4$ due to minimal lift production as $\alpha < 0$. The large circulation gradient results in a root vortex forming.

The rotor loading predicted by the BEM method is compared against experimental estimates by measuring the flow induced by the rotor. Two approaches were used, the axial momentum balance outlined in chapter 2 and vortex-sheet-theory (VST) (Johnson 1980). The estimates by VST are presented first in the following section.

6.0.4 Rotor loading predictions by VST

In VST, the wake is assumed to consist of a series of infinitely long helical vortex filaments. The induced velocities of these filaments are determined via the Biot-Savart law (Medici et al. 2011) shown in equation 2.5 in chapter 2. VST is a highly idealised model at low Reynolds numbers as the wake becomes unstable via interaction between filaments as shown in chapter 5. The current model turbine also generates a coherent root vortex at early vortex ages. Nevertheless, qualitative agreement with experimental data has been achieved (Medici et al. 2011). The centre-line velocity deficit, $\frac{U_{CL}}{U_\infty}$ upstream of the rotor is used to determine the axial interference factor by equation 6.3,

$$\frac{U_{CL}}{U_\infty} = 1 - \bar{a}[1 + \xi(1 + \xi^2)^{-0.5}], \quad (6.3)$$

where U_{CL} is the centre-line velocity and $\xi = x/R$ is the dimensionless upstream distance.

The upstream velocity profile was evaluated by the 2D LDV system placed on a 3D traverse outlined in chapter 3. The measurement domain was $-5.5 \leq x/R \leq -0.3$. \bar{a} is determined by treating the rotor as an actuator disk and calculating the thrust loading from

equation 6.4,

$$T = 2\rho\pi R^2 U_\infty^2 \bar{a}(1 - \bar{a}), \quad (6.4)$$

Therefore by minimising the residuals of equation 6.3, \bar{a} and T can be determined. U_{CL}/U_∞ on the symmetry axis for λ_d (blue) and λ_R (red), is shown in figure 6.8. The error bars indicate the local stream-wise turbulence intensity, I_u . The centre-line velocity reduces due to pressure increase toward the rotor plane. The solid black line represents the VST prediction for a_{opt} . The dashed blue and red lines represent \bar{a} values of $\bar{a} = 0.21$ and $\bar{a} = 0.25$. These values are within the rms values of the experimental data in all but the closest measurement point. The VST predictions are lower than the BEM predictions of $\langle \bar{a} \rangle = 0.27$ and $\langle \bar{a} \rangle = 0.28$ for λ_d and λ_R . Here, $\langle \cdot \rangle$ represents a spatial average taken over the BEM radial locations.

The decrease in velocity occurs over a narrower range compared to the theoretical predictions. However the velocity deficit increases above VST close to the origin due to the stagnation point which forms on the experimental model nose cone. U_{CL}/U_∞ will tend to zero at $x/R \sim -0.2$, with the current experimental setup. This trend has also been seen in experimental models where a nose cone and hub section are present (Medici et al. 2011).

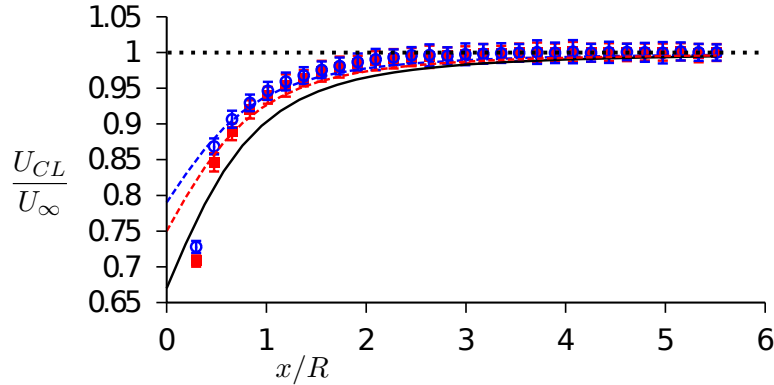


FIGURE 6.8: Upstream velocity profile of the optimum Glauert rotor operating at $\lambda_d = 3.5$ (blue) and $\lambda_R = 6.07$ (red). Error bars represent the rms magnitudes. The dashed blue and red lines represent the VST (Johnson 1980) predictions for $\bar{a} = 0.21$ and $\bar{a} = 0.25$. The solid line is the VST predictions for a_{opt} .

The non-dimensional thrust coefficient is calculated from equation 10.13. Using the \bar{a} estimates, $C_T = 0.66$ for λ_d and $C_T = 0.75$ for λ_R . The C_T predictions from the BEM analysis are $C_T = 0.79$ for λ_d and $C_T = 0.81$ for λ_R . The thrust coefficient predictions are less than the optimum of $C_T = 0.89$ due to reduced performance of the blade airfoil at the experimental Reynolds number. The difference is however drastically reduced compared to

the geometrically scaled blades. The current data highlight the difficulty to achieve dynamic similarity between model and full scale.

The phase-averaged wake structure is investigated using PIV in the following section to determine a loading estimate by the 1D momentum theory.

6.0.5 Phase-locked averaged wake structure

The phase-averaged wake structure at λ_d is presented to determine a loading estimate by 1D momentum theory in the current section. The average is taken over all blade phase angles, *i.e.* ($0^\circ \leq \Phi \leq 360^\circ$). The PIV data was captured at a fixed sample frequency of 1Hz meaning realisations are minimally correlated in time. Data was captured for $x/R \leq 8.5$ allowing characterisation of near wake evolution.

The average streamwise velocity wake contour is shown in figure 6.9. The line represents the wake boundary, defined as $\bar{u}/U_\infty = 1$. Wake expansion is evident by the radial movement of the wake boundary. Wake expansion is also depicted in axial velocity profiles extracted from the velocity fields as shown in figure 6.10. The left figure shows profiles at 1.0R resolution in the range, $0.5 \leq x/R \leq 7.5$, whereas the right figure profiles in the range, $1.0 \leq x/R \leq 8.0$. The red and blue lines indicate the first and last profile in the range. The minimum velocity deficit occurs at $y/R \sim 0.6$ immediately behind the rotor. Momentum transfer shifts this minimum location toward the rotational axis with downstream distance. By $x/R = 8.0$, the wake appears as a smooth profile with the velocity reducing toward the rotational axis.

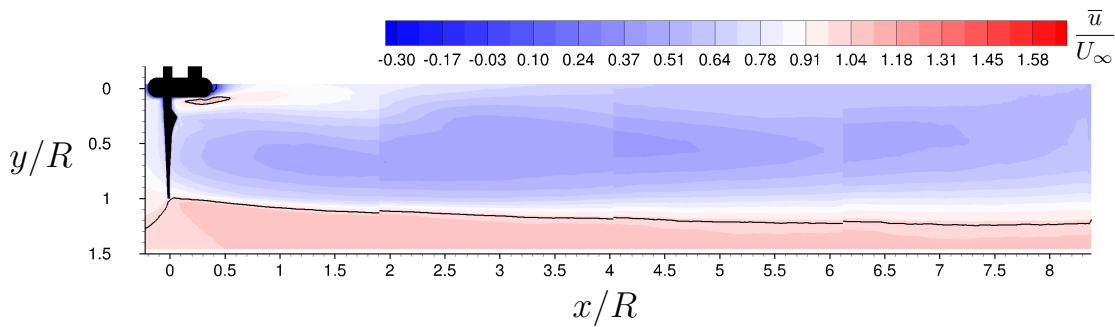


FIGURE 6.9: Phase-averaged near wake axial velocity field near the design tip speed ratio, $\lambda_d = 3.55$. Wake expansion is evident by the line indicating the wake boundary, $\bar{u}/U_\infty = 1$

In 1D momentum theory, the axial interference factor used to determine rotor loading is found by measuring the velocity in the rotor plane, U_D . However, obtaining the axial interference factor in the rotor plane is problematic due to the presence of the rotor. Therefore, as an alternative, the velocity deficit in the far wake, U_w , is used. The velocity profile at $x/R = 8$ is used for this purpose. The average axial interference factor value was then

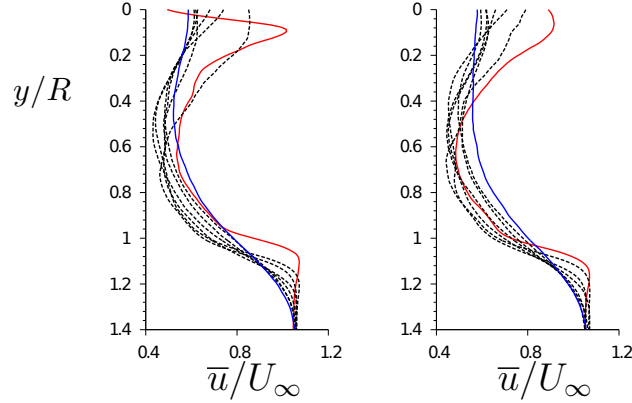


FIGURE 6.10: Phase-averaged near wake axial velocity profiles near the design tip speed ratio, $\lambda_d = 3.55$. left: $0.5 \leq x/R \leq 7.5$, right: $1.0 \leq x/R \leq 8.0$, $1.0R$ resolution. The red and blue lines indicate the first and last profile in the range. By $x/R = 8.0$, the wake velocity deficit reduces smoothly toward rotational axis.

$\langle \bar{a} \rangle = 0.5 [1 - \langle \bar{u}/U_\infty \rangle] = 0.195$, lower than both the BEM and VST predictions. The thrust loading of the rotor from 1D momentum theory, using equation 10.13 is then $C_T = 0.63$.

An interesting wake feature of the Glauert rotor design is visible in figures 6.9 and 6.10. The velocity deficit does not increase monotonically toward the wake centreline as seen in prior studies (Alfredsson and Dahlberg 1979; Medici and Alfredsson 2006). Instead, the velocity deficit reduces in the root region due to the lifting surface terminating at $x/R = 0.24$. A similar phenomena was seen in Krogstad and Adaramola (2011). The primary design goal of the optimum Glauert rotor was to generate coherent tip and root vortices. The root region termination point encourages swirl aiding root vortex formation.

In addition to the velocity deficit in the wake, the turbulence intensity is elevated by the rotating blades and the vortices they create. The breakdown of the tip and root vortices is a source of turbulent kinetic energy (TKE), k , in the wake and poses a risk to other turbines in a wind farm. In the region of vortex breakdown, complex vortex interactions occur, *e.g.* see figure 2.4, including vortex stretching and straining leading to a very turbulent environment. As this process is still not fully understood, accounting for the fatigue loading it will induce on wake affected turbines is very difficult. For this reason, the region of vortex breakdown in the wake should be avoided as a wind energy installation. Here, the TKE is calculated from the resolvable Reynolds stress components, $\overline{u'^2}$, $\overline{v'^2}$, and $\overline{u'v'}$. The vertical and transverse Reynolds stress components are assumed to be equal, *i.e.* $\overline{v'^2} = \overline{w'^2}$. The mean TKE field is thus determined from equation 6.5.

$$\bar{k} = 0.5(\overline{u'^2} + 2\overline{v'^2})/U_\infty^2. \quad (6.5)$$

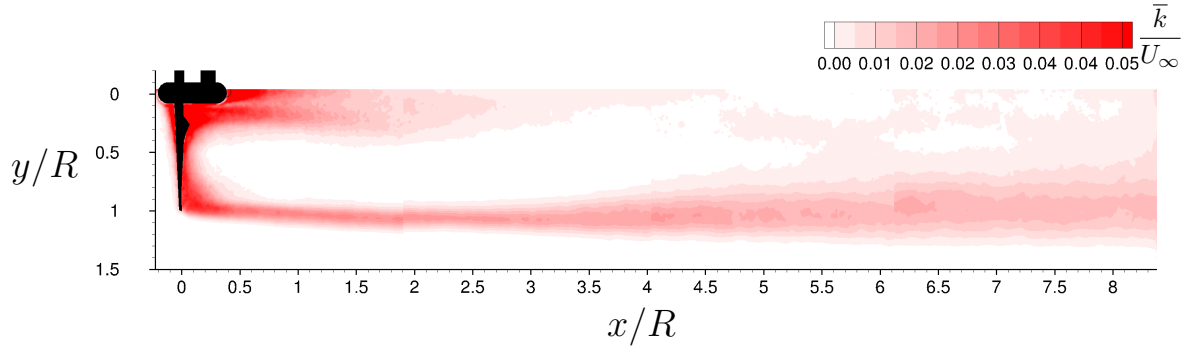


FIGURE 6.11: Phase-averaged near wake turbulent kinetic energy, \bar{k}/U_∞^2 , field near the design tip speed ratio, $\lambda_d = 3.55$. Elevated \bar{k} correspond to vortex locations and regions of intense mixing in the wake.

The phase averaged TKE field is shown in figure 6.11. The main regions of elevated TKE are the tip, root and immediately downstream of the blade. The region immediately downstream of the blade contains turbulent kinetic energy due to the blade wakes. The root vortices and mixing in the root region lead to the elevated levels of TKE adjacent to the nacelle. Figure 6.11 indicates the root region is more turbulent than the tip region and is consistent with prior studies (Hu et al. 2012). The streamwise turbulence intensity has a similar form to the TKE field (Porté et al. 2010). The TKE field supports the notions presented for rapid root vortex cessation in chapter 5. The spreading of the tip vortex shear layer is made visible by \bar{k}/U_∞^2 . The TKE magnitude remains largely constant and does not reveal a peak as seen in the streamwise turbulence intensity field (Porté et al. 2010). However, the TKE layer begins to thicken from $x/R \geq 3 - 3.5$, which may indicate onset of vortex breakdown. Evolution of the tip and root vortices is investigated in section 6.0.6.

The TKE field revealed turbulent fluctuations which were localised to the tip and root vortex shear layers and immediately behind the blade. In a phase average, the wake vortices appear as a continuous band as shown in figure 6.12. The contour levels are consistent with figure 6.3. The vorticity associated with the tip vortices reveals they form in-board of the tip in a similar fashion to the straight vortex filaments presented in chapter 4. The vortices form inboard of the tip due to a negative radial velocity component immediately downstream of the blade (Micallef et al. 2012). The vorticity field corresponds well with the elevated TKE regions of figure 6.11.

The phase averaged data revealed that wake expansion occurs close to the design tip speed ratio. Turbulent kinetic energy was also generated in the tip and root regions and downstream of the blade. To investigate the vortices which generate the TKE in the tip and

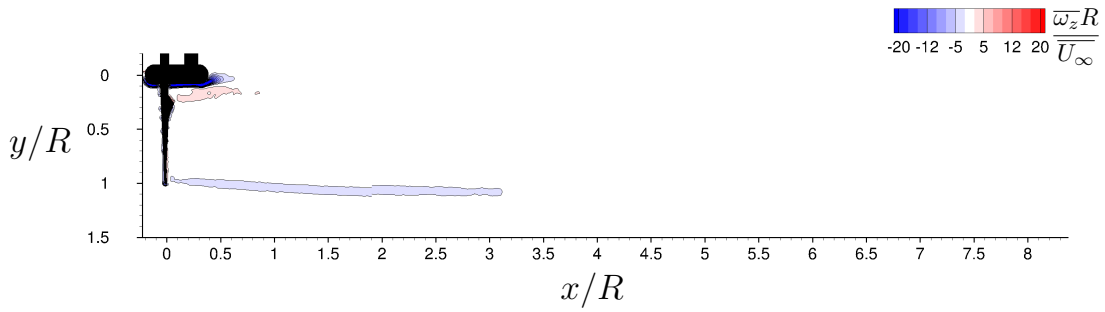


FIGURE 6.12: Near wake out-of-plane vorticity, $\overline{\omega_z}R/U_\infty$, field near the design tip speed ratio, $\lambda_d = 3.55$.

root regions a phase-locking technique is necessary. Again, a single blade was phase-locked in-line with the tower and thus appears in the measurement plane. The influence of the tower support structure and the evolution of the tip and root vortices is presented in the following section.

6.0.6 Tower causes the faster breakdown of vortices in bottom half of wake

The vortices in the near wake are investigated by the phase-locking technique used in chapter 5. The entire wake is characterised to investigate the effect of the tower on near wake structure. Few researchers have investigated the effect of the tower on the wake (Whale 1996; Zahle et al. 2009). Zahle et al. (2009) investigated the complex tower-rotor interaction of the NREL Phase VI turbine. They showed in great detail the wake of the tower caused large fluctuating blade loads and the earlier diffusion of the tip vortices in the bottom half of the wake compared to those in the top half of the wake (Zahle et al. 2009). However, this study was conducted on a downwind turbine and the dynamics of the rotor-tower interaction will be different for an upwind turbine. An experimental study investigating a upwind turbine is that of Whale (1996), however this study suffered from low spatial resolution. There is thus a need to characterise the evolution of the tip and root vortices in the bottom half of the wake in an upwind turbine configuration. The phase-locked average axial and radial velocity contour plots at λ_d are shown in figures 6.13 and 6.14. A deflection of the wake toward the bottom half ($y/R \leq 1$) is evident in figure 6.13 in a similar fashion to the phase averaged wake. An additional possible cause of the wake deflection toward the bottom half of the wake is the free surface of the water channel acting a momentum sink via surface deformation. As the free surface is $\sim 1.3D$ from the rotational axis, this mechanism is unlikely but cannot be discounted completely. It should be noted however that no obvious surface deformations in

the wake were visible during data acquisition.

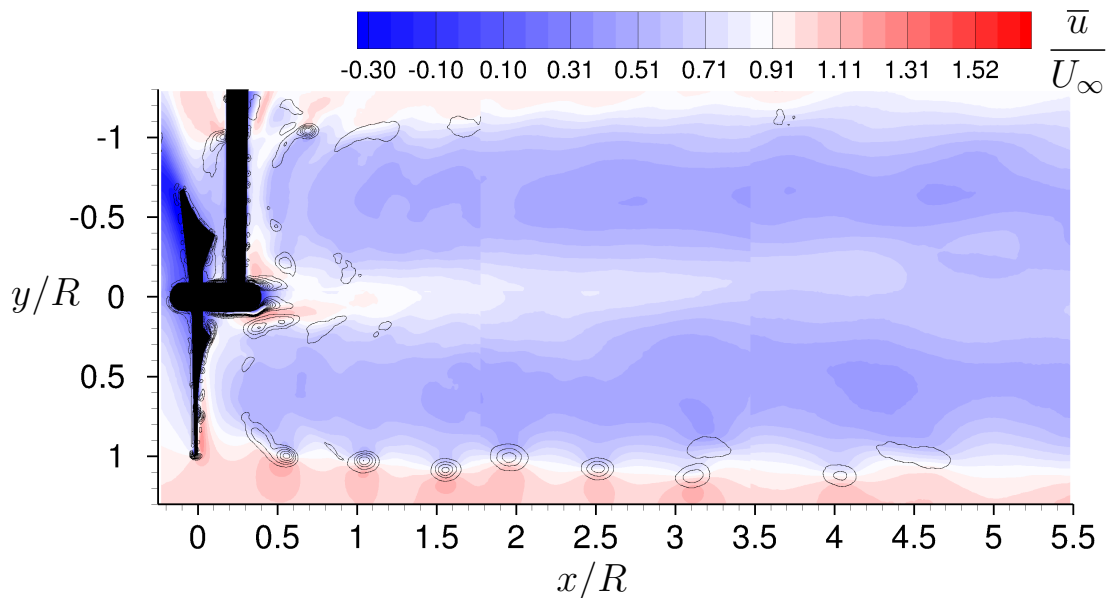


FIGURE 6.13: Near wake axial velocity contour plot at the design tip speed ratio, $\lambda_d = 3.5$. Contour lines indicate location of tip and root vortices.

Figure 6.13 is compared to the flow visualisations of Brown (1971). In a propeller wake, the peak velocity occurs at a similar radial position, $y/R \approx \pm 0.5$ to figure 6.13. However, unlike figure 6.13, the velocity maximum is upstream of the tip and root vortices due to the direction of thrust. The contour lines in figure 6.13 indicate the dominant vortices present in the near wake.

To further illustrate the development of the wake, velocity profiles in the range, $0.5 \leq x/R \leq 5$, are presented in figure 6.15. The left of figure 6.15 represents velocity profiles in the range $0.5 \leq x/R \leq 4.5$ with $1.0R$ resolution. Whereas, the right of figure 6.15 represents velocity profiles in the range $1.0 \leq x/R \leq 5.0$ with the same resolution. The red and blue lines represent the first and last profiles in the range. The wake is not symmetrical due to the presence of tip and root vortices at different ages. The vortices in the bottom half of the wake are 60° younger than those in the top half of the wake.

The contour lines in figures 6.13 and 6.14 revealed the presence of coherent tip and root vortices. The following section characterises vortex evolution in the wake of the optimum rotor.

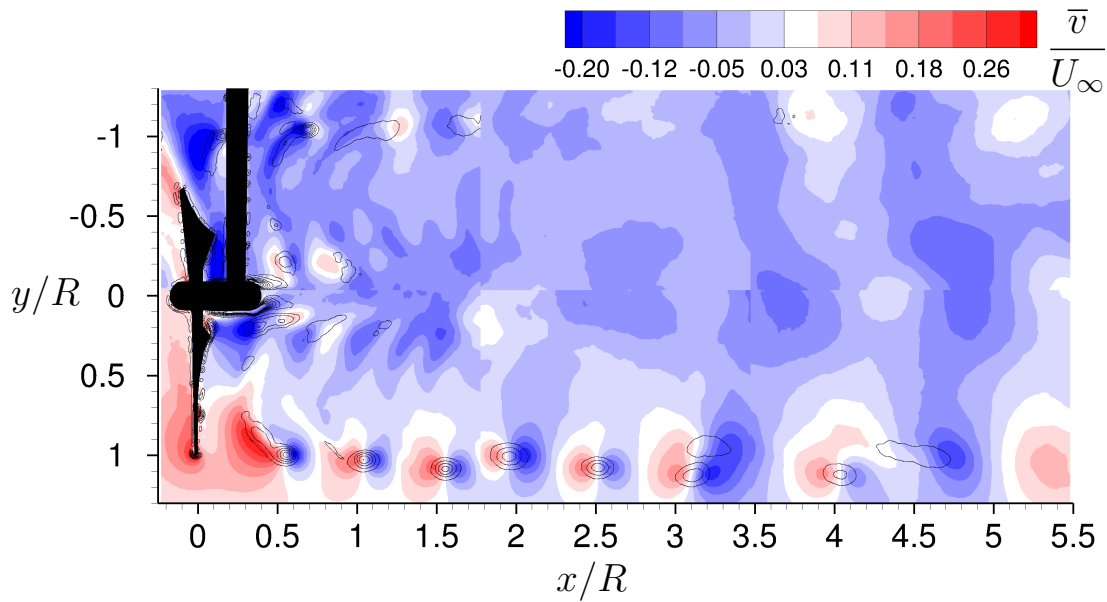


FIGURE 6.14: Near wake radial velocity contour plot at the design tip speed ratio, $\lambda_d = 3.5$. Contour lines indicate location of tip and root vortices.

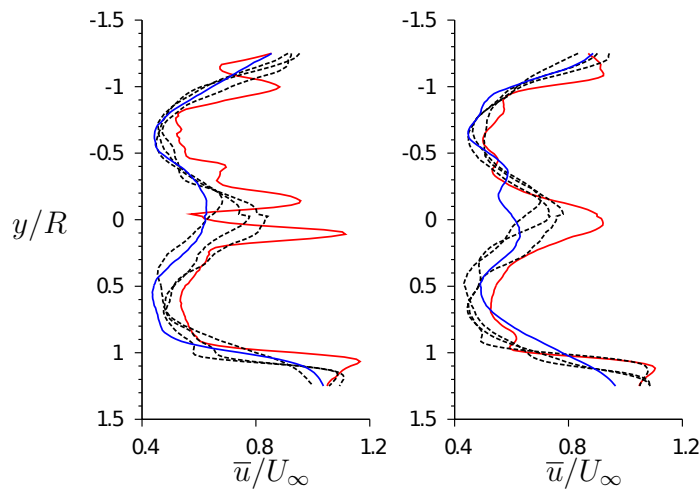


FIGURE 6.15: Near wake phase-locked axial velocity profiles at the design tip speed ratio, $\lambda_d = 3.5$. left: $0.5 \leq x/R \leq 4.5$, right: $1.0 \leq x/R \leq 5.0$, $1.0R$ resolution. Red and blue lines indicates first and last profile in the range. Jet like structures due to the lifting surface termination in the root section are clearly evident at $x/R = 0.5$.

6.0.7 Stable helical vortex system

It has been shown that the tip and root vortices interact leading to wake instability. It remains to be seen whether a stable helical filament configuration exists. Okulov (2004) and later numerically by Walther et al. (2007), showed stable configurations of tip and root vortices exist when the induced velocities of the tip and root vortices match. Such an equilibrium is very difficult to obtain experimentally. However, helical filaments with a large pitch show

minimal interaction (Grant and Parkin 2000). This phenomenon was evident in the results of chapter 5 as the wake became unstable closer to the rotor plane with reducing helical pitch.

A stable wake configuration was achieved by reducing the number of blades and hence filaments. However, in doing so, the solidity and performance of an optimum Glauert rotor reduces as shown in figure 6.16. This figure was created using the empirical formula of Wilson and Lissaman (1974), equation 3.20, introduced in chapter 3. The red, blue and black lines indicate a one, two and three bladed turbine respectively. Turbine performance reduces with blade number as less power is extracted.

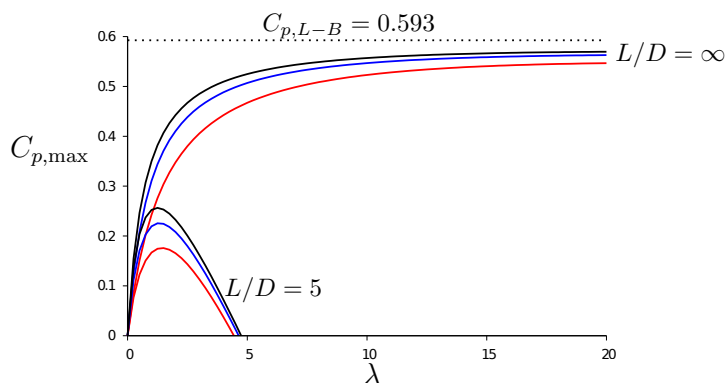


FIGURE 6.16: The affect of blade number on the attainable power coefficient attainable with an optimum Glauert rotor. red: 1 blade, blue: 2 blades and black: 3 blades. L/D ratio of 5 and ∞ shown.

Due to the cost of manufacture of the experimental models, a one-bladed configuration of the three-bladed optimum rotor was used to generate the stable wake. The one-bladed configuration was tested at a tip speed ratio approaching runaway of $\lambda = 5.71$. The pitch increases by a factor 3 compared to the three-blade configuration at λ_R which minimises interaction between the tip and root vortices. A total of 100 image pairs were captured over the axial range $x/R \leq 9R$.

The phase-locked average induced streamwise velocity field behind the one-bladed rotor is shown in figure 6.17. Wake expansion is minimal due to the low rotor loading. The induced velocities of the tip vortices are visible over the entire measurement domain. They are visible for a longer distance compared to the three bladed results in figure 6.13. The velocity gradients decrease due to viscous diffusion.

The out-of-plane vortical wake of the one-bladed configuration is shown in figure 6.18. Interaction between tip vortices is absent in the one-bladed configuration. The tip vortices thus remains stable for longer compared to the three-blade case in figure 6.3. The difference in tip speed ratio between the one and three blade cases is of secondary importance to the

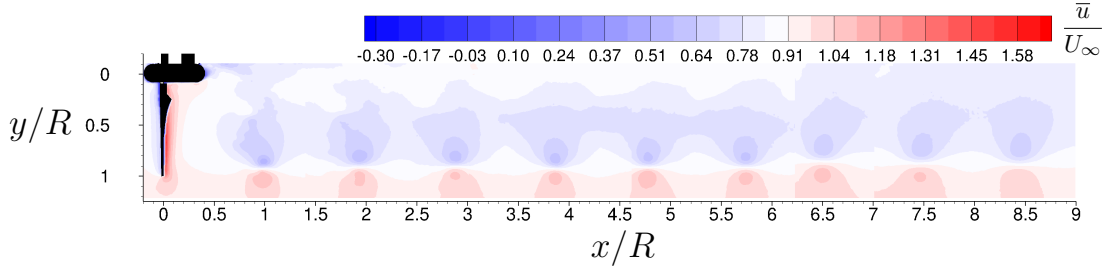


FIGURE 6.17: Phase-locked average streamwise velocity field of a one-blade configuration of the optimum 3 bladed rotor at a tip speed ratio approaching runaway of $\lambda = 5.71$

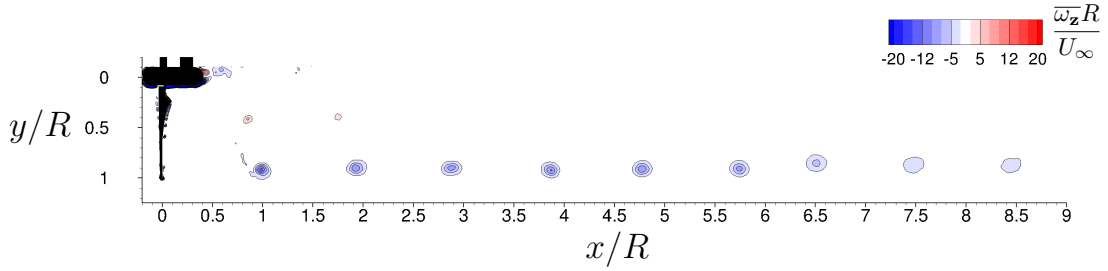


FIGURE 6.18: Vortical wake of the on-bladed optimum rotor configuration at a tip speed ratio approaching runaway of $\lambda = 5.71$

change in helical pitch. The tip vortices remain stable in the one-bladed configuration until $x/R \leq 8.45$ compared to $x/R \leq 1.95$ in the three blade case. The results show that a stable configuration is possible when interaction is minimised. The tip and root vortices diffuse due to viscous and turbulent diffusion.

To confirm the stability of the one-bladed rotor wake, the axial (left) and radial (right) tip (black) and root (red) vortex positions are shown in figure 6.19. The vortex positions were determined by both the maximum of the λ_{ci}^2 field and the maxima/minima of the Γ_1 field. There is minimal difference between the two methods, so the Γ_1 results are presented in figure 6.19. The tip vortex positions collapse accurately onto a linear line of best fit. The root vortices on the other hand vary more about their line of best fit. The tip vortices form further inboard of the tip with $\bar{y}/R = 0.92$ compared to the three blade configuration. In a similar fashion to the three bladed runaway case of figure 6.3 and the BEM predictions of figure 6.7, the root vortices form inboard of the lifting surface termination point due to the large $\partial\Gamma_B/\partial r$ value. The average radial position of the root vortex at a vortex age of 360° is $\bar{y}/R = 0.41$. The spacing between the tip and root vortices is minimal at $y_{tip} - y_{root} = 0.51R$. However, it is difficult to ascertain from the phase-locked averaged data whether the tip and root vortices interact. No correlations were found between the tip and vortex instantaneous positions.

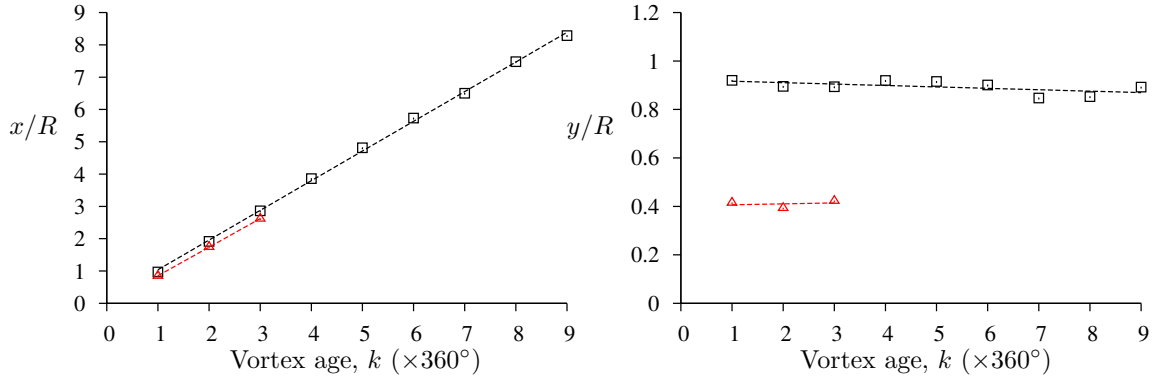


FIGURE 6.19: Trajectory of the tip vortices of the single bladed optimum rotor at a tip speed ratio approaching runaway of $\lambda = 5.71$.

Tip and root vortex properties were evaluated using the methodologies outlined in chapter 3. The variation of the tip (black) and root (red) vortex circulation (left) and core radius (right) with vortex age is shown in figure 6.20. The dashed line and hollow symbols indicate the vortex properties determined by the Γ_2 method whereas the solid lines and symbols present the λ_{ci}^2 method results.

Vortex circulation is approximately conserved across the measurement domain indicating the long timescales of both viscous and turbulent decay for a stable wake configuration. Minimal viscous decay was also seen for the tip vortex circulation of the static 3D wing in figure 4.13. However, the nonmonotonic variation of vortex circulation indicates a limitation of the 2D measurement technique as circulation can be diffused in the out-of-plane direction. The λ_{ci}^2 derived circulation is less than the Γ_2 derived circulation due to the more restrictive threshold λ_{ci}^* contour. The λ_{ci}^* contour encapsulates all eddying motion above a fixed freestream value. As angular momentum of the vortices is diffused to the surrounding flow, the maximum swirl above λ_{ci}^* reduces. The λ_{ci}^* contour will thus contain less circulation as seen in figure 6.20. Γ_2^* on the other hand, is based on the evolving velocity field. Γ_2 is thus the preferable method of vortex circulation calculation. The root vortex circulation is at all times less than the tip vortex circulation. The root vortices diffuse faster than the tip vortices due to their reduced strength and location near the more turbulent central wake region.

The vortex core radius also shows the more restrictive nature of the λ_{ci}^* threshold compared to the Γ_2^* threshold. However, the trends are repeated in each method. The core radius is approximately constant until $VA = 6 \times 360^\circ$, after which the core expansion increases. The core expands due to viscous and turbulent diffusion. There is large scatter in the root vortex results and the small number of realisations do not allow conclusions to be drawn.

The circulation results are compared to an estimate of the trailing vortex system strength

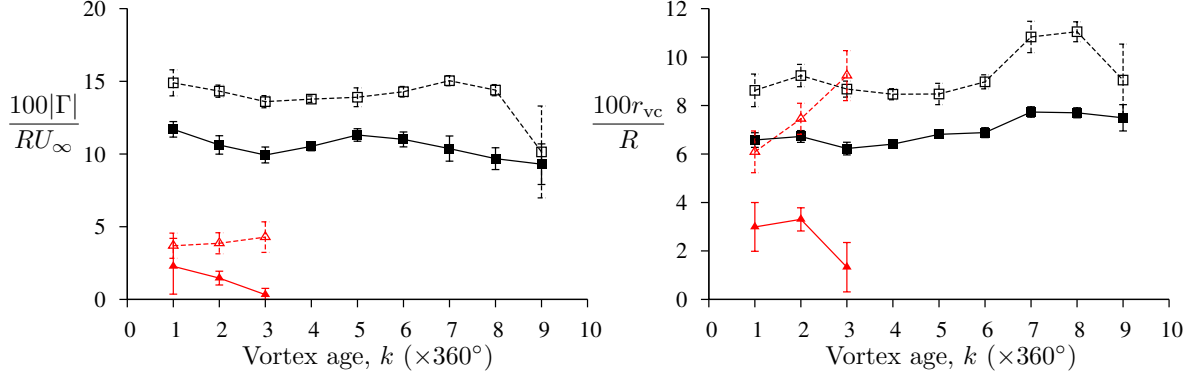


FIGURE 6.20: Mean tip (black) and root (red) vortex property variation with vortex age for the one bladed configuration at a tip speed ratio approaching runaway of $\lambda = 5.71$. Left: non-dimensionalised circulation and right, non-dimensionalised core radius. Dashed line and hollow symbols, Γ_2 data, solid line and symbols, λ_{ci}^2 data.

obtained by a lifting line vortex model. Integrating equation 2.3 across the blade span, the total circulation of the trailing vortex system can be determined. The circulation distribution obtained using the BEM method of appendix 10 is arbitrarily integrated in two sections. The root region wake circulation is obtained by integrating equation 2.3 from $x/R = 0$ to $x/R = 0.5$. Whereas, the tip region circulation is obtained by integrating from $x/R = 0.5$ to $x/R = 1$. The wake circulation in the tip and root regions each equal $\Gamma_{LL} = 0.27$. The lifting line model thus over predicts the experimentally derived circulation. The over prediction arises from the Reynolds number difference between the airfoil performance data and the experimental conditions. The result highlights the need for airfoil performance data at the experimental Reynolds numbers.

The one-bladed vorticity field of figure 6.18 revealed interaction between tip vortices is minimal. Therefore, the 2D stability of the helical tip vortices in the measurement plane without vortex interaction (*i.e.* mutual inductance mode) can thus be determined. The probability density functions for the axial (left) and radial (right) meander motions are presented in figure 6.21. Root vortex meander was not investigated due to rapid cessation of the root vortex signal. Each curve and set of data points represent a tip vortex at a particular vortex age ($k \times 360^\circ$). While figure 6.21 is only generated from one hundred realisations, meander in the radial direction appears to conform to a normal distribution more accurately than the axial positions. Further, the distributions are wider in the axial direction.

The fitting parameter, σ , of the normal distribution at each vortex age characterises the magnitude of meander in each axis. The meander of the tip vortices over a wide vortex age range is presented in figure 6.22. Meander in the axial direction is larger than that

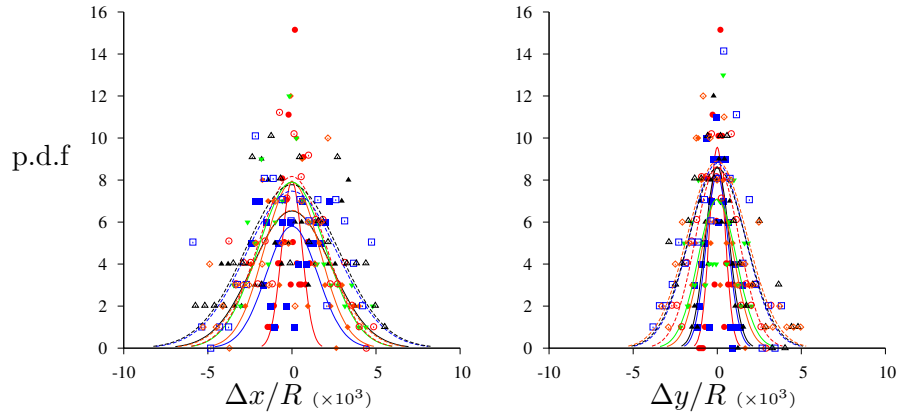


FIGURE 6.21: Normalised probability density functions of the axial (left) and radial (right) instantaneous deviations from the phase-locked tip vortex mean position. One-bladed optimum rotor configuration at a tip speed ratio approaching runaway of $\lambda = 5.71$. Curves represent tip vortices at different vortex ages, ($k \times 360^\circ$). Solid red circle/line: $k = 1$, solid blue square/line: $k = 2$, solid black triangle/line: $k = 3$, solid orange diamond/line: $k = 4$, solid green nabla/line: $k = 5$, hollow/dashed red circle/line: $k = 6$, hollow/dashed blue square/line: $k = 7$, hollow/dashed black triangle/line: $k = 8$, hollow/dashed orange diamond/line: $k = 9$.

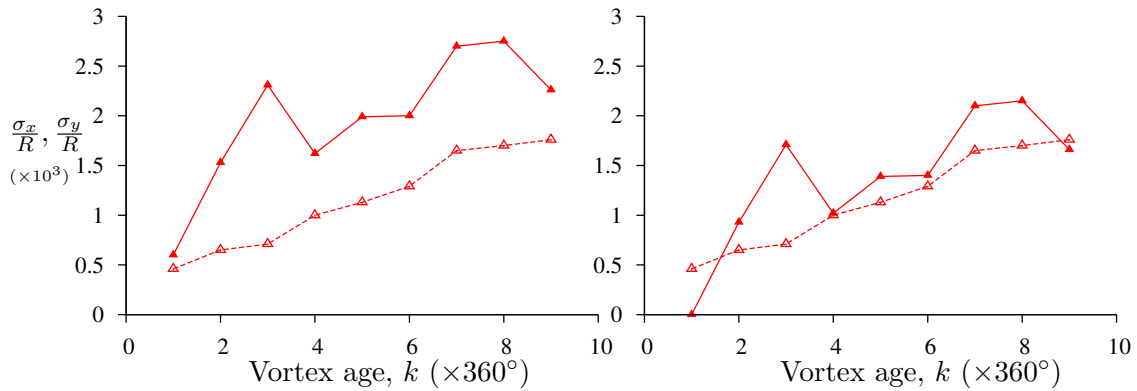


FIGURE 6.22: Tip vortex meander magnitude variation with vortex age. Left: raw results, right: results corrected for water channel sloshing (*i.e.* $\sigma_x = \sigma_x - \sigma_x(\text{VA}=360^\circ)$). Single bladed optimum rotor at a tip speed ratio approaching runaway of $\lambda = 5.71$.

in the radial direction. The left figure indicates the data extracted from figure 6.21. The instantaneous trace of the axial tip vortex positions reveal they are affected by the sloshing in the water channel. These velocity fluctuations contribute to the apparent meander of the tip and root vortices. To overcome this issue, the axial meander of the youngest tip vortex ($\text{VA} = 360^\circ$) is assumed to be due solely to the sloshing motion. The meander in the axial direction is thus scaled by the amount in the $\text{VA} = 360^\circ$ tip vortex. The assumption allows decoupling of the sloshing-induced and self-induced motion of the vortices. This assumption is most accurate at early vortex ages where self induced meander of fixed wing trailing vortices is minimal (Green 1995; Ebert and Wood 2001).

The right of figure 6.22 presents the adjusted meander of the tip vortices. The meander in

the radial direction increases quite linearly. The magnitude of the meander in both axes are now comparable except at a vortex age of $VA = 1080^\circ$. No physical explanation is available for the increase of meander at this vortex age.

It is clear that when the helical pitch is increased dramatically by removing two blades, the tip vortices persist to large distances in the wake. However, despite the interaction between tip vortices being minimised, tip vortex meander increases with vortex age. The mutual induction instability mode is one of three modes which were determined to affect helical vortex filaments in the seminal work by Widnall (1972). The increase in meander is possibly due to the long-wave and/or short-wave (Widnall 1972) instability modes. The explicit existence of such instability modes could not be deduced from the phase-locked average measurements. The tip and root vortices of a three-bladed configuration will now be investigated.

6.0.8 Near-wake vorticity field and vortex properties

The induced velocity fields of the three-bladed rotor configuration presented in figures 6.13 and 6.14, revealed tip and root vortices. It is important to understand how these vortices evolve to minimise their influence on other turbines in a wind farm setting. Several mechanisms contributing to the rapid cessation of the root vortex signal were introduced in chapter 5. The phase averaged data in section 6.0.5 confirmed the likely mechanisms for root vortex breakdown. The current section focuses on mechanisms which affect evolution of the tip vortex.

The phase-locked averaged vorticity map of the three bladed optimum Glauert rotor operating at $\lambda = 3.55$ is shown in figure 6.23. Once again, the tip and root vortices in the top ($y/R \geq 1$) and bottom ($y/R \leq 1$) wake halves are the dominant vortical structures in the near wake. Tip vortices are clearly visible near the tip radial position ($y/R \pm 1$). Root vortices on the other hand are visible ($y/R \pm 0.15$) near the lifting surface termination point. The orientation of the vortices in the two wake halves is opposite due to the different orientation of the helical filaments. Further, the vortex age of the tip vortices in the lower wake half are 60° less than those in the upper wake half due to the phase-locking technique.

Root vortices are only visible in the near wake for $VA \leq 360^\circ$. Figure 6.23 indicates the root vortex is not as coherent the tip vortices at the same vortex age. This is due to the complexity of the flow in the root region highlighted by the TKE plot of figure 6.11. The swirl velocity causing roll-up of the root vortices is adjacent to the nacelle boundary layer. The velocity gradients in the nacelle boundary layer will affect the roll up process by reducing

the induced velocity field of the vorticity sheet emanating from the root section of the blade.

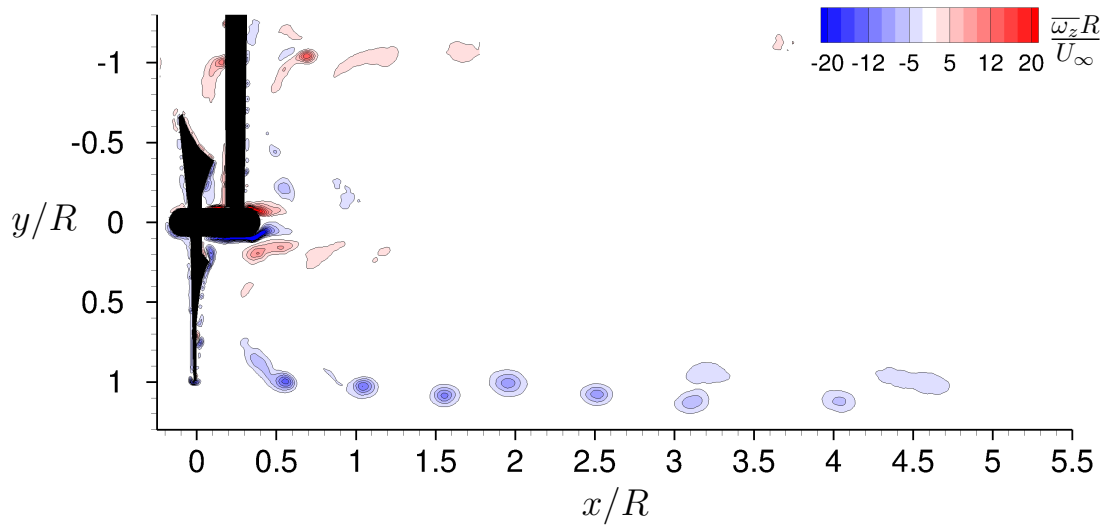


FIGURE 6.23: Near wake vorticity contour plot at the design tip speed ratio, $\lambda_d = 3.5$. Tip vortices are seen in both the upper (red) and lower (blue) portions of the wake. Root vortices are also seen in the upper (blue) and lower (red) portions of the wake. The vortices in the lower part of the wake are 60° younger than those in the upper half of the wake. The vortices in the lower half of the wake degenerate rapidly due to the wake of the tower structure.

Figure 6.23 highlights the detrimental effect the tower structure has on the vortices in the bottom half of the wake. As highlighted earlier, aside from Whale (1996), the effect of the tower on the vortex structures in the wake has rarely been investigated experimentally. The magnitude of the tip vortex vorticity in the bottom wake half decreases faster than those in the top wake half in a similar fashion to Zahle et al. (2009). The rapid degeneration of the vortices in the lower wake half is due to the wake of the tower structure. The blade bound circulation leaves the blade as a loose bundle which rolls-up into the tip and root vortices. The tower section begins at $x/R = 0.18$. This distance corresponds to the axial location of a tip vortex with a vortex age of 60° in the lower half of the wake. Tip and root vortex roll-up is therefore affected by the interaction with the tower. The tower cross section is elliptical and will thus generate a von-Kármán vortex street. The axis of the von-Kármán vortex street is aligned with the y -axis so is not revealed by the $\bar{\omega}_z R / U_\infty$ contours in figure 6.23. However, the vortices shed by the tower structure increase the turbulence in the bottom half of the wake and impedes the formation of compact tip and root vortices.

The blade wakes can be used as a proxy of completion of vortex roll-up. The vorticity within the blade wakes is entrained by the tip and root vortices during roll-up. Blade wakes attached to the tip vortices are visible in both the top and bottom wake halves. In the top

half of the wake, tip vortex roll-up (presence of the blade wakes) occurs until a vortex age of 240° . However, in the bottom half, a blade wake is present next to the tip vortex for $VA \leq 300^\circ$. This implicitly confirms the detrimental effect the tower has on the tip vortex roll-up process. A weaker initial vortex in the more turbulent bottom wake half degenerates faster than the tip vortices in the top wake half.

A more quantitative measure to determine when vortex roll-up is complete is achieved by investigating vortex circulation. Completion of fixed wing-tip vortex roll-up is denoted by an invariance of vortex circulation with vortex age (Green 1995). At a higher Reynolds number and using a commercial micro-wind turbine, tip vortex roll-up was completed by $VA = 174^\circ$ (Grant and Parkin 2000). However, vortex roll-up is dependent on rotor geometry and operating Reynolds number making comparisons between studies difficult. It is expected that vortex roll-up takes longer with the current model due to the reduced aerodynamic performance of the rotor blades at the experimental Reynolds number.

The tip vortex circulation (left) and core radius (right) in the top (black) and bottom (red) halves of the wake is shown in figure 6.24. Where interaction between vortices occurs, the properties of the interacting pair are characterised. The circulation of the two interacting vortices is approximately equal to twice that of the single vortices. The increased scatter of circulation values in figure 6.24 compared to the one-bladed results is an indication of the added wake complexity. Figure 6.24 confirms the tip vortices in the bottom half of the wake are much weaker than those in the top half. The current results are also compared to lifting line theory predictions. Lifting line theory predicts a tip and root vortex circulation of $\Gamma = 0.24$ at λ_d . Again, lifting line theory over-predicts the circulation of the wake vortices due to the Reynolds number effect.

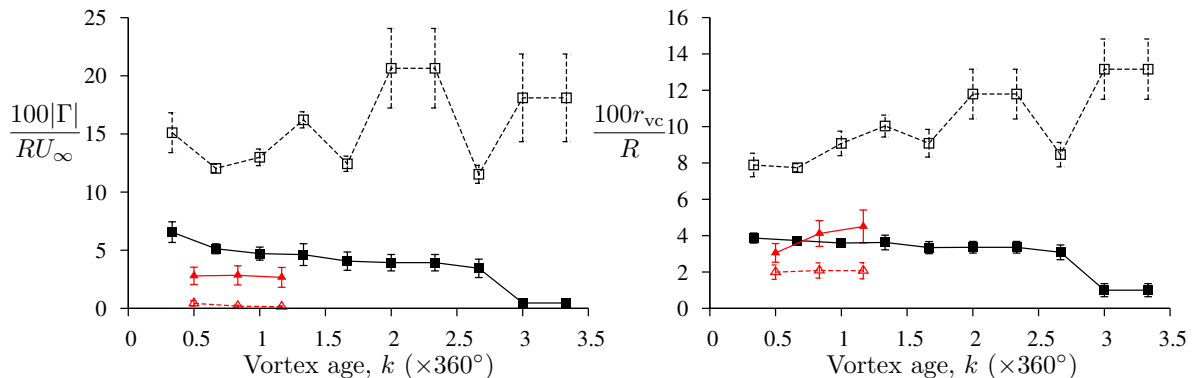


FIGURE 6.24: Tip vortex properties in the top (black) and bottom (red) wake halves for the three bladed optimum rotor at a tip speed ratio near the design $\lambda = 3.55$. Circulation is shown on the left whereas vortex radius is shown on the right.

The entire wake profile (figure 6.23) and vortex properties revealed the turbine tower affects the stability and strength of the tip and root vortices in the lower half of the wake. As the tip vortices in the top half of the wake persist further downstream, they pose the greatest risk to downstream turbines in a wind farm setting. For this reason, the tip and root vortices in the top half of the wake will now be investigated in further detail.

The phase-locked average position of the tip (black) and root (red) vortices determined by the maximum of the Γ_1 field are shown in figure 6.25. The axial positions are shown on the left whereas the radial positions are shown on the right. The tip vortex axial position line of best fit is applied to the vortex ages prior to onset of vortex interaction. The shaded area indicates where vortex interaction occurs determined from figure 6.23. The tip vortex axial positions are described well by the linear fit at early vortex ages. The radial positions on the other hand varied more around the unit radial location.

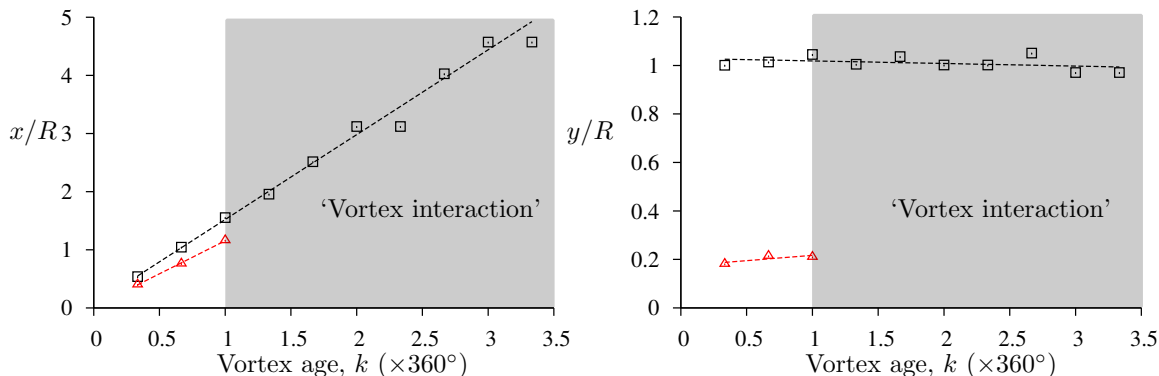


FIGURE 6.25: Axial (left) and radial (right) tip (black) and root (red) vortex positions in the top half of the wake at $\lambda = 3.55$. The shaded region indicates where vortex interaction occurs.

In the three filament system shown in figure 6.23, interaction occurs in a similar fashion to Felli et al. (2011). They noted that the coalescence process between tip vortices occurred in a ‘multi-step’ fashion which is dependent on the number of blades. For their three filament system, an initial grouping of two filaments occurs with a ‘single’ filament progressing downstream on its normal trajectory. A secondary grouping then occurs between the ‘single’ filament and the previously paired filaments Felli et al. (2011). A similar phenomena is seen in figure 6.23 and is a significant result of the current research. However, as noted by Sørensen (2011), the stability problems of wind turbines and marine propellers are analogous but the wakes are not the same. In the former energy extraction occurs at the rotor plane whereas energy is added at the rotor plane by the latter. It must be noted that numerical simulations have not always managed to capture this ‘multi-step’ process, *e.g.* a vorticity snapshot (figure 8) from the unsteady simulations of Ivanell et al. (2007), appear to agree with the currents

results and those of Felli et al. (2011). However, figure 13 in (Ivanell et al. 2010), reveals the pairing occurs between adjacent vortices in a one step process. This may highlight an effect of the symmetry boundary conditions imposed on the flow. The 'multi-step' grouping mechanism seen in figure 6.23 appears universal for helical vortex systems.

Wake expansion is evident for $VA \leq 360^\circ$. The difference in radial position of the tip vortex at $\sim 1.55R$ and $\sim 1.95R$ is the first indication of interaction between adjacent tip vortices. The interaction between the induced velocity fields causes the mutual induction instability mode. The mutual interaction causes the well known 'leap-frogging' phenomena seen in vortex rings (Green 1995). The closed vortex filaments can interact in a stable manner. However, interaction between helical filaments leads to instability and has been seen in helicopter (Stack 2004), marine propeller (Felli et al. 2011) and wind turbine (Alfredsson and Dahlberg 1979) studies.

By $x/R \sim 3.1$, the interaction has progressed further such that the axial position of vortices initially spaced by $h/3$ apart are now approximately equal. It is evident from the vorticity contours that the relative strengths of the vortices differ and this will promote the interaction. By $x/R \sim 4.5$, the two vortices have coalesced into a single patch of vorticity. The location of vortex interaction, $x/R \sim 3.1$, correlates well to the axial location where the TKE layer begins to thicken in figure 6.11. Further, the location of vortex coalescence compares well with the results of Montgomerie and Dahlberg (2003), who noted vortex pairing occurred 'a little before $x/R = 4$ downstream'. They also compare well to the numerical simulations of Ivanell et al. (2010) who found pairing had occurred by $x/R = 5$. This result is quite surprising given the different rotor geometries and Reynolds number of the aforementioned studies. The interaction between tip vortices is a source of TKE and downstream turbines should avoid this turbulent region. The data suggest, the onset of tip vortex interaction can be gauged from non-phase locked data by the thickening of the elevated TKE layer. Prior to investigating the mechanism of the pairing instability in section 6.0.10, the flow states on the rotor at λ_d are presented in the following section.

6.0.9 Rotor blade flow structure at λ_d

The phase-locked average vorticity field presented in figure 6.23 showed blade wakes connected to the tip and root vortices at early vortex ages. Further, the BEM analysis implicitly depicted $\partial\Gamma_B(r)/\partial r \neq 0$ across the span in figure 6.7. It is important to investigate the flow states on the rotating blades and the wakes they create at λ_d . They are presented in the current

section. The geometrically scaled blade experienced large regions of flow separation due to minimal blade twist. A large amount of twist was incorporated in the optimum Glauert rotor design to minimise flow separation. The flow states around the blade at several spanwise locations were determined using the experimental setup shown in figure 6.26. U_∞ is in the positive x -direction with the blade rotating in the negative z -direction. As the blade appears in the field of view, a mask file was created to avoid erroneous vectors appearing within the blade. Fluctuations in the tip speed ratio required enlarging the airfoil profile dimensions. The mask file was generated by averaging a random sample of instantaneous frames. The airfoil profile will be shown in white in the velocity and vorticity fields. The region in shadow increases toward the blade root due to the increased twist of blade. Without employing mirrors, the aluminium blades created dark regions aft of the blade. A rotor blade was thus created out of polycarbonate to maximise transmission of the laser sheet through the blade and hence minimise dark regions in the field of view.

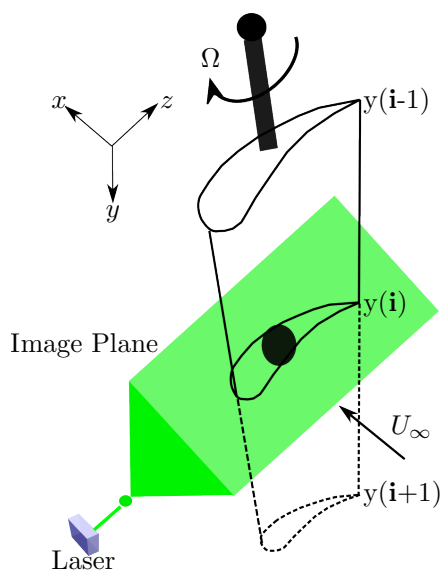


FIGURE 6.26: Experimental setup to determine the tangential velocity component and the spanwise circulation distribution. U_∞ is aligned with the positive x direction and the blade rotates at an angular speed Ω . The laser sheet illuminates an x - z plane. The camera is perpendicular to the laser sheet indicated by the black circle in the middle of the image plane.

Data was captured over the spanwise range $0.393 \leq y/R \leq 1.09$, in increments of $\Delta y = 0.087R$. Data was also taken at the lifting surface termination point in the root region. The laser sheet was moved to the desired spanwise location by the computer controlled traverse. The location of the spanwise measurement planes are shown in figure 6.27. A total of 560 image pairs were taken at each spanwise location. The images were temporally averaged to produce mean azimuthal, $\bar{\mathbf{w}}$, and streamwise, $\bar{\mathbf{u}}$ velocity fields around the airfoil.

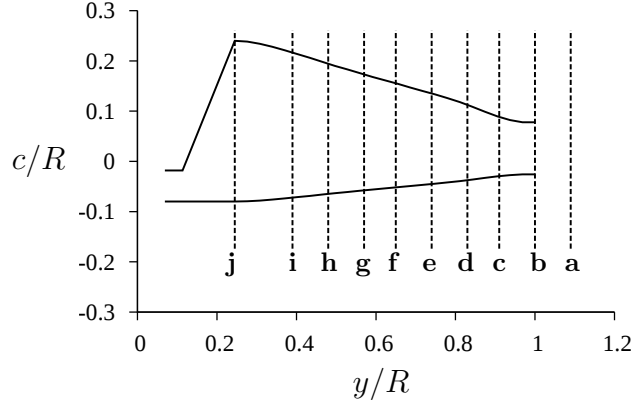


FIGURE 6.27: Plan form view of the blade with dashed lines illustrating the spanwise locations where data was captured in the x - z plane. **a)** $y/R = 1.09$, **b)** $y/R = 1.00$, **c)** $y/R = 0.91$, **d)** $y/R = 0.83$, **e)** $y/R = 0.74$, **f)** $y/R = 0.65$, **g)** $y/R = 0.57$, **h)** $y/R = 0.48$, **i)** $y/R = 0.39$, **j)** $y/R = 0.24$.

The axial velocity fields in the vicinity of the blade are shown in figures 6.28 and 6.29. Refer to figure 6.27 for the spanwise locations. The origin is located at the quarter chord position determined from the mask file. A reflection off the nacelle is the cause of the erroneous vectors downstream of the rotor plane.

The velocity field outboard of the tip (**a)** $y/R = 1.09$) displays a speed-up downstream of the trailing edge due to pressure equalisation occurring at the tip. Pressure equalisation causes a 3D fluid flow from the pressure to suction surfaces of the blade and causes the tip vortex to form. Inboard of the tip ($y/R \leq 1$), a wake is present downstream of the blade. Shear in the wake reveals the trajectory of the trailing edge vorticity sheet. This vorticity sheet is visualised as the blade wakes in the phase-locked vorticity fields. The vorticity in this sheet is either entrained by the tip vortex or diffused to the background flow. Evidence of tip vortex formation is shown at $z/R = 0.5$ and $x/R = 0.1$ for the tip profile. As the field of view is not orthogonal to the tip vortex axis, the velocity field appears skewed. For $y/R \leq 1$, only the shear layer is present in the field of view as the tip vortex forms slightly inboard of the tip.

Flow separation is shown by the solid black line which encapsulates the region of flow reversal in figures 6.28 through to 6.31. Separation occurs between $0.57 \leq y/R \leq 0.74$. Further, it likely occurs for $y/R \leq 0.57$ but parallax does not allow it to be visualised. When visualised, the separation point always occurs between $0.75 \leq c \leq 1$. The minimal flow separation depicted in the axial velocity fields gives confidence the blade design is operating efficiently at the experimental Reynolds number. Therefore, the vorticity shed into the wake will be primarily due to $\partial\Gamma_B(r)/\partial r$.

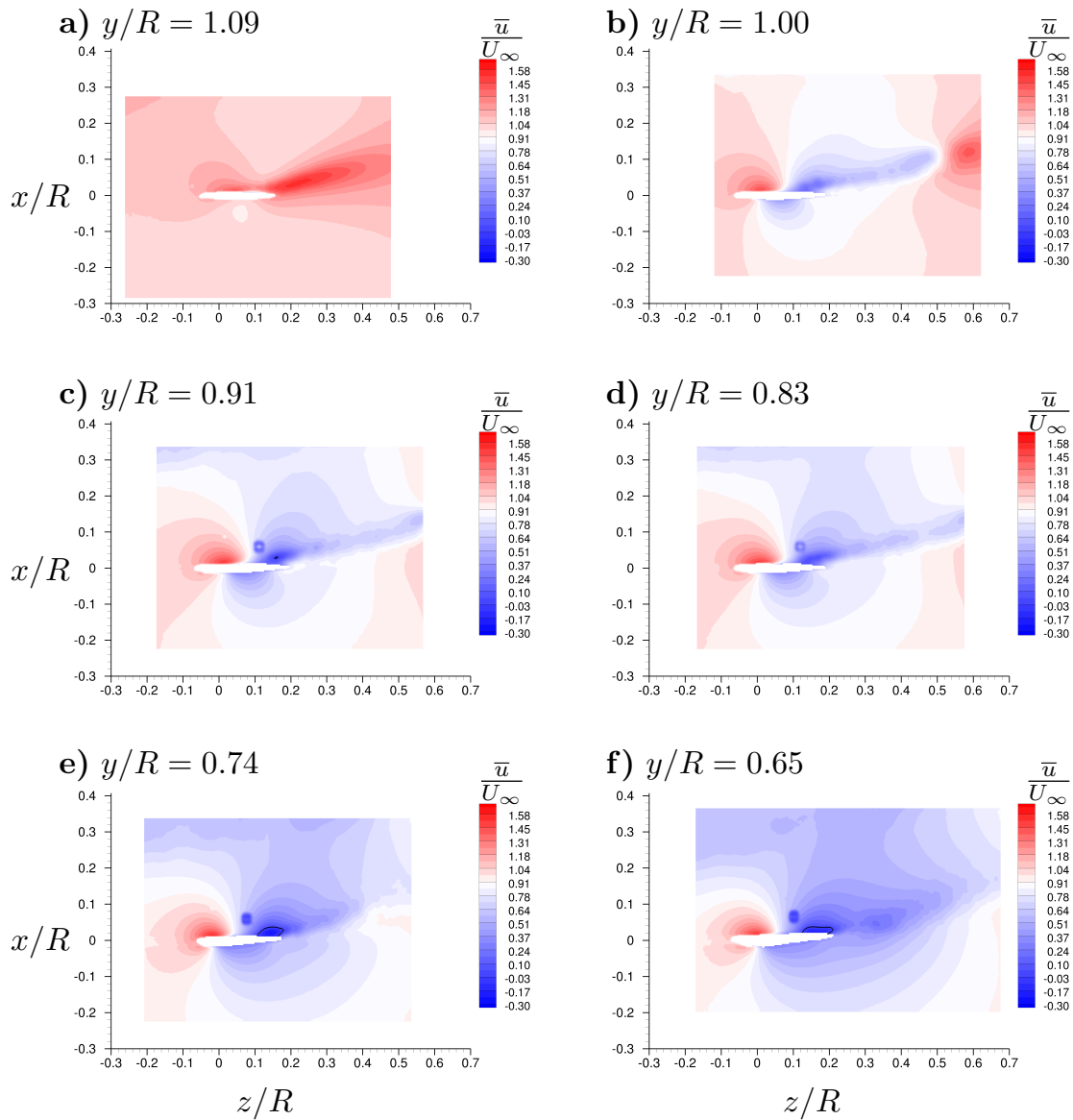


FIGURE 6.28: Axial velocity profiles generated by the rotating wind turbine blade at spanwise positions $0.65 \leq y/R \leq 1.09$. The solid black line encapsulates region of entirely negative flow. The airfoil profile is shown in white.

The azimuthal velocity fields at the same spanwise locations are shown in figures 6.30 and 6.31. It must be remembered, the azimuthal velocity component is generated solely at the rotor. Further, $\bar{\mathbf{w}} \sim 0$ in a large portion of the field of view. The rotor induces an azimuthal velocity component in the wake due to the reactionary force imparted on the flow by the blades. The azimuthal velocity component also reveals the trajectory of the trailing edge vorticity sheet. It is largest close to the tip due to the increase in blade loading. For $y/R \leq 0.75$, the wake of the previous blade is visible. The large chord of the research oriented blade produces a high solidity in the root region.

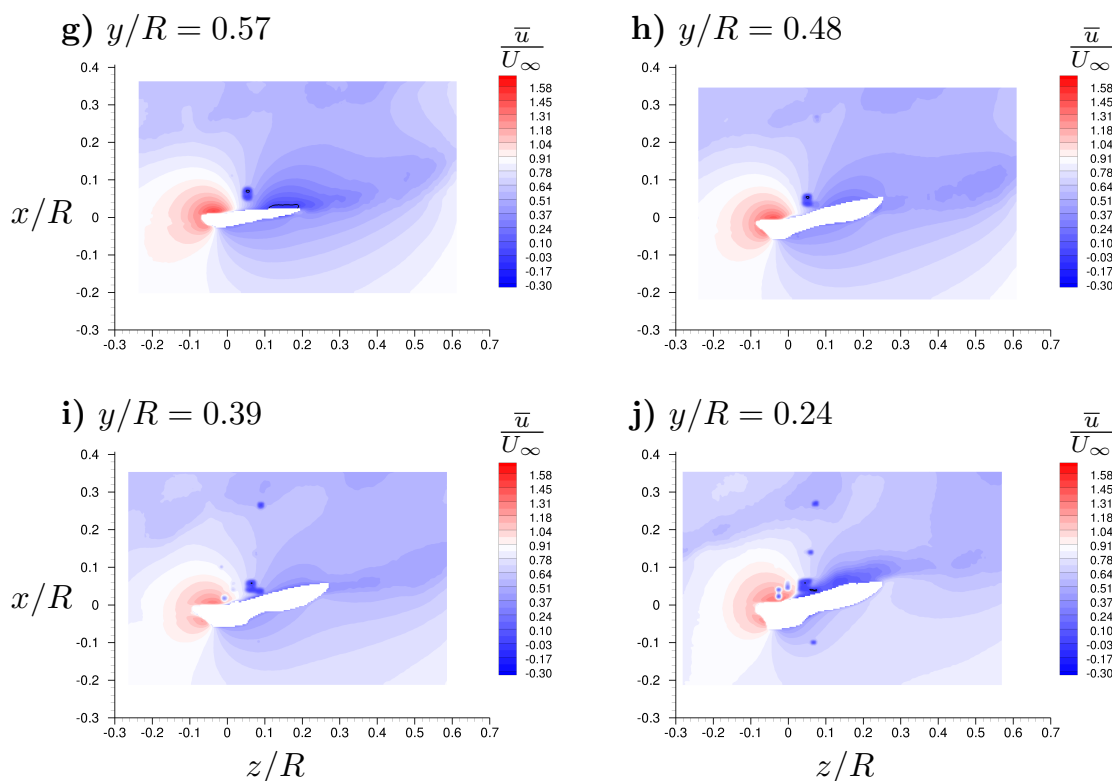


FIGURE 6.29: Caption as for figure 6.28 for spanwise positions $0.245 \leq y/R \leq 0.57$.

The blade $\bar{\mathbf{u}}$ and $\bar{\mathbf{w}}$ velocity fields allow the blade bound circulation distribution, $\Gamma_{B,\text{exp}}(r)$, to be determined. $\Gamma_{B,\text{exp}}(r)$ is important as the strength of the trailing vortex system behind a planar wing is controlled by its gradient, $\partial\Gamma_{B,\text{exp}}/\partial r$ (Betz 1935). For the one-blade and three-blade configurations, $\Gamma_B(r)$ was estimated by lifting line theory. The theory overestimated the circulation contained in the tip and root vortices. The difference arose due to a combination of 3D effects and the lower experimental Reynolds number of the rotating blades compared to the 2D airfoil performance data. The velocity fields indicate separation was restricted to the $0.57 \leq y/R \leq 0.74$, so for the purpose of determining $\Gamma_{B,\text{exp}}$, the flow will be considered two-dimensional.

The blade bound circulation distribution is determined by equation 3.5. However, the choice of integration path influences $\Gamma_{B,\text{exp}}(r)$ heavily (Bhagwat and Leishman 2000). The chosen path must only consider blade bound vorticity and not wake vorticity (Bhagwat and Leishman 2000). In rotary wing systems, small integration contours are desirable to avoid vorticity in the wakes of other blades. The integration path used here is calculated from the blade leading and trailing edges obtained from the mask file. The integration path length, I_l/R , is incrementally increased to investigate its effects on $\Gamma_{B,\text{exp}}$. As I_l increases, $\Gamma_{B,\text{exp}}$

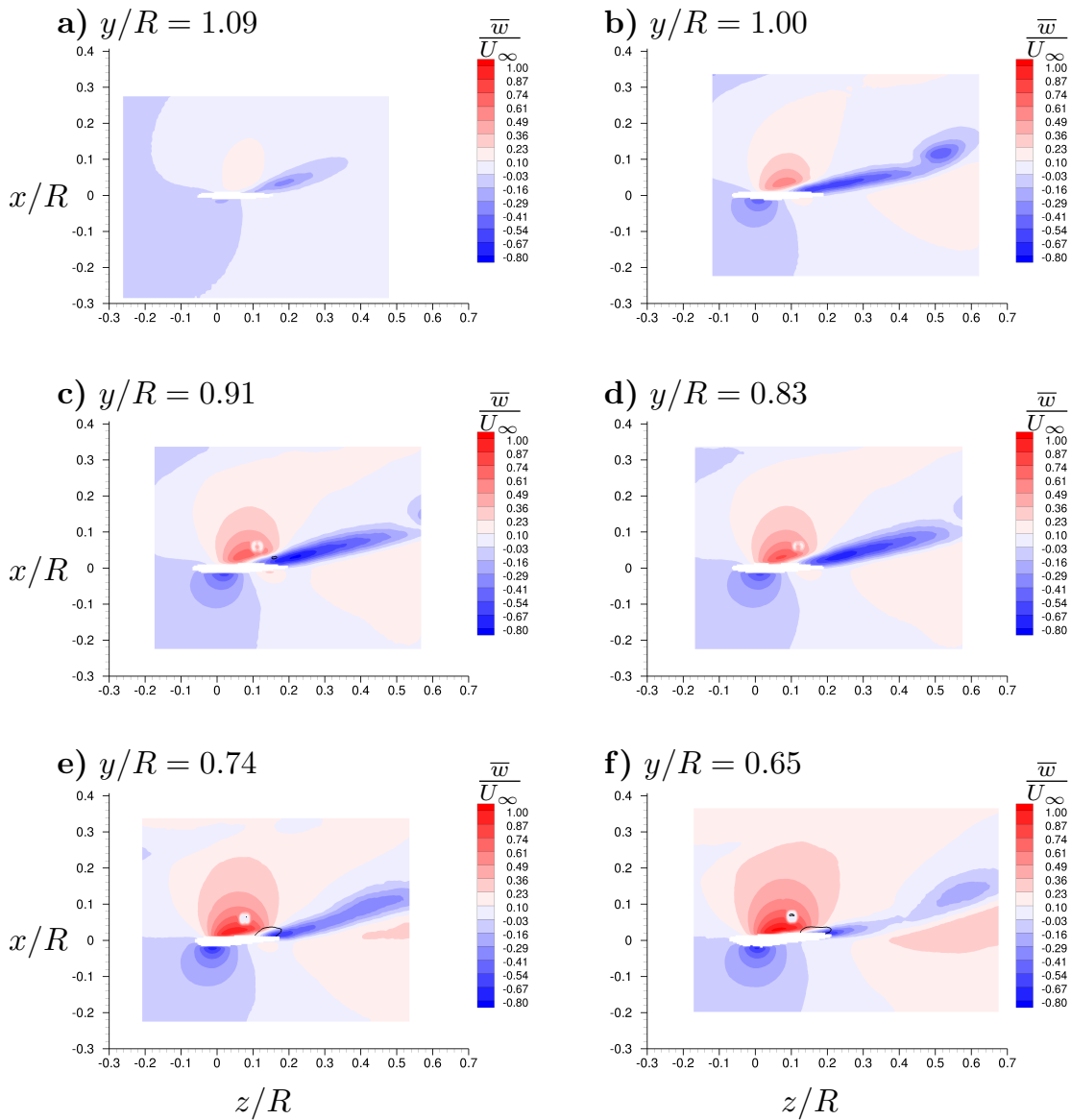


FIGURE 6.30: Azimuthal velocity profiles generated by the rotating wind turbine blade at spanwise positions $0.65 \leq y/R \leq 1.1$. Flow separation can be seen. Airfoil section is shown in white.

increases rapidly before reaching an asymptotic value as shown for several spanwise locations in figure 6.32. Similar phenomenon were reported in helicopter wakes (Bhagwat and Leishman 2000). The dip in the circulation distribution before a return to the asymptotic value is due to a reflection off the nacelle. The asymptotic value was recorded for each spanwise location to determine the $\Gamma_{B,\text{exp}}(r)$ distribution.

The experimentally derived circulation distribution, $\Gamma_{B,\text{exp}}(r)$, is compared to the BEM predictions of section 6.0.3 in figure 6.33. There is a larger variation in $\Gamma_{B,\text{exp}}(r)$ compared to the BEM predictions. The experimental results indicate a greater circulation than the BEM predictions in the internal half of the blade ($y/R \leq 0.74$). These points are erroneous as the

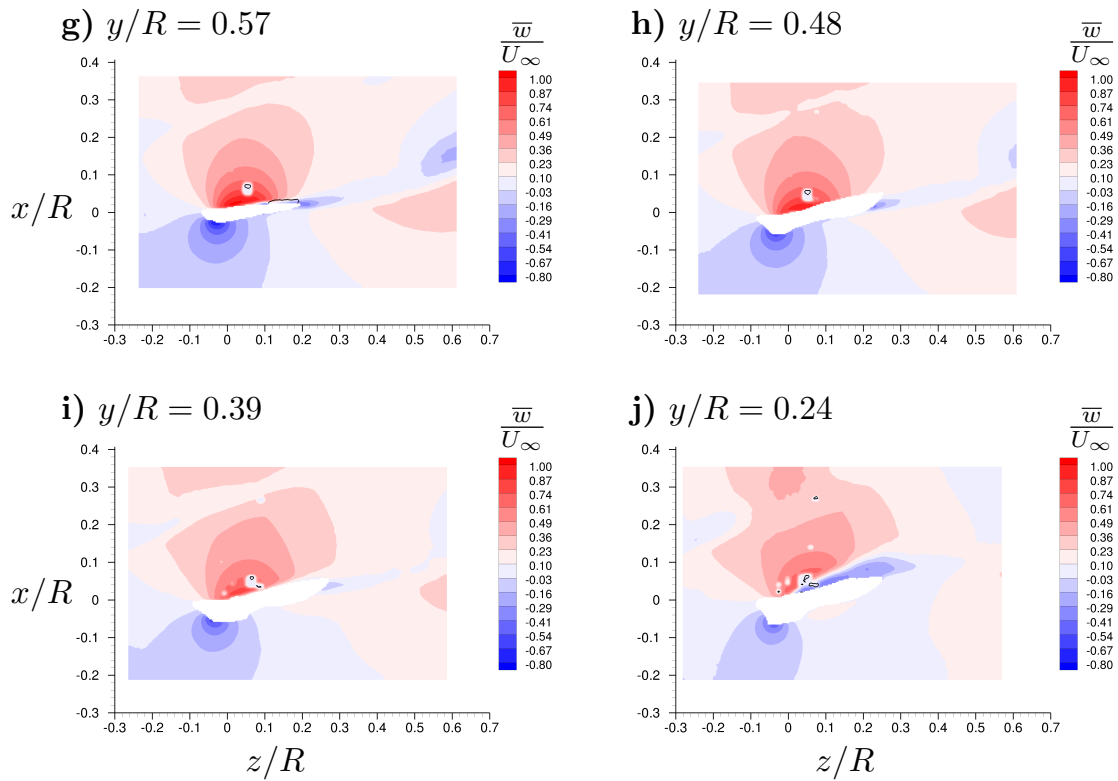


FIGURE 6.31: Azimuthal velocity profiles generated by the rotating wind turbine blade at spanwise positions $0.245 \leq y/R \leq 0.57$. Flow separation can be seen. Airfoil section is shown in white.

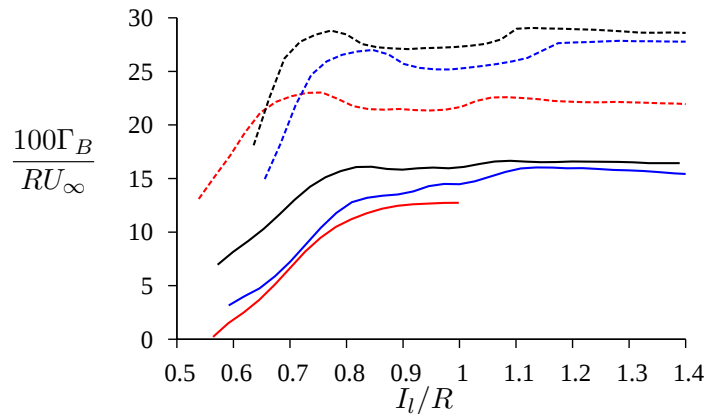


FIGURE 6.32: Dependence of blade bound circulation on the integration path length. Solid red: b), solid blue: c), solid black: d), dashed red: e), dashed red: f), dashed red: g).

Reynolds number of the 3D rotating wing as shown in figure 6.6 is less than the 2D airfoil data of Jacobs and Sherman (1937). The discrepancy most probably arises from the restricted optical access due to the twist of the blade. Blade twist does not allow imaging of the blade surfaces accurately. Where both surfaces of the airfoil are clearly visible ($y/R \geq 0.74$), the experimental data under predict the BEM data as expected. Greater confidence is thus held in the $y/R \geq 0.74$ data. $\Gamma_{B,\text{exp}}$ reduces in the tip region due to tip effects. A non-zero circulation

value, $\Gamma(1.09) = 0.012$, was calculated outboard of the tip. As the BEM method stipulates, $\Gamma_B(r \geq 1) = 0$, the $\Gamma(1.09)$ value is used as the measure of uncertainty in figure 6.32.

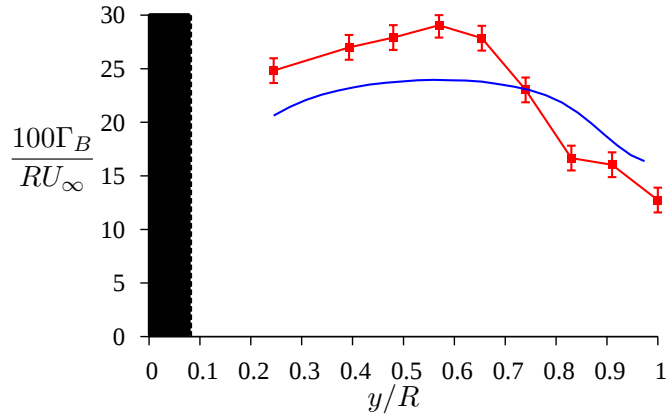


FIGURE 6.33: Spanwise variation of the blade bound circulation calculated by experimentally (red) and by a BEM method (blue) at λ_d . Error bars indicate the circulation calculated at $y/R = 1.09$.

The gradient of $\Gamma_{B,\text{exp}}(r)$ is integrated in the tip region to determine the blade bound circulation shed into the wake. As flow separation was present between $0.57 \leq y/R \leq 0.74$, these values are not used in the integral. Thus evaluating equation 2.3 between $y/R = 0.83$ and $y/R = 1$ allows an estimation of the blade bound circulation shed into the wake in the tip region. The blade bound circulation shed into the wake in the tip region was $\Gamma_B = 0.17$, larger than both the average tip vortex circulation $\bar{\Gamma} = 0.151$ at $\text{VA} = 120^\circ$ and the average of the tip vortices prior to the onset of interaction, *i.e.* $\text{VA} \leq 600^\circ$. This latter value was $\langle \Gamma \rangle = 0.1375$. It is unsurprising that the total blade bound circulation in the tip region is not contained in the tip vortices. A portion of Γ_B exists in the trailing edge vorticity sheet. Further, Γ_B reduces in the wake due to viscous and turbulent diffusion. It must be noted that the trailing vortex system presented in Betz (1935) is a highly idealised model. The current results do not adhere to this idealised model.

6.0.10 Pairing instability affecting the tip vortices

The transition to general wake instability seen in the phase-locked average vorticity map of figures 6.23 and 6.3 occurs in a similar fashion to leapfrogging in vortex rings. If the helical pitch is small, adjacent vortices interact as shown in figure 2.6. However, leapfrogging cannot occur in a HAWT wake due to the connectedness of the filaments. The induction leads to vortex entanglement and a pairing instability rather than leapfrogging. By representing the vortex wake of a HAWT as a series of vortex rings, Bolnot et al. (2011) found a pairing instability occurs when unstable perturbations propagate upstream faster than the advection

speed of the vortices (Bolnot et al. 2011). However, the pairing instability violated the axisymmetric notation of the initial vortex system.

The phase-locked average planar PIV data revealed the pairing instability when the pitch reduces. The onset of the mutual inductance mode was deduced from the phase-locked position of the tip vortices at a particular vortex age. It should be noted that the pairing instability is just one of several instability mechanisms which likely affect the vortices. However, with planar PIV data, it is difficult to investigate the existence of 3D instability mechanisms. These include the short-wave and long-wave instability modes predicted by analytical studies (Widnall 1972). In chapter 5, vortex meander was proposed as a mechanism to deduce where the wake becomes unstable. The meander of the tip and root vortices at λ_d is presented in the following section.

Meander of tip and root vortices at λ_d

The meandering motions of the tip and root vortices will now be investigated. The scatter of instantaneous vortex positions is shown in figure 6.34. The colour of the data points represents the blade number which created the tip vortex. The two interacting vortices were evaluated as a single vortex and are purple owing to the contributions of the blue ($VA = 720^\circ$) and red ($VA = 840^\circ$) tip vortices. Tip vortex coalescence has occurred by $x/R \sim 4.5$. The scatter plot reveals meander is not equal in both axes in the current setting as indicated by Hu et al. (2012). The tip vortex fluctuations are largest in the axial direction. The scatter plot reveals qualitatively that meander increases with vortex age.

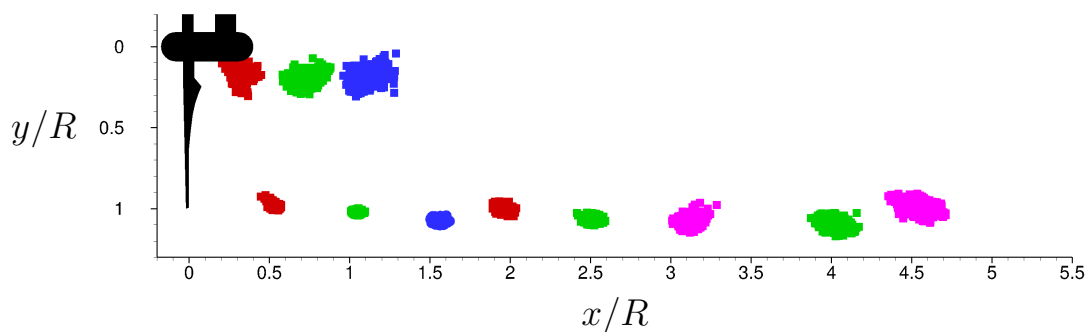


FIGURE 6.34: Scatter plot of tip and root vortex meander for the three bladed optimum Glauert rotor operating at $\lambda = 3.55$. Colour indicates blade number which created vortex. Meander magnitude increases with vortex age.

The magnitude of the meander is presented in figure 6.35. The hollow symbols and dashed line represent meander in the radial direction whereas the solid symbols and lines represent meander in the axial direction. Tip vortex results are shown in black with root vortex results

shown in red. The root vortices meander more than the tip vortices at an equivalent vortex age. The reduced strength and turbulence in the root region cause the larger meander.

Meander of the tip vortices is largest in the axial direction. The uncertainty in the meander magnitude is estimated as $\pm 6\%$. In a similar fashion to the one-blade results, the magnitude of the axial meander is corrected for the water channel sloshing. The meander is taken relative to the earliest vortex realisation, *i.e.* at a vortex age of 120° . The adjusted meander is shown on the right of figure 6.35. Meander at a vortex age of 120° is larger than that at 240° due to the blade wake. Comparing figure 6.23 to 6.34, the scatter plot indicates vortices within the blade wake were sometimes detected. Aside from the reduction in meander between 120° and 240° , vortex meander increases with vortex age. There is a sharp increase when the meander of the interacting vortices is characterised. The turbulent interaction results in large scatter of the identified vortices.

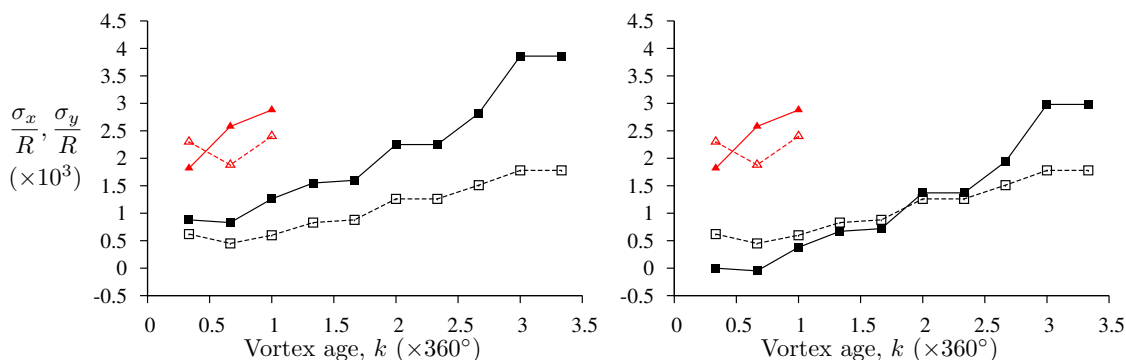


FIGURE 6.35: Tip and root vortex meander in the radial (hollow) and axial (filled) directions at λ_d . Left: raw results, right: results corrected for water channel sloshing (*i.e.* $\sigma_x = \sigma_x - \sigma_x(\text{VA}=120^\circ)$). Meander magnitude increases with vortex age.

The origins of vortex meander in fixed wing tip vortices were outlined in chapter 2. The experimental data contain numerous perturbations which could trigger instability in the tip vortices. It must be remembered that the current results are not anomalous as numerous experimental investigations of unperturbed helical tip vortices have captured the vortex pairing phenomena (Alfredsson and Dahlberg 1979; Caradonna 1999; Montgomerie and Dahlberg 2003; Felli et al. 2011). Flow field turbulence has been proposed as a mechanism to excite the vortex cores (Jaquin et al. 2001). The freestream turbulence level was 1.2% which is larger than that found in wind tunnels. The effect of freestream turbulence intensity is investigated in chapter 7. A further mechanism which could trigger an instability is the inherent coning angle ($\psi = 0.5^\circ$) of a single blade as outlined in chapter 3. This coning angle reduces the normal force coefficient and hence blade loading of a single blade. The difference

in vortex strength may trigger the mutual inductance instability mode at an earlier vortex age compared to an equally loaded turbine would experience. Although the origins of the meander are difficult to ascertain, the meander characterisation process reveals that the wake is unstable by the continual growth of the meander amplitude. The effect of tip speed ratio is investigated in the following section.

6.0.11 The effect of tip speed ratio

The wake structure of a HAWT turbine at λ_R was presented in figures 6.2 and 6.3. It was confirmed wake structure was independent of the two regulation methods. The streamwise velocity and vorticity fields of the drive cases are reproduced in figures 6.36 and 6.37. Velocity profiles are also shown of the right of figure 6.36 for $0.5 \leq x/R \leq 3.5$ with $0.5R$ resolution. The red and blue lines represent results at $x/R = 0.5$ and $x/R = 3.5$. The tip and root vortex shear layers are evident in these profiles by the large gradients at $y/R \sim 1$ and $y/R \sim 0.4$ respectively. The shear layers weaken with axial distance due to viscous diffusion and instabilities which affect the vortices. The velocity deficit is fairly constant across a large portion of the blade ($0.5 \leq y/R \leq 0.9$) indicating efficient turbine operation. The velocity deficit in the root region is reduced due to the low solidity in the root region $y/R \leq 0.24$. Similar phenomenon were seen in the wake velocity contours of Krogstad and Adaramola (2011) at high tip speed ratios ($\lambda = 8.25$ and $\lambda = 9.15$). However, it is not seen in Ebert and Wood (2002) runaway study due to the lifting surface extending to rotational axis.

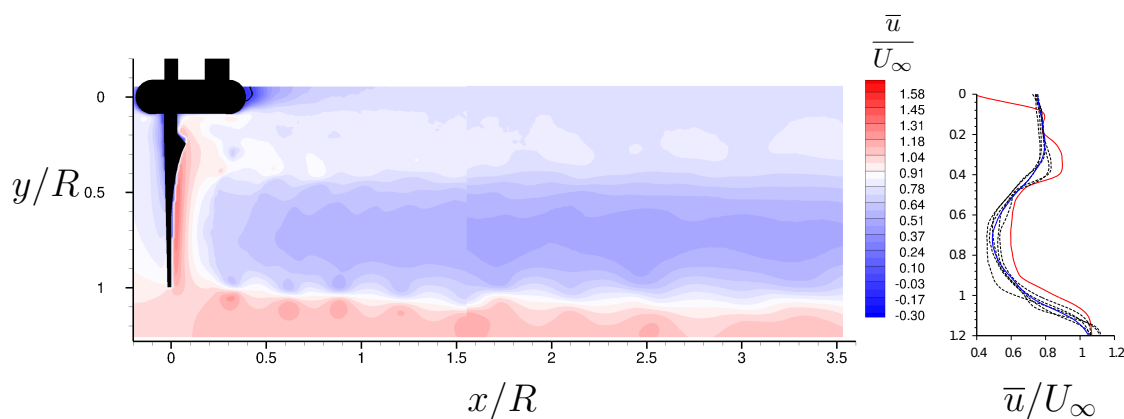


FIGURE 6.36: Average streamwise velocity field (left) and profiles in the range $0.5 \leq x/R \leq 3.5$ with $0.5R$ resolution at the runaway tip speed ratio in the top half of the wake.

Figure 6.37 indicates for the first time that tip AND root vortices can co-exist in a HAWT wake and persist for some distance. Tip vortices are once again situated close to

the unit radius, whereas root vortices form at $y/R = 0.4$, near the root region lifting surface termination point. The root vortices form at $y/R = 0.4$ due to the large $\partial\Gamma_B(r)/\partial r$ value as shown in figure 6.7. Blade wakes are visible at early vortex ages (VA $< 360^\circ$) in figure 6.37. The blade wakes are visualised by ω_z due to the skew in the wake.

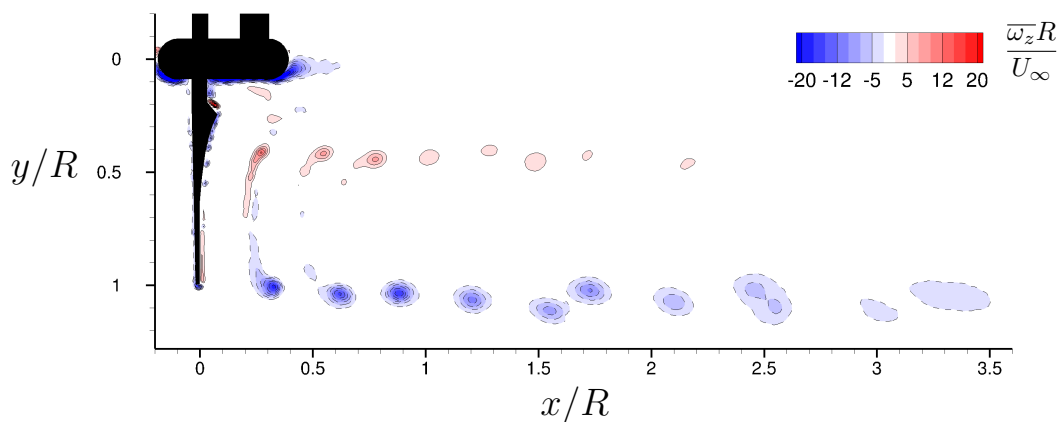


FIGURE 6.37: Vortex wake at the runaway tip speed ratio in the top half of the wake.

The tip vortices of a one-blade configuration at $\lambda \sim \lambda_R$ were not affected by the mutual inductance instability mode. Like the three blade configuration at λ_d , figure 6.37 indicates the mutual inductance mode is present at λ_R . The runaway tip speed ratio cases thus allow a direct evaluation of the effect of helical pitch on wake stability.

Interaction between tip vortices becomes evident in figure 6.37 for $x/R \geq 1.5$. The two interacting tip vortices are 600° and 720° old. The younger vortex (VA = 600°) moves radially outward whereas the older vortex (VA = 720°) moves inward due to the resultant induced velocity as shown schematically in figure 2.6. The root vortices at the same vortex age in figure 6.37, *i.e.* located at $y/R \sim 0.4$ and $1.25 < x/R < 1.5$, move in the opposite direction to the tip vortices due to their opposite orientation. This is the first time mutual interaction between root vortices has been seen experimentally. As the vortex age of the two interacting tip vortices increases, entanglement progresses as evident at $x/R \sim 2.5$, where the vortices are now 960° and 1080° old. By $x/R \sim 3.3$, vortex coalescence has occurred fully and the two tip vortices appear as a single patch of vorticity. The tip vortex signature decreases rapidly thereafter due to the spatial smoothing of the phase locking technique.

The phase-locked trajectories of the tip and root vortices shown in figure 6.38 were evaluated by the maximum of the Γ_1 field. The dashed lines represent a linear regression applied to the vortex positions. The shaded area indicates where vortex interaction occurs as estimated

from figure 6.37. The axial misalignment between the tip and root vortices grows with vortex age.

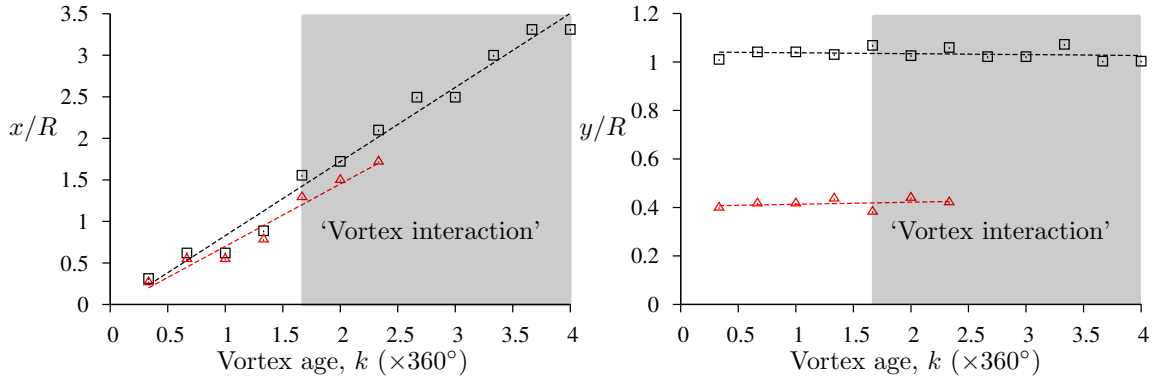


FIGURE 6.38: Axial (left) and radial (right) tip (black) and root (red) vortex positions in the top half of the wake at $\lambda_R = 6.07$. The shaded region indicates where vortex interaction occurs.

Vortex properties were also evaluated to investigate evolution in a runaway state. The circulation of the tip and root vortices at λ_R is shown on the left of figure 6.39. The dashed lines and hollow symbols represent results using the Γ_2 method whereas the solid lines and symbols are λ_{ci}^2 results. The more restrictive nature of the λ_{ci}^* contour is shown in figure 6.39. Lifting line theory at λ_R predict blade bound circulation in the tip and root regions of $\Gamma_B = 0.16$. According to the fixed wing trailing vortex system of Betz (1935), this circulation will be contained in the tip and root vortices. The total blade bound circulation predicted by lifting line theory is not present in the tip and root vortices.

Figure 6.39 shows the circulation of the tip vortices is more than twice that of the root vortices. The circulation of the three blade configuration is less than the one blade data of figure 6.20. Lifting line theory also predicts greater blade bound circulation in the one blade configuration. Further, unlike the one-blade data of figure 6.20, circulation of both the tip and root vortices reduces slowly due to viscous diffusion until vortex coalescence occurs. When vortex coalescence occurs, the circulation of the newly formed vortex structure is the sum of the vortex components prior to coalescence. This is evident at vortex ages of 960° and 1200° for the tip vortex results. This work quantifies the qualitative visualisations of (Felli et al. 2011). The unpaired third tip vortex filament is largely unaffected as indicated by the result at a vortex age of 1080° .

As vorticity/angular momentum is diffused into the background flow due to viscosity, the vortex radius increases with vortex age. The variation of vortex core radius with vortex age is shown on the right of figure 6.39. The vortex radius determined from the λ_{ci}^2 method is constant prior to decreasing as the region above the λ_{ci}^* value reduces with vortex age. The Γ_2

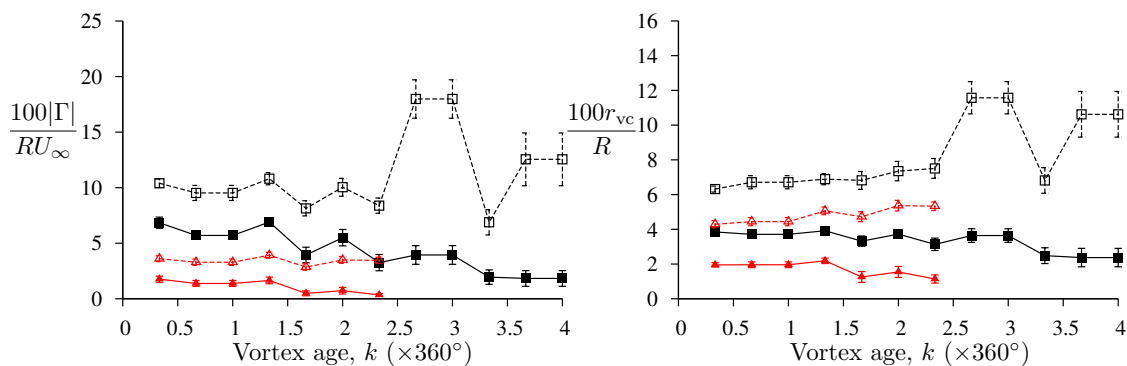


FIGURE 6.39: Mean tip (black) and root (red) vortex property variation with vortex age for the three bladed configuration at $\lambda_R = 6.07$. Left: non-dimensionalised circulation and right, non-dimensionalised core radius. Dashed line and hollow symbols, Γ_2 data, solid line and symbols, λ_{ci}^2 data.

derived data on the other hand, correctly show the tip and root vortex radii increase steadily prior to vortex coalescence. The coalesced vortex radius is nearly twice that of the initial vortices. The vortex radius of the three-blade configuration is less than the one-blade data of figure 6.20.

The vortices at runaway also experience meander. The scatter plot of the instantaneous positions at λ_R is shown in figure 6.40. Meander magnitude especially in the root vortices appears less than that at λ_d as shown in figure 6.34. The root vortices at λ_R are situated further toward the tip and the influence of the turbulent region adjacent to the nacelle will be reduced.

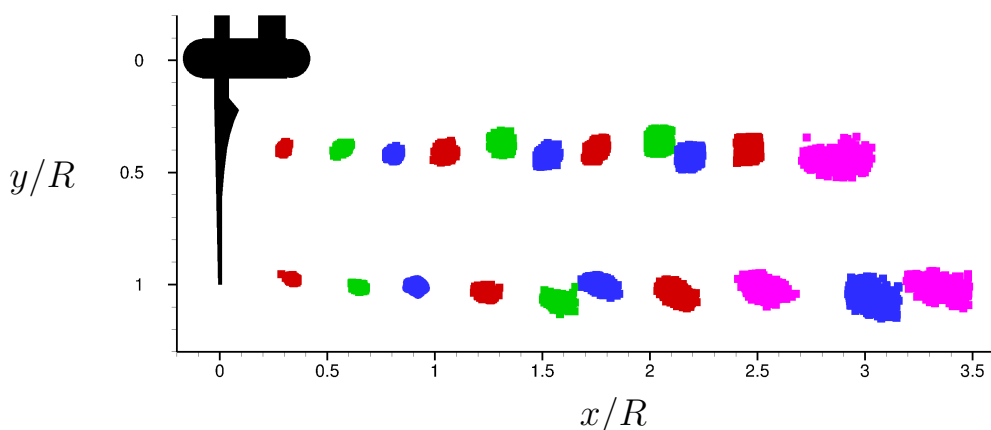


FIGURE 6.40: Scatter plot of tip vortex meander for the optimum Glauert rotor operating at λ_R . Colour indicates blade number which created vortex. Meander magnitude increases with vortex age.

The meander magnitude at λ_R is characterised in figure 6.41. Meander magnitude increases with vortex age in a similar fashion to λ_d . Meander in the axial direction is again

6.1. Summary of optimum Glauert rotor wake data

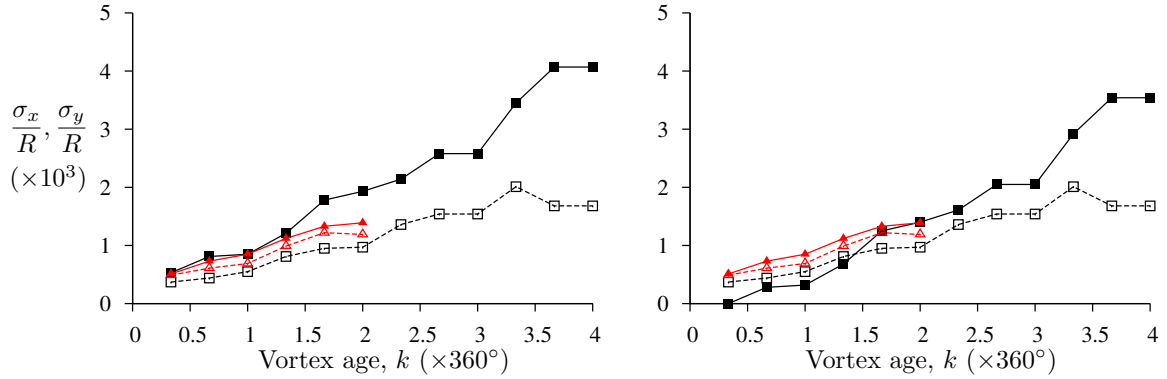


FIGURE 6.41: Tip (black) and root (red) vortex meander in the radial (hollow) and axial (filled) directions for the optimum Glauert rotor operating at λ_R . Left: raw results, right: results corrected for water channel sloshing (*i.e.* $\sigma_x = \sigma_x - \sigma_{x(\text{VA}=120^\circ)}$). Meander magnitude increases with vortex age.

larger than that in the radial direction. The uncorrected (left) axial meander of the tip and root vortices at early vortex ages is very similar. The effect of pitch and implicitly vortex interaction on meander magnitude can be evaluated by comparing figures 6.41 and 6.22. Meander in the three blade configuration is much larger than the single blade configuration. As an example, the radial meander of the one-blade configuration at a vortex age of $\text{VA} = 2880^\circ$ is approximately equal to a vortex half as old in the three-blade configuration. Further, the axial meander of the one blade configuration is half that of the three blade configuration at the same vortex ages. The correlation between vortex interaction and meander is clearly evident.

6.1 Summary of optimum Glauert rotor wake data

In this chapter the near wake of an optimum Glauert rotor was characterised at several tip speed ratios. Although expected, driving the turbine was shown to have no effect on wake structure at runaway for the first time. The phase-locked average wake was characterised by a velocity deficit and existence of coherent tip and root vortices. The turbine tower affected vortex roll-up and caused the rapid degeneration of the tip and root vortices in the bottom half of the wake at λ_d . The distance the tip vortices persist in the top half of the wake was dependent on blade number and tip speed ratio.

Rotor performance was predicted by a BEM method. The data indicate the wake location of root vortex cessation is dependent on proximity to the turbulent region adjacent to the nacelle. The work is the first to observe interaction between root vortices. The blade bound circulation distribution was also determined experimentally and found to be less than the

BEM predictions. The results highlight the need for accurate airfoil performance data.

Vortex interaction lead to vortex coalescence and wake breakdown. Vortex interaction initially occurred between two filaments in agreement with prior experimental studies. Vortex interaction was absent in the tip vortices of a single blade rotor operating near runaway. However, meander increased with vortex age for all cases. The increase in meander for the one-blade configuration is a possible indication of other (3D) instability mechanisms. These mechanisms could not be deduced here. Meander in the axial direction was larger most probably due to a sloshing in the water channel. Methods to reduce the sloshing motion were outlined in chapter 3. To account for the sloshing induced meander, the magnitude of the axial meander was taken relative to the earliest vortex realization (*i.e.* 120° or 360°). The axial and radial meander magnitudes were more comparable after the correction for sloshing. The wake became unstable sooner with increasing tip speed ratio contributing further experimental evidence that the mutual induction instability mode is dominant. In the following chapter, the effect of freestream turbulence intensity on wake stability is investigated.

Chapter 7

The Effect of Turbulence on the Near-Wake

This chapter details the evolution of horizontal axis wind turbine wakes subjected to various levels of freestream turbulence intensity. It is important to understand wake evolution under the influence of freestream turbulence intensity as wind turbines exclusively operate in a turbulent flow field, the atmospheric boundary layer. It does this by presenting wake velocity fields and showing how the wake recovers downstream. It also shows how the coherent tip and root vortices evolve and whether a similar mutual induction instability mode exists in a turbulent flow field. Particular attention is then paid to characterising vortex property evolution with increasing I_u . The meander of the tip and root vortices is also detailed and compared to the low inflow turbulence results of chapter 6.

7.0.1 The wind turbine operating environment

Wind turbines operate in a turbulent environment, the atmospheric boundary layer (ABL). A turbulent flow field increases the dynamic loading of turbines, reducing turbine lifetime. Wind farm siting should consider turbulence effects when evaluating proposed turbine layouts. The wind shear and turbulence intensity present in ABL flow are decoupled here, with the problem simplified to a turbulent flow field free of shear.

Turbulence is the random velocity fluctuations in a flow field. In chapter 3, the velocity field was decomposed into a mean, $\bar{\mathbf{u}}(\mathbf{x})$, and fluctuating, $\mathbf{u}'(\mathbf{x}, t)$, component in equation 3.11. Where $\bar{\mathbf{u}}(\mathbf{x})$ is evaluated over a time period T as in equation 7.1,

$$\bar{\mathbf{u}}(\mathbf{x}) = 1/T \int_0^T \mathbf{u}(\mathbf{x}, t) dt. \quad (7.1)$$

The root-mean-square (*rms*) velocity is evaluated to characterise the turbulent motion about the mean. The streamwise *rms* velocity is calculated via equation 7.2.

$$u_{rms}(\mathbf{x}) = \sqrt{\frac{1}{N} \left(\sum_{i=1}^N (\mathbf{u}'(\mathbf{x})^2) \right)} \quad (7.2)$$

where N is the number of samples and $\mathbf{u}'(\mathbf{x})$ is the fluctuating velocity component.

The magnitude of turbulent fluctuations is characterised by turbulence intensity, which is defined in each coordinate axis as the ratio of the *rms* velocity to U_∞ . The streamwise turbulence intensity is defined in equation 7.3. The turbulence intensity can be 20% and above in atmospheric flows.

$$I_u = \frac{u_{rms}}{U_\infty} \quad (7.3)$$

Turbulence is considered homogeneous when turbulent quantities are spatially invariant. Further, turbulence is considered isotropic when the two-point velocity correlations are zero, *i.e.* $\overline{u'v'} = \overline{u'w'} = \overline{v'w'}$ (Tennekes and Lumley 1972). Therefore in isotropic turbulence, turbulence intensity is equal in all directions, *i.e.* $I_u = I_v = I_w$ (Pope 2000). Isotropic turbulence is difficult to achieve in an experimental setting.

Turbulent kinetic energy, k , is a measure of the energy contained within the turbulent eddies. It is calculated using equation 7.4.

$$k = \frac{1}{2}(u_{rms}^2 + v_{rms}^2 + w_{rms}^2) \quad (7.4)$$

However, the fluctuating velocity components in all three axes are difficult to obtain simultaneously. The premise of homogeneity is thus commonly applied to turbulent flow fields. Turbulence at a specific spatial location is homogeneous if it is invariant in time. This occurs if turbulence production is invariant in time. Accepting the premise of homogeneity, the fluctuations in the spanwise and wall-normal directions are assumed to be equal. Thus, equation 7.4 reduces to $k = 0.5(u_{rms}^2 + 2v_{rms}^2)$. The turbulent velocity field was measured using a 2D LDV system.

The spatial and spectral structure of a turbulent flow can also be characterised. The turbulent flow field consists of eddies of differing length scale. Three length scales are important in the study of turbulence studies. The different length scales control various dynamical effects and how the turbulence interacts with the mean flow field. The length scales are, from largest to smallest, the Taylor macro (integral length) scale, Λ_{u_x} , the Taylor micro scale, λ , and the Kolmogorov length scale, η (Tennekes and Lumley 1972). Λ_{u_x} is a measure of the

largest eddy size of the turbulence. It represents the longest correlation distance between two spatial points in the flow.

The effect of freestream turbulence on wind turbine wakes has primarily been investigated from a wake recovery point of view. The velocity deficit was found by Medici and Alfredsson (2006) to be minimally affected by the freestream turbulence intensity in the near-wake. Turbulence effects become noticeable for $x/D \geq 2$ and depend on turbulence intensity (Alfredsson and Dahlberg 1981). Freestream turbulence intensity increases the transfer of momentum throughout the wake, leading to faster wake recovery (Alfredsson and Dahlberg 1979; Medici and Alfredsson 2006; Troldborg et al. 2007). After breakdown of the tip vortices, the turbulence level in the wake becomes quite uniform (Alfredsson and Dahlberg 1979).

The mechanism by which the tip vortices breakdown in low freestream turbulence flow was shown in chapter 6 to be due to a mutual induction instability mode leading to vortex coalescence. It remains to be seen whether a similar mutual induction instability mode occurs within a turbulent flow-field. The simulations by Troldborg (2008) indicated elevated freestream turbulence intensity causes earlier breakup of the tip and root vortices. This study used the actuator line method to investigate the wake evolution of the Tjæreborg wind turbine for two in-flow turbulence intensities. The turbine support structures were not modelled. In a uniform flow field, tip vortices persisted until $10R$. The Tjæreborg wind turbine is described in chapter 3 and investigated in chapter 5. In the simulated turbulent flow field ($I_u = 14\%$), the tip vortices become unstable by $2R$ as shown in figure 7.1. Vorticity signatures of tip vortices persisted to $6R$ and the wake become fully turbulent by $10R$ (Troldborg et al. 2007).

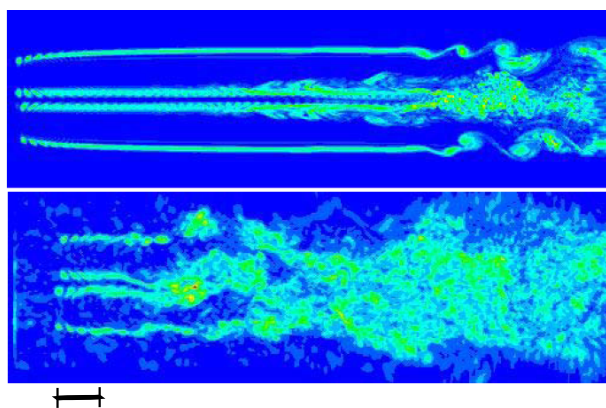


FIGURE 7.1: The effect of inflow turbulence on the evolution of numerically generated wake vortical structures behind the Tjæreborg wind turbine at the design tip speed ratio of $\lambda_d = 7.07$ (Troldborg et al. 2007). Iso-contours of vorticity on an equivalent x - y plane through the rotational axis. Top: uniform inflow, $I_u \sim 0\%$. Bottom: turbulent inflow, $I_u = 14\%$. Scale bar represents $1R$.

With increasing freestream turbulence intensity, the tip and root vortices become increas-

ingly perturbed. Diffusion of the tip and root vortices will be enhanced due to turbulent diffusion. Whether this affects the tip vortex breakdown mechanism is currently unknown. The optimum Glauert rotor was thus subjected to various levels of I_u to investigate the effect of turbulence on wake evolution.

7.0.2 Turbulence production by passive grids

The freestream turbulence intensity was varied using grids placed upstream of the wind turbine models. Grids of various designs are widely used as a method of suppressing or increasing turbulence levels in experimental facilities (Laws and Livesey 1978; Kurian and Fransson 2009). Turbulence generating structures can be separated into two categories, passive and active turbulence grids. Active turbulence grids (Makita 1991) actuate flat plates attached to the grid structure to produce the desired Taylor macro length scale, $\Lambda_{u,x}$, turbulence intensity and velocity shear profile. However, they are complex structures and are expensive to implement.

Passive grids on the other hand are most commonly simple bi-plane structures which can be easily modified and positioned. Turbulence is generated by the breakdown of the jets emanating from the grid openings. A passive turbulence grid geometry is defined by the mesh size, M , and the bar width, b , as shown on the left in figure 8.11. Each bar in the grid formation has a stagnation pressure point such that the flow must speed up through the grid openings to maintain mass conservation. Each bar will thus shed a sheet of vorticity from the shear layers which form at the edges of the bars. In isolation, the wake behind a bar in the grid will form the well known Kàrmàn vortex street. However, the biplanar nature of the turbulence grids causes interaction between wakes (Fox 1992) and a homogeneous turbulent flow field results with distance downstream.

The solidity, σ , given by equation 8.7, controls the pressure drop, C_p , across the grid and affects the $\Lambda_{u,x}$ and I_u of the turbulence generated (Laws and Livesey 1978). An optimum solidity of 34% exists for passive turbulence grids (Comte-Bellot and Corrsin 1966), with grid solidity higher than 43% leading to general wake instabilities of the jets passing through the grids (Bradshaw 1965).

$$\sigma = \frac{b}{M} \left(2 - \frac{b}{M} \right) \quad (7.5)$$

However, the turbulence generated by passive grid structures is anisotropic (*i.e.* $I_u/I_v \equiv u_{rms}/v_{rms} \neq 1$). To improve the isotropy of the generated turbulence, Vonlanthen and

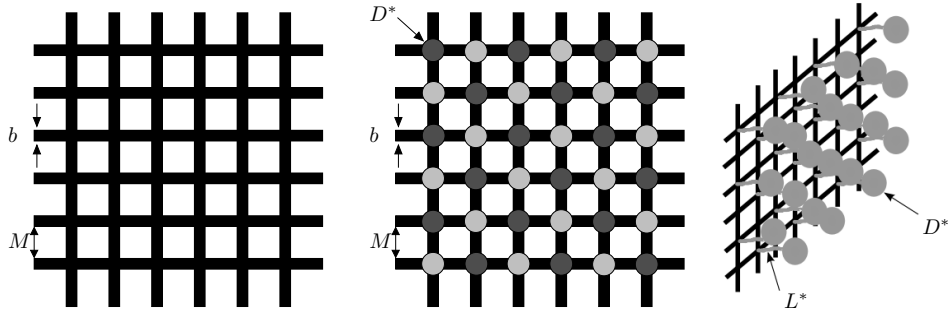


FIGURE 7.2: Passive turbulence grid geometries. Left: Grids are defined by the mesh size, M , and the bar width, b . Centre: Tethered sphere turbulence grid with sphere diameter to mesh size ratio, $D^* = 0.75$. Shade of sphere indicates tether length; light: $L^* = 1.5$, dark: $L^* = 2$. Right: isometric view of tethered sphere grid, only spheres of a single tether length are shown for clarity.

Monkewitz (2011) attached neutrally buoyant spheres to the nodes of a passive turbulence grid to produce a novel, active way of increasing the mixing downstream of the grid. This ‘tethered sphere’ grid (TSG) increased the turbulence intensity and achieved a modest improvement of the isotropy compared to the grid alone.

Three turbulence grids were used in the current study. The geometrical properties and the characteristics of the turbulence generated by the two traditional passive turbulence grids can be seen in table 7.1. To improve the isotropy and increase the intensity of the turbulence generated, a TSG was constructed following Vonlanthen and Monkewitz (2011).

The TSG used turbulence grid 2 shown in table 7.1 as the base structure. Tethered spheres were attached to the grid nodes as shown in figure 8.11 to improve mixing downstream of the grid and hence isotropy of the turbulence generated. The spheres were constructed of celluloid (‘table tennis’) balls of diameter 38 mm, which were filled with water to minimise buoyancy effects. The current TSG design operated with a sphere diameter to mesh size ratio, $D^* = D/M \sim 0.76$, shown to produce the largest turbulence intensity (Vonlanthen and Monkewitz 2008). The spheres were connected to the nodes via elastic cords. The spheres were arranged in a staggered arrangement to ensure freedom of movement arising from vortex induced vibration of the tethered spheres. The tether lengths, $L^* = L/D$, varied from 1.5 – 2. An isometric schematic of the TSG is shown on the right in figure 8.11. The turbulence intensity of the four flow/grid configurations investigated are shown in table 7.1. I_u ranges from 1.20% with no grid to 6.20% with the TSG. The macro length and time scales are commonly calculated from the velocity auto-correlations (O’Neill et al. 2004; Thacker et al. 2010). However, the turbulence length scale could not be determined here due to the low data rates of both the PIV and LDV systems (Thacker et al. 2010). With no direct

Turbulence properties				
	No Grid	Grid 1	Grid 2	Grid 3
Mesh size (M)	-	$0.11R$	$0.44R$	$0.44R$
Bar width (b)	-	$0.013R$	$0.044R$	$0.044R$
Solidity	-	23.6%	18.7%	18.7%*
Intensity (I_u)	1.20%	1.68%	2.26%	6.2%
Tip speed ratio, λ	3.50	3.24	3.26	3.73
Measurement position, x/M	-	140	35.5	28.7
Re Number (Re_M)	-	3.1×10^3	12×10^3	12×10^3

TABLE 7.1: Turbulence properties of the four flow/grid settings investigated. Grid 1: small grid; Grid 2: large grid; Grid 3: tethered sphere grid. *Note: the solidity ratio of the tethered sphere grid is based on the grid support structure, an alternate solidity ratio could be defined based on the projected area of the spheres, this value is 45%.

measurement of the Taylor macro-length scale, $\Lambda_{u,x}$ is estimated from M . Hence, the effect of turbulence length scale was not investigated explicitly. $\Lambda_{u,x}$ of the TSG was shown by Vonlanthen and Monkewitz (2011) to be similar in magnitude to the sphere diameter.

The evolution of the turbulent flow field in the middle of the channel as measured by the LDV is shown in figure 7.3. The solid black circles indicate $I_u(x)$ for grid three whereas the solid red squares indicate $I_u(x)$ for grid two. The hollow symbols indicate the $I_v(x)$ relationships. Spatial smoothing was undertaken by a moving average using the nearest neighbour. The form of the turbulence decay behind the grids is shown in figure 7.3. The results for grid one are not shown as this grid only elevated the turbulence level minimally.

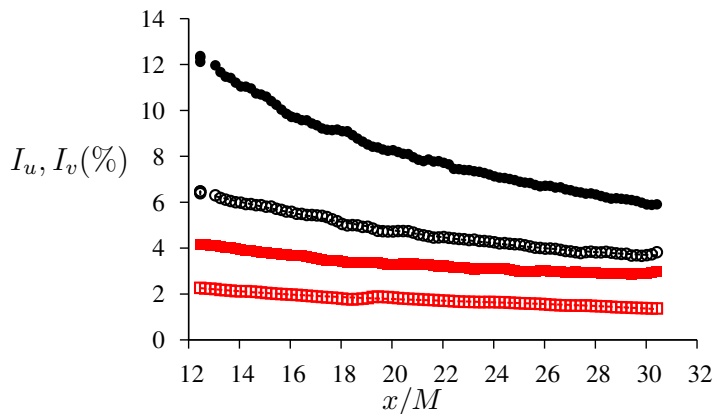


FIGURE 7.3: Streamwise and normal turbulence intensity variation with streamwise distance as measured by the LDV; black circles – grid 3, red squares – grid 2. Solid symbols, I_u , hollow symbols, I_v .

The figure also highlights the anisotropic nature of the generated turbulence. Grid generated turbulence is inherently anisotropic (Comte–Bellot and Corrsin 1966; Kurian and Fransson 2009). Vonlanthen and Monkewitz (2011) indicated a modest increase in isotropy of the TSG turbulence over a stand-alone grid but here we see no such improvement in the

isotropy. This is possibly due to the reduced Reynolds number of the current tests compared to $Re_M = 2 \times 10^4$ used in Vonlanthen and Monkewitz (2011).

The structure of the wake varies with freestream turbulence intensity (Alfredsson and Dahlberg 1979; Troldborg et al. 2007) but turbine performance varies little with increasing I_u (Sicot et al. 2006). This is due to the reduced magnitude of I_u at the rotating blades. The local turbulence intensity, $I_u(r)$, the turbulent fluctuations at the blade sections, is given by equation 7.6.

$$I_u(r) = u_{\text{rms}}/U_{\text{rel}}. \quad (7.6)$$

$I_u(r)$ is the ratio between the streamwise fluctuations (a fixed quantity) and the relative velocity, U_{rel} . Unlike U_∞ , U_{rel} increases approaching the tip due to the angular velocity component. $I_u(r)$ thus varies across the blade span as shown in figure 7.4. The local turbulence intensity variation for grids one, two and three are shown by the solid red, blue and black lines respectively. The dashed black line shows the increase in U_{rel} derived from the BEM analysis presented in chapter 6. The data are linearly interpolated between the rotational axis and the root region lifting surface termination point ($x/R = 0.24$). $I_u(r)$ clearly reduces with increasing radial distance from the rotational axis.

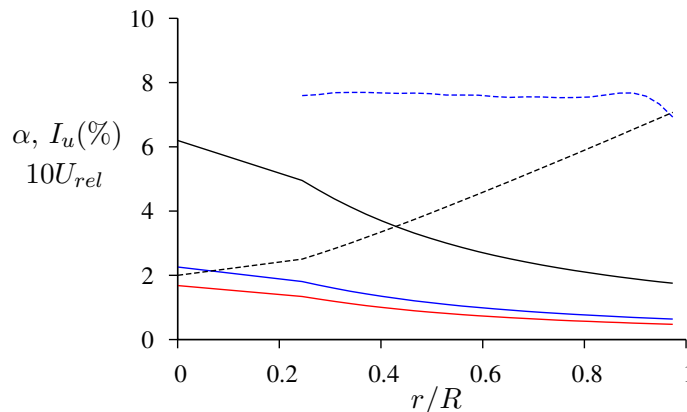


FIGURE 7.4: Local turbulence intensity, $I_u(r)$, distribution at $\lambda_d = 3.5$. Dashed blue and black lines indicates BEM derived α and U_{rel} distributions. Red line: grid 1, blue line: grid 2, black line: grid 3.

The variation in $I_u(r)$ is important for rotor performance. Airfoil performance at moderate Reynolds numbers reduces minimally with increasing turbulence intensity in the attached regime (Sicot et al. 2006; Swalwell et al. 2004). In the pre-stall region and early stages of stall, the lift coefficient increases and the reduction in performance is delayed to a larger angle of attack (Swalwell et al. 2004). This is attributable to the delayed separation from the

leading edge.

The large blade twist incorporated into the optimum Glauert rotor encourages attached flow across the entire span. The BEM calculations in chapter 6, indicate $\alpha \sim 7.5^\circ$ across the entire span at λ_d as shown by the dashed blue line in figure 7.4. As $\alpha = 7.5^\circ$ is on the border of the attached and pre-stall regime (see figure 3.18 in chapter 3), the lift coefficient will be affected minimally by the freestream turbulence intensity. Further, most of the torque contributing to the turbine power is generated in the outer 50% of the blade (Sicot et al. 2006) where the $I_u(r)$ is minimal. The blade bound circulation will thus vary little with added freestream turbulence intensity. Here, the effect of I_u on rotor performance will be characterised by the tip and root vortex properties in the near wake.

7.0.3 The effect of I_u on the near-wake velocity and vorticity fields

Freestream turbulence aids mixing throughout the wake leading to faster wake recovery (Alfredsson and Dahlberg 1979; Medici and Alfredsson 2006; Troldborg et al. 2007). The phase-averaged wake profile in a low turbulence case was presented in figure 6.9 in chapter 6. The average wake profile is shown for turbulence grid 3 in figure 7.5. This figure was constructed from data taken at several axial positions. Slight velocity gradients between adjacent positions suggest greater than 600 frames are required for full convergence. However, the structure of the wake and the difference to the low turbulence case is captured adequately with the 600 frames. Comparing figures 6.9 and 7.5, wake expansion is greater in the high turbulence case due to the larger tip speed ratio. The tip speed ratio is larger due to the pressure drop created by the blockage of turbulence grid 3. A jet structure is once again present close to the nacelle due to the termination of the lifting surface prior to the rotational axis. However, the jet appears less intense in the high turbulence case.

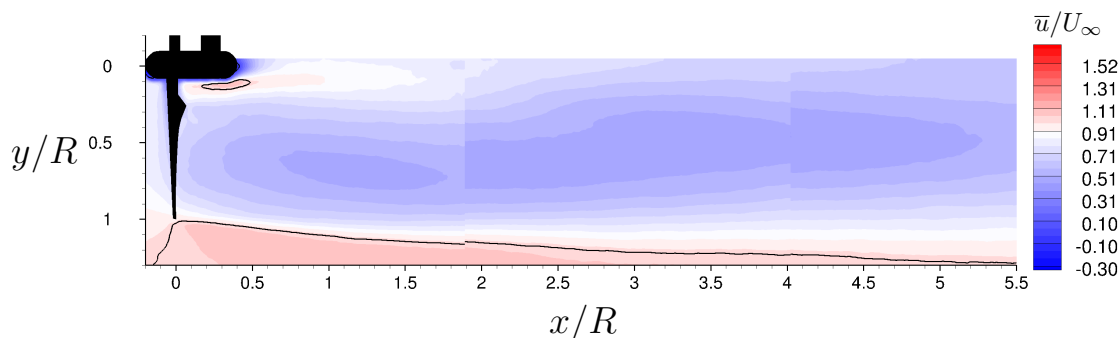


FIGURE 7.5: Average streamwise velocity contours downstream of turbulence grid 3, $I_u = 6.2\%$, $\lambda = 3.73$, $x/M = 28.7$.

The phase-locked average near wake velocity fields reveal the effect of freestream turbulence intensity more clearly. The near wake velocity fields for grids 1, 2 and 3 are shown in figures 7.6, 7.7 and 7.8 respectively. The velocity field recovers at a faster rate with increasing I_u . Transition to the far wake will thus occur sooner with increasing I_u allowing the use of simplified engineering models. However, transition distances to the far wake heavily depend on the turbine operating and flow field conditions.

Estimates of transition distance to the far wake vary from $x/R = 2$ (Vermeer et al. 2003) to between $6 \leq x/R \leq 10$ (Crespo et al. 1999). The near wake ceases when the rotor is no longer discernible. Signatures of the rotor in the wake are the blade wakes, tip vortices and increased turbulence. In the low turbulence case, the blade wakes for $\lambda = 3.5$ was no longer evident by $1R$, as shown in figure 6.23. Velocity profiles show the wake reached a developed state by $1.5R$. The velocity deficit reduced with distance but the velocity profile varied minimally. The tip vortices, however, persist for much further into the wake. Vortex coalescence occurred between two filaments between $x/R = 3.1$ and $x/R = 4.5$. Coalescence between the remaining tip vortex and the initial vortex pair occurs soon after $x/R = 4.5$. Therefore in the low in-flow turbulence case at $\lambda = 3.5$, transition to the far wake can be said to occur after $x/R = 4.5$.

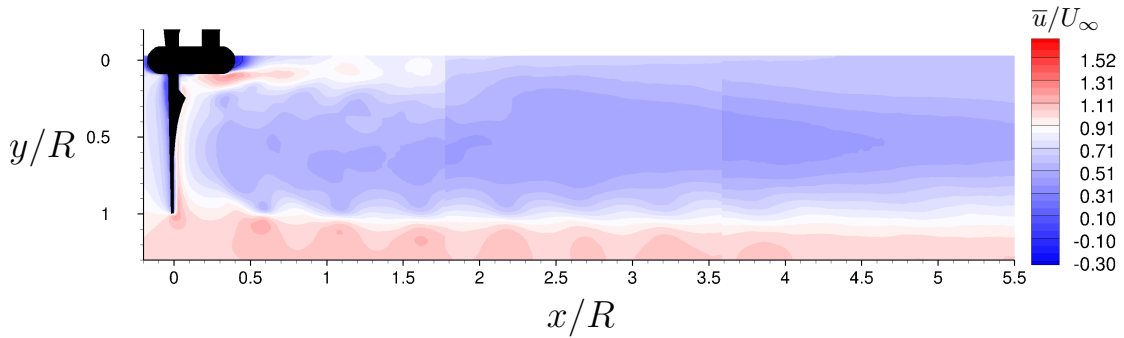


FIGURE 7.6: Phase-locked averaged streamwise velocity contours downstream of turbulence grid 1, $I_u = 1.68\%$, $\lambda = 3.24$, $x/M = 140$.

As the lifting surface terminates prior to the rotational axis, a jet ($\bar{u}/U_\infty \geq 1$) forms next to the nacelle. Velocity gradients caused by the tip vortices are visible close to the unit radius and persist far into the wake for grids 1 and 2. The velocity fields for turbulence grids 1 and 2 are very similar because there is very little difference in the turbulence intensity between these two cases (0.6%). The velocity profile behind turbulence grid 3 on the other hand shows more effects arising from the large increase in turbulence intensity. The tip vortex velocity gradients disappear closer to the rotor plane with increasing I_u . Wake expansion is also larger

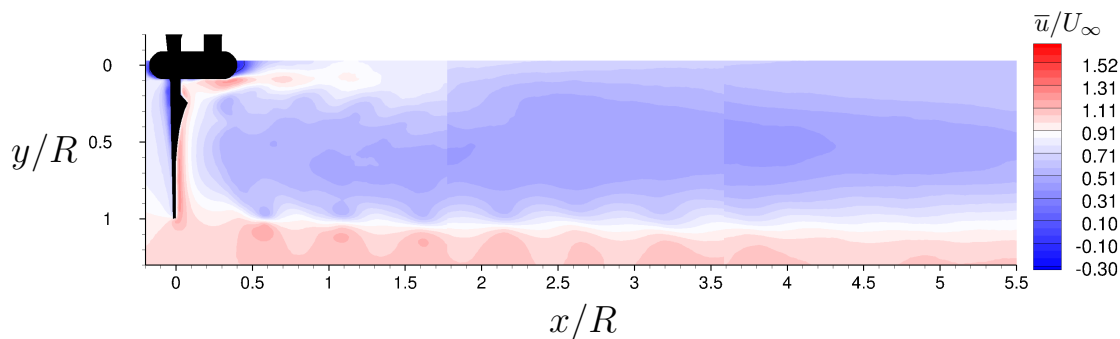


FIGURE 7.7: Phase-locked averaged streamwise velocity contours downstream of turbulence grid 2, $I_u = 2.26\%$, $\lambda = 3.26$, $x/M = 35.5$.

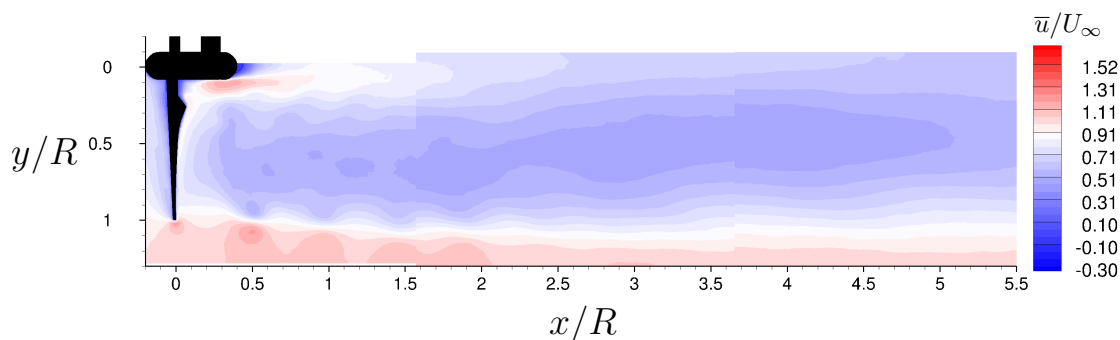


FIGURE 7.8: Phase-locked averaged streamwise velocity contours downstream of turbulence grid 3, $I_u = 6.2\%$, $\lambda = 3.73$, $x/M = 28.7$.

for turbulence grid 3 compared to grids 1 and 2.

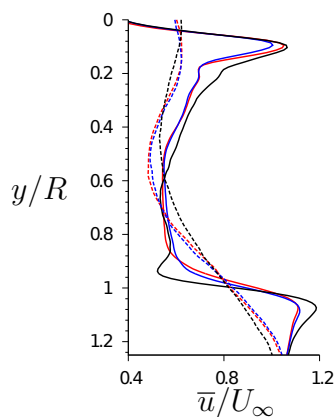


FIGURE 7.9: Evolution of the streamwise velocity component at two wake locations in the three turbulence intensity levels. solid lines: $x/R = 0.5$, dashed lines: $x/R = 5.5$. Red lines: grid 1, blue lines: grid 2, black lines: grid 3.

Velocity deficit profiles at two axial locations, $x/R = 0.5$ and $x/R = 5.5$, are plotted for the three I_u levels in figure 7.9. The velocity profiles are very similar across a large portion of the blade span at $x/R = 0.5$. The velocity gradient between $0.9 \leq y/R \leq 1.1$ in the turbulence grid 3 profile is due to a tip vortex. The tip vortex appears due to the reduction

in pitch in the grid 3 case. By $x/R = 5.5$, the wake profile has become uniform with recovery occurring fastest for the grid 3 case. The minimum velocity also occurs closer to the rotational axis in the case of turbulence grid 3.

While velocity gradients in the streamwise velocity fields indicate the presence of tip and root vortices, the out-of-plane vorticity fields, $\overline{\omega_z}R/U_\infty$, reveal the vortex locations more clearly. The phase-locked average vorticity fields are shown in figures 7.10, 7.11 and 7.12. Both tip and root vortices are visible in the figures. However, the number of tip and root vortices depends on I_u . The magnitude of the vorticity at $VA = 120^\circ$ reveals the initial strength of the tip and root vortices are similar for all turbulence cases. The initial strength of the trailing vortex system is directly related to the blade bound circulation generated on the blades. The present findings are thus in agreement with the turbine performance force data of Sicot et al. (2006). The intensity of the blade wakes reduce at a faster rate with increasing turbulence intensity. The blade wakes cease between $240^\circ \leq VA \leq 360^\circ$ for turbulence grids 1 and 2. Whereas, the blade wakes have ceased by 240° for turbulence grid 3. It will be shown this has a direct impact on tip vortex circulation.

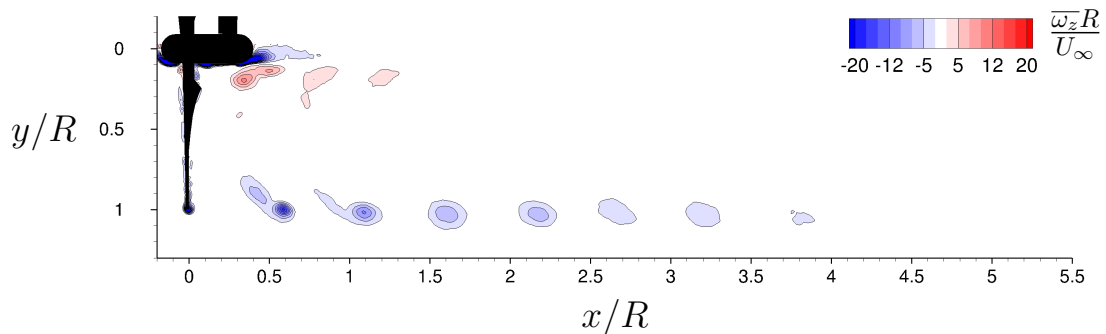


FIGURE 7.10: Phase-locked average out-of-plane vorticity field, $\overline{\omega_z}R/U_\infty$, behind turbulence grid 1, $I_u = 1.68\%$, $\lambda = 3.24$, $x/M = 140$

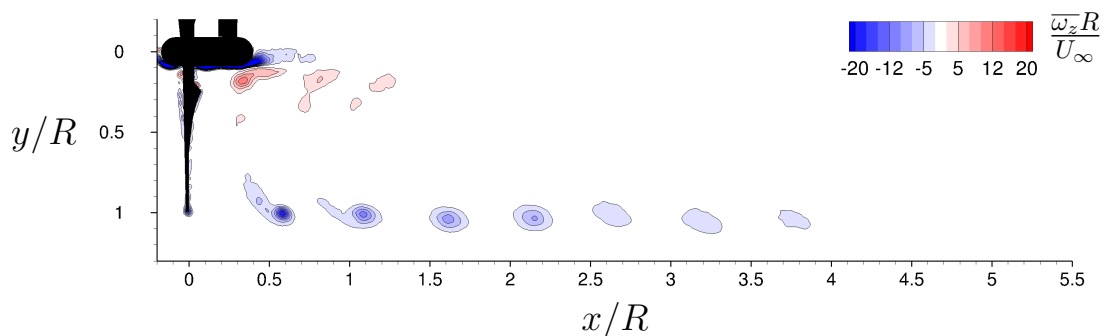


FIGURE 7.11: Phase-locked average out-of-plane vorticity field, $\overline{\omega_z}R/U_\infty$, behind turbulence grid 2, $I_u = 2.24\%$, $\lambda = 3.26$, $x/M = 35.5$

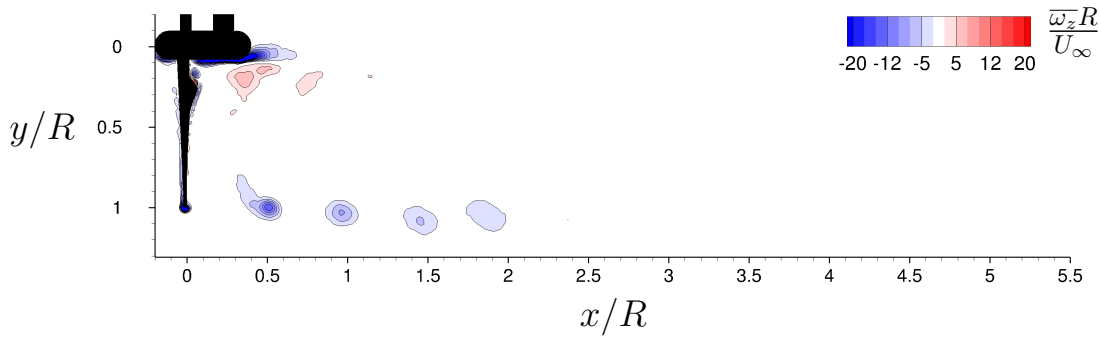


FIGURE 7.12: Phase-locked average out-of-plane vorticity field, $\bar{\omega}_z R / U_\infty$, behind turbulence grid 3, $I_u = 6.2\%$, $\lambda = 3.73$, $x/M = 28.7$

The vorticity fields reveal the tip and root vortices are not present closer to the rotor plane with increasing turbulence intensity, agreeing with the results of Troldborg et al. (2007). However, unlike the low turbulence case in chapter 6, the vorticity fields show no evidence of mutual induction between adjacent vortices. In the absence of the mutual induction instability mode, the one bladed results revealed the tip vortices reduce in strength primarily by viscous diffusion. Turbulent diffusion becomes more important with increasing turbulence intensity. The turbulent flow field also causes highly perturbed filaments (Troldborg et al. 2007). Such perturbations can appear as meandering motions. The magnitude of the out-of-plane vorticity is reduced by the phase-locked averaging process. To alleviate the issues of spatial smoothing of vortex properties due to the perturbed filaments, the instantaneous vortex properties were evaluated. The evolution of the tip and root vortex properties with vortex age is presented in the following section with vortex meander characterised in the section after.

7.0.4 Evolution of vortex properties with I_u

The phase-locked instantaneous vortex properties are evaluated in a similar fashion to the low turbulence case. Tip and root vortex property evolution resulting from the effects of increased turbulence intensity can thus be determined. The turbulent velocity fields were passed through the energy based filter (see chapter 3) and reconstructed using the threshold criteria of Epps and Techet (2010). The Γ_1 (Graftieaux et al. 2001) and λ_{ci}^2 (Zhou et al. 1999) criteria are both used to determine the vortex centre locations. Sub grid scale accuracy is achieved using a 2D polynomial fit within a 9 point neighbourhood around the grid specified maximum/minimum. The tip vortex axial positions do not vary for the two identification methods employed. However, the radial positions do vary more. The λ_{ci}^2 criteria tended to locate vortices in the nacelle boundary layer closer to the rotational axis. The evaluation

radius for the Γ_1 method meant such regions were not considered. For this reason, the Γ_1 method was chosen to indicate the locations of both the tip and root vortices.

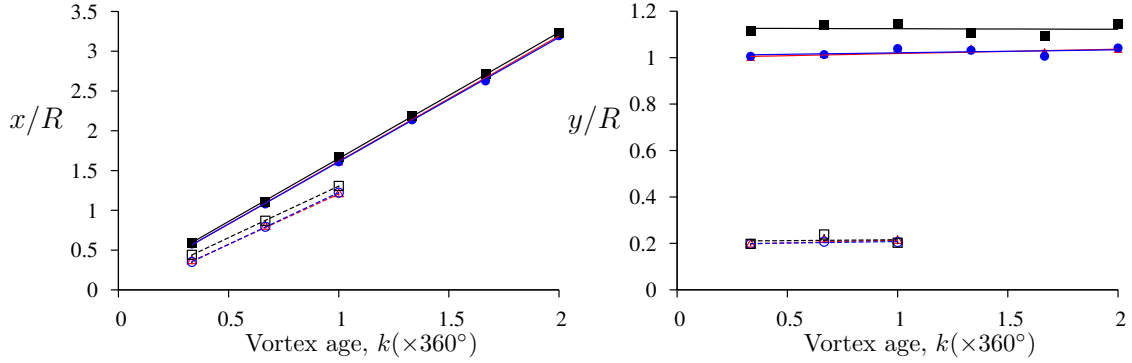


FIGURE 7.13: Mean axial (left) and radial (right) vortex positions for the three turbulence intensities. Solid lines and solid symbols: tip vortices, dashed lines and hollow symbols: root vortices. Red: grid 1, Blue: grid 2; Black: grid 3.

The axial and radial vortex locations are shown on the left and right of figure 7.13. An axial misalignment occurs here in a similar fashion to the low freestream turbulence cases between a tip and root vortex at a given vortex age. The tip vortices advect in a more uniform and higher velocity flow field compared to the root vortices embedded in the turbulent central wake region. This is evident by the separate trendlines in figure 7.13, for the tip and root vortices. The trendlines accurately describe the tip and root vortex axial positions with fitting coefficients in a least squares sense greater than 99%. Further, the trendlines for the tip and root vortex positions diverge slightly with streamwise distance as the axial misalignment increases. There is more scatter in the radial positions, as can be seen on the right of figure 7.13. A similar trend was seen in the low turbulence case in chapter 6. The vortex positions of turbulence grids 1 and 2 show excellent agreement due to the comparable turbulence intensity and tip speed ratio. The vortex positions arising from turbulence grid 3 deviate from these due to the larger tip speed ratio (see table 7.1) in this configuration. The larger tip speed ratio causes a reduction in pitch (axial positions) and larger wake expansion (radial positions). The vortex trajectories confirm the absence of the mutual inductance instability mode.

The instantaneous vortex properties were deduced using both the Γ_2 (Graftieaux et al. 2001) and λ_{ci}^2 criteria. The Γ_2 method is the Galilean invariant version of the Γ_1 parameter. The two methods were outlined in chapter 3. The threshold contour of the λ_{ci}^2 method is based on the instantaneous freestream $\langle \lambda_{ci}^2 \rangle$ fields. The threshold only considers the top 1% of the tip and root vortex eddying motion above freestream values, *i.e.* $\lambda_{ci}^* = \overline{\langle \lambda_{ci}^2 \rangle} + 3\overline{\langle \sigma_{\lambda_{ci}^2} \rangle}$.

The λ_{ci}^* threshold denotes the entire region where eddying motion exists. This is similar to the a_2 radius of the ‘VM2’ vortex model (Roy 2008). On the other hand, the threshold for the Γ_2 method, $\Gamma_2^* = \pm 2/\pi$, encapsulates the region of solid body rotation (Graftieaux et al. 2001).

Vortex properties such as maximum tangential velocity, $V_{\theta,max}$, vortex radius, r_{vc} , and circulation, Γ , are presented as temporal averages of the filtered instantaneous realisations. Instantaneous vortex properties outside 3σ values for the x , y and Γ distributions were discarded. The mean and standard deviation values of the vortex property distributions are presented in the following figures.

How the tip (left) and root (right) vortex circulation varies with vortex age is shown in figure 7.14. The dashed lines and hollow symbols represent the Γ_2 derived values. Whereas, the solid lines and symbols represent the λ_{ci}^2 derived values. Figure 7.14 indicates the effect of more restrictive λ_{ci}^2 , *i.e.* smaller area, threshold compared to the Γ_2 method. However, the data trends exist in both identification methods. The minimal effect of turbulence intensity on rotor performance is confirmed by the comparable initial strength of the tip vortices. Only the root vortex results evaluated using the Γ_2 method are shown due to the tendency of the λ_{ci}^2 method to identify vortex structures in the nacelle boundary layer.

There are two competing forces acting on the vortex circulation. Circulation of the tip vortex increases during the vortex roll-up process due to entrainment of the trailing edge vorticity sheet by the tip vortex. Simultaneously, the angular momentum in the vortex is being transferred to the base flow by viscous and turbulent diffusion. The one-bladed results revealed viscous diffusion occurs slowly over large wake distances. The phase-locked average vorticity maps of figures 7.10, 7.11 and 7.12 showed the faster diffusion of the blade wakes with I_u . This vorticity would have been entrained by the tip vortex.

From the λ_{ci}^2 tip vortex results depicted by the solid lines, it can be seen that the vortex circulation behind turbulence grids 1 and 2 are approximately conserved until a vortex age of 480° . The circulation then reduces before a slight recovery. The origins of the reduction and recovery of circulation are difficult to realise due to the few vortex realisations. There is no obvious reason for the dip in circulation, although a similar phenomena (albeit at an earlier vortex age) has been seen previously (Grant and Parkin 2000). The 3rd turbulence grid circulation results on the other hand show almost monotonic reduction with vortex age. The faster diffusion of the blade wakes shown in figure 7.12 means the tip vortices in the case of turbulence grid 3 cannot entrain the same amount of blade bound circulation as those in

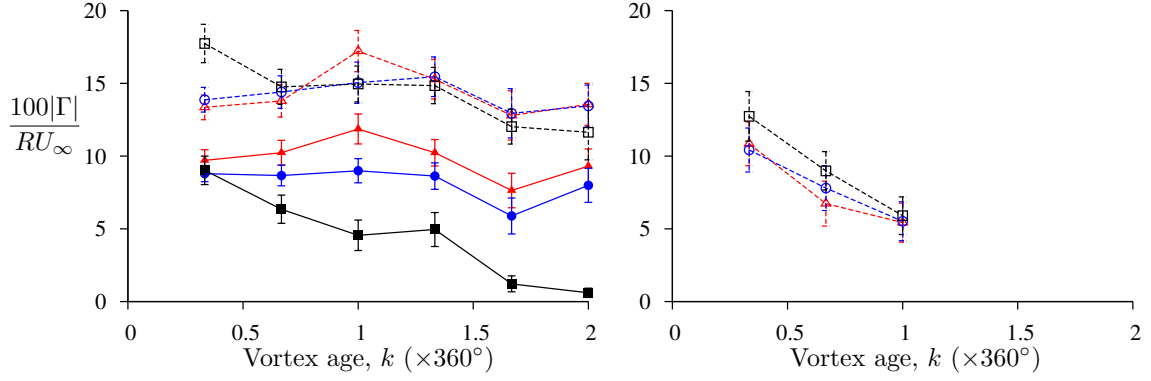


FIGURE 7.14: Mean tip (left) and root (right) vortex circulation determined by the two vortex identification mechanisms. Solid lines and solid symbols: λ_{ci}^2 , dashed lines and hollow symbols: Γ_2^* . Red: grid 1, Blue: grid 2; Black: grid 3.

turbulence grid cases 1 and 2. Further, turbulent diffusion of the vortices will be larger for turbulence grid 3.

Similar trends are also seen in the Γ_2 results. Aside from the $VA = 120^\circ$ result of turbulence grid 3 (which is erroneous), circulation is approximately conserved. This is due to Γ_2^* being based on the evolving velocity field rather than a freestream derived threshold value. The region experiencing such a rotation increases with vortex age as shown in figure 7.15. Γ_2 is thus the preferred method of vortex circulation calculation. Again, the fluctuations in the Γ_2 circulation magnitude are a possible indication of the planar measurement technique to capture all vortex dynamics (*e.g.* out-plane-diffusion of vorticity). This is especially true in the highly turbulent flow fields generated by the turbulence grids.

The root vortex circulation results on the right of figure 7.14 indicate the initial circulation of the root vortices is slightly less than that of the tip vortices. The larger chord and twist incorporated in the root region of the Glauert rotor were not enough to ensure tip and root vortices of equal strength. The root vortex circulation decreases rapidly with vortex age. This is due to the turbulent nature of the flow field in the vicinity of the turbine support structures.

In a low turbulence viscous flow field, vortex circulation is primarily diffused to the base flow by viscous diffusion. However, in a turbulent flow field, the transfer of angular momentum to the base flow occurs faster due to added turbulent diffusion. The vortex core radius expands due to both viscous and turbulent diffusion. The evolution of the tip (left) and root (right) vortex core radii with vortex age for the three turbulence grids are shown in figure 7.15. Once again the λ_{ci}^2 method is more restrictive compared to the Γ_2 method.

When the focus is on the λ_{ci}^2 results, it becomes clear that at early vortex ages ($VA < 360^\circ$),

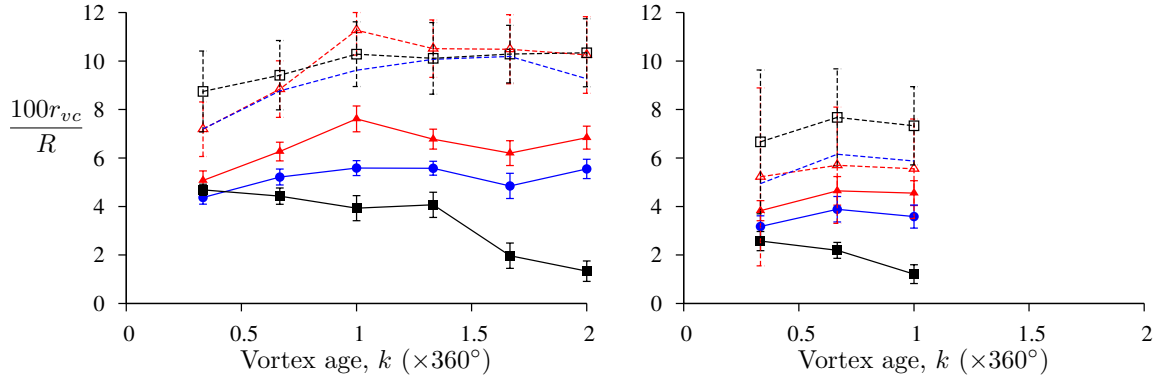


FIGURE 7.15: Mean tip (left) and root (right) vortex core radius determined by the two vortex identification mechanisms. Solid lines and solid symbols: λ_{ci}^{2*} , dashed lines and hollow symbols: Γ_2^* . Red: grid 1, Blue: grid 2, Black: grid 3.

core expansion occurs for turbulence grids 1 and 2. The core radius reduces thereafter due to the fixed value of the λ_{ci}^* contour. The λ_{ci}^* contour encapsulates all eddying motion above a fixed freestream value. As angular momentum of the vortices is diffused to the surrounding flow, the maximum swirl above λ_{ci}^* reduces. The λ_{ci}^* contour will then denote a smaller vortex, as seen in figure 7.15. Such a core reduction phenomena occurs from earlier vortex ages for the turbulence grid 3 results due to enhanced diffusion of vortex angular momentum by the higher I_u . The trends are similar for both the tip and root vortices.

When the focus is on the Γ_2 results from figure 7.15, the core radius can be seen to expand with vortex age. Thus, the Γ_2 threshold contour, being based on the evolving wake velocity field, captures the evolving vortex property most accurately. The Γ_2 method is thus the most suitable method tested here to evaluate vortex properties such as circulation and vortex radius.

The decay of the mean maximum, $\overline{V_{\theta,max}}$, and azimuthally averaged, $\overline{\langle V_{\theta} \rangle}$, tangential velocity components are shown on the left and right of figure 7.16. The tangential velocity components were extracted along Γ_2^* . The tip vortex, $\overline{V_{\theta,max}}$ and $\overline{\langle V_{\theta} \rangle}$ components shown on the left decay almost linearly. However the initial decay of the root vortex $\overline{V_{\theta,max}}$ and $\overline{\langle V_{\theta} \rangle}$ components is more rapid initially. This is most probably due to the high turbulence in the central wake region.

The average tangential velocity component, $\overline{\langle V_{\theta} \rangle}$, is used in analytical vortex models to determine vortex circulation (Bhagwat and Leishman 2002). Several researchers (Grant and Parkin 2000; Dobrev et al. 2008) have estimated the circulation of HAWT tip vortices by assuming the vortex cores are circular and using equation 7.7.

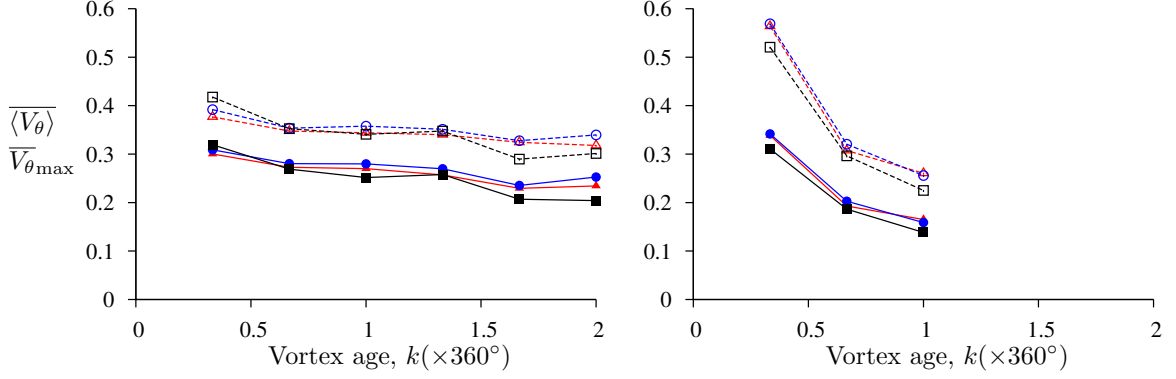


FIGURE 7.16: Mean maximum, $\overline{V_{\theta_{\max}}}$, (dashed lines hollow symbols) and azimuthally averaged, $\langle V_\theta \rangle$, (solid lines and solid symbols) tangential velocity of the tip (left) and root (right) vortices along Γ_2^* . Red: grid 1, Blue: grid 2: Black: grid 3.

$$\Gamma_{\text{est}} = 2\pi r_{\text{vc}} \overline{\langle V_\theta \rangle} \quad (7.7)$$

where $\overline{\langle V_\theta \rangle}$ is the azimuthally averaged mean tangential velocity along a threshold contour and r_{vc} is the vortex core radius.

However, the vortex cores are not expected to be circular as they intersect the measurement plane at the wake skew angle, approximately equal to $\phi(R)$, the angle of U_{rel} to the rotor plane at the tip. To avoid possibly erroneous assumptions of vortex core shape, a line integral (equation 3.5) is used here to determine vortex circulation. The difference between vortex circulation estimated using equation 7.7 and the results of figure 7.14 is shown in figure 7.17. The figure illustrates the variation in assuming the cores are circular. The difference generally increases with vortex age as the tip vortices start to breakdown.

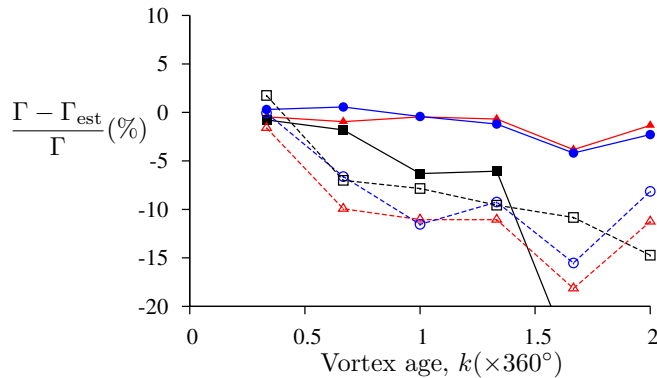


FIGURE 7.17: Mean difference between the line integral derived tip (left) vortex circulation and that calculated by equation 7.7. Solid lines and solid symbols: λ_{ci}^2 , dashed lines and hollow symbols: Γ_2^* . Red: grid 1, Blue: grid 2: Black: grid 3.

7.0.5 Meander of the tip and root vortices in a turbulent flow field

The helical tip and root vortices are perturbed due to I_u as visualised in figure 7.1. The causes of meander in a low turbulence flow setting were presented in chapter 6. Increasing I_u is expected to enhance the meander. Meandering motions of the tip and root vortices are visualised by the distribution of the instantaneous positions in figures 7.18, 7.19 and 7.20. In the figures, the colour distribution indicates the blade which created the vortex. The axial misalignment between a tip and root vortex at the same vortex age is visualised clearly.

Figures 7.18, 7.19 and 7.20 qualitatively indicate the root vortices meander more than the tip vortices at an equivalent vortex age. This is possibly due to the reduced strength of the root vortices as shown in figure 7.14. Further, the interaction of the rotating blades and the turbine support structures with the fluid make the flow in the root region highly complex (Zahle and Sørensen 2011).

The instantaneous position distributions also indicate meander in the axial direction is larger than in the radial direction in a similar fashion to a low turbulence in-flow case. Meander increases with vortex age but interaction between adjacent tip vortices appears absent. Meander increases with I_u as the filaments are more perturbed. Meander is largest for the tip vortices behind turbulence grid 3. It was shown in figure 7.14 that vortex strength reduced at a faster rate with increasing I_u . This is due to enhanced turbulent diffusion.

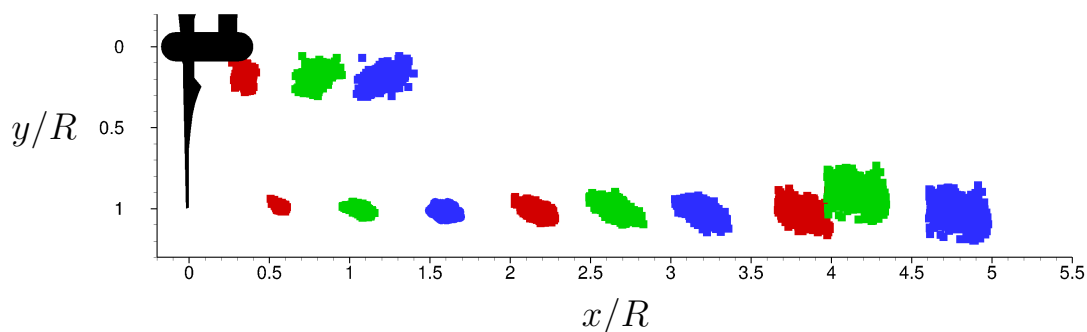


FIGURE 7.18: Tip and root vortex scatter in the measurement plane behind turbulence grid 1, $I_u = 1.68\%$, $\lambda = 3.24$, $x/M = 140$.

The magnitude of meander is once again characterised by the standard deviation of a normal distribution fitted to the probability distribution function of the deviations from the mean (Devenport et al. 1996; Heyes et al. 2004). The low turbulence in-flow case results from chapter 6 are also included. The meander magnitudes are compared for the various turbulence intensity values in figure 7.21. Tip and root vortex meander is presented on the left and right respectively. The solid lines and symbols represent meander in the axial direction. Whereas,

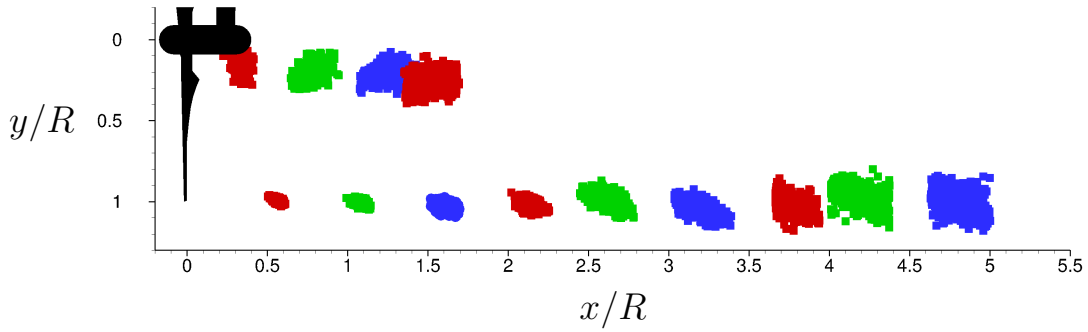


FIGURE 7.19: Tip and root vortex scatter in the measurement plane behind turbulence grid 2, $I_u = 2.26\%$, $\lambda = 3.26$, $x/M = 35.5$

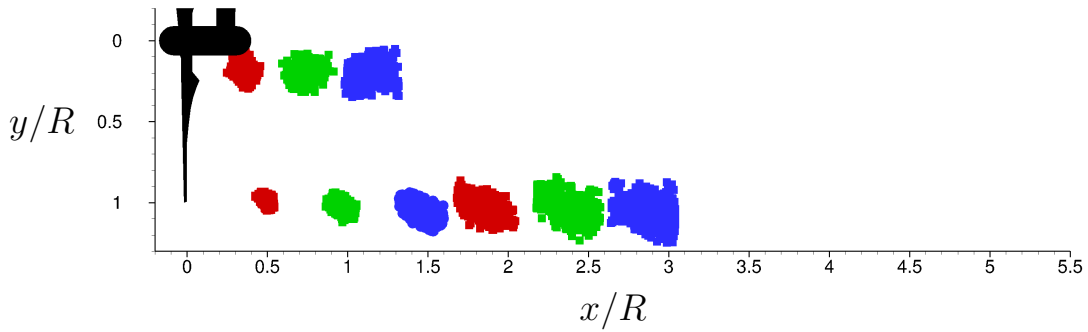


FIGURE 7.20: Tip and root vortex scatter in the measurement plane behind turbulence grid 3, $I_u = 6.2\%$, $\lambda = 3.73$, $x/M = 28.7$.

the dashed lines and hollow symbols on the other hand represent meander in the radial direction. The uncertainty estimation for the meander characterisation process is $\pm 6\%$.

Focussing on the tip vortex results, the larger meander in the axial direction is quantified by figure 7.21. Where tip vortex interaction occurs in the low turbulence intensity results of chapter 6, the meander of the pair of vortices is characterised. This occurs at vortex ages of 2–2.33 and 3–3.33. Meander is seen to increase with both vortex age and turbulence intensity. Meander of the tip vortices behind grids 1 and 2 collapse onto the same trend due to the minimal difference in turbulence intensity. This suggests turbulence scale has a minimal effect on the meander of the helical vortices in a wind turbine wake at this I_u . Meander is largest for the grid 3 results. The highly turbulent flow field behind grid 3 perturbs the filament greatly increasing the meandering of the tip vortices.

The root vortices on the other hand do not display the same difference in meander seen in the tip vortex results. The larger meander of the root vortices compared to the tip vortex at an equivalent vortex age is seen qualitatively in figures 7.18, 7.19 and 7.20 is quantified by figure 7.21. It is due to the turbulence in the root region which arises from the interaction of

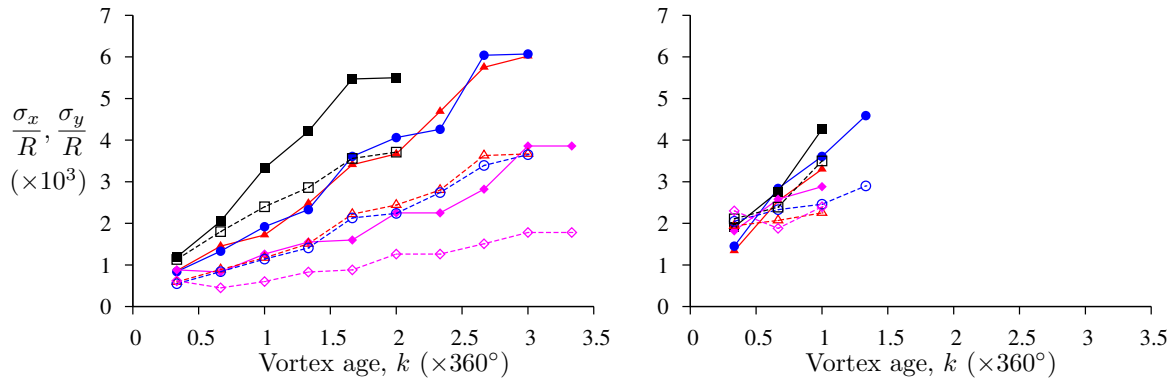


FIGURE 7.21: Vortex meander of the tip (left) and root (right) vortices with varying freestream turbulence intensity. Hollow symbols: radial meander, solid symbols: axial meander. Magenta: no grid, red: grid 1, blue: grid 2, black: grid 3.

the oncoming flow with the rotating blades and the tower support structures.

There is a clear relationship between meander magnitude and freestream turbulence intensity. Further, the mutual induction instability mode does not appear when the freestream turbulence intensity is elevated, albeit minimally. The change in turbulence intensity level between the no grid case of chapter 6 and grid one is only 0.48% yet the mutual induction instability mode is absent in the latter. This highlights the sensitivity of the flow structures to flow field perturbations. In the absence of the mutual inductance instability mode, the tip and root vortices degenerate by viscous and turbulent diffusion. The transfer of momentum throughout the wake by turbulent processes is thus an important mechanism for wake recovery. Such processes are visualised by investigating the Reynolds stress fields, presented in the following section.

7.0.6 Momentum transfer in the wake due to turbulent processes

The Reynolds stress fields are important as they illustrate the apparent normal and shear stresses arising from the fluctuating velocity field. Wake recovery occurs through the transfer of the high momentum freestream flow into the central wake region. The Reynolds stresses play an important role in this process. Investigating the Reynolds shear stress field, $\overline{\mathbf{u}'\mathbf{v}'}$, permits the average momentum flux due to turbulent motions to be determined. In a predominately axial flow field like that in a wind turbine wake, positive and negative Reynolds shear stresses can be associated with the transport of streamwise momentum in the positive and negative vertical directions. Due to the turbulent nature of the base flow, the Reynolds shear stresses could be expected to increase with increasing freestream turbulence intensity.

The Reynolds shear stress field for the low turbulence inflow case is shown in figure 7.22.

The lines indicate the phase-locked average vorticity field and the positions of the tip and root vortices. The Reynolds shear stress field tends to be stronger in the central wake, the tip and root vortices and the blade wake regions. The Reynolds shear stress field highlights the turbulent nature of the central wake region better than the vorticity field. The shear layer trajectory toward the rotational axis is also evident downstream of the nacelle.

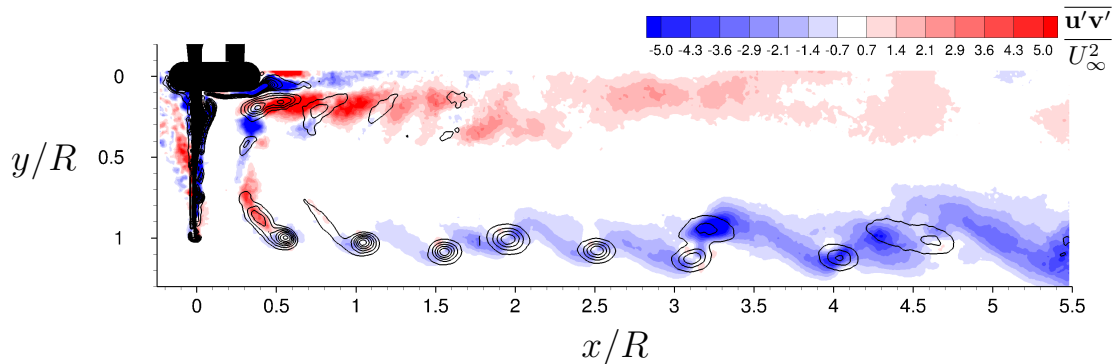


FIGURE 7.22: Reynolds shear stress, $\overline{\mathbf{u}'\mathbf{v}'}$, field in a low turbulence (no grid) inflow case. $\lambda = 3.5$

The central wake region is bounded by a region of positive $\overline{\mathbf{u}'\mathbf{v}'}$ where the root vortices are located. A meandering rectilinear vortex generates a characteristic quadrant $\overline{\mathbf{u}'\mathbf{v}'}$ pattern Heyes et al. (2004); Iungo et al. (2009). In this pattern, quadrants of the same sign Reynolds shear stress are located diagonally opposite each other. This quadrant pattern is absent in the vicinity of the root vortex due to flow turbulence. The Reynolds shear stresses here are quite intense, contributing to the rapid diffusion of the root vortices. The diffusion of the root vortices is evident by the lines representing vorticity and the decrease of vortex circulation in figure 7.14.

The tip vortices on the other hand do show a quadrant pattern in the $\overline{\mathbf{u}'\mathbf{v}'}$ field. Whilst small regions of positive $\overline{\mathbf{u}'\mathbf{v}'}$ exist in the vicinity of the tip vortex, negative components are more prevalent. This is due to the larger meander in the axial direction compared to the radial direction as shown in figure 7.21. Negative Reynolds shear stresses are found in the remnants of the blade wakes. The intensity of these regions increases with interaction between adjacent vortices.

One of the major findings the Reynolds shear stress fields reveal is the relative position of the blade wakes to the vortex cores themselves. The blade wakes of preceding tip vortices are initially separated from the tip vortex core as indicated by the fields between $0.5 \leq x/R \leq 1$. During vortex roll-up, the separation between the blade wake and tip vortex reduces until bridging occurs. There is a correlation between the position where bridging first occurs and the first indication of the mutual inductance instability mode, *i.e.* between $VA = 360^\circ$ and

$VA = 480^\circ$. Such an interaction had previously been proposed as the instability mechanism trigger in marine propeller wakes (Felli et al. 2006). Once bridging occurs, a negative band of $\overline{\mathbf{u}'\mathbf{v}'}$ exists with maximums at the vortex locations. Prior to vortex coalescence, the interaction creates significant Reynolds shear stresses, *e.g.* at $x/R = 3.15$. Post vortex coalescence, the intensity of the $\overline{\mathbf{u}'\mathbf{v}'}$ field increases.

The Reynolds shear stress fields behind turbulence grids 1, 2, and 3, are shown in figures 7.23, 7.24 and 7.25. The intensity of the $\overline{\mathbf{u}'\mathbf{v}'}$ field increases with I_u . The quadrant pattern of the $\overline{\mathbf{u}'\mathbf{v}'}$ field is most prominent in the turbulence grid 3 results. This is explained by the initially uniform meander in both axes as shown in figure 7.21. A distinct quadrant pattern will occur if the meandering motions have no preferential direction. The quadrant pattern reduces with distance as the meandering motions become larger and more prevalent in a single (axial) axis.

The blade wakes are more intense from earlier vortex ages compared to the low turbulence in-flow case. Bridging between the blade wake and a tip vortex occurs from $x/R \geq 1$ but the mutual induction instability mode is absent. The turbulence generated by the grids alters the vortex induced velocity fields such that mutual inductance between vortices does not occur. Further, the perturbed nature of the filaments reduces the phase-locked interaction between adjacent vortices. The vortices do not appear to interact in a phase-locked sense. This is a limitation of the phase-locked averaged measurements.

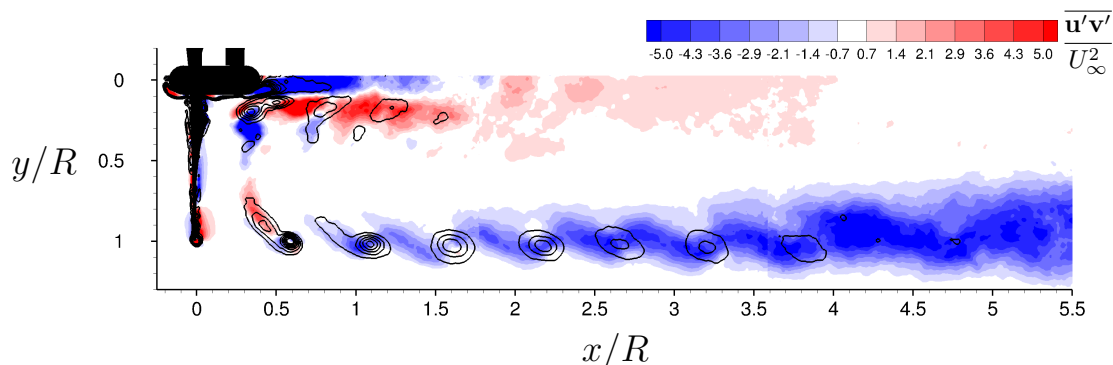


FIGURE 7.23: Reynolds shear stress, $\overline{\mathbf{u}'\mathbf{v}'}$, field behind turbulence grid 1. $\lambda = 3.24$, $x/M = 140$, $I_u = 1.68\%$.

7.1 Summary of the near-wake turbulence data

In this chapter, the evolution of the wake of a HAWT subjected to various levels of freestream turbulence intensity has been investigated. The work is the first to investigate evolution of a HAWT's tip and root vortices in various I_u levels. Passive turbulence grids were used to

7.1. Summary of the near-wake turbulence data

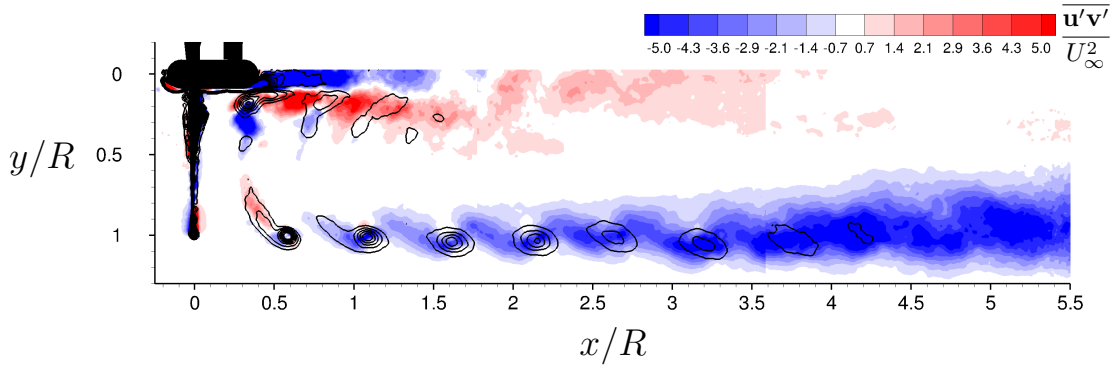


FIGURE 7.24: Reynolds shear stress, $\overline{\mathbf{u}'\mathbf{v}'}$, field behind turbulence grid 2. $\lambda = 3.26$, $x/M = 35.5$, $I_u = 2.2\%$.

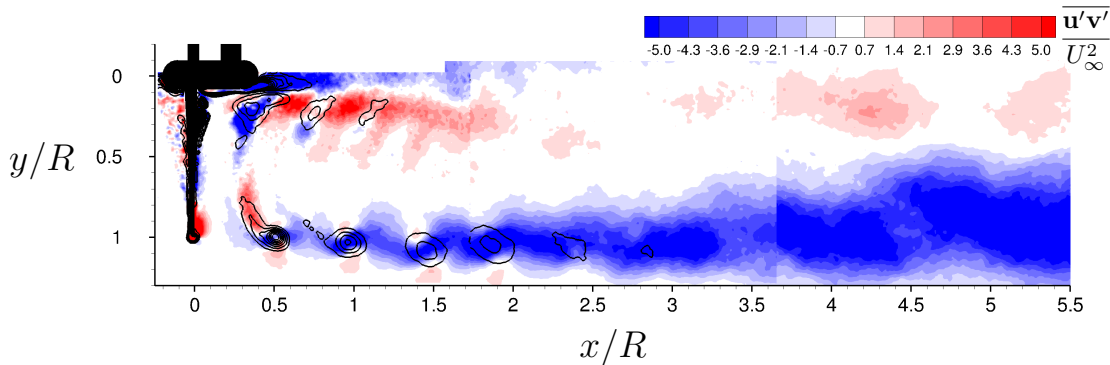


FIGURE 7.25: Reynolds shear stress, $\overline{\mathbf{u}'\mathbf{v}'}$, field behind turbulence grid 3. $\lambda = 3.73$, $x/M = 28.7$, $I_u = 6.2\%$

elevate the freestream turbulence intensity. A novel tethered sphere design was constructed which elevated the turbulence intensity significantly compared to the stand alone grid.

Utilising the coupled nature of near wake and blade aerodynamics, turbine performance was evaluated by calculating the tip and root vortex properties. The initial strength of the tip and root vortices was comparable suggesting minimal turbulence effect on turbine performance. This is due to the lower local turbulence intensity at the blade sections compared to the freestream value. The results are in agreement with prior rotor performance data.

The mutual induction instability mode was absent in a turbulent flow field. The results highlight the sensitivity of vortex interaction to flow field parameters. Turbulent diffusion is responsible for the faster breakdown of both the tip and the root vortices. Vortex meander increased with freestream turbulence intensity as the turbulent flow field perturbed the filaments more with increasing I_u .

The present chapter highlighted the different mechanism of wake breakdown in a turbulent flow field. The effect of turbulent length scale could not explicitly be revealed. A direct measurement of turbulent length scales is required for further understanding of the interaction

between flow field and wake dynamics.

The findings of the present chapter highlight the change in wake evolution with increasing freestream turbulence intensity. The results confirmed turbine performance is affected minimally by a turbulent in-flow and the coherent vortical structures breakdown faster in a turbulent flow field, both beneficial in a wind farm siting sense. The change in structural loading of the turbine must of course be also evaluated to truly characterise the effect of turbulence intensity on a HAWT.

7.1. Summary of the near-wake turbulence data

Declaration for section 2 of Chapter 8

Declaration by candidate

In the case of section 2 of Chapter 8, the nature and extent of my contribution to the work was the following:

Nature of contribution	Extent of contribution (%)
M. Sherry designed the experimental model, oversaw model construction, conducted the experiments and processed the data. He developed tools to analyse the data and present it in the form seen in the manuscript. M. Sherry wrote the manuscript.	80

The following co-authors contributed to the work.

Name	Nature of contribution	Extent of contribution (%) for student co-authors only
John Sheridan	J. Sheridan guided research and contributed to manuscript formulation and revision.	10
David Lo Jacono	D. Lo Jacono assisted in the data analysis. He contributed to manuscript formulation and revision.	10

Candidate's Signature [REDACTED] Date 03/07/2012

Declaration by co-authors

The undersigned hereby certify that:

- 1) the above declaration correctly reflects the nature and extent of the candidate's contribution to this work, and the nature of the contribution of each of the co-authors.
- 2) they meet the criteria for authorship in that they have participated in the conception, execution, or interpretation, of at least that part of the publication in their field of expertise;
- 3) they take public responsibility for their part of the publication, except for the responsible author who accepts overall responsibility for the publication;
- 4) there are no other authors of the publication according to these criteria;
- 5) potential conflicts of interest have been disclosed to (a) granting bodies, (b) the editor or publisher of journals or other publications, and (c) the head of the responsible academic unit; and
- 6) the original data are stored at the following location(s) and will be held for at least five years from the date indicated below:

Location(s) NEWCASTLE UNIVERSITY

Signature 1 [REDACTED] Date 26/06/12
 Signature 2 [REDACTED] Date 26/06/12

Declaration for section 3 of Chapter 8

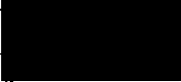
Declaration by candidate

In the case of section 3 of Chapter 8, the nature and extent of my contribution to the work was the following:

Nature of contribution	Extent of contribution (%)
M. Sherry designed the experimental model, oversaw model construction, conducted the experiments and processed the data. He developed tools to analyse the data and present it in the form seen in the manuscript. M. Sherry wrote the manuscript.	80

The following co-authors contributed to the work.

Name	Nature of contribution	Extent of contribution (%) for student co-authors only
John Sheridan	J. Sheridan guided research and contributed to manuscript formulation and revision.	10
David Lo Jacono	D. Lo Jacono assisted in the data analysis. He contributed to manuscript formulation and revision.	10

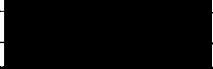
Candidate's Signature		Date	03/07/2012
-----------------------	---	------	------------

Declaration by co-authors

The undersigned hereby certify that:

- 1) the above declaration correctly reflects the nature and extent of the candidate's contribution to this work, and the nature of the contribution of each of the co-authors.
- 2) they meet the criteria for authorship in that they have participated in the conception, execution, or interpretation, of at least that part of the publication in their field of expertise;
- 3) they take public responsibility for their part of the publication, except for the responsible author who accepts overall responsibility for the publication;
- 4) there are no other authors of the publication according to these criteria;
- 5) potential conflicts of interest have been disclosed to (a) granting bodies, (b) the editor or publisher of journals or other publications, and (c) the head of the responsible academic unit; and
- 6) the original data are stored at the following location(s) and will be held for at least five years from the date indicated below:

Location(s) MONASH UNIVERSITY

Signature 1		Date	26/06/12
Signature 2		Date	28/06/12

7.1. Summary of the near-wake turbulence data

Declaration for section 1 of Chapter 8

Declaration by candidate

In the case of section 1 of Chapter 8, the nature and extent of my contribution to the work was the following:

Nature of contribution	Extent of contribution (%)
M. Sherry designed the experimental model, oversaw model construction, conducted the experiments and processed the data. He developed tools to analyse the data and present it in the form seen in the manuscript. M. Sherry wrote the manuscript.	80

The following co-authors contributed to the work.

Name	Nature of contribution	Extent of contribution (%) for student co-authors only
John Sheridan	J. Sheridan assisted analysis of results through discussion and research guidance. He contributed to manuscript formulation and revision.	10
David Lo Jacono	D. Lo Jacono assisted in the data analysis and presentation of data. He contributed to manuscript formulation and revision	10

Candidate's Signature [REDACTED] Date 03/07/2012

Declaration by co-authors

The undersigned hereby certify that:

- 1) the above declaration correctly reflects the nature and extent of the candidate's contribution to this work, and the nature of the contribution of each of the co-authors.
- 2) they meet the criteria for authorship in that they have participated in the conception, execution, or interpretation, of at least that part of the publication in their field of expertise;
- 3) they take public responsibility for their part of the publication, except for the responsible author who accepts overall responsibility for the publication;
- 4) there are no other authors of the publication according to these criteria;
- 5) potential conflicts of interest have been disclosed to (a) granting bodies, (b) the editor or publisher of journals or other publications, and (c) the head of the responsible academic unit; and
- 6) the original data are stored at the following location(s) and will be held for at least five years from the date indicated below:

Location(s) MONASH UNIVERSITY.

Signature 1 [REDACTED] Date 26/06/12
 Signature 2 [REDACTED] Date 26/06/2012

Chapter 8

Complex terrain chapter Summary

This chapter presents research that characterises flow over complex terrain. Wind farms are commonly placed in complex terrain, which alters the undisturbed wind significantly. This is especially true in Australia where a large proportion of wind farms are located in coastal regions (*e.g.* see figure 2.8 in chapter 2). A forward facing step is used here as a representative example of a two-dimensional escarpment or coastal cliff. The details of the experimental model were presented in chapter 3. Flow over complex terrain was investigated to gain a better understanding of the separating and reattaching flow fields wind turbine maybe subjected to if placed in such complex terrain. The benefits and drawbacks of placing turbines in complex terrain can then be evaluated, meaning wind farm designers can make critical judgements on whether these locations are a suitable wind farm location. The references are collated at the end of the chapter to avoid repetition in the text body.

The results in the following chapter are split into three sections.

Section 8.1

This section details results of a forward facing step (FFS) immersed in a turbulent boundary layer. A wide Re_h range (1 400–19 000) and three δ/h ratios (0.83–2.5) are investigated to determine the sensitivity of the recirculation region dimensions.

This work was published in the *Journal of Wind Engineering and Industrial Aerodynamics* in 2010. The paper was titled 'An experimental investigation of the recirculation zone formed downstream of a forward facing step'. The co-authors were D. Lo Jacono and J. Sheridan. The manuscript appeared in volume 98, pages 888-894. The paper has been reformatted to maintain consistency with other thesis chapters.

The results show the flow over a FFS is complex with a recirculation region forming down-

stream of the step edge. The trajectory of the separated shear layer is dependent on the height of the step and this influences the distance required for reattachment. Two regimes exist depending on the δ/h ratio and the Re_h . In the first regime, for $1.4 \times 10^3 \leq Re_h \leq 8.5 \times 10^3 \pm 600$, the recirculation region dimensions are strongly dependent on the Reynolds number. In the second regime, for $8.5 \times 10^3 \pm 600 \leq Re_h \leq 19 \times 10^3$, this dependency reduces. The recirculation region exists in a quasi-steady state with the dynamics of the region illustrated by a phase-binning technique using proper orthogonal decomposition (POD).

Section 8.2

Wind turbines are located in the atmospheric boundary layer, a highly turbulent environment. Section 8.2 provides results of a FFS subjected to several levels of freestream turbulence intensity. The turbulence level was varied using passive turbulence grids.

This work has been submitted to the *Journal of Wind Engineering and Industrial Aerodynamics* in 2012. The paper was titled 'The effect of turbulence on flow over a forward facing step'. The co-authors were D. Lo Jacono and J. Sheridan. The paper has been reformatted to maintain consistency with other chapters.

The results show increased freestream turbulence intensity reduces the mean reattachment length. The Reynolds shear stress components revealed an increase in the transfer of momentum toward the step with increasing turbulence intensity. This momentum transfer helps to overcome the recirculation region above the step and cause earlier reattachment.

Section 8.3

Wind farm locations are not limited to coastal cliffs. They are often placed in the vicinity of topological features where the slope angle is less than 90° . For slope angles less than 90° , the topological feature is here termed a two-dimensional escarpment. Flow separation may still occur above such topological features.

Section 8.3 details the recirculation region above a 2D escarpment with various escarpment angles ($30^\circ \leq \theta \leq 90^\circ$). This work has been drafted for submission to *Journal of Wind Engineering and Industrial Aerodynamics* in 2012.

A wide Re_h range (2 400–13 700) for a single δ/h ratio of 1.25 was investigated. The recirculation region dimensions are dependent on the escarpment angle and Reynolds number.

In this flow the turbulence production was constrained to the separated shear layer, a region that should be avoided when installing wind turbines. The investigation reveals turbines placed in complex terrain may produce greater power but this benefit must be balanced against the detrimental effects of increased turbulence and a vertical velocity component.

8.1 An experimental investigation of the recirculation zone formed downstream of a forward facing step

8.1.1 Abstract

An experimental investigation of the recirculation zone formed downstream of a forward facing step immersed in a turbulent boundary layer has been undertaken using particle image velocimetry. Bluff body flow is observed with the fixed separation point located at the leading edge of the step. The recirculation region dimensions are characterised over a range of Reynolds numbers (1 400–19 000), with Re_h based on the step height and the free stream velocity. Turbulent perturbations are produced in the free shear layer which develops between the recirculating flow close to the step and the free stream flow. Contour maps of amplification factor, streamwise perturbation velocity and Reynolds stresses are constructed, providing insight into optimal placement of structures within such topographical features. The mechanisms affecting the reattachment distance, namely the turbulent mixing within the boundary layer and the velocity deficit in the boundary layer, are discussed.

8.1.2 Introduction

Separating and reattaching flow phenomena are of particular interest for wind engineering applications. One area of wind engineering which has seen rapid development in recent times is wind energy. Wind turbines are commonly sited in the vicinity of topological features such as coastal cliffs and escarpments in the atmospheric surface layer due to the localised wind speed up effects such features produce. Wind flow in the vicinity of such topographical features is highly complex with flow separation occurring adjacent to regions of high shear. The current one-dimensional numerical models used by the wind industry in their planning process are unable to predict flow separation. Turbines placed within the recirculation region atop a cliff will be subjected to fluctuating loads and high vertical shear forces due to the turbulent nature of the flow. Optimal turbine placement beyond the highly distorted recirculation region will ensure estimated power production is achieved, while not subjecting the turbine to unknown fluctuating loads.

There have been a number of works dealing with obstacles immersed in turbulent boundary layers. The majority of these have concentrated on flow over a backward facing step (BFS) and a comprehensive review of these studies can be found in Eaton and Johnston (1981). Studies dealing with separating and reattaching flow over a forward facing isolated step (FFS) are less numerous, most probably due to the unsteady nature of the flow and

8.1. An experimental investigation of the recirculation zone formed downstream of a forward facing step

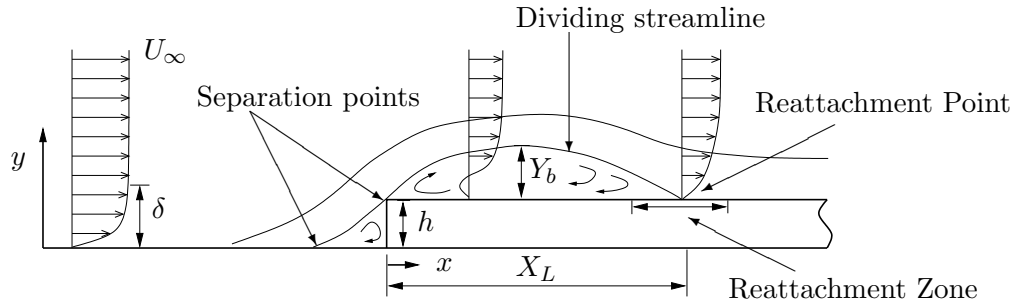


FIGURE 8.1: Flow features over a forward facing step (FFS). Left to right: upstream boundary layer profile, upstream recirculation, step face, recirculation region of present interest, reattachment point.

the presence of two recirculation regions (Eaton and Johnston 1981). In addition researchers also face difficulty in obtaining accurate data in the recirculation region and attributing flow behaviour to an individual flow parameter due to the dependence of results on a large number of flow parameters (Bradshaw and Wong 1972). The flow over a FFS has a number of unique features that are shown in figure 8.1. The turbulent boundary layer approaches the obstacle from left to right. The blockage of the step causes an adverse pressure gradient, with the consequence that the flow separates at $\sim 1-1.2h$ upstream of the step and reattaches to the vertical step wall at $\sim 0.6h$ above the ground surface (Leclercq et al. 2001). The upstream recirculation region contains near stagnant fluid which acts as an ‘equivalent’ slope angle (Bowen and Lindley 1977). This equivalent slope angle reduces the severity of the step-induced flow deflection and significantly influences the reattachment length as shown in section 8.3.

The blunt leading edge of the FFS acts as the sole fixed separation point for this geometry. A recirculation occurs behind the step, extending from the leading edge to the reattachment point, denoted as X_L . Hence, a strong shear layer develops between the low velocity reverse flow close to the wall and the mean free stream flow, increasing local mixing and the turbulent intensity within the boundary layer. As the step height becomes much larger than the boundary layer thickness (*i.e.* $\delta/h \ll 1$), the geometry resembles that of a blunt flat plate. It is known that in the case of a blunt flat plate, the free stream turbulence level significantly influences the reattachment length although this mechanism remains unclear (Hillier and Cherry 1981). The separation region experiences a weak regular vortex shedding which leads to an accumulation of vorticity within the recirculation region. This accumulation process sees the region grow in size until a large scale vortex is ejected from the recirculation region with a resulting reduction in recirculation region size and hence reattachment length (Kiya

TABLE 8.1: Reattachment length results from previous FFS studies including important study parameters, boundary layer height to step height ratio δ/h , step length aspect ratio L/h , and Reynolds number Re_h .

Study	δ/h	L/h	Re_h	X_L
Largeau and Moriniere (2007)	≤ 0.3	≥ 9	$2.88-12.82 \cdot 10^4$	3.5-5
Hattori and Nagano (2010)	0.33-0.66	23.3	$0.9-3 \cdot 10^3$	1.82-2.04
Bergeles and Athanassiadis (1983)	0.48	4	$2.7 \cdot 10^4$	3.75
Moss and Baker (1980)	0.7	12.7	$5 \cdot 10^4$	4.7
Gasset et al. (2005)	~ 0.7	> 6	$5 \cdot 10^4$	5.0
Zhang (1994)	0.7	32	–	4.02
Leclercq et al. (2001)	0.7	10	$1.7 \cdot 10^5$	3.2
Current Study	0.83-2.5	≥ 11.1	$1.4-19 \cdot 10^3$	1.9-4
Arie et al. (1975)	1.96	4	–	2.5
Farabee and Casarella (1986)	2.4	> 10	$2.1 \cdot 10^4$	~ 3
Camussi et al. (2008)	5	> 8	$8.8-26.3 \cdot 10^3$	1.5-2.1
Castro and Dianat (1983)	5.2	2	$5 \cdot 10^4$	1.4
Agelinchaab and Tachie (2008)	9.3	6	$1.92 \cdot 10^3$	4.1

and Sasaki 1983). The vorticity accumulation process induces a low frequency oscillation of the shear layer. Therefore, the unsteady behaviour of the shear layer implies that the reattachment point also fluctuates (within a ‘reattachment zone’ as shown in figure 8.1).

The mean reattachment position, X_L , is sensitive to several parameters, such as the body aspect ratios, L/h , W/h , streamwise length and spanwise width to step height ratios respectively, and the upstream boundary layer thickness to step height ratio, δ/h (Castro 1979). A sufficiently large model L/h ratio is required to consider the step truly ‘isolated’. The three dimensionality of the recirculation region increases with reductions in the W/h aspect ratio (Largeau and Moriniere 2007). A single dominant parameter affecting X_L is difficult to determine due to the complex coupled relationship between the two separated regions involved in the FFS geometry (Bradshaw and Wong 1972).

The previous recirculation studies involving a FFS immersed in a turbulent boundary layer can broadly be separated into two categories. Studies are grouped together based on the upstream boundary layer thickness to the step height ratio, δ/h . The two categories are thus for studies conducted with an approaching boundary layer thickness greater than the step height, *i.e.* $\delta/h > 1$ and conversely studies with a boundary layer thickness less than the step height, *i.e.* $\delta/h < 1$. Studies conducted with $\delta/h > 1$ have clearly shown that the reattachment length is heavily dependent on δ/h (Agelinchaab and Tachie 2008; Arie et al. 1975; Camussi et al. 2008; Castro and Dianat 1983; Farabee and Casarella 1986), whereas

8.1. An experimental investigation of the recirculation zone formed downstream of a forward facing step

when $\delta/h < 1$ it seems that the reattachment length is weakly affected by this ratio, and is usually situated around $4h$ to $5h$ depending on Reynolds number (Bergeles and Athanassiadis 1983; Gasset et al. 2005; Hattori and Nagano 2010; Largeau and Moriniere 2007; Moss and Baker 1980; Zhang 1994). The reattachment length in previous studies was determined via a variety of different experimental methods including flow visualisation techniques (Arie et al. 1975; Bergeles and Athanassiadis 1983; Camussi et al. 2008; Castro and Dianat 1983; Largeau and Moriniere 2007), hot wire anemometry (Bergeles and Athanassiadis 1983; Moss and Baker 1980), surface pressure measurements (Castro and Dianat 1983; Farabee and Casarella 1986; Largeau and Moriniere 2007; Leclercq et al. 2001), laser doppler velocimetry (Leclercq et al. 2001), particle image velocimetry (Agelinchaab and Tachie 2008; Camussi et al. 2008; Largeau and Moriniere 2007) and numerical models (Gasset et al. 2005; Hattori and Nagano 2010; Zhang 1994). Results from previous researchers are summarised in table 8.1.

The purpose of this study is to investigate the velocity fields over a FFS immersed in a turbulent boundary layer for various δ/h ratios over a wide Reynolds number range. Insight into the flow topology above the forward facing step geometry will aid the optimal placement of wind turbines sited within complex terrain.

8.1.3 Experimental facilities

The free surface water channel has a working section of $600 \times 800 \times 4000$ mm and a working speed range of $0.09 \text{ m/s} < U_\infty < 0.46 \text{ m/s}$. The channel walls are constructed of glass allowing easy optical access. Flow uniformity is achieved through the use of an upstream honeycomb section and fine turbulence screen. The flow passes through a 3:1 contraction to accelerate the mean flow and reduce the residual streamwise turbulence intensity to 1%.

The experiments were conducted over a wide Reynolds number range, $1400 < Re_h < 19000$. The Reynolds number is defined in equation 8.1,

$$Re_h = \frac{U_\infty h}{\nu}, \quad (8.1)$$

where U_∞ is the free stream velocity, h is the step height, and ν is the kinematic viscosity of the working fluid. The flow passes through a final turbulence screen situated $16.67h_{\min}$ and $56.67h_{\min}$ upstream of the model leading edge and forward facing step edge respectively. Here, h_{\min} is the minimum step height of 15 mm. The turbulence screen has a mesh diameter of $0.84h_{\min}$, and a solidity ratio of 22% producing a turbulence level of 1.43%. The final turbulence screen serves to regulate the turbulence level between subsequent measurement

days.

A Nd:YAG (Minilite PIV, CONTINUUM) laser of wavelength 532 nm was used to produce a pulsed laser sheet of 2 mm thickness. The flow was seeded with polyamide particles of mean diameter 50 μm and specific gravity of 1.06 g/cm^3 .

Two CCD PIV camera systems with different resolutions were used in conjunction with a 200 mm lens. System one had a maximum resolution of 4008×2672 pixels whilst system two had a maximum resolution of 2004×1336 pixels. The results were invariant of the camera system used. A minimum magnification factor of 50 pixels/mm was employed giving a field of view (FOV) of $5.34h_{\text{min}} \times 3.46h_{\text{min}}$ and $2.67h_{\text{min}} \times 1.73h_{\text{min}}$ for system one and two respectively. A multi-step interrogation window with an initial size of 64×64 pixels to a final size of 32×32 pixels with 50% overlap was used. This allowed instantaneous velocity maps of 250 by 167 vectors and 125 by 83 vectors to be captured for system one and two respectively. The velocity vector resolution of the velocity maps was 0.64 mm by 0.64 mm. The camera was re-positioned using a manual traversing mechanism with camera alignment ensured prior to data acquisition.

A total of 400 independent image pairs were captured for each spatial position and Reynolds number. The image pairs were captured at 1 Hz so individual velocity realisations are minimally correlated. Whilst the recirculation zone's presented were all the result of averaging of the turbulent flow, convergence (via variance of the fluctuating cross velocity product from the cumulative mean) was shown to occur prior to 400 image pairs. Therefore 400 images pairs were deemed an acceptable compromise between convergence of the results and excessive use of disk space. A total of 1000 image pairs were used for the POD analysis to allow sufficient data samples in each phase bin. The raw data was processed on a 20 CPU (Beowulf) cluster that allowed rapid analysis of results. Validated cross correlation PIV software developed in-house was employed to generate the displacement fields (Fouras et al. 2008).

8.1.4 Experimental model

The experimental model was constructed of acrylic and polycarbonate for rigidity. The step height h , was varied from 15 to 45 mm through the use of perspex spacers giving a L/h and W/h range of 11.1–33.3. The employed aspect ratios, were above the critical aspect ratios to ensure both reattachment to the top surface and that the model is representative of an isolated step in every flow setting ($L/h > 10$) (Castro and Dianat 1983) and that the flow is

8.1. An experimental investigation of the recirculation zone formed downstream of a forward facing step

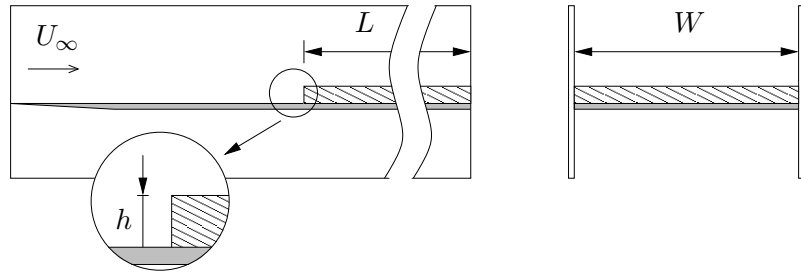


FIGURE 8.2: Schematic of the polycarbonate and acrylic experimental model used in the current study. Height of end plates is 210 mm

nominally two dimensional at mid span ($W/h > 10$) (de Brederode and Bradshaw 1972).

The model was fitted with end plates to minimise 3D edge effects and all edges bar the FFS leading edge were formed into an asymmetric 5° taper to minimise blockage effects. The maximum blockage ratio ($h = 45$ mm) in the current tests was 9.73%. No corrections were made to adjust the results due to blockage affects. A schematic of the model can be seen in figure 8.2. The model was suspended within the channel in an inverted position. In this configuration, any free surface effects of the water channel were minimised. A boundary layer formed upstream of the step with the profile as shown in figure 8.3. The boundary layer profile was measured at a distance $9h_{\min}$ upstream of the step over the entire velocity range producing a Reynolds number range of $37\,000 < Re_x < 183\,200$. The boundary layer thickness varied by 10% across this Re_x range, thus it was assumed constant and the maximum thickness was used as a scaling parameter. The boundary layer had a thickness $y = \delta = 2.5h_{\min}$ where $u(y) = 0.99U_\infty$, a shape factor of $H = 1.63$ and a momentum thickness of $0.27h$. The maximum u_{rms} and v_{rms} components within the boundary layer were $\sim 0.2U_\infty$ and $\sim 0.05U_\infty$ respectively. The different step heights gave a δ/h range of $0.83 < \delta/h < 2.5$. A total of 2500 image pairs were utilised for convergence of the boundary layer profile results.

8.1.5 Results

The recirculation zone dimensions using the PIV results were determined by calculating the streamlines (see equation 8.2), above the step surface.

$$\Psi = \int_0^y (\bar{u}/U_\infty) d(y/h), \quad (8.2)$$

where \bar{u} is the temporal average of the streamwise velocity component. It has the advantage of not propagating a PIV error in the streamwise direction (Jacono et al. 2009). For the data analysis, the Cartesian coordinate system was fixed at the step leading edge. The mean reattachment distance, X_L , occurred where the dividing streamline, $\Psi = 0$, (from here

on denoted as Ψ_0) bifurcated at the step surface and the region of negative flow ceased. At the reattachment point, one arm of the dividing streamline returns upstream into the recirculation region and the second continues downstream. The height of the recirculation region is defined as the maximum height of the dividing streamline above the step, Y_b such that $\max(\Psi_0) = \Psi_0(Y_b)$.

A typical mean streamwise velocity, \bar{u} , contour line plot obtained from the PIV measurements is shown in figure 8.4. The flow is from left to right, with the length and velocity scales non dimensionalised against the step height, h , and freestream velocity, U_∞ , respectively. The Reynolds number, Re_h of figure 8.4, is 6741. The recirculation region is indicated by the solid line (Ψ_0), while the dashed contour lines depict reverse flow. Further, the region between the largest dashed contour line and the adjacent solid line indicates the mean position of maximum shear within the recirculation region. The mean reattachment length, X_L , and the mean height of the recirculation region, Y_b of figure 8.4 are $2.90h$ and $0.36h$ respectively.

Moss and Baker state that the BFS is the simplest bluff body geometry due to minimum flow deflection of the streamlines (Moss and Baker 1980). Two instabilities affect the separated region behind a BFS, a convective instability and an absolute instability (Dandois et al. 2007). The convective instability appears in the form of Kelvin–Helmholtz vortices in the free shear layer whereas the absolute instability results in the low frequency flapping of the shear layer (Dandois et al. 2007).

The recirculation zone downstream of a BFS exists in a quasi steady state due to the higher deflection of the incoming flow. While the instability mechanisms affecting a BFS flow were not the primary focus of the current study, some comments can be made regarding the

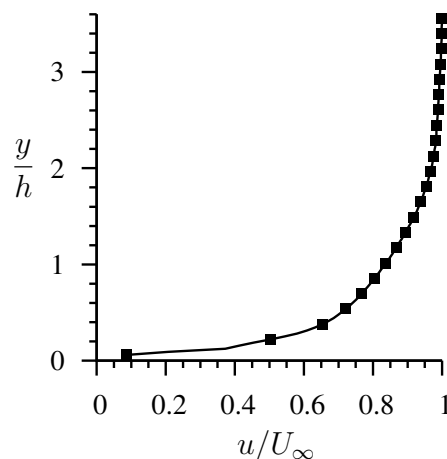


FIGURE 8.3: The upstream boundary layer profile measured at $9h_{h=15\text{ mm}}$ upstream of the step using 2500 independent PIV images. Only every fifth data point is presented for clarity.

8.1. An experimental investigation of the recirculation zone formed downstream of a forward facing step

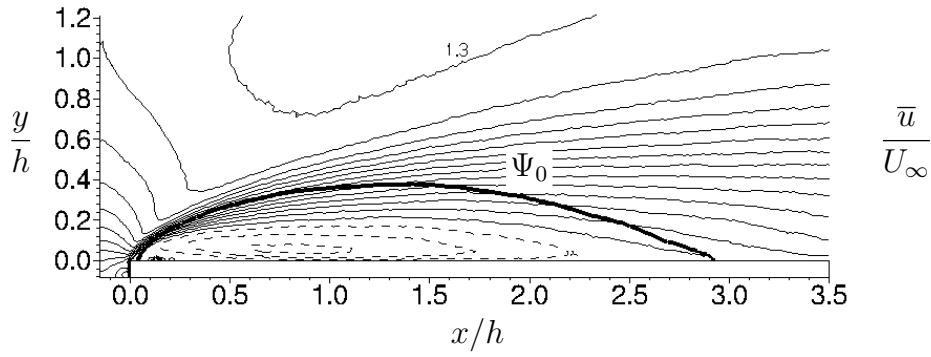


FIGURE 8.4: General bluff body flow features of the FFS flow, contour lines of mean streamwise velocity \bar{u} ; reference value of $1.3 \bar{u}/U_\infty$ shown with line increments equal to $0.2 \bar{u}/U_\infty$; solid line is the dividing streamline Ψ_0 , dashed contour lines depict region of entirely negative flow, $\delta/h = 1.25$, $Re_h = 6741$.

low frequency flapping of the shear layer. The recirculating flow within the separated region is ejected when the region can no longer sustain the amount of entrained fluid. This ejection process causes the free shear layer to flap. This flapping motion causes the reattachment position to oscillate around the mean reattachment position creating a reattachment zone as shown in figure 8.1.

The flapping of the shear layer was investigated using the ‘snapshot’ proper orthogonal decomposition (POD) technique (Sirovich 1987). The basis of POD is that an input data set can be represented by an orthogonal set of temporal and an orthonormal set of spatial modes. The advantage of POD is that it creates an optimal set of basis functions in terms of energy (here kinetic) within a given flow. We utilised the snapshot POD technique here to perform a spatial kinetic energy decomposition on the fluctuating velocity component. The energy level of the resulting eigenvalues gives an indication of the dominant temporal structures within a flow. The technique has successfully been applied to other bluff body geometries (Kostas et al. 2005; Mathis et al. 2009; van Oudheusden et al. 2005). Using a similar technique as (van Oudheusden et al. 2005), the phase angle (ϕ) between the first two temporal eigenvalues ($a_1(t)$ and $a_2(t)$) is calculated, and the resulting distribution binned into 8 phases ($\phi = 0, \pi/4, 2\pi/4, \dots, 7\pi/4$) to determine the spatial structure within the highest energy portion of the flow. The corresponding binned fields were temporally averaged, resulting in the contours of mean streamwise velocity and associated dividing streamlines shown in figure 8.5. In figure 8.5, phase progression is from top to bottom spanning two pages. The contours display the movement of the recirculation region within the two highest energy modes of the flow. Performing a temporal average as in figure 8.4 masks the dynamical movement of

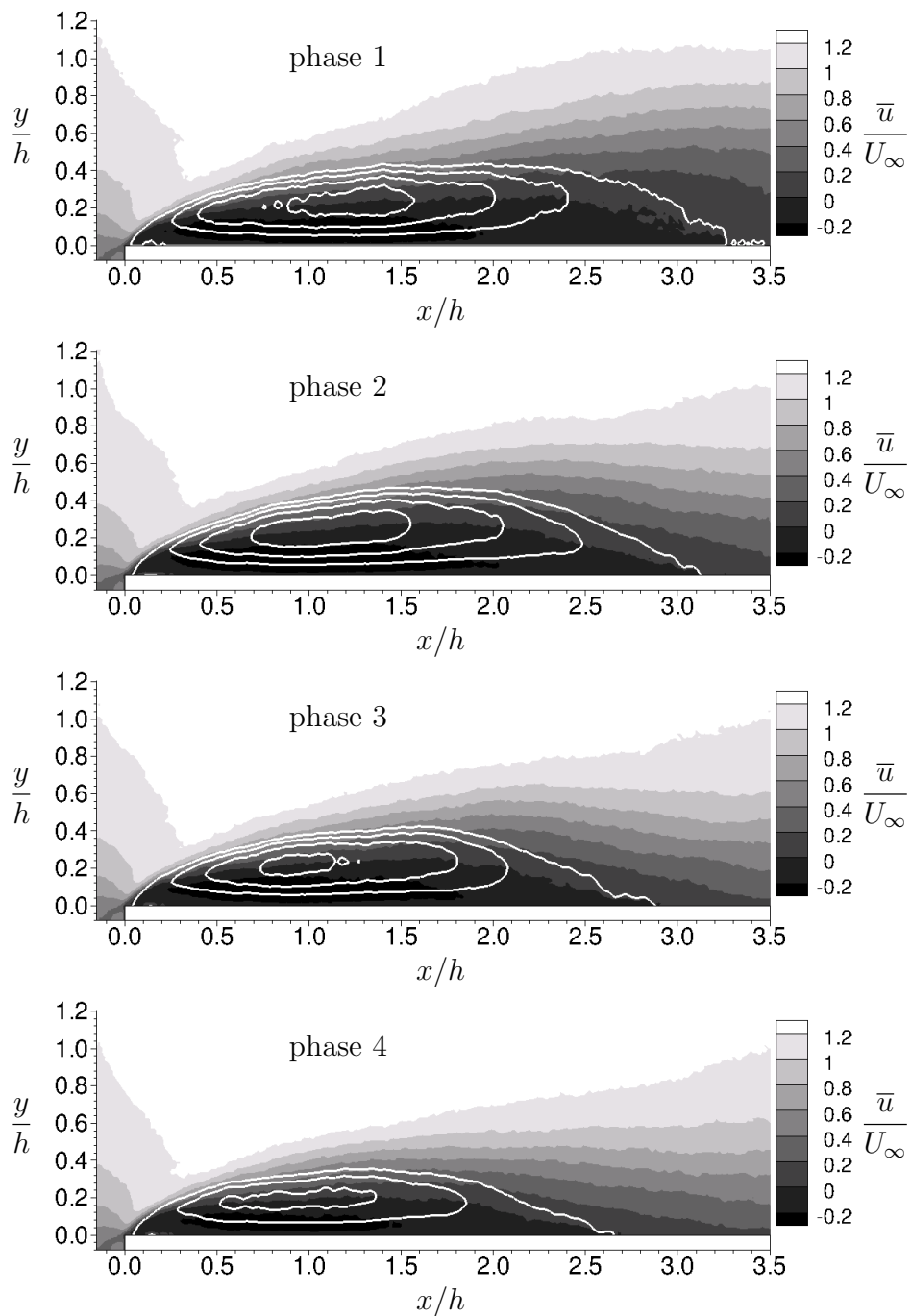
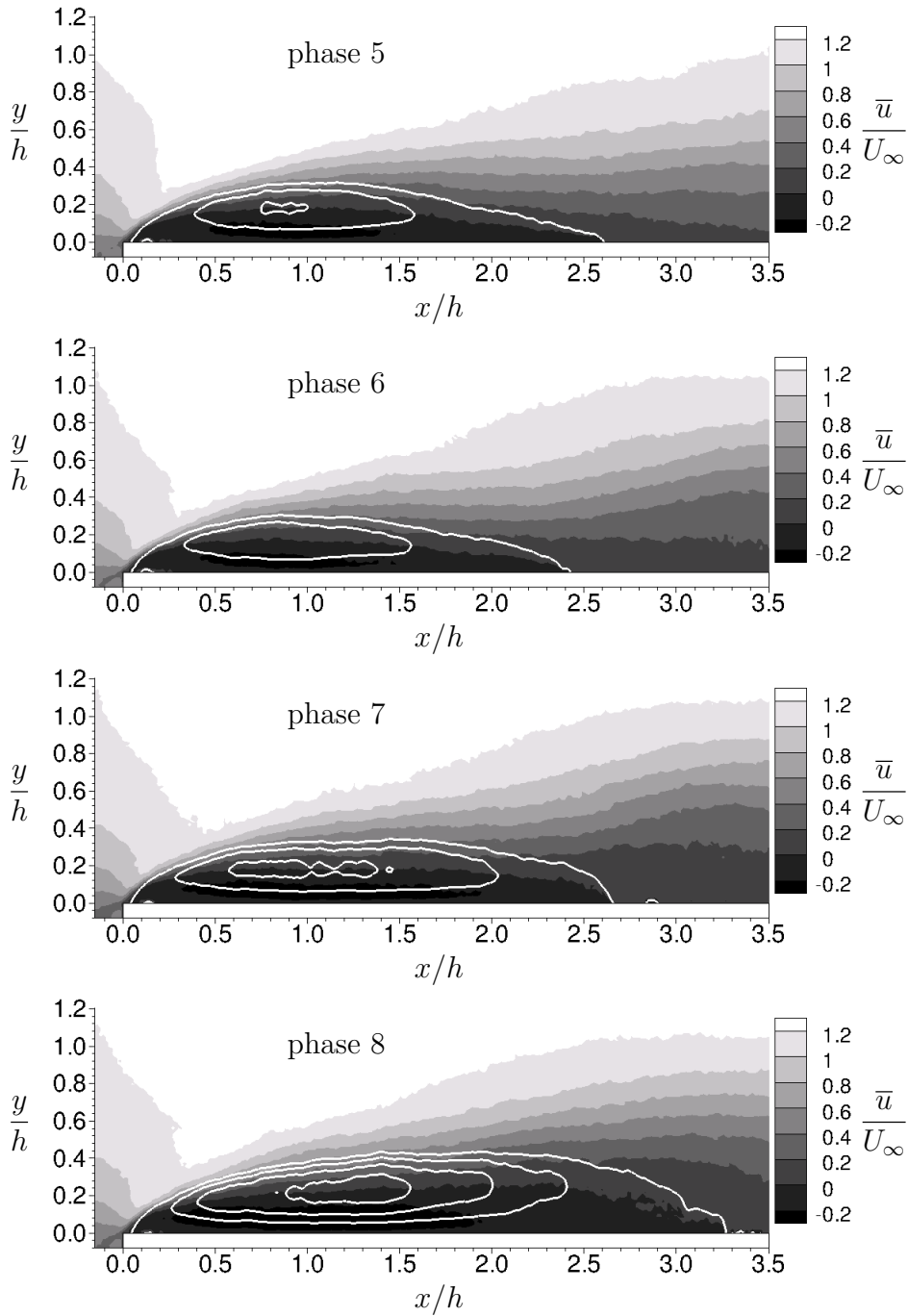


FIGURE 8.5: Eight phase averages from a POD analysis of the FFS shear layer dynamics for $\delta/h=1.25$, $Re_h=6741$. Phase progression is from top to bottom, 1–4 ($0 - 3\pi/4$) this page, 5–8 ($\pi - 7\pi/4$) on following page, contours of mean velocity \bar{u} ; white solid streamlines indicate dynamics of recirculation region shape and size.

the recirculation region. The POD thus provides further insight into the dynamics of the unsteady recirculation region.

The maximum adverse flow within the recirculation region for the Reynolds number range investigated is between 24–36% of the freestream velocity. Such a level of adverse flow in-

8.1. An experimental investigation of the recirculation zone formed downstream of a forward facing step



indicates the cause of the expansion and contraction of the recirculation region shown by the POD results is most likely due to the global instability mode which affects laminar separation bubbles at smaller Reynolds numbers (Castro 2005). In figure 8.5, the reattachment zone (based on the distribution of phase averaged mean reattachment lengths and recirculation zone heights) extends from $2.36h$ – $3.28h$ in the streamwise direction and $0.31h$ – $0.49h$ in the wall normal direction. The mean reattachment length and mean recirculation zone height (*i.e.* temporal average of all eight phases shown in figure 8.4) for this flow setting are

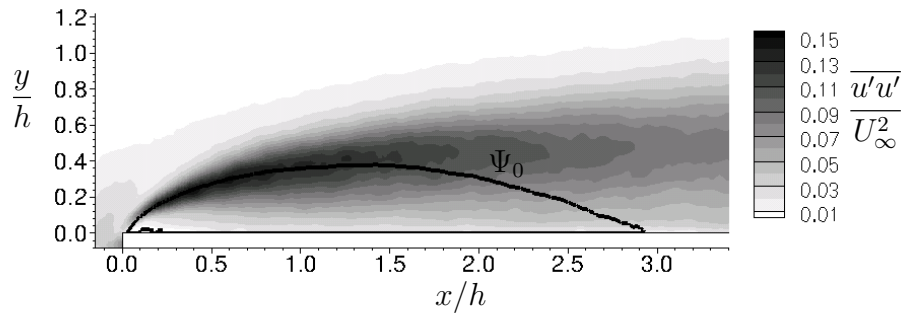


FIGURE 8.6: Streamwise perturbations within the shear layer above a FFS for $\delta/h = 1.25$; $Re_h = 6741$, contours of $\overline{u'u'}/U_\infty^2$; solid line is the dividing streamline Ψ_0

$X_L = 2.90$ and $Y_b = 0.36$ which are $\sim 2\%$ and $\sim 10\%$ different respectively to the average reattachment length and recirculation zone height obtained from the dominant POD mode data only. Therefore the phase decomposition via a POD analysis is an accurate method to capture the dominant flow topology.

The onset of the convective instability - that resulting in the formation of Kelvin–Helmoltz (KH) vortices - was not investigated in the current study.

The free shear layer can be seen from the turbulent velocity component plots of figures 8.6 and 8.7. Figure 8.6 displays the square of the streamwise perturbation field ($\overline{u'u'}/U_\infty^2$) and figure 8.7 displays the non-dimensionalised Reynolds shear stress ($-\overline{u'v'}/U_\infty^2$) component.

It can be seen from the $\overline{u'u'}/U_\infty^2$ field of figure 8.6 that the streamwise Reynolds stresses are generated in the separated shear layer. This Reynolds stress term has a small magnitude close to the step surface, rises to a peak in the free shear layer before reducing to a low value in the free stream in a similar fashion to that seen in the Moss and Baker study (Moss and Baker 1980). At a given streamwise distance downstream from the leading edge, the peak value of this Reynolds stress is located at a similar height to the dividing streamline, Ψ_0 until the dividing streamline curves back toward the step surface. The stress distribution then flattens out and reduces in intensity with downstream distance. The peak stress maximum occurs prior to the streamwise location of the maximum height of the recirculation zone, *i.e.* $\Psi_0(Y_b)$.

The Reynolds shear stress component shown in figure 8.7 has a negative value close to the separation point before changing sign further downstream. The initial negative values of the Reynolds shear stress corresponds to a production region of the Reynolds stress component (Hattori and Nagano 2010). Positive Reynolds shear stress values arise when velocity fluctuations in the wall normal direction and a positive mean velocity gradient

8.1. An experimental investigation of the recirculation zone formed downstream of a forward facing step

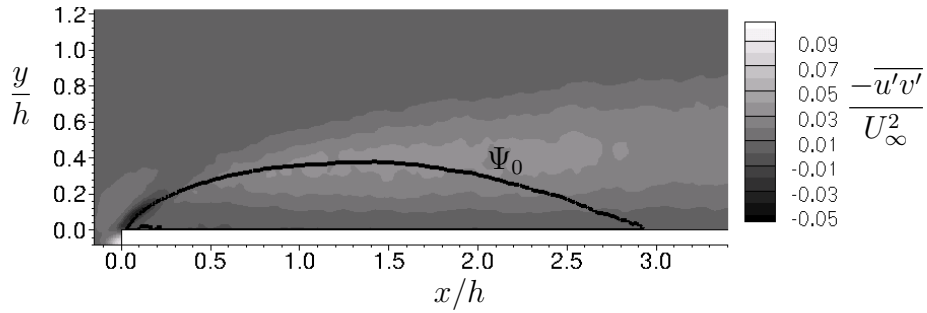


FIGURE 8.7: Reynolds shear stress contours produced above a FFS for $\delta/h = 1.25$; $Re_h = 6741$, contours of $-\overline{u'v'}/U_\infty^2$; solid line is the dividing streamline Ψ_0

$(\delta\overline{U}/\delta y + \delta\overline{V}/\delta x)$ occur (Hattori and Nagano 2010). In a similar fashion to the streamwise Reynolds stress distribution, the Reynolds shear stress profile also then flattens out and spreads through turbulent mixing.

Turbulent mixing is the principal mechanism promoting reattachment. This mixing entrains higher velocity free stream fluid into the recirculation region to overcome the momentum deficit created by the separation above the step. The maximum streamwise perturbation occurs in the free shear layer just downstream of the step for all Reynolds numbers, a direct result of the bluff nature of the body.

The variation in reattachment length, X_L , with Reynolds number, Re_h , can be seen in figure 8.8. Trends for the three different δ/h ratios are indicated by separate trend lines. It is evident that the variation of X_L with Re_h for a given δ/h ratio (individual trend line) is monotonic over the entire Re_h range. The blockage caused by the step, although different for all three δ/h ratios investigated was at all times less than 10% and so not the source of the variation in X_L with Re_h .

As the Reynolds number increases for a given δ/h ratio, the upstream flow is deflected further into the free stream, elongating the recirculation region. It is known for flow over a blunt flat plate that vortex shedding from the recirculation region occurs above a threshold Reynolds number, $Re_h \sim 800$ (Ota et al. 1981). As the Reynolds number increases past this critical value, the shear layer becomes susceptible to Kelvin-Helmholtz instabilities at intermediate Reynolds numbers (see flow visualisations in Cherry et al. (1984)). Figure 8.8 reveals the apparent existence of two distinct regimes. In regime 1 ($Re_h \leq 8500$), a linear trend of increasing reattachment length with Reynolds number exists. It is expected that in regime 1, laminar separation occurs from the fixed separation point with transition occurring in the shear layer before turbulent reattachment. In regime 2 ($Re_h \geq 8500$), the reattachment

length becomes less sensitive to Reynolds number increases. Regime 2 is an indication that the shear layer transition point moves very close to the fixed separation point such that it could be considered turbulent separation-turbulent reattachment. The regime change is postulated to occur at a lower Reynolds number in forward facing step geometries compared to blunt flat plate geometries due to the turbulent structures within the oncoming boundary layer. As shown by the spread of results obtained by previous researchers in table 8.1, results are heavily dependent on a number of flow parameters.

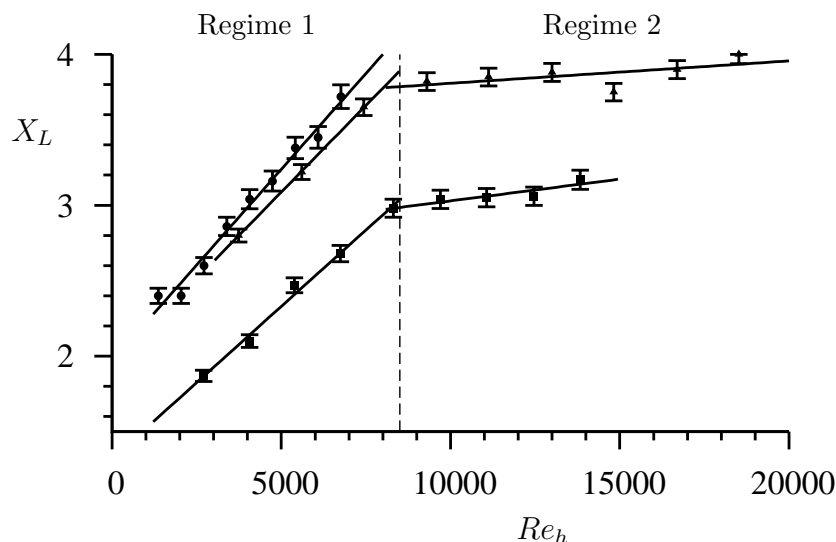


FIGURE 8.8: Variation of X_L with Re_h for three δ/h ratios, $0.83 < \delta/h < 2.5$, \bullet : $\delta/h = 2.5$; \blacksquare : $\delta/h = 1.25$; \blacktriangle : $\delta/h = 0.83$.

The change of regimes may also be due to the flow becoming increasingly three dimensional. It has been shown that flow over a forward facing step becomes increasingly three dimensional with decreases in the W/h ratio (Largeau and Moriniere 2007). In the current study with the three step heights simulated, the W/h ratio changes by a factor of 3 (whilst at all times remaining > 10 ensuring nominally 2D flow).

Increases in W/h ratio produces more ‘branching structures’ between the upstream and downstream recirculation regions (Largeau and Moriniere 2007). Unlike the Largeau and Moriniere study, which permitted three dimensional flow around the side of the model, here the experimental models were fitted with end plates which would emphasise this mechanism to transport fluid from the upstream recirculation region to that downstream. As measurements were only taken at the mid span and in one plane, the current results cannot reveal three dimensional fluid movement over the step.

When δ/h is less than unity, the free stream velocity will interact with the leading edge of the step directly. The free stream velocity, being larger than that within the boundary

8.1. An experimental investigation of the recirculation zone formed downstream of a forward facing step

layer, will cause a greater perturbation to the flow field resulting in the flow being deflected further into the free stream. However, the higher free stream velocity above the free shear layer will counteract the increased flow deflection and will limit shear layer expansion. In this way as δ/h becomes much lower than unity ($\delta/h \ll 1$) the influence of the upstream boundary layer is reduced and the results will more closely approximate separated flow over a blunt flat plate (Cherry et al. 1984; Hillier and Cherry 1981; Ota et al. 1981).

Conversely, when δ/h is greater than unity, the flow will be deflected less into the freestream due to the reduced velocity within the boundary layer. In this case, the reattachment length will be affected significantly by an increase in Reynolds number due to the velocity gradient in the boundary layer. Turbulence within the boundary layer will enhance mixing between the free stream and recirculating flow close to the step, promoting reattachment. It is for this reason that results obtained from $\delta/h > 1$ studies are heavily dependent on Re_h as shown in table 8.1. Variance between previous researchers results can be partially explained by the different boundary layer profiles and length scales therein, which would affect the free shear layer dynamics.

The mean reattachment length obtained by Agelinchaab and Tachie, is higher than any X_L obtained at a comparable Reynolds number in the current study. Free surface effects are an inherent parameter influencing results in water channel studies. A free surface will act as a momentum sink where the flow acceleration created by the step blockage can be released via surface deformation, prolonging separation. Closed channel studies however will see a higher velocity and hence greater momentum above the step due to the solid boundaries and the requirement for mass conservation. The higher momentum of the free stream flow will promote turbulent mixing between the flow within the recirculating region and the free stream, leading to earlier reattachment. In the current study, free surface effects of our open channel setup have been minimised through investigating the model in an inverted position.

The model length to height ratio, L/h , is also a controlling factor affecting reattachment to the top surface of a forward facing step (Bergeles and Athanassiadis 1983; Castro and Dianat 1983). This value appears heavily dependent on the δ/h ratio simulated. Bergeles and Athanassiadis showed with a simple flow visualisation method that a minimum L/h ratio of 4 is required for mean shear layer reattachment to the top surface when $\delta/h < 1$ (Bergeles and Athanassiadis 1983), whereas Castro and Dianat determined a minimum L/h of ~ 1.75 to ensure mean shear layer reattachment when $\delta/h > 1$ (Castro and Dianat 1983). In light of this, a large majority of the previous studies listed in table 8.1 were conducted

on models where the influence of trailing edge separation on leading edge separation cannot be discounted. It is proposed that the expansion of the test section at the trailing edge of a model will act as a momentum sink promoting reattachment and hence affect the free shear layer dynamics at the leading edge. It is for this reason that recirculation regions can form on the short experimental bodies in the Arie et al.; Bergeles and Athanassiadis; Castro and Dianat studies (Arie et al. 1975; Bergeles and Athanassiadis 1983; Castro and Dianat 1983).

Further, flow does not reattach to the top surface of the block geometry investigated, in addition to the FFS geometry, in the Moss and Baker study, despite having the same dimensions and being conducted at the same Reynolds number as the Castro and Dianat study. This is clearly a δ/h ratio effect and the mechanism for the difference has been attributed to the turbulence within the boundary layer as outlined earlier. This hypothesis adds another parameter to an already complicated relationship, which contributes to the spread of results in table 8.1.

The offset between results at the same Reynolds number in figure 8.8 is due to a combined effect of the upstream flow conditions, principally the boundary layer thickness and body geometry effects.

8.1.5.1 Wind turbine placement

Wind turbines are commonly sited in complex terrain to take advantage of the wind speed-up effects the terrain produces. Figure 8.4 displays the region of increased wind speed above the step, beneficial in a wind energy sense. The maximum power available to a wind turbine through a given area increases with the cube of the mean wind speed, as shown in equation 8.3,

$$P_{max} = \frac{1}{2}\rho AU_{\infty}^3, \quad (8.3)$$

where A is the turbine swept area. From equation 8.3 it follows that a slight increase in wind speed can lead to significant additional energy generation.

The degree of advantage of turbines placed in complex terrain in an energy yield sense can be ascertained through the amplification factor, A_z , defined as the ratio of the wind speed above the topology to that at the same height above flat ground, as shown in equation 8.9,

$$A_z = \frac{u(x, z)}{u(x_o, z)}. \quad (8.4)$$

The amplification factor can also be viewed as a power production multiplier for a turbine situated in complex terrain compared against a turbine sited on uniform ground. Rearranging equation 8.3, we obtain,

8.1. An experimental investigation of the recirculation zone formed downstream of a forward facing step

$$P_{max_c} = A_z^3 P_{max_u}, \quad (8.5)$$

where P_{max_c} is the maximum power available to a wind turbine sited in complex terrain, P_{max_u} is the power available to the same turbine sited in uniform terrain and A_z , is the amplification factor.

An amplification factor contour map for a δ/h ratio of 1.25 is shown in figure 8.9. The dashed line in figure 8.9 depicts where A_z has a unit value. The maximum amplification factor in figure 8.9 is located very near the step surface ($y/h = 0.044$) above the fixed separation point in the region of high shear. The magnitude of the maximum amplification factor is largely Reynolds number independent with a value between 7–8. The magnitudes of amplification factor at larger y/h ratios ($y/h > 0.2$) are consistent with previous studies above a forward facing step (Bowen and Lindley 1977). However, the shape of the contour line plot presented in the Bowen and Lindley (1977) study (figure 4a) is different to figure 8.9 here due to the large δ/h ratio ($\delta/h = 20$) simulated. Such a large δ/h ratio will restrict the formation of a recirculation region and alter the dynamics of the free shear layer above the step surface.

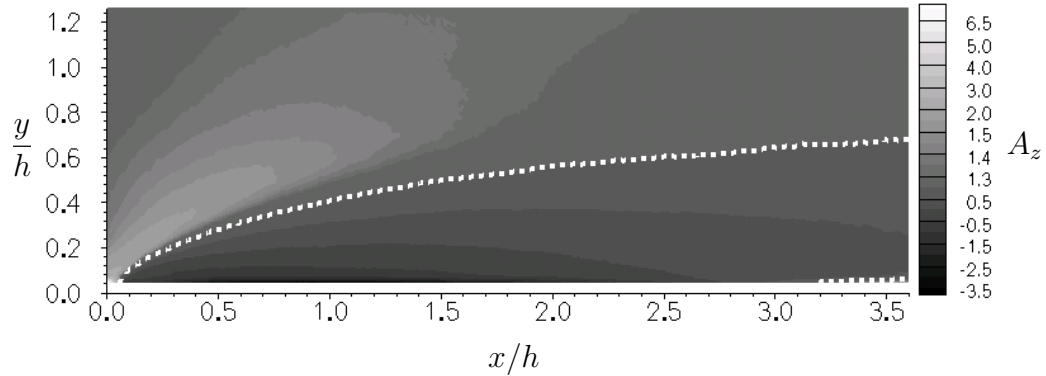


FIGURE 8.9: Contours of the amplification factor, A_z above a FFS for $\delta/h = 1.25$; $Re_h = 6741$. Dashed line indicates position where A_z has a unit value

Whilst placing turbines in complex terrain is beneficial in a wind energy sense, *i.e.* $P_{max_c} > P_{max_u}$ in figure 8.9, complex terrain produces regions of high shear and turbulence as shown in figures 8.6 and 8.7. The fluctuating loads these regions will induce on turbine components make it difficult to quantify the fatigue loading a turbine will experience during its serviceable lifetime. These regions are therefore undesirable as a wind energy installation site and a compromise must be reached between higher energy yields and detrimental fluctuating loads.

Whilst the Reynolds numbers simulated in the current investigation differ to those found

in the field by several orders of magnitude an example of optimal turbine placement can be estimated from figures 8.6, 8.7 and 8.9. Ensuring the minimum position of any blade tip is greater than $0.6h$ where h is the cliff height, will result in increased power production due to A_z while restricting detrimental effects of turbulence on turbine components within the shear layer.

8.1.6 Forward facing step section summary

The recirculation region formed downstream of a forward facing step immersed in a turbulent boundary layer has been investigated using the particle image velocimetry technique. The principal dimension of the recirculation region, the reattachment length, X_L , has been obtained for a wide Reynolds number range and several boundary layer thickness to step height ratios, δ/h .

The reattachment length tended to increase with Reynolds number for a given δ/h ratio. The range of reattachment lengths obtained in the current study was $1.9h < X_L < 4h$. Two regimes were found to exist in the results. The first regime exists for Reynolds numbers less than approximately 8500, where the reattachment length is heavily dependent on the Reynolds number. In the second regime, which exists for Reynolds numbers greater than 8500, the reattachment length is only weakly affected by Reynolds number. Surprisingly, this regime change occurred independently of the δ/h ratio. The regime change is postulated to occur due to shear layer transition immediately after separation and a change in the dynamic between the recirculation regions upstream and downstream of the step. The planar nature of the experimental technique employed here could not reveal this change and may form part of the ongoing work in the area.

The offset between results at the same Reynolds number is due to a combined effect of the upstream flow conditions, principally the boundary layer thickness and body geometry effects. The enhanced local mixing produced by the shear layer above the step and the elevated turbulence intensity within the boundary are thought to be the primary mechanisms promoting reattachment. The complexity of forward facing step flow was highlighted by the dependence of the mean reattachment length, X_L , on a number of flow parameters.

Clearly, these results confirm that wind engineers would be well-advised to consider the flow separation and increased turbulence that complex topographic features produce when siting turbines in complex terrain.

8.2 The effect of turbulence on flow over a forward facing step

8.2.1 Abstract

Wind turbines are frequently sited in complex terrain featuring topographic features which can be simplified to a forward facing step. While such features have the potential to induce desirable outcomes, such as higher velocities, they also result in flow separation, which can have undesirable effects on turbine performance. Here the effect of inlet turbulence of different intensities on the recirculation region above a forward facing step is investigated using particle image velocimetry in a water channel. The inlet turbulence intensity was varied using two traditional grids and a third, novel tethered sphere design, which was shown to greatly increase the turbulence intensity. Bluff body geometry effects were found to be more dominant than the inlet turbulence intensity in the early stages of separation. Downstream of the bluff body dominated separated region, turbulence promotes reattachment. Turbulence redistributes momentum between the freestream and the reversed flow within the recirculation region. The contour maps of the streamwise velocity and Reynolds shear stresses presented here provide new insight into optimal placement of structures within such topographical features.

8.2.2 Introduction

Wind turbines are now an established method of generating eco-friendly electricity. Wind turbines are clustered in groups, known as wind farms, to maximise energy extraction from a suitable area. The process of selecting a suitable area and subsequent optimisation of a wind farm layout is known as wind farm siting. Flat terrain with a high average wind speed and proximity to the electricity transmission grid are two key wind farm siting criteria. However, with the rapid expansion of the wind industry in the last decade, suitable flat terrain with a favourable wind resource is becoming scarce. Wind farms are therefore commonly sited close to complex terrain, such as cliffs and escarpments, to take advantage of the wind speed up produced by the local topography. However, flow separation may occur in complex terrain causing increased wind shear and turbulence intensity, both of which can reduce turbine life expectancy. Wind farm planning tools such as the wind atlas analysis and application program (WAsP) (Mortensen et al. 1993) were developed using linearized boundary layer models and as a result can break down in complex terrain (where slope > 0.3) (Petersen et al. 1998b). These one-dimensional models are unable to predict where flow separation occurs. Recently, wind engineers have embraced three-dimensional computational fluid dynamics (CFD) models to investigate the wind flow over prospective wind farm sites. Whilst requiring significant

computing power, the models are likely to increase the accuracy of wind energy predictions but clearly need to be properly validated. A blind comparison of numerical microscale model predictions of flow over complex terrain can be found in Bechmann et al. (2011).

Complex terrain is defined here as any local topographical feature that alters the undisturbed wind speed and causes flow separation, *e.g.* cliffs, hills, escarpments and embankments. A prospective wind farm site may contain many complex terrain features where interaction between several topographical features creates a very turbulent and challenging modelling environment. An isolated cliff, hill or escarpment provides a simplified complex terrain topology. Sherry et al. (2010) investigated the flow field over a cliff/escarpment using a model forward facing step (FFS) immersed in a turbulent boundary layer in a water channel. They found the mean reattachment length, X_L , is sensitive to the boundary layer, δ , to step height, h , ratio (δ/h) and the Reynolds number, Re_h . The effect of inlet turbulence intensity has not been investigated for boundary layer flow over a FFS.

Wind farms are situated within the atmospheric boundary layer (ABL). ABL flow is very turbulent due to the mixing arising from differential heating of the earth's surface. The streamwise turbulence intensity, I_u , can reach 20% in complex terrain (Petersen et al. 1998a), which is higher than I_u found in naturally developing experimental boundary layers. The turbulence intensity is defined as the ratio of the root mean square of the fluctuating streamwise velocity component to the mean streamwise velocity as shown in equation 8.6.

$$I_u = u_{rms}/U_\infty \quad (8.6)$$

Inlet turbulence intensity promotes reattachment in separating and reattaching bluff body flows (Bearman and Morel 1983; Melbourne 1993). The mean reattachment length, X_L , reduces with increasing turbulence intensity for a bluff flat plate (Saathoff and Melbourne 1997; Cherry et al. 1984). Saathoff and Melbourne (1997) noted a change in shear layer and vorticity shedding dynamics from the recirculation region with increasing inlet turbulence intensity using flow visualisations. Inlet turbulence produces a perturbation in the separated shear layer that causes the shear layer to impinge earlier on the flat plate surface compared to the undisturbed flow case. This shear layer impingement is the cause of the large scale shedding of vortex structures from the recirculation region and also the large surface pressure fluctuations within the recirculation region (Saathoff and Melbourne 1997). However, the effect of inlet turbulence intensity on the flow of a boundary layer over a forward facing step appears not to have been investigated.

8.2. The effect of turbulence on flow over a forward facing step

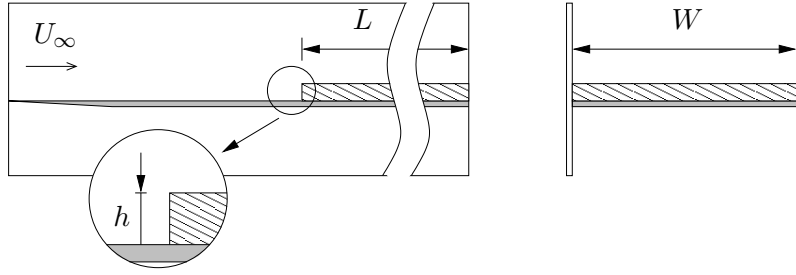


FIGURE 8.10: Schematic of the polycarbonate and acrylic experimental model used in the current study. h fixed at 30 mm, $L = W = 500$ mm. Height of end plates is 210 mm

The objective of the current study was thus to investigate the effect of inlet turbulence intensity on the separating and reattaching flow field downstream of a complex terrain feature, here modelled as a FFS.

8.2.3 Experimental Method

The experiments were undertaken in a free surface water channel with test section dimensions of $0.6 \times 0.8 \times 4$ m and a freestream velocity range of $0.06 \text{ m/s} \leq U_\infty \leq 0.46 \text{ m/s}$. The channel walls are constructed of glass allowing easy optical access. Flow uniformity is achieved through the use of an upstream honeycomb section and fine turbulence screen. The flow passes through a 3:1 contraction to accelerate the mean flow and reduce the residual streamwise turbulence intensity to 1.45%.

The experiments were conducted over a Reynolds number range of $6\,531 < Re_h < 7\,371$. The Reynolds number is defined as $Re_h = U_\infty h / \nu$, where h is the step height, and ν is the kinematic viscosity of the working fluid. The experimental model is a forward facing step geometry constructed of perspex and polycarbonate. Additional details of the experimental model can be found elsewhere (Sherry et al. 2010). The step height was fixed at $h = 30$ mm giving length and width aspect ratios of 16.67. A schematic of the experimental model is shown in figure 8.10 with an image of the model in the channel shown in figure 8.12. The turbulence grids where employed were placed $8.34h$ and $28.34h$ upstream of the model tapered leading edge and FFS face respectively.

A pulsed Nd:YAG laser (Minilite PIV, CONTINUUM) of wavelength 532 nm was used to produce a laser sheet of 2 mm thickness. The flow was seeded with polyamide particles (Vestosint, DEGUSSA AG) of mean diameter $50 \mu\text{m}$ and specific gravity of 1.06 g/cm^3 . A CCD particle image velocimetry (PIV) camera (pco.4000, PCO AG) with a resolution of $4\,008 \times 2\,672$ pixels and a 105 mm lens (AF 105, NIKKOR) acquired the raw images. Validated cross correlation PIV software that was developed in-house was used to process the images (Fouras

et al. 2008). The interrogation window was refined using a multi-step algorithm from an initial size of 64×64 pixels to a final size of 32×32 pixels with 50% overlap. This resulted in instantaneous velocity maps of 249 by 166 vectors. The velocity vector resolution of the velocity maps was $0.0154h$ and the field of view in physical space measured $3.8h \times 2.5h$.

A total of 500 image pairs were captured for each Reynolds number and turbulence grid setting. The image pairs were captured at 1 Hz so individual velocity realisations are minimally correlated in time. Whilst the recirculation zones presented are the result of averaging of the turbulent flow, convergence (via variance of the fluctuating cross velocity product from the cumulative cross product mean) in the separated shear layer occurs prior to 500 image pairs (not shown). The raw data was processed on a 20 CPU (Beowulf) cluster, which allowed rapid analysis of results.

8.2.3.1 Turbulence Grids

The inlet turbulence intensity was varied using grid structures placed upstream of the model. Grids of various designs are widely used as a method of suppressing or increasing turbulence levels in experimental facilities (Laws and Livesey 1978; Kurian and Fransson 2009). Turbulence generating structures can be separated into two categories, passive and active turbulence grids. Active turbulence grids (Makita 1991) actuate flat plates attached to the grid structure to produce the desired integral length scale, L_u , turbulence intensity and velocity shear profile. However, they are complex structures and are expensive to implement.

Passive grids on the other hand are most commonly simple bi-plane structures which can be easily modified and positioned. Turbulence is generated by the breakdown of the jets emanating from the grid openings. A passive turbulence grid geometry is defined by the mesh size, M , and the bar width, b , as shown on the left in figure 8.11. The solidity, σ , given by equation 8.7, controls the pressure drop across the grid and affects the integral length scale and intensity of the turbulence generated (Laws and Livesey 1978). An optimum solidity of 34% exists for passive turbulence grids (Comte-Bellot and Corrsin 1966), with grid solidities higher than 43% leading to general wake instabilities of the jets passing through the grids (Bradshaw 1965).

$$\sigma = \frac{b}{M} \left(2 - \frac{b}{M} \right) \quad (8.7)$$

However, the turbulence generated by passive grid structures is anisotropic (*i.e.* $I_u/I_v \equiv u_{rms}/v_{rms} \neq 1$) with the fluctuations in the streamwise direction, u_{rms} , larger than those in

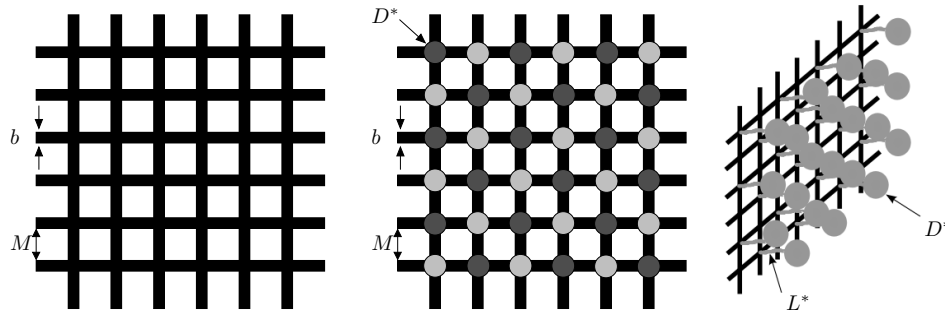


FIGURE 8.11: Passive turbulence grid geometries. Left: Grids are defined by the mesh size, M , and the bar width, b . Centre: Tethered sphere turbulence grid with sphere diameter to mesh size ratio, $D^* = 0.75$. Shade of sphere indicates tether length; light: $L^* = 1.5$, dark: $L^* = 2$. Right: isometric view of tethered sphere grid, only spheres of a single tether length are shown for clarity.

the spanwise, w_{rms} , and vertical, v_{rms} , directions. A summary by Comte–Bellot and Corrsin (1966) found that the anisotropy ratio, u_{rms}/v_{rms} , for grids of solidity in the range 0.34 to 0.44 ranged from 1.1 to 1.3. To improve the isotropy of the generated turbulence, Vonlanthen and Monkewitz (2011) attached neutrally buoyant spheres to the nodes of a passive turbulence grid to produce a novel, active way of increasing the mixing downstream of the grid. This ‘tethered sphere’ grid increased the turbulence intensity and achieved a modest improvement of the isotropy compared to the grid alone.

Three turbulence grids were used in the current study. The geometrical properties and the characteristics of the turbulence generated by the two traditional passive turbulence grids can be seen in table 8.2. To improve the isotropy and increase the intensity of the turbulence generated, a novel ‘tethered sphere’ turbulence grid (TSG) design was constructed following Vonlanthen and Monkewitz (2011). The TSG used turbulence grid 2 shown in table 8.2 as the base structure. Tethered spheres were attached to the grid nodes as shown in figure 8.11 to improve mixing downstream of the grid and hence isotropy of the turbulence generated. The spheres were constructed of celluloid (‘table tennis’) balls of diameter 38 mm, which were filled with water to minimise buoyancy effects. The current TSG design operated with a sphere diameter to mesh size ratio, $D^* = D/M \sim 0.76$, shown to produce the largest turbulence intensity (Vonlanthen and Monkewitz 2008). The tether lengths, $L^* = L/D$, varied from 1.5 – 2 to ensure freedom of movement arising from vortex induced vibration of the tethered spheres. An isometric schematic of the TSG is shown on the right in figure 8.11. The turbulence intensity of the four flow/grid configurations investigated are shown in table 8.2. I_u ranges from 1.45% with no grid to 9.90% with the TSG. Figure 8.12 shows the TSG located upstream of the inverted experimental model in the water channel facility.

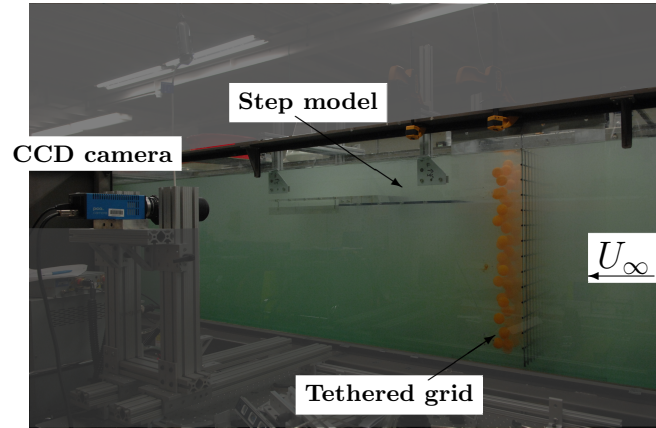


FIGURE 8.12: Experimental setup showing the tethered sphere turbulence grid upstream of forward facing step model in the FLAIR water channel.

	No Grid	Grid 1	Grid 2	Grid 3
Mesh size (M)	-	$0.42h$	$1.67h$	$1.67h$
Bar width (b)	-	$0.05h$	$0.17h$	$0.17h$
Solidity	-	23.6%	18.7%	18.7%*
Intensity (I_u)	1.45%	1.85%	3.18%	9.90%
Re Number (Re_M)	-	3.1×10^3	12×10^3	12×10^3

TABLE 8.2: Turbulence properties of the four flow/grid settings investigated. Grid 1: small grid; Grid 2: large grid; Grid 3: tethered sphere grid.*Note: the solidity ratio of the tethered sphere grid is based on the grid support structure, an alternate solidity ratio could be defined based on the projected area of the spheres, this value is 45%.

A 2D laser doppler velocimeter (LDV) (ColourBurst model 9201, TSI) was used to accurately characterise the turbulence intensity generated by the various grids. The data rates achievable in the water channel facility ($\sim 100\text{Hz}$) did not permit the length scales of the turbulence to be determined. The integral length scale, L_u , can be estimated from the grid mesh size, M . L_u of the TSG was shown to be of similar magnitude to the sphere diameter (Vonlanthen and Monkewitz 2011). Table 8.2 shows the tethered sphere grid increases the turbulence intensity by a factor of three compared to the base grid.

8.2.4 Results

The recirculation zone dimensions using the PIV results were determined by calculating the streamfunction (see equation 8.8), above the step surface.

$$\mathbf{u} = \frac{\delta \Psi}{\delta y}, \Psi = \int_0^\infty (\bar{\mathbf{u}}/U_\infty) d(y/h), \quad (8.8)$$

where $\bar{\mathbf{u}}$ is the temporal average of the streamwise velocity component. Equation 8.8 is an accurate estimation of the streamfunction. It has the advantage of not propagating a PIV error in the streamwise direction (Jacono et al. 2009; Sherry et al. 2010).

8.2. The effect of turbulence on flow over a forward facing step

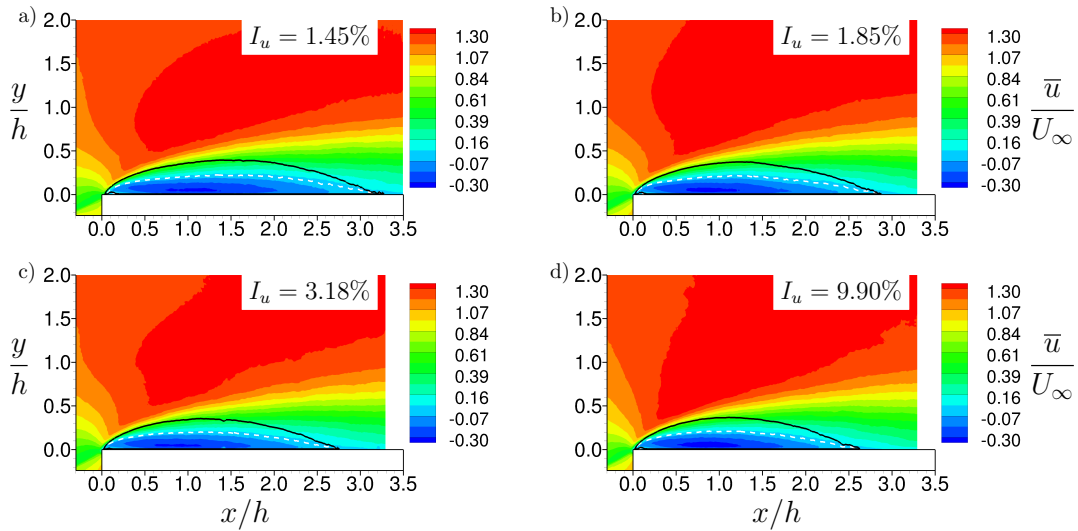


FIGURE 8.13: General bluff body flow features of the FFS flow in four different inlet turbulence intensities for $\delta/h = 1.25$. Isocontours of mean streamwise velocity, \bar{u}/U_∞ ; solid line is the dividing streamline Ψ_0 ; dashed white line encapsulates region of entirely negative flow. a) $I_u = 1.45\%$, $Re_h = 7371$; b) $I_u = 1.85\%$, $Re_h = 7267$; c) $I_u = 3.18\%$, $Re_h = 7250$; d) $I_u = 9.90\%$, $Re_h = 6531$.

For the data analysis, the Cartesian coordinate system was fixed at the step leading edge. The mean reattachment length is defined by the point where the dividing streamline, $\Psi = 0$, (from here on denoted as Ψ_0) bifurcated on the step surface and the region of negative flow ceases. At the reattachment point, one arm of the dividing streamline returns upstream into the recirculation region and the second continues downstream. The height of the recirculation region, Y_b , is defined as the maximum height of the dividing streamline above the step. The isocontours of the mean streamwise velocity, \bar{u} , obtained from the PIV measurements for the four inlet turbulence cases are shown in figure 8.13. The flow is from left to right, with the length and velocity scales made dimensionless by h and U_∞ respectively. The Reynolds number, Re_h ranges from a minimum of 6531 for the highest inlet turbulence intensity (9.90%) to a maximum of 7371 for the lowest turbulence intensity (1.45%). It was decided to keep the upstream experimental conditions similar, meaning the Reynolds number could vary because the different pressure drops caused by the different solidity of the turbulence grids could affect the velocity. However, the Reynolds number is at all times below the Reynolds number dependence threshold of $Re_h \sim 8500$ seen in the Sherry et al. (2010) study. The current results will thus contain some Reynolds number dependence in addition to the varying turbulence intensity. The variation in X_L over the Reynolds number range tested is estimated to be $0.145h$ based on the results of Sherry et al. (2010) at a single low turbulence intensity.

The region of maximum velocity speed up ($\bar{u}/U_\infty = 1.3$) is seen above the step for all turbulence intensities in figure 8.13. From a wind energy production perspective this region is a desirable location for a turbine. These results show that its location is largely independent of the freestream turbulence intensity, being primarily determined by the bluff body's geometry. An ideal wind turbine, ($P_{avail} = 0.5\rho AU_\infty^3$), placed in an area with a 30% increase in average wind speed could produce 55% more energy. The recirculation region is shown by the solid line (Ψ_0), while the white dashed contour line encapsulates the region of entirely negative flow. The white dashed line also shows the mean position of the maximum shear within the recirculation region.

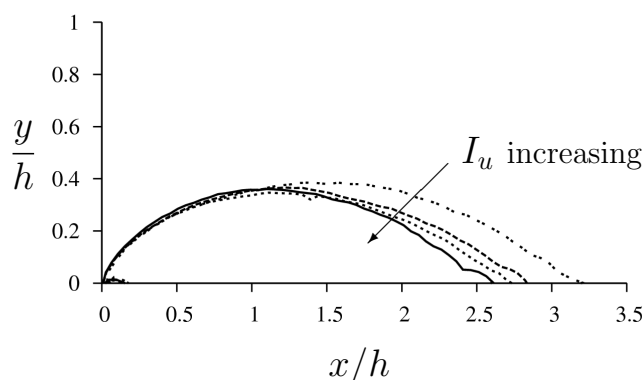


FIGURE 8.14: Recirculation region reduction with elevated inlet turbulence intensity. Recirculation region downstream of a FFS depicted by dividing streamline (Ψ_0) for the four different inlet turbulence settings, all cases with $\delta/h = 1.25$. Dashed line: no grid $I_u = 1.45\%$, $Re_h = 7371$; long dashed line: small grid $I_u = 1.85\%$, $Re_h = 7267$; dotted line: large grid $I_u = 3.18\%$, $Re_h = 7250$; solid line: tethered sphere grid $I_u = 9.90\%$, $Re_h = 6531$.

The locus of points that defines the dividing streamline was extracted for each turbulence case and the results are shown in figure 8.14. One can clearly see the effect of inlet turbulence intensity. The mean reattachment position, X_L , reduces by 19% as I_u increases by 85%. However, the recirculation region height, Y_b , varies very little with turbulence intensity, again indicating that the bluff body geometry effects dominate the initial separation region. This dominance is evident in figure 8.14 where the initial trajectory of the separated shear layer is seen to be insensitive to an increase in turbulence intensity. Turbulence effects become more prominent past the point where the recirculation region reaches its maximum height and the separated shear layer curves back toward the step surface. Here the effects of geometry are less and the freestream flow conditions (*e.g.* I_u , δ/h) become increasingly important. Increased entrainment in the separated shear layer due to the turbulence intensity reduces curvature away from the step surface promoting reattachment (Gartshore (1973) in Melbourne (1993)), (Bearman and Morel 1983). The results for the four turbulence cases are summarised in

table 8.3.

Considering the average velocity profiles, *e.g.* figure 8.13, in isolation could lead to an interpretation that the inlet turbulence has little effect on the recirculation region downstream of a forward facing step. From a wind energy perspective, the benefit arising from the flow speed-up is present for all turbulence intensities. The recirculation region dissipates faster with increased turbulence intensity, which is also positive in respect to wind farm siting. The mean reattachment position reduces with increasing freestream turbulence levels due to the enhanced mixing between the recirculating and freestream flow which allows faster momentum recovery close to the step. It can also be seen from figure 8.14 and table 8.3 that a three fold increase in I_u between grid 2 and the TSG only results in a 5% reduction in mean reattachment length. This could indicate that there is an asymptotic limit on the effect of I_u .

Alternatively, it could be that there is an effect due to the length scale of the grid generated turbulence. The integral length scale is the relevant length scale when considering how the turbulence interacts with the mean flow (Tennekes and Lumley 1972). It is responsible for most of the transfer of momentum throughout the flow field. The integral length scale weakens vortex shedding behind bluff bodies by changing the mean flow and reducing the spatial correlation of the flow (Melbourne 1993). Other bluff body separating and reattaching flows (blunt flat plate and rectangular prism with a rear splitter plate) have shown minimal effect of the integral length scale (Bearman and Morel 1983).

Small scale turbulence on the other hand, is known to increase mixing in the separated shear layer above bluff body geometries thus promoting reattachment ((Gartshore 1973) in (Melbourne 1993)). Gartshore (1973) in (Melbourne 1993) showed the flow over rectangular bluff bodies is most susceptible to small scale turbulence applied locally on the stagnation streamline. However, the boundary layer and recirculation region upstream of a FFS makes this flow more complex compared to that past rectangular bluff bodies.

Further, in boundary layer flow, the wall suppresses turbulent fluctuations in the wall normal direction. Thus if the integral length scale is larger than the boundary layer thickness, the grid generated turbulence will interact with the separated shear layers in a different fashion to that in a freestream (Bearman and Morel 1983). The invariance of the separated shear layer trajectory with increasing turbulence intensity is suggestive of similar small scale turbulence levels on the stagnation streamline upstream of the FFS. The effect of turbulence length scale was not investigated here. However, in boundary layer flow over a FFS, its effect is thought

to be secondary to that of the turbulence intensity.

	No Grid	Grid 1	Grid 2	Grid 3
I_u [%]	1.45	1.85	3.18	9.90
X_L [h]	3.24	2.87	2.76	2.62
Y_b [h]	0.396	0.374	0.354	0.368

TABLE 8.3: Summary of the recirculation region dimensions with the differing inlet turbulence intensities.

The mean flow results revealed that the largest effect on the flow fields arising from the different freestream turbulence intensities was in the reduction in the mean reattachment length. The height of the recirculation zone, Y_b , and the initial trajectory of the separated shear layer were largely independent of the freestream turbulence intensity. Further, the region of increased wind speed above the step was present for all turbulence cases. The mean results illustrate how complex terrain features could be deemed an appropriate and even desired location for a wind farm.

8.2.4.1 Reynolds stress generation

However, the extra power output from the increased wind speed in complex terrain is only one wind farm optimisation parameter. Other factors requiring consideration in wind farm layout optimisation include fatigue loading and infrastructure costs. One source of wind turbine fatigue loading arises from the fluctuating velocity components, \mathbf{u}' and \mathbf{v}' , *i.e.* turbulent fluctuations.

Complex terrain alters the undisturbed wind speed, U_∞ , with flow separation elevating the turbulent velocity fluctuations, \mathbf{u}' and \mathbf{v}' . Hence, a prospective wind farm site in complex terrain should be analysed for the turbulence produced by the terrain. The resulting flow could have a pronounced effect on turbines sited in such complex terrain.

The mean Reynolds stresses, $\overline{\mathbf{u}'\mathbf{u}'}$, $\overline{\mathbf{v}'\mathbf{v}'}$ and $\overline{\mathbf{u}'\mathbf{v}'}$ provides insight into the turbulent nature of the wind flow above the FFS. This turbulent flow enhances mixing, which promotes reattachment. Turbulence is created by the separation from the FFS blunt leading edge. A high inlet turbulence intensity will elevate turbulence levels within the recirculation region and in particular within the separated shear layer promoting reattachment. The increase in inlet turbulence intensity cannot however be linearly superimposed on the fluctuations in a turbulent boundary layer flow (Bearman and Morel 1983). Vertical profiles of the three Reynolds stress components above the FFS at several streamwise locations, $0 < x/h < 3.0$, for all turbulence cases are shown in figure 8.15. The Reynolds stress profiles reveal the

8.2. The effect of turbulence on flow over a forward facing step

spreading of the separated shear layer, by $3h$ downstream it has reached a width that is of the order of the cliff height.

The longitudinal Reynolds stress field, $\overline{\mathbf{u}'\mathbf{u}'}$, provides an indication of the streamwise perturbations above the terrain and within the recirculation region. This Reynolds stress component is responsible for dynamic blade loading due to its effect on the local angle of attack. Dynamic turbine loads can be approximated by an unsteady blade element momentum model using a dynamic stall model (Hansen 2008). The top row of figure 8.15 shows the longitudinal Reynolds stress profiles above the forward facing step. It is evident from figure 8.15 that the magnitude of $\overline{\mathbf{u}'\mathbf{u}'}$ increases with inlet turbulence intensity. For all inlet turbulence cases, the perturbation field reaches a maximum at $y(Y_b)$, *i.e.* the vertical height where the dividing streamline bends back to the step surface. For the TSG, the perturbation magnitude reaches $0.2U_\infty$. The magnitude of $\overline{\mathbf{u}'\mathbf{u}'}$ reduces with downstream distance after this maximum location.

The vertical Reynolds stress component is also higher in the recirculation region as shown by the middle row of profiles in figure 8.15. Turbulent eddies redistribute momentum from the higher freestream flow to the recirculation region close to the step surface. The magnitude of the vertical Reynolds stress increases with inlet turbulence intensity and is highest for the TSG. The vertical Reynolds stress component increases the dynamic misalignment of the inlet wind to the rotor plane (*i.e.* rotor tilt angle + $\overline{\mathbf{v}'\mathbf{v}'}$) and will affect the spanwise blade loading. It is thus indicative of the variable loading across the rotor plane. Wind turbine components not designed to operate in high off axis load cases, *e.g.* yaw gears, will be affected by the vertical Reynolds stress component and may require more frequent maintenance.

The Reynolds shear stress fields provide insight into the mixing mechanisms promoting reattachment. The Reynolds shear stress component is shown in the bottom row of profiles in figure 8.15. Reynolds shear stresses are created above the step due to the turbulent motions within the flow. They are representative of the transfer of mean momentum due to orthogonal turbulent fluctuations. Thus, a larger Reynolds shear stress component indicates more mixing (*i.e.* streamwise-momentum change vertically and vice versa) caused by the fluctuating (turbulent) velocity components. The mean velocity fields indicated reattachment occurs earlier with increasing turbulence intensity. The increased fluctuating velocity components in the elevated inlet turbulence cases will increase entrainment in the separated shear layer. This results in a larger flux of momentum toward the step surface promoting reattachment. The increase in momentum flux toward the step surface is reflected in the Reynolds shear

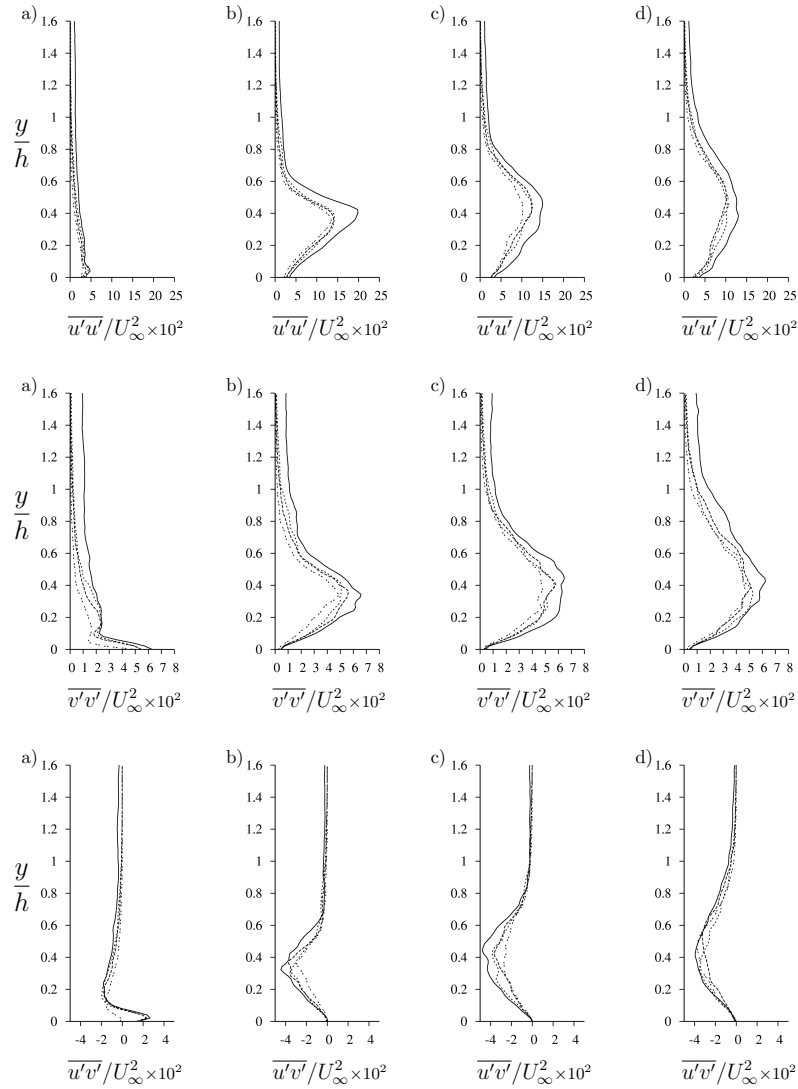


FIGURE 8.15: Reynolds stress profiles. Top: streamwise; centre: vertical; and bottom: shear profiles above the forward facing step subjected to various inlet turbulence intensities at numerous downstream distances in the wake for $\delta/h = 1.25$. Dashed line: no grid: $I_u = 1.45\%$, $Re_h = 7371$; long dashed line: small grid $I_u = 1.85\%$, $Re_h = 7267$; dotted line: large grid $I_u = 3.18\%$, $Re_h = 7250$; solid line: tethered sphere grid $I_u = 9.9\%$, $Re_h = 6531$. a) $x = 0h$, b) $x = 1h$, c) $x = 2h$, d) $x = 3h$.

stress fields.

Figure 8.16 indicates the topology of the Reynolds shear stress field is similar in all turbulence cases. For each inlet turbulence level, positive Reynolds shear stresses are generated close to the separation point. The positive Reynolds shear stress close to the separation point are due to flow deflection in the positive wall-normal direction and a streamwise momentum flux. Hattori and Nagano (2010) has described this region as a production region of the Reynolds shear stress component. The streamwise extent of this region changes less than $\sim 3\%$ despite the large change in inlet turbulence intensity. This highlights how the bluff

8.2. The effect of turbulence on flow over a forward facing step

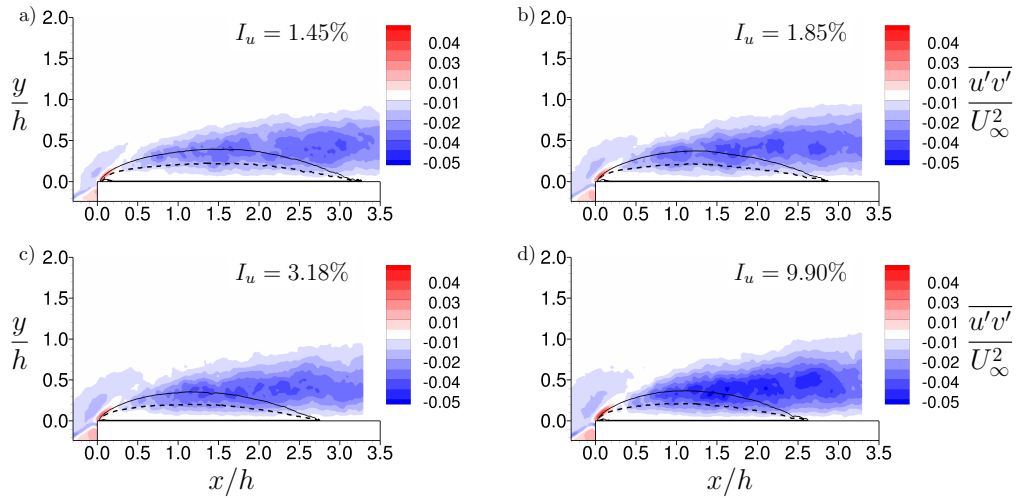


FIGURE 8.16: Reynolds shear stress contours above a forward facing step subjected to various inlet turbulence intensities for $\delta/h = 1.25$. Isocontours of $\overline{u'v'}/U_\infty^2$; solid line is the dividing streamline Ψ_0 , dashed line encapsulates region of entirely negative flow. a) $I_u = 1.45\%$, $Re_h = 7371$, b) $I_u = 1.85\%$, $Re_h = 7267$, c) $I_u = 3.18\%$, $Re_h = 7250$, and d) $I_u = 9.9\%$, $Re_h = 6531$.

body's geometry dominates the initial region of this separating and reattaching flow.

The Reynolds shear stress component becomes negative downstream of the production region when the influence of the separation point and strong velocity gradients reduce. A negative Reynolds shear stress means there will be a flux of streamwise momentum toward the step surface. This momentum transfer toward the step surface overcomes the reverse flow within the recirculating region. In this region the inlet turbulence promotes reattachment. Vertical profiles of the Reynolds shear stress component are shown in the bottom row of figure 8.15. The magnitude of this component increases with inlet turbulence intensity. In a similar fashion to the longitudinal and vertical Reynolds stress components, it is maximum at the bubble height confirming inlet turbulence enhances mixing and promotes reattachment. A wind turbine placed in this region will experience a fluctuating cross velocity component across the rotor plane of up to 40% of the freestream velocity.

8.2.5 The effect of turbulence section summary

Wind turbines are commonly placed in complex terrain to take advantage of the wind speed up effects caused by the terrain. Flow over a forward facing step, here representative of complex terrain, was subjected to various levels of freestream turbulence intensity in a water channel and was investigated using planar particle image velocimetry. Two traditional passive turbulence grids and a third novel tethered sphere design, which was shown to dramatically increase the turbulence intensity, were used to vary the freestream turbulence intensity. The

data shows bluff body geometry effects dominate close to the separation point with the height of the recirculation region, Y_b largely independent of freestream turbulence intensity. However, the mean reattachment length, X_L did vary with the freestream turbulence intensity, with a 19% reduction in X_L with an 85% increase in I_u . The maximum speed-up was ~ 1.3 for all turbulence cases, which would clearly result in increased power production from wind turbines placed in this region. The flow field above complex terrain is however quite turbulent. This is shown by the Reynolds stress fields. Reynolds stress generation above the step increased with freestream turbulence intensity and this is the reason for earlier reattachment. However, Reynolds stresses will also increase the dynamic loading wind turbines experience in complex terrain, a factor that needs to be considered in wind farm planning.

8.3 The recirculation region downstream of 2D escarpments

8.3.1 Abstract

The recirculation region formed downstream of two dimensional (2D) escarpments immersed in a turbulent boundary layer has been characterised in a water channel. Particle image velocimetry (PIV) captures velocity fields above the escarpment surface allowing extensive analysis. Wind turbines are commonly sited downstream of the escarpment apex to take advantage of the wind speed up the escarpment produces. However, the flow above the escarpment is complex with separation likely. The appropriateness of escarpment sites as a wind farm location is analysed and discussed. The escarpment angle, θ , and Reynolds number, Re_h , are varied over a narrow range with the effect on the recirculation region dimensions presented. Reducing escarpment angle leads to a reduction in the mean reattachment length. Contour maps of the amplification factor, A_z , Reynolds shear stresses, $\overline{\mathbf{u}'\mathbf{v}'}$, and mean turbulence production, P_k , are constructed providing insight into the optimal placement of structures such as wind turbines within these topographical features.

8.3.2 Introduction

Separating and reattaching flows are of particular interest in the wind engineering field. One area of wind engineering that has seen rapid development in recent times is the wind energy field. Wind turbines are commonly sited in the vicinity of topological features such as coastal cliffs and escarpments in the atmospheric surface layer due to the localized wind speed up effects such features produce. The speed up effect generated by the topology can be characterised by the *amplification factor*, A_z (Bowen and Lindley 1977), defined as the ratio of the wind speed above the topology to that at the same height above flat ground as shown in equation 8.9. An alternative characterisation is by the *fractional speed up ratio*, ΔS (Taylor 1998), calculated as shown in equation 8.10. Kondo et al. (2002) present a scalar equivalent to equation 8.9, which they term the *topographic multiplier*, TM.

$$A_z = \frac{\mathbf{u}(\mathbf{x}, \mathbf{z})}{\mathbf{u}(\mathbf{x}_0, \mathbf{z})}, \quad (8.9)$$

$$\Delta S = \frac{\mathbf{u}(\mathbf{z}) - \mathbf{u}_0(\mathbf{z})}{\mathbf{u}_0(\mathbf{z})} = A_z - 1 \quad (8.10)$$

The ideal power available to a wind turbine was presented in equation 8.3. As P_{avail} increases with the cube of velocity, a small increase in U_∞ caused by the topographical

feature will lead to a significant increase in available power. Therefore, purely from an energy yield perspective, the benefit of placing turbines in topographical features is obvious.

The fractional speed-up ratio is highly dependent on a number of flow properties, including boundary layer to cliff height ratio, δ/h , boundary layer shear exponent, n , escarpment angle and turbulence intensity and atmospheric stability. Investigations of separating and reattaching flows over 2D escarpments are rare. The only known full scale investigation of 2D escarpment flow is by Emeis et al. (1995) over the Hjärdemål site. The site had a escarpment 16 m high with a slope angle of 28° (Emeis et al. 1995). This study revealed maximum speed-up occurs under stably stratified conditions (Emeis et al. 1995). The region of speed-up extends further above the step with increasing atmospheric instability (Emeis et al. 1995).

In small scale experimental studies, A_z reaches a unit value at approximately 1/3 up the slope (Bowen and Lindley 1977; Kondo et al. 2002). The early study by Bowen and Lindley (1977) investigated the flow over four 2D escarpments ($\theta = 14^\circ, 26.5^\circ, 45^\circ, 90^\circ$) immersed in a simulated atmospheric boundary layer (ABL). Kondo et al. (2002) on the other hand, investigated five 2D escarpments ($\theta = 7.5^\circ, 15^\circ, 30^\circ, 45^\circ, 60^\circ$) immersed in a turbulent boundary layer. They found the flow did not separate for escarpment angles below θ_{crit} . Separation was also absent for a curved surface with average slope angle of 24° (Kondo et al. 2002).

At full scale, a unit A_z value is reached between halfway up the slope and the crest depending on atmospheric stability (Emeis et al. 1995). As the upstream recirculation region was not the focus of the current study, this cannot be confirmed here. Values of A_z downstream of the apex range from 1.3–1.8 (Berg et al. 2011; Bowen and Lindley 1977; Kondo et al. 2002; Emeis et al. 1995). It is maximum at the apex, where a pressure minimum and velocity maximum occurs.

Flow separation can occur in complex terrain, causing increased wind shear and turbulence intensity, both of which can reduce turbine life expectancy. Common wind farm planning tools such the wind atlas analysis and application program (WAsP) (Mortensen et al. 1993) were developed using linearized boundary layer models and as a result can break down in complex terrain (where slope > 0.3 or equivalently $\theta \geq 17^\circ$) (Petersen et al. 1998b). This limit is the critical slope value, $\theta_{\text{crit}} = 17^\circ$, above which flow separation occurs (Oke 1987). In the Hjärdemål measurements, flow separation was not detected for very low wind speeds (Emeis et al. 1995). One-dimensional models are unable to predict where flow separation occurs. Recently, wind engineers have embraced three-dimensional (3D) computational fluid dynamics

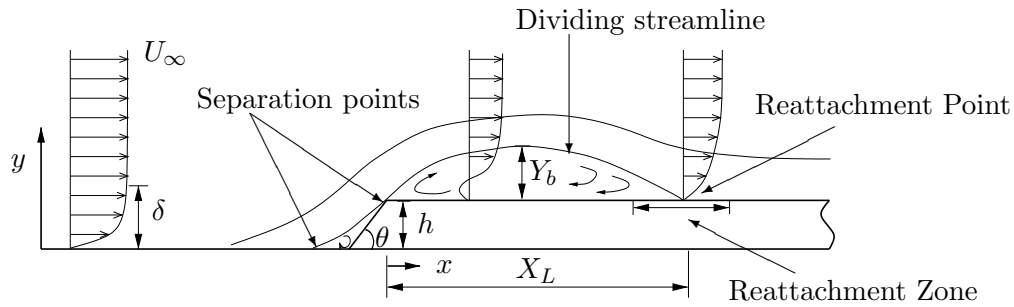


FIGURE 8.17: Flow features over a 2D escarpment. Left to right: upstream boundary layer profile, upstream recirculation, angled step face, recirculation region of present interest, reattachment point.

(CFD) models to investigate the wind flow over prospective wind farm sites. Whilst requiring significant computing power, the models are likely to increase the accuracy of wind energy predictions but clearly need to be properly validated. A blind comparison of numerical microscale model predictions of flow over complex terrain can be found in Bechmann et al. (2011).

Complex terrain is defined here as any local topographical feature that alters the undisturbed wind speed and causes flow separation, *e.g.* cliffs, hills, escarpments and embankments. A prospective wind farm site can contain many complex terrain features, where interaction between several topographical features creates a very turbulent and challenging modelling environment. An isolated cliff, hill or escarpment provides a simplified complex terrain topology. Sherry et al. (2010) investigated the flow field over a cliff/escarpment using a model forward facing step (FFS) immersed in a turbulent boundary layer in a water channel. They found the mean reattachment length, X_L , is sensitive to the boundary layer to step height ratio, δ/h , and the Reynolds number, Re_h . A thorough literature review revealed that the escarpment angle, θ , has only received minimal previous investigation.

However, there have been a number of works dealing with topological features immersed in turbulent boundary layers. Two dimensional isolated hills of smooth curved profiles have received considerable attention in the past with a review of experimental and numerical studies of various hill profiles presented in the papers by Taylor (1998) and Bitsuamlak et al. (2004) respectively. An alternative obstacle geometry that has been studied minimally is the flow over two dimensional (2D) escarpments. A 2D escarpment is defined as an angled surface connecting two elevations as shown in figure 8.17. The main flow features in a mean sense are shown in figure 8.17. As turbines are placed downstream of the escarpment apex, only the downstream recirculation region is investigated here.

The flow fields produced by isolated hills and 2D escarpments are quite different. In

the former, the flow reattaches downstream of the hill in the leeward region, whereas in the latter, the flow reattaches to the top surface of the escarpment. The current study is limited to 2D escarpment geometries where the flow reattaches to the top surface. As the escarpment angle increases, the feature approaches a forward facing step geometry. The FFS geometry is included here for reference.

Turbulence production increases with escarpment angle (Bowen and Lindley 1977) due to the separated shear layer which forms above the apex. Kondo et al. (2002) showed turbulent kinetic energy production was elevated compared to flat terrain. The trends are consistent between the two studies with differences most likely attributable to δ/h ratio and Reynolds number effects. The δ/h ratio of the Bowen and Lindley (1977) and Kondo et al. (2002) studies were 20 and ~ 3 respectively.

The appropriateness of locating a wind farm near an escarpment must be determined not only from an energy yield perspective. The turbulent nature of the flow field must also be considered. The prior experimental studies of flow over 2D escarpments were conducted at a single Reynolds number and no measurements of the recirculation zone were reported. The purpose of the current section is to evaluate the flow topology over 2D escarpments at several Reynolds numbers and escarpment angles. Specific focus is given to characterisation of the recirculation region's dimensions. The variation of the amplification factor and turbulence production fields with escarpment angle and Reynolds number were also of interest.

8.3.3 Experimental setup

The FLAIR water channel was used for the 2D escarpment studies. This facility was introduced in chapter 3. The experiments were conducted over a wide Reynolds number range as shown in table 8.4. The Reynolds numbers definitions are given in equations 8.1. Water temperature fluctuations occasionally occurred during experimental runs. This temperature variability changes the fluid viscosity. A conservative estimate of the temperature fluctuations is $\pm 0.1^\circ C$. This variability was incorporated into the Re_h uncertainty. The Reynolds numbers of the current study are much less than the Bowen and Lindley (1977); Kondo et al. (2002) studies.

The flow passes through a turbulence screen situated 250 mm upstream of the leading edge of the model and serves to regulate the turbulence level between subsequent measurement days. The turbulence screen has a mesh diameter, $M = 12.6$ mm and a solidity ratio, $\sigma = 22\%$ producing a turbulence level, $I_u = 1.43\%$.

8.3. The recirculation region downstream of 2D escarpments

θ	30°	45°	60°	90°
Re_h	2.74–13.60	2.49–12.32	2.46–12.21	2.77–13.74

TABLE 8.4: The Reynolds number ranges based on the various Reynolds number definitions. All values in units of thousands

A Nd:YAG laser (Minilite PIV, CONTINUUM) of wavelength 532 nm and energy content 25mJ was used to produce a pulsed light sheet 2 mm thick. The light sheet was delivered into the channel from below using a plane mirror and a cylindrical lens. Beam alignment was checked before each data acquisition session ensuring a laser sheet of high quality. The flow was seeded with reflective polyamide particles of mean diameter $50\mu\text{m}$ and specific gravity of 1.06 g/cm^3 .

A CCD PIV camera (.pco4000, PCO AG) of maximum resolution 4008×2672 pixels was used in conjunction with a 200mm lens. The FFS data was captured at full resolution. The minimum binning function of 2 in each axis was used for the angled escarpments reducing the resolution to 2004×1336 pixels. A minimum magnification factor (MF) of 50 pixels/mm was utilised giving a field of view (FOV) of $40\text{ mm} \times 26\text{ mm}$. With this magnification factor the particles had an image diameter of 2.5 pixels. The time delay between images pairs was optimised to ensure an average pixel displacement between 5 to 8 pixels. This average pixel displacement minimised the number of filled vectors when used in conjunction with an integration window of 32×32 pixels with 50% overlap. This allowed an instantaneous velocity map of 125 by 83 vectors to be captured. A total of 400 image pairs were recorded for each position and flow setting. The camera was re-positioned using a manual traversing mechanism with camera alignment ensured prior to data acquisition. The raw data was processed on a 20 CPU (Beowulf) cluster which allowed rapid analysis of results. Validated cross correlation PIV software developed in-house was employed to generate the velocity and vorticity fields (Fouras et al. 2008). Where used, second order central difference schemes were used to evaluate derivative terms.

Uncertainty in the resolved velocity components largely arises as a random error component due to turbulent motions in the flow field. The fractional error, ϵ in estimating the mean velocity is given by equation 8.11 (Grant and Owens 1990). Here $N = 400$ such that ϵ is 0.166% of U_∞ , with a 98% confidence level.

$$\epsilon = \frac{z_c I_u}{\sqrt{N}} \tag{8.11}$$

8.3.4 Experimental model

An in-depth analysis of the model geometry is presented in Sherry et al. (2010). The Cartesian coordinate axis origin is placed at the apex of the escarpment. Here, a single escarpment height $h = 30$ mm was investigated. The aspect ratio based on model width to step height was $AR = 16.67$. The escarpment angle, θ , was varied over the range, $30^\circ \leq \theta \leq 90^\circ$, by using machined acrylic wedges placed upstream of the step. θ is the angle between the slope face and the ground plane upstream of the step as shown in figure 8.17. The model aspect ratios, L/h and W/h were above the critical aspect ratios to ensure reattachment to the top surface (Castro and Dianat 1983) in every flow setting and nominally two dimensional flow at mid span respectively (de Brederode and Bradshaw 1972).

A natural boundary layer formed upstream of the step with the profile as shown in figure 8.3. The natural boundary layer has a boundary layer thickness $\delta = 2.7h_{h=15mm}$ measured at a distance $9h_{h=15mm}$ upstream of the step. A power law profile was not fitted to the boundary layer profile. A total of 2500 image pairs were utilised for a convergence of the boundary layer profile results. The upstream boundary layer to step height thickness ratio was $\delta/h = 1.25$.

8.3.5 Results

The escarpment angle was the primary independent variable of interest. Its effect on the flow field downstream of the apex are presented below.

Isocontours of the mean streamwise velocity, \bar{u} , obtained from the PIV measurements for the four escarpment angles are shown in figure 8.18 for the minimum Reynolds number. The vertical range of the 90° data is larger than the other escarpment angles range due to the camera setup used. Details of this setup are given in section 8.1. The flow in figure 8.18 is from left to right, with the length and velocity scales made dimensionless by h and U_∞ respectively. The Reynolds numbers of figure 8.18 is shown in table 8.4 as the lower bound of the Reynolds number ranges.

The recirculation zone dimensions using the PIV results were determined in a similar fashion to Sherry et al. (2010). The mean reattachment length is defined by the point where the dividing streamline, $\Psi = 0$, (from here on denoted as Ψ_0) bifurcated on the step surface and the region of negative flow ceases. At the reattachment point, one arm of the dividing streamline returns upstream into the recirculation region and the second continues downstream. The height of the recirculation region, Y_b , is defined as the maximum height of the

8.3. The recirculation region downstream of 2D escarpments

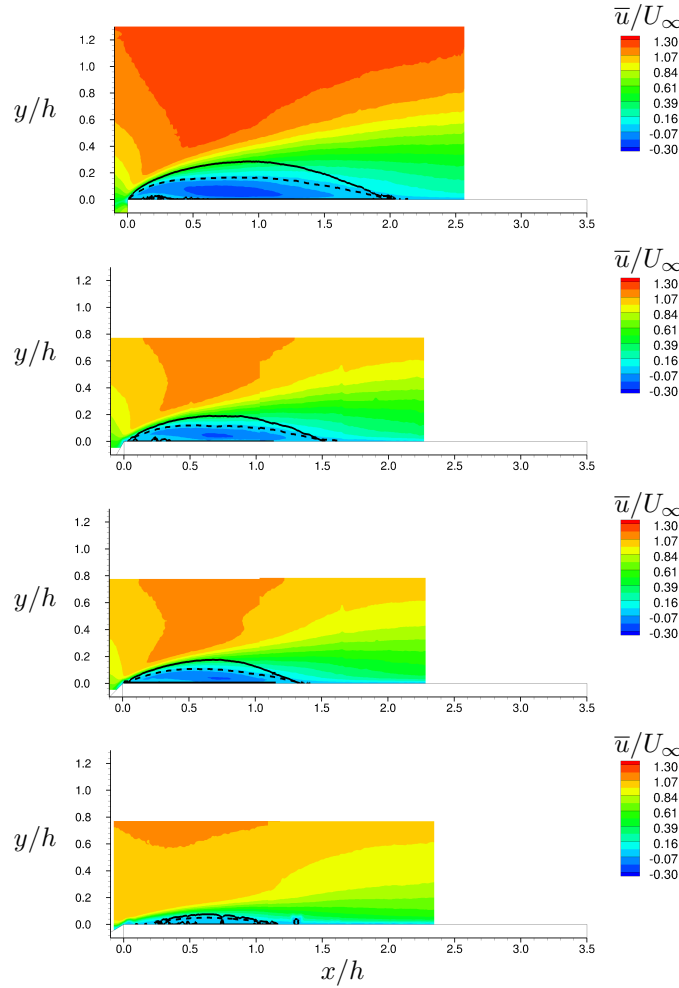


FIGURE 8.18: Streamwise velocity, \bar{u}/U_∞ , variation with escarpment angle, θ for the minimum Reynolds number.

dividing streamline above the step. The uncertainty in characterising the recirculation region dimensions is conservatively estimated as $0.04h$.

As the flow approaches the escarpment it is deflected above the step due to the blockage caused by the bluff body. Large velocity gradients are seen above the escarpment between $x/h = 0$ and $x/h = 1$. The velocity gradient magnitude increases with θ . As the escarpment angle is at all times greater than θ_{crit} , a separated shear layer forms downstream of the apex. A recirculation region is created downstream of the separation point until reattachment occurs in the reattachment zone. The recirculation region is shown by the solid line (Ψ_0), while the dashed contour line encapsulates the region of entirely negative flow. Figure 8.18 indicates the recirculation region increases in size with θ for the Reynolds number shown.

The trajectory of the separated shear layer depends on the escarpment angle. This initial separation angle is dependent on both the escarpment angle and whether an upstream recir-

ulation region develops. The upstream recirculation region and oncoming boundary layer are the principal differences between a blunt flat plate and the current flow. The upstream recirculation region acts as an effective slope (Bowen and Lindley 1977) causing a reduction in the separation angle of the separated shear layer. It is reasonable to expect the recirculation region will reduce in size with reducing θ . As wind turbines are almost exclusively placed downstream of the apex, only this region was investigated, meaning any change in the upstream recirculation region could not be detected here.

The recirculation region dimensions were extracted for each escarpment angle and Reynolds number combination. The recirculation region dimensions have not been documented previously for angled escarpments (Bowen and Lindley 1977; Emeis et al. 1995; Kondo et al. 2002). The PIV fields allow calculation of the mean streamfunction (equation 8.8) and hence the recirculation region dimensions, X_L and Y_b . The mean reattachment distance, X_L determined by Ψ_0 is shown in figure 8.19. Estimates of measurement uncertainty are shown by the error bars. Uncertainty in Re_h arises from variations in U_∞ and ν , the water kinematic viscosity.

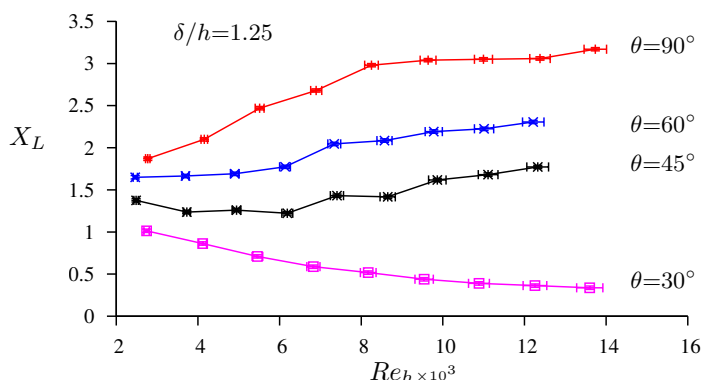


FIGURE 8.19: Variation in reattachment length, X_L , with Reynolds number for various step angles

Figure 8.19 is the most interesting result obtained from the 2D escarpment investigations. It shows that the mean recirculation region length depends on both θ and Re_h . X_L is important to determine if a wind turbine support structure will be affected by the recirculation region. Section 8.1 indicated two regimes exist for the FFS and a δ/h ratio of 1.25. For $Re_h \leq 8.25 \times 10^3 \pm 690$, X_L is strongly dependent on the Reynolds number. Whereas, for $Re_h \geq 8.25 \times 10^3 \pm 690$, X_L is minimally dependent of Re_h . The two regimes become less apparent with reducing escarpment angle. For $45^\circ \leq \theta \leq 90^\circ$, X_L generally increases over the Re_h range investigated. However, between $30^\circ \leq \theta \leq 45^\circ$, a change in flow topology occurs whereby X_L monotonically reduces with Re_h by $\theta = 30^\circ$. This is most probably due to a weakening of the upstream recirculation region between $\theta = 45^\circ$ and $\theta = 30^\circ$. The upstream

8.3. The recirculation region downstream of 2D escarpments

recirculation region will likely be minimal for $\theta = 30^\circ$ due to the acute slope angle. X_L decreases with Re_h due to an increase in turbulent mixing above the escarpment. Turbulent mixing above the escarpment will be demonstrated by Reynolds shear stress contours and a quadrant analysis of the $\mathbf{u}'\mathbf{v}'$ field.

The height of the recirculation region, Y_b , on the other hand is important for rotor loading. The variation of Y_b with θ and Re_h is shown in figure 8.20. The same uncertainty limits apply as in figure 8.19. The height of the recirculation region steadily increases with Re_h , for $\theta \geq 60^\circ$. In a similar fashion to X_L , Y_b reduces monotonically with Re_h . Figure 8.18 indicates Y_b is largely determined by the separation angle from the escarpment apex. The effect of increasing recirculation region height corresponds to larger minimum turbine hub heights. This increases the complexity of the turbine as the nacelle assemblies become larger and heavier.

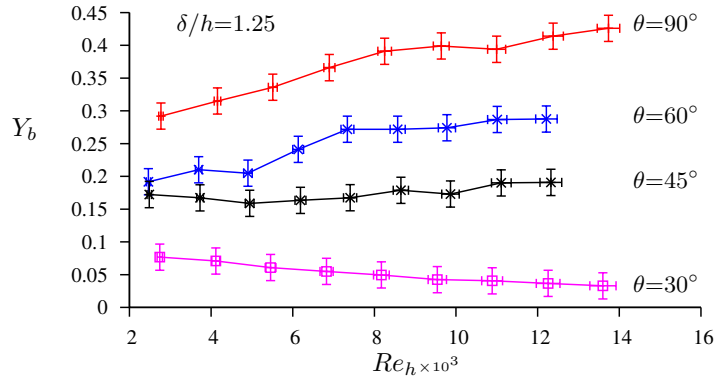


FIGURE 8.20: Variation in recirculation region height, Y_b with Reynolds number and escarpment angles

The axial position of the maximum recirculation region height, X_{Y_b} is also important for turbine placement in complex terrain. If the rotor plane cuts through the recirculation region at X_{Y_b} , large fluctuating loads will result. It is at this location, that momentum transfer toward the step is large. The variation of X_{Y_b} as a ratio of X_L with Re_h and θ is shown in figure 8.21. The recirculation zone is fairly symmetrical across the Re_h range investigated for $\theta \geq 45^\circ$. The recirculation region becomes asymmetrical for $\theta = 30^\circ$ presumably due to the acute separation angle. The reduction in symmetry could also arise from a weakening of the upstream recirculation region.

The region of velocity speed up ($\bar{\mathbf{u}}/U_\infty > 1.0$) is seen above the step for all escarpment angles in figure 8.18. From a wind energy production perspective this region is a desirable location for a turbine. To gauge the gain of energy production in complex terrain compared to that in flat terrain, A_z is calculated using equation 8.9. Investigation of A_z is limited here

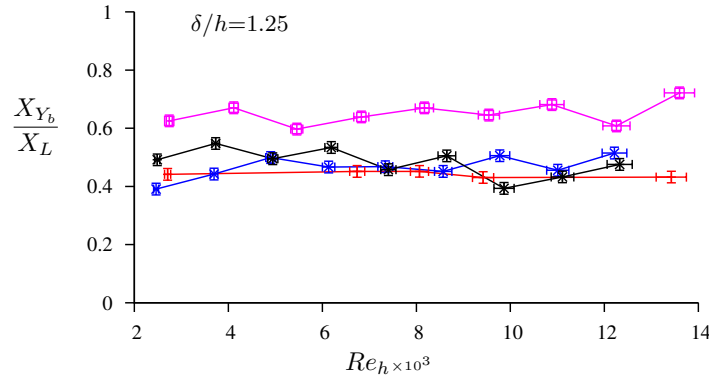


FIGURE 8.21: Variation in axial position of Y_b with Reynolds number and escarpment angle.

to $y/h < 0.8$ due to the spatial extent of the measurements. A_z can be thought of a power production multiplier as in equation 8.12 which was introduced in section 8.1.

$$P_{max_c} = A_z^3 P_{max_u}, \quad (8.12)$$

where P_{max_c} is the maximum power available to a wind turbine situated in complex terrain and P_{max_u} is the power available to the same turbine.

Regions where $A_z > 1$, a turbine will produce greater power compared to the same turbine placed in a boundary layer flow in flat terrain. The effect of escarpment angle on the amplification factor is shown in figure 8.22. A_z is maximum at the apex for all escarpment angles and Reynolds numbers. The dashed line indicates the region where A_z obtains a unit value. The unit A_z value follows Ψ_0 until approximately X_{Y_b} , where unlike Ψ_0 , it continues on approximately the same trajectory. Minimum turbine hub heights should be greater than the $A_z = 1$ contour to achieve gains in power production. The minimum hub height reduces with θ .

A_z is greatest for the lowest escarpment angle. A smaller obstruction to the flow will allow smoother flow over the step and a more uniform velocity gradient. As the escarpment angle increases toward a vertical cliff ($\theta = 90^\circ$), the recirculation zone downstream of the escarpment apex increases with a corresponding reduction in the amplification factor. The present results agree with those of Bowen and Lindley (1977).

The amplification factor fields indicate the potential increased energy yields by turbines placed in complex terrain. However, turbulence is generated in the separated shear layer and in the recirculation region. Average turbulent kinetic energy production, P_k , is evaluated for approximately 2D flow by equation 8.13,

8.3. The recirculation region downstream of 2D escarpments

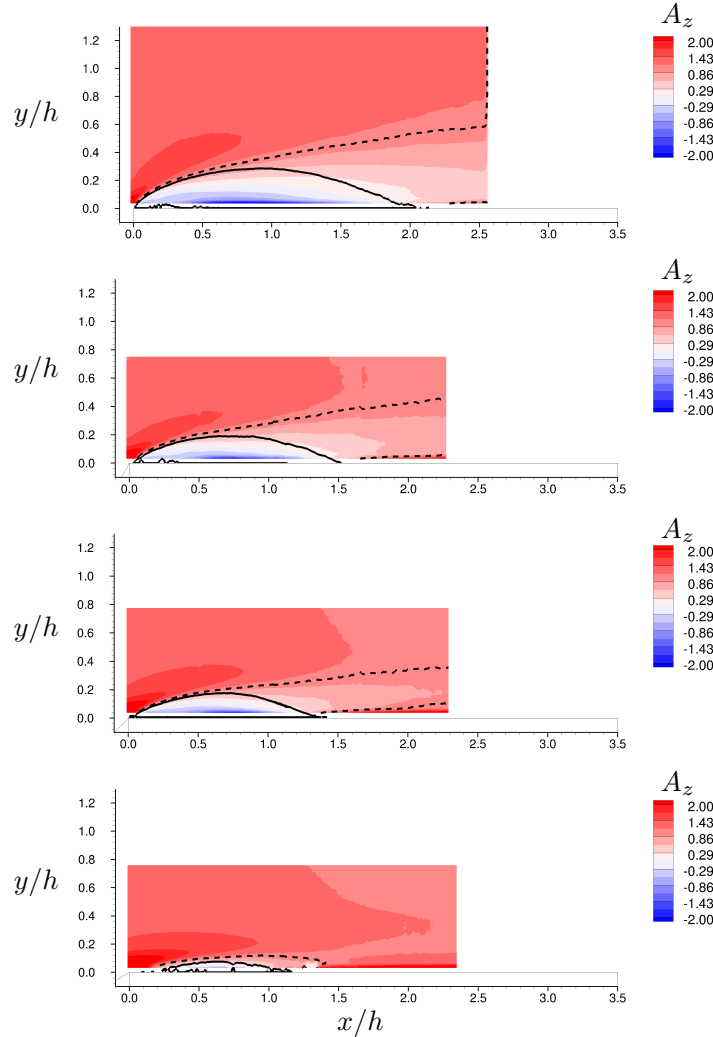


FIGURE 8.22: Variation of the amplification factor, A_z , with escarpment angle, θ , above a 2D escarpment for the minimum Reynolds number. Dashed lines represent a unit A_z value. Solid line represent the dividing streamline.

$$P_k = -\overline{u'u'} \frac{\partial \bar{u}}{\partial x} - \overline{u'v'} \left(\frac{\partial \bar{u}}{\partial y} + \frac{\partial \bar{v}}{\partial x} \right) - \overline{v'v'} \frac{\partial \bar{v}}{\partial y}. \quad (8.13)$$

where $\overline{u'u'}$, $\overline{v'v'}$ and $\overline{u'v'}$ are the Reynolds longitudinal, normal and shear stress components respectively. The 2D assumption implies not only a zero transverse velocity, $\bar{w} \sim 0$, but also requires that the Reynolds shear stress components involving the transverse velocity be zero, *i.e.* $-\overline{u'w'} = -\overline{v'w'} \sim 0$ (Kondo et al. 2002). This assumption is most accurate in the mid plane where the measurements were taken.

How the turbulent kinetic energy production varies with escarpment angle is presented in figure 8.23. The turbulence production term is made dimensionless by the factor, U_∞^3/h . Ψ_0 is also shown in the figures by the solid line to indicate the boundaries of the recirculation region. Turbulence production is constrained to the separated shear layer where strong

velocity gradients exist. P_k increases with θ as the escarpment causes a larger perturbation to the upstream flow. Turbulence production reduces downstream of X_{Y_b} due to the transfer of freestream momentum toward the escarpment surface in the reattachment process. The turbulent kinetic energy production region should be avoided for wind energy installations. Such turbulent regions will cause intense dynamic loading on the turbine.

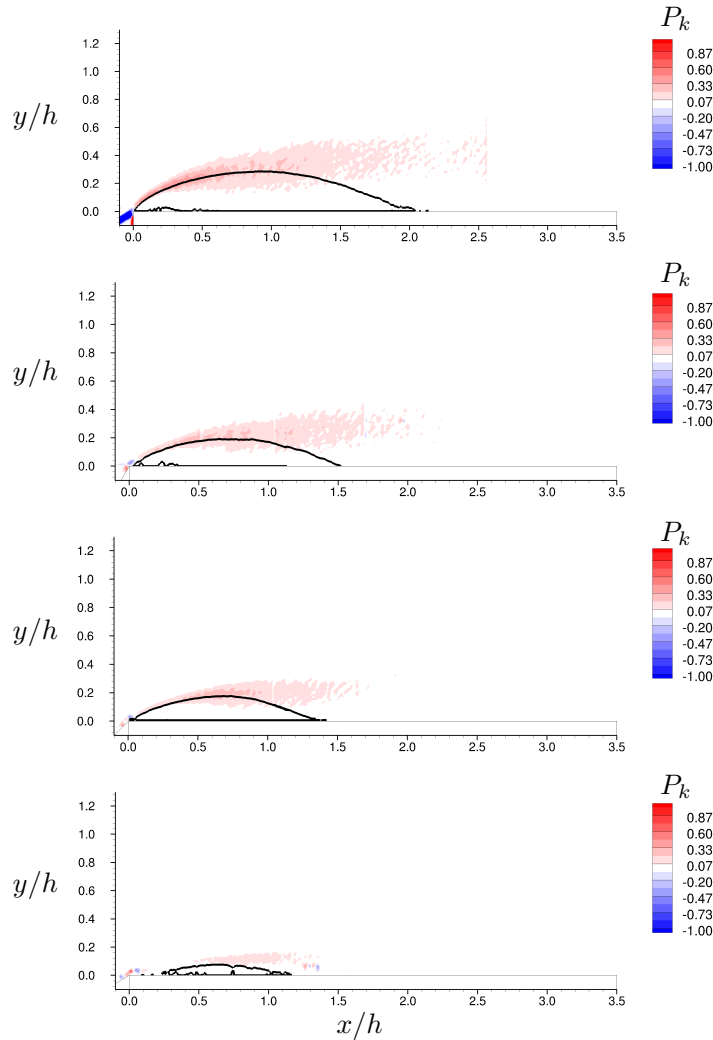


FIGURE 8.23: Average turbulence kinetic energy production term, P_k , variation with escarpment angle, θ , for the minimum Reynolds number. The production term is made dimensionless by the factor U_∞^3/h .

The unsteadiness above the escarpment can be ascertained by the mean Reynolds stress components. The Reynolds shear stress component, $\overline{\mathbf{u}'\mathbf{v}'}/U_\infty^2$, indicates the momentum flux due to turbulent fluctuations. Isocontours of $\overline{\mathbf{u}'\mathbf{v}'}/U_\infty^2$ are shown in figure 8.24. In a similar fashion to the turbulence production term, P_k , the Reynolds shear stress is confined to the boundaries of the recirculation region. The Reynolds shear stress magnitude increases with escarpment angle. Immediately downstream of the apex, $\overline{\mathbf{u}'\mathbf{v}'}/U_\infty^2$ has a positive value

8.3. The recirculation region downstream of 2D escarpments

which represents a vertical transfer of streamwise momentum. The Reynolds shear stress field changes sign further downstream as streamwise momentum is transferred toward the escarpment surface to overcome the recirculation region.

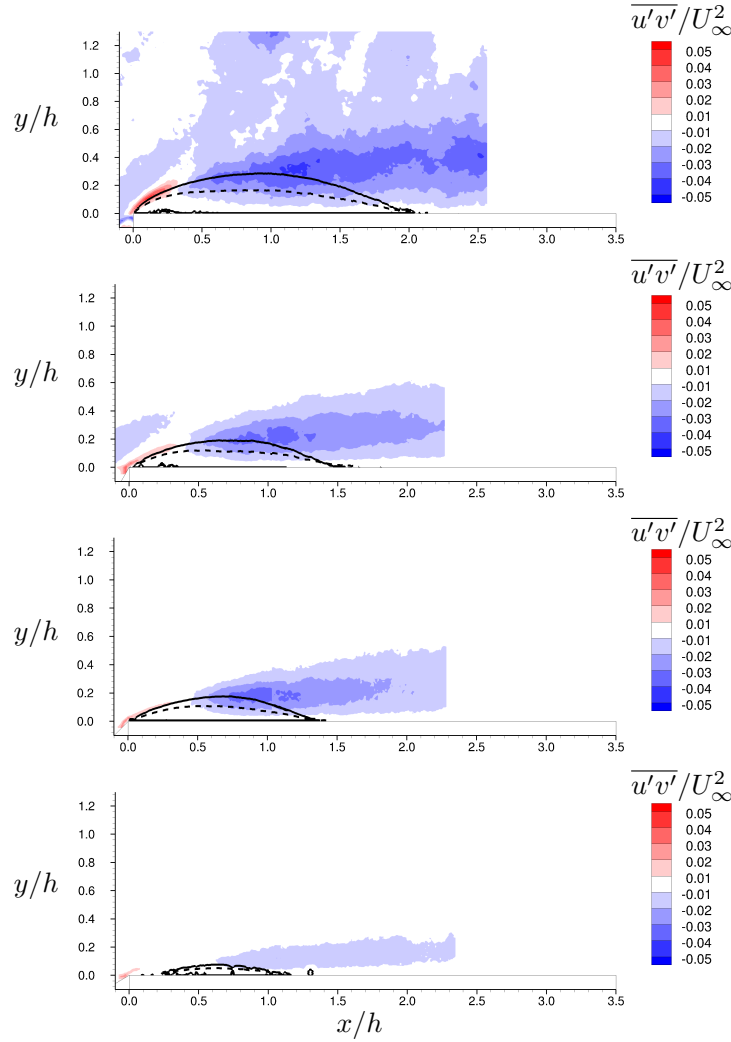


FIGURE 8.24: Reynolds shear stress, $\overline{\mathbf{u}'\mathbf{v}'}/U_\infty^2$, variation with escarpment angle, θ , for the minimum Reynolds number.

8.3.6 Quadrant analysis

To gain further insight into the mechanics of turbulent momentum transport, the $\mathbf{u}'\mathbf{v}'$ field is partitioned into quadrants (Emeis et al. 1995). Events contributing to reattachment can then be determined from a statistical viewpoint. The quadrants are defined as in figure 8.25. The $\mathbf{u}'\mathbf{v}'$ plane is separated into quadrants; Q1: $\mathbf{u}' > 0, \mathbf{v}' > 0$; Q2: $\mathbf{u}' < 0, \mathbf{v}' > 0$; Q3: $\mathbf{u}' < 0, \mathbf{v}' < 0$; and Q4: $\mathbf{u}' > 0, \mathbf{v}' < 0$. Flux events in the first and second quadrants lead to an upward transport of momentum whereas those in the third and fourth lead to a downward transport of momentum. Slow moving air ($\mathbf{u}' < 0$) ejected from the recirculation region are termed

‘ejections’ and contribute to second quadrant events (Emeis et al. 1995). ‘Sweeps’ on the other hand are fast air ($\mathbf{u}' > 0$) moving downward and contribute to fourth quadrant events (Emeis et al. 1995). We are primarily interested in sweeps as these events aid reattachment.

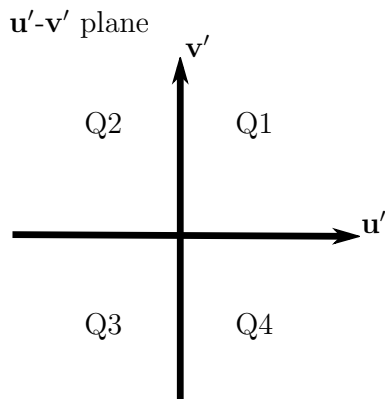


FIGURE 8.25: Partition of the \mathbf{u}' - \mathbf{v}' plane into quadrants. Events in the second quadrant are termed ‘ejections’, whereas events in the fourth quadrant are termed ‘sweeps’ (Emeis et al. 1995).

The number of events in each quadrant is determined from the instantaneous fluctuating velocity fields. U_∞ is subtracted from each instantaneous field to give the fluctuating velocity field. A sample quadrant analysis for the 90° step at the minimum Reynolds number is shown in figure 8.26. The contours represent the percentage of events in the particular quadrant arising from the $N = 600$ PIV fields. Bluff body dominance is evident close to the separation point in the first quadrant results of figure 8.26. The prevalence of first quadrant events indicates the coupled nature of the velocity speed-up with a vertical velocity component. The speed up is beneficial in a wind energy sense (*e.g.* see figure 8.22), whereas the vertical velocity component increases rotor misalignment for upwind turbines (Yoshida 2006). Rotor misalignment creates a variable loading across the rotor plane.

Flow within the recirculation region is made up of events in the second and third quadrants. Close to the separation point in the shear layer, ejection events dominate. This is due to the boundary layer step height velocity, *i.e.* $\mathbf{u}_0(h) < U_\infty$. This velocity is $\mathbf{u}_0(h) = 0.97U_\infty$. Despite, a streamwise velocity below the freestream value, the flow is deflected above the step creating a vertical velocity component.

The relaxation of bluff body dominance is evident between X_{Y_b} and X_L . The turbulent nature of the flow field ensures a near even distribution of second and third quadrant events between Y_b and downstream of X_{Y_b} . There is a case for this region to be termed the ‘reattachment mixing zone’. The mechanism of reattachment is evident in this zone from events in quadrants three and four. In the reattachment mixing zone, third quadrant events transfer

8.3. The recirculation region downstream of 2D escarpments

slow moving (compared to U_∞) fluid toward the escarpment surface. Sweep events also transfer higher momentum fluid into this zone from above as shown in quadrant 4. The turbulent nature of the ‘reattachment mixing zone’ make it unsuitable as a wind turbine location.

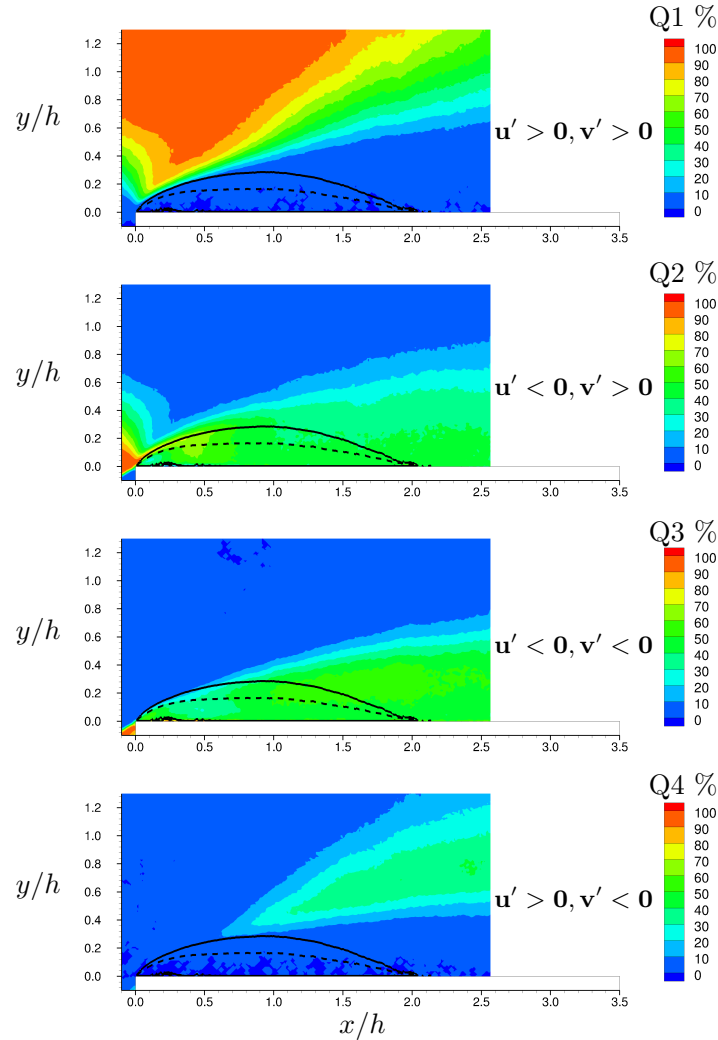


FIGURE 8.26: Quadrant analysis of the $\mathbf{u}'\mathbf{v}'$ field for $\theta = 90^\circ$ and $Re_h = 2.77 \times 10^3$.

8.3.7 2D escarpment studies summary

This present study investigated the turbulent recirculation region downstream of 2D escarpments with four different escarpment angles. The data show the recirculation region depends on both the escarpment angle and the Reynolds number. The recirculation region generally increased with Reynolds number for $\theta \geq 45^\circ$. The wind speed-up induced by the terrain was evident for all escarpment angles. The largest velocities were found above the FFS. The amplification factor, A_z used to assess the benefit of placing turbines atop 2D escarpments was largest at the apex where the largest velocity gradients exist. It reduced within the

recirculation region and recovered downstream of the reattachment point.

However, the beneficial wind speed-up is accompanied by turbulence production in the separated shear layer which forms downstream of the apex. Turbulence production increases with escarpment angle as the velocity gradient intensifies above the escarpment apex. Turbulent momentum transfer above the escarpment was visualised by the Reynolds shear stress fields. A quadrant analysis of the $\mathbf{u}'\mathbf{v}'$ field revealed the beneficial wind speed up is accompanied by a vertical velocity component. The vertical velocity component increases the rotor misalignment and variable loading across the rotor plane. Sweep events ($\mathbf{u}' > 0, \mathbf{v}' < 0$) occur downstream of the maximum recirculation region height above the 'reattachment mixing zone'. Such events transport streamwise momentum toward the step surface to overcome the adverse flow within the recirculation region.

Placement of turbines on top of 2D escarpments is not straight-forward. Turbines placed within the recirculation region on top of an escarpment will be subjected to large fluctuating loads. The beneficial wind speed-up cannot be de-coupled from the vertical velocity component which is a non-beneficial aspect of complex terrain. The separated shear layer should be avoided as a wind energy installation site due to the production of turbulent kinetic energy and strong velocity gradients.

Chapter 9

Thesis Summary

This thesis has addressed open research questions pertinent to wind farm siting in a water channel facility.

In particular, the tip and root vortices in the near-wake of a wind turbine were characterised using velocity and vorticity fields. The coupling between the blade aerodynamics and near-wake structure was effectively shown using two rotor designs. A geometrically scaled rotor generated both tip and root vortices at the three tip speed ratios investigated. The root vortices ceased close to the rotor plane due to their proximity to the turbine support structures. The tip vortices persisted further into the wake displaying characteristics of vortex interaction. However, the wake contained intense blade wakes in addition to the tip and root vortices. A BEM analysis and flow visualisations on a static 3D wing, highlighted the poor aerodynamic performance due to laminar separation of the geometrically scaled rotor. It was concluded that geometric scaling is unsuitable for wind turbine wake studies.

The wake vorticity field of the optimum Glauert rotor on the other hand was shown to be much more uniform indicating superior rotor performance. Root vortex formation and persistence into the wake was observed to be dependent on λ and hence Γ_B . The tip vortices are the longest lasting structures in the wake, confirming the need to consider these structures in wind farm siting. The tower wake was observed to cause the rapid destruction of the tip vortices in the bottom half of the wake. Wake structure was shown to be dependent on tip speed ratio. Further, the design criteria of dynamic similarity was not achieved due to the Reynolds number difference between the model and the tabulated airfoil data used in the optimum rotor analysis.

A stable configuration was achieved by increasing the helical pitch significantly. The results support the assertion that the mutual induction instability mode is the dominant instability mechanism leading to wake breakdown. Mutual induction between vortices was

shown to cause vortex coalescence, providing quantitative data to the flow visualisations in figure 2.5. The pairing instability occurred earlier in the wake with increasing λ as the pitch reduced. At runaway, vortex interaction was observed in both the tip and root vortices.

The vortex property data closest to the rotor plane suggested the effect of freestream turbulence on rotor performance was minimal. However, the effect of turbulence intensity on the vortices in the near wake was significant. The pairing instability was absent in the phase-locked average vorticity fields. The perturbed vortices instead degenerated at a rapid rate due to turbulent diffusion.

Meander of fixed wing trailing vortices at very low Reynolds numbers was confirmed to be Gaussian for angles of attack where flow separation is minimal. The effect of unsteadiness in the trailing vortex sheet on meander appeared to be significant. Meander of the helical tip and root vortices was observed to increase with vortex age. The effect of freestream turbulence on meander was significant.

In the course of this research, the flow over complex terrain was also investigated. The flow over 2D escarpments is dominated by bluff body separation from the apex. The effect of freestream turbulence intensity was reduced because of the bluff body dominance. Further, the reattachment distance reduced with escarpment angle as the separated shear layer protruded less above the escarpment. Sweep events, $\mathbf{u}' > \mathbf{0}, \mathbf{v}' < \mathbf{0}$, were observed to aid reattachment. The transient state of the recirculation region was characterised using POD phase averaging.

The region of wind speed-up, desirable in a wind energy sense was located close to the apex where the maximum velocity occurs. However, the speed-up was coupled to a vertical velocity component which would increase rotor misalignment for upwind turbines. Moreover, within the recirculation region, the results revealed a turbine would produce less power than one in uniform terrain. Further, significant turbulence generation was observed in the separated shear layer. A turbine placed near the separated shear layer will experience higher rotor loading. The experimental analysis confirmed the complex nature of flow over 2D escarpments. The results suggest a thorough analysis of the flow structure is required in complex terrain caution is complex terrain that without such terrain is an unsuitable location for a wind farm.

9.1 Recommendations for Future Work

Some of the ideas which emerged during candidature could not be pursued due to both time and facility limitations. In the following, some future possible directions of the research to

characterise both the near wake of a wind turbine and flow over complex terrain are presented.

For future investigations of the near-wake of a wind turbine, it would be highly interesting to further investigate the pairing instability using Stereo PIV (SPIV) or even tomographic PIV (3D-PIV). Only access to the full nine component velocity gradient tensor can reveal whether an elliptical deformation of the core occurs as predicted by Walther et al. (2007). Further, a more robust vortex meandering characterisation procedure would be possible with the full velocity gradient tensor.

The wind turbine wake experiments also had several limitations, *e.g.* the low tip chord Reynolds numbers meant viscous diffusion will be more prevalent than that at full-scale. A study with the same blade geometry at a higher Reynolds number could quantify the Reynolds number effect. Moreover, the blade coning angle of the experimental model was an inherent perturbation in the vortex system. Although, minimising perturbations in an experimental setting is a formidable task, attempts should be made to replicate the stable helical double triplet simulated in the Walther et al. (2007) study.

It would also be interesting to investigate the flow over complex terrain further to deduce the transient nature of the recirculation region. Lastly, it would be very interesting to combine the two thesis research topics and investigate wake evolution of turbines placed in complex terrain. Only with further analysis can engineering models to predict loads on structures, such as wind turbines, placed in complex terrain be developed.

Chapter 10

Appendix

10.1 Analytical models of a HAWT

Although wind turbines are highly complex machines, their performance can be evaluated accurately under certain conditions by simplified engineering models. The models depend on the method of rotor discretisation. In the simplest models, the rotor is treated as axisymmetric disk. The loading on the rotor is thus constant across the disk. This rotor discretisation is used in actuator disk methods and are the simplest method to assess global effect of the rotor. An axial momentum balance determines the thrust loading acting on the disk.

The forces generated by the rotor blades are determined by splitting the blade into elements. This blade element theory also assumes axisymmetric steady flow. Annular independence is assumed in blade element theory allowing two-dimensional airfoil properties to be consulted to determine the forces generated in each element.

Coupling the blade element theory and axial momentum balance results in the industry standard blade element momentum (BEM) method. BEM methods are used widely as a design and analysis tool in industry. It was in this capacity that a standard BEM model (Hansen 2008) was used in conjunction with the tip loss correction model of Shen et al. (2005).

The performance of the model turbines was assessed using a BEM method in the absence of a direct load measurements. Turbine rotor loading is commonly deduced by the load on the generator (*e.g.* (Ebert and Wood 1997), (Medici and Alfredsson 2006)) or a force balance applied to the tower (*e.g.* (Corten et al. 2004), (Hu et al. 2012)). The first method was not available in the experimental setup (details in chapter 3) due to an external motor driving the turbine. Calibration of the force balance is difficult due to necessity to assume a uniformly distributed load and uncertainty in determining the loading centre. Further, the BEM based optimum rotor analysis of Glauert (1937) was used to design a research orientated blade. The

methodology of this blade design is presented in this chapter with the final blade geometry presented in chapter 3.

An overview of the engineering models used to assess rotor performance follows. It begins with the simplest one dimensional momentum theory of wind turbines without and including wake rotation. Blade element theory is then presented to determine the aerodynamic forces generated by the blade elements. Momentum theory and blade element theory are then coupled resulting in the well known BEM method. The BEM conditions for an optimised rotor (Glauert 1937) is also presented to be used in a research orientated blade design in chapter 3. The BEM methods simplify the rotor geometry a great deal. The corrections required to account for flow features due to a finite number of blades and heavily loaded rotors and also presented. The following analysis is presented in numerous wind energy texts such as Wilson and Lissaman (1974); Hansen (2008); Burton et al. (2001); Snel (1998); Manwell et al. (2002). The references are presented here to avoid repetition.

10.1.1 One-dimensional momentum method without wake rotation

The engineering models used in the wind industry are based on earlier techniques developed for propellers. In the simplest model, 1D axial momentum theory, the wind turbine is treated as an axi-symmetric stationary *actuator disk* of area, $A = 2\pi R^2$. The thrust force acting on such a disk is equal to the pressure difference across the disk multiplied by the area,

$$T = A(p_u - p_d), \quad (10.1)$$

where p_u and p_d are the upstream and downstream disk surface pressures.

In this theory, a control volume is constructed around the disk as in figure 10.1. The flow is assumed to be stationary and incompressible. An axial momentum balance deduces the flow induced by the disk. Axial momentum theory was developed for propellers by Rankine (1865); Froude (1878, 1889). Betz (1920) applied the axial momentum theory to wind turbines.

Applying conservation of momentum and energy relations, the thrust acting on and power extracted by the actuator disk are determined.

In the control volume, continuity states that,

$$\dot{m} = \rho A_\infty U_\infty = \rho A_D U_D = \rho A_w U_w, \quad (10.2)$$

where \dot{m} is the streamtube mass flow, U_∞ is the freestream velocity, U_D and U_w are the disk and far wake velocities respectively.

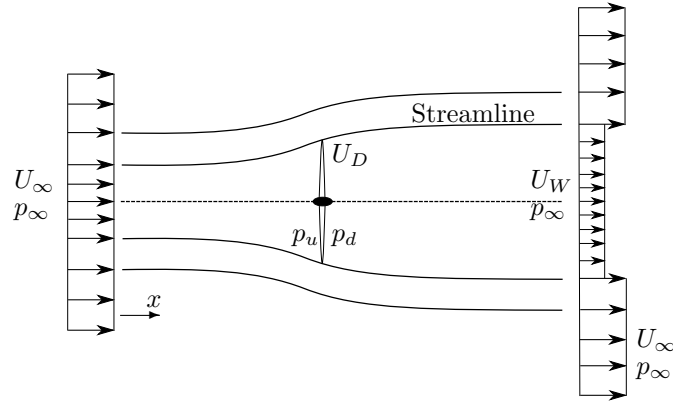


FIGURE 10.1: One dimensional streamtube analysis of a wind turbine

Conservation of axial momentum leads to equation 10.3,

$$T = \dot{m}(U_\infty - U_W) = \rho A U_D (U_\infty - U_W), \quad (10.3)$$

where T is the thrust acting on the disk. A gradual pressure recovery occurs downstream of the disk until it returns to p_∞ . In this pressure recovery process, the velocity reduces to its minimum level, U_W .

The control volume energy balance is,

$$E = \frac{1}{2} \dot{m} (U_\infty^2 - U_W^2). \quad (10.4)$$

The pressure drop across the disk is determined using Bernoulli's equation. Due to the energy extraction by the disk, Bernoulli's equation is not valid for the flow through the disk. It is applied in two steps, from p_∞ upstream to p_u and from p_d to p_∞ in the far wake. Applying Bernoulli's equation to the two steps and after eliminating U_D by combining the two equations with equation 10.1, an expression for the thrust becomes,

$$T = 0.5 A \rho (U_\infty - U_W)^2 \quad (10.5)$$

Combining equations 10.3 and 10.5 results in the relationship between U_D , U_W and U_∞ .
i.e.

$$U_D = 0.5(U_\infty + U_W), \quad (10.6)$$

which states that U_D is the average of U_W and U_∞ .

The shaft power extracted by the disk is the energy (eqn 10.4) per unit time. As \dot{m} is the mass flow through the disk, the power for the ideal 1D turbine is,

$$P = 0.5\rho A(U_\infty^2 - U_W^2)U_D. \quad (10.7)$$

The axial interference factor due to induction by the rotor is defined as,

$$a = 1 - U_D/U_\infty. \quad (10.8)$$

Further, from equation 10.6, it follows that the induction in the wake is twice that at the rotor plane, *i.e.* $U_W = U_\infty(1 - 2a)$. Due to the 1D nature of the momentum balance, $a \leq 0.5$ as no recirculation can occur in the wake.

Substituting a into equations 10.7 and 10.3, the equations for the extracted power and thrust become,

$$P = 2\rho AU_\infty^3 a(1 - a)^2, \quad (10.9)$$

and

$$T = 2\rho AU_\infty^2 a(1 - a). \quad (10.10)$$

The maximum power available to the disk is shown in equation 10.11,

$$P_{avail} = 0.5\rho U_\infty^3 A. \quad (10.11)$$

Further normalising equation 10.7 by equation 10.11, the power coefficient is defined as,

$$C_P = \frac{P}{0.5\rho U_\infty^3 A} = 4a(1 - a)^2, \quad (10.12)$$

and a thrust coefficient likewise follows as,

$$C_T = \frac{T}{0.5\rho U_\infty^2 A} = 4a(1 - a). \quad (10.13)$$

Betz (1920) determined that the maximum power is extracted when the derivative of P with respect to a is zero, *i.e.* $dP/da = 0$. This occurs at $a = 1/3$, giving the well known upper limit of $C_{P,max} = (16/27) = 0.593$. This factor is referred as the Betz or the Lanchester–Betz–Joukowski limit. It represents the maximum amount of the kinetic energy that can be captured by an axi-symmetric disk.

General momentum theory assumes all kinetic energy extraction occurs at the disk. Further, the efficiency of the turbine is not taken into account in equation 10.12 and losses due

to wake rotation are not considered. To take into account the efficiency of the turbine, the kinetic energy flowing through A is not AU_∞ but rather AU_D . The maximum efficiency is 88.8% at the Betz limit (Wilson and Lissaman 1974).

The wake losses due to wake rotation are incorporated into the analysis by considering the rotation of the actuator disk. The effect of rotation is presented in the section which follows.

10.1.2 One dimensional momentum method with wake rotation

The actuator disk concept is a highly simplified wind turbine model. In reality, wind turbines contain a finite number of blades. The force experienced by the turbine blade applies equally and in the opposite direction to the air which passes over the blade. Wake rotation thus occurs in the opposite direction to the rotating blades. Wake rotation is a source of ‘lost’ energy (that is not converted to angular momentum of the blades) for low blade rotation rates (high torque). The ratio between the turbine angular velocity, ΩR , and U_∞ is known as the tip speed ratio, was introduced in equation 2.2. λ is the principal independent variable in the study of wind turbine wakes.

In considering wake rotation, the rotor is separated into annular segments, as shown in figure 10.2.

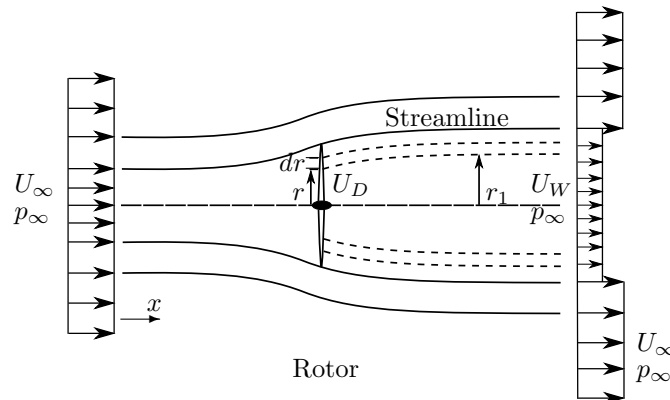


FIGURE 10.2: One dimensional streamtube analysis of a wind turbine with wake rotation

In considering the rotation of the disk, the control volume now rotates at Ω . The angular velocity of the air flow relative to the disk increases from Ωr to $\Omega r + u_t$ between the leading and trailing edges. The tangential interference factor is defined as $a_t = u_t/2\Omega r$. At the rotor mid plane, the total induced velocity, \mathbf{w} , has a component in the axial (aU_∞) and tangential ($r\Omega a_t$) directions.

Equation 10.3 related the thrust force acting on the entire disk to the pressure difference

across the disk. An equivalent expression for the pressure difference across the blades in a rotating control volume is constructed (Glauert 1935) as,

$$\Delta p = \rho(\Omega r + u_t)u_t r^2. \quad (10.14)$$

The thrust experienced by an annular segment of width dr is given by

$$dT = \Delta p A = [\rho(\Omega r + u_t)u_t r^2] 2\pi r dr. \quad (10.15)$$

Introducing the angular interference factor into equation 10.15 results in an expression for the conservation of angular momentum as

$$dT = 4a_t(1 + a_t)\frac{1}{2}\rho\Omega^2 r^2 2\pi r dr. \quad (10.16)$$

A similar thrust coefficient expression can be derived from equation 10.13 for an annular segment as,

$$dT = 4a(1 - a)\frac{1}{2}\rho U_\infty^2 2\pi r dr. \quad (10.17)$$

Eliminating the thrust from equation 10.16 and equation 10.17 results in the energy relation as,

$$\frac{a(1 + a)}{a_t(1 + a_t)} = \frac{\Omega^2 r^2}{U_\infty^2} = \lambda(r)^2. \quad (10.18)$$

The energy relation reveals an important assumption in the control volume analyses. If α is below stall, equation 10.18 can be derived directly from the velocity diagram in figure 10.3. Equation 10.18 states \mathbf{w} is perpendicular to U_{rel} and thus is only due to the lift force.

The power extracted by the turbine is now determined by an angular momentum balance. The torque exerted on the rotor must equal the change in angular momentum in the wake. Within an annular area, the torque and hence power acting on the rotor is determined by Euler's turbine equation,

$$P = Q\Omega = \Omega \dot{m}(r_1 u_{t,\infty} - r_2 u_{t,w}), \quad (10.19)$$

where Q is the torque applied to the rotor, $u_{t,\infty}$ and $u_{t,w}$ are the tangential velocity components in the freestream (where they equal 0) and in the wake.

Thus for an annular rotor segment, the power produced is,

$$dP = \dot{m}\Omega r u_t = 2\pi r^2 \rho U_D \Omega u_t dr, \quad (10.20)$$

where u_t is the tangential velocity component at the trailing edge.

The total power the rotor produces can be determined by introducing the a and a_t relations into equation 10.20 and integrating from 0 to R . This results in the power production equation,

$$P = 4\pi\rho\Omega^2 U_\infty \int_0^R a_t(1-a)r^3 dr. \quad (10.21)$$

The power integral is made dimensionless by introducing the local rotation ratio, $\lambda(r) = \Omega r/U_\infty$, and λ as defined in equation 2.2. A power coefficient results (10.22):

$$C_P = \frac{8}{\lambda^2} \int_0^\lambda a_t(1-a)\lambda(r)^3 d\lambda(r). \quad (10.22)$$

The axial and angular momentum balances do not consider the forces acting on the blade elements, for this blade element theory is used. It will be outlined in the following section.

10.2 Blade element theory

Blade element theory calculates the aerodynamic forces generated on the blade. The rotor plane is once again divided into annular elements of width dr as in figure 10.2. The velocity and force components in an annular element are shown in figure 10.3. The parameters in figure 10.3 are introduced in the following analysis. The flow in the annular element is assumed to be steady and approximately two dimensional. Rotor loading is assumed to be axi-symmetric and each annular element acts independently of all others. Airfoil performance data can thus be used to determine the forces acting on the rotating blades.

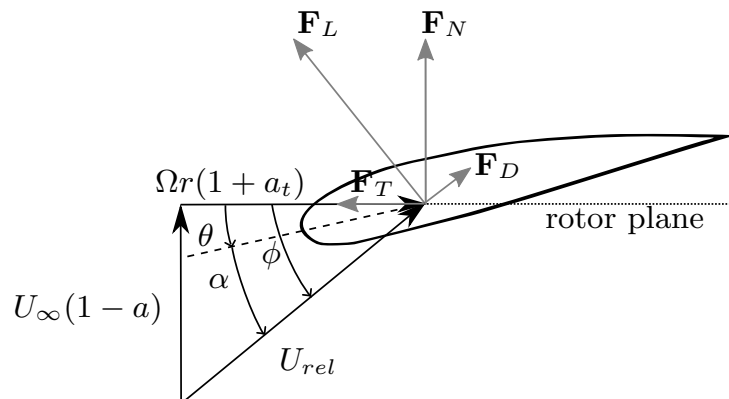


FIGURE 10.3: Velocity diagram at the rotor plane at a given spanwise location, r . The angle ϕ is the sum of α -local blade angle of attack and θ -local blade pitch angle.

The angle of attack, α , is given by,

$$\alpha = \phi - \theta, \quad (10.23)$$

where θ is the local blade twist angle and, the angle of the relative wind, ϕ , is defined by,

$$\tan \phi = \frac{(1 - a)U_\infty}{(1 + a_t)\omega r}. \quad (10.24)$$

From figure 10.3, the relative velocity component can be expressed in terms of ϕ and the interference factors,

$$U_{rel} \sin \phi = U_\infty(1 - a), \quad (10.25)$$

$$U_{rel} \cos \phi = \Omega r(1 + a_t). \quad (10.26)$$

The lift and drag forces acting in the annular element are given by equations 10.27 and 10.28.

$$L = \frac{1}{2}\rho U_{rel}^2 c C_l, \quad (10.27)$$

$$D = \frac{1}{2}\rho U_{rel}^2 c C_d. \quad (10.28)$$

The normal, F_N , and tangential, F_T force components are of interest. They are calculated by,

$$F_N = L \cos \phi + D \sin \phi, \quad (10.29)$$

$$F_T = L \sin \phi - D \cos \phi, \quad (10.30)$$

or in non-dimensional form,

$$\begin{aligned} C_n &= \frac{F_N}{0.5\rho U_{rel}^2 c}, \\ C_n &= C_l \cos \phi + C_d \sin \phi, \end{aligned} \quad (10.31)$$

$$\begin{aligned}
C_t &= \frac{F_T}{0.5\rho U_{rel}^2 c}, \\
C_t &= C_l \sin \phi - C_d \cos \phi.
\end{aligned}
\tag{10.32}$$

The local solidity, $\sigma(r)$, for the annular control volume is given by,

$$\sigma(r) = \frac{c(r)B}{2\pi r},
\tag{10.33}$$

where B is the number of blades and $c(r)$ is the blade chord in the control volume at radius r .

The normal and tangential forces are used to determine the thrust and torque in the annular control volume. The thrust acting on the B blades is determined by substituting equation 10.25 into equation 10.31, with the result,

$$\begin{aligned}
dT &= BF_N dr, \\
dT &= 0.5\rho c B \frac{U_\infty^2 (1-a)^2}{\sin^2 \phi} C_n dr.
\end{aligned}
\tag{10.34}$$

A similar expression is constructed for the torque acting on the blades by substituting equation 10.26 into equation 10.32, with the result,

$$\begin{aligned}
dQ &= rBF_T dr, \\
dQ &= 0.5\rho c B \frac{U_\infty (1-a)\Omega r(1+a)}{\sin \phi \cos \phi} rC_t dr.
\end{aligned}
\tag{10.35}$$

10.3 BEM method

Glauert (1935) coupled the thrust force and torque acting on the disk to the fluid forces being generated at the airfoil sections. Coupling the 1D actuator disk momentum method to the aerodynamic forces generated at the blade elements results in the blade element momentum (BEM) method. Turbine designers use the BEM method to evaluate performance of single and multiple turbines in wind farms.

Conserving both axial and angular momentum from the general momentum method, the differential thrust, dT , and differential torque, dQ , acting in the blade elements are;

$$dT = 4\pi r \rho U_\infty^2 a(1-a) dr,
\tag{10.36}$$

and

$$dQ = 4\pi r^3 \rho U_\infty \Omega (1 - a) a_t dr. \quad (10.37)$$

The blade element forces are determined from equations 10.34 and 10.35. These expressions are equated to those determined from the 1D momentum method with wake rotation. This is the premise of the BEM method. Equation 10.36 is equated to 10.34 to give an expression for the axial interference factor as in equation 10.38. The expression for the solidity, equation 10.33 has also been used in equation 10.38.

$$a = \frac{1}{\frac{4 \sin^2 \phi}{\sigma C_n} - 1}. \quad (10.38)$$

Equation 10.37 is equated to 10.35 to give an expression for the axial interference factor as in equation 10.39.

$$a_t = \frac{1}{\frac{4 \sin \phi \cos \phi}{\sigma C_t} - 1}. \quad (10.39)$$

10.3.1 Optimum turbine

Glauert (1935) developed an analysis for an optimum rotor by maximising the power output (equation 10.22) for a given tip speed ratio, λ . With knowledge of the operating Reynolds number, an airfoil with a high lift to drag ratio, C_l/C_d is chosen. This $C_{l,opt}/C_{d,opt}$ ratio occurs at a specific angle of attack, α_{opt} , Reynolds number, Re_{opt} , and hence tip speed ratio, λ_{opt} . These parameters form the design criteria for the optimum turbine.

If the velocity diagram of figure 10.3 represents uniform flow in the dr streamtube, the flow should be approximately two-dimensional. If drag forces are not considered (a reasonable assumption at small α , where the flow is attached), the total induced velocity, \mathbf{w} , is perpendicular to the relative velocity, \mathbf{U}_{rel} and is due to the lift force only.

The differential form of power was presented in equation 10.22. This is a function of two variables, requiring a separate relation between λ and the interference factors a and a_t . The conservation of both axial and angular momentum leads to the energy relation given in equation 10.18.

To maximise equation 10.22, the function $f(a, a_t) = a_t(1 - a)$ must be maximised while conforming to equation 10.18. The function is maximum when $df/da = 0$. Differentiating $f(a, a_t) = a_t(1 - a)$ and equation 10.18 with respect to a yields equations 10.40 and 10.41,

$$(1 - a) \frac{da_t}{da} = a_t, \quad (10.40)$$

$$\lambda(r)^2(1 + 2a_t) = (1 - 2a). \quad (10.41)$$

Combining these two relations with equation 10.18, results in the optimum relationship between the interference factors. This relationship states,

$$a_t = \frac{1 - 3a}{4a - 1}. \quad (10.42)$$

Substituting this relationship into equation 10.18 results in the optimum relationship between $\lambda(r)$ and a . The optimum relationship is shown in equation 10.43.

$$16a^3 - 24a^2 + a(9 - 3\lambda(r)^2) - 1 + \lambda(r)^2 = 0. \quad (10.43)$$

$$\lambda(r) = (4a - 1) \sqrt{\frac{1 - a}{1 - 3a}}. \quad (10.44)$$

Inspecting the roots of equation 10.44, shows the optimum range of the axial interference factor is $1/4 \leq a \leq 1/3$.

The optimum twist angle is found by rearranging equation 10.23 and using α_{opt} . The optimum chord is found by equation 10.38 and the optimum a and a_t values.

$$\frac{c(\lambda(r))}{R} = \frac{8\pi a \lambda(r) \sin^2 \phi}{(1 - a) B C_n \lambda}. \quad (10.45)$$

where C_n is derived from equation 10.31 using the lift and drag coefficients achieving the desired $C_{l,\text{opt}}/C_{d,\text{opt}}$ ratio.

With knowledge of λ , B , α_{opt} and hence $C_{l,\text{opt}}/C_{d,\text{opt}}$, the chord distribution is determined (ignoring tip losses) from equation 10.45 (Hansen 2008).

This optimisation process was used to design an optimum Glauert rotor in chapter 3.

10.3.2 Correction for tip losses

The BEM analysis treats the turbine as a uniformly loaded actuator disk. The rotor design must also consider the interaction between the blade bound circulation and shed vorticity in the wake. This interaction causes induced drag which alters the local flow angle in the tip and possibly root region.

Reduced rotor performance caused by the tip losses associated with a finite number of blades can be incorporated into the optimum rotor design by the tip loss correction of Prandtl. In the Prandtl tip loss correction, the wake is assumed to consist of a series of vortex sheets. The induced velocities of which alter the flow at the blades. Prandtl's tip loss factor is the ratio between the induced velocity at the blade section and the average in the wake $F = \bar{a}/a$ (Hansen 2008). Glauert (1935) introduced an approximate formula of the Prandtl tip loss function shown in equation 10.46 that allowed it to be implemented in BEM computer codes.

$$F = \frac{2}{\pi} \cos^{-1}[\exp(-\frac{B(R-r)}{2r \sin \phi})]. \quad (10.46)$$

However, the Prandtl tip loss correction formula produces non-physical results at the tip (Shen et al. 2005). Shen et al. (2005) introduced an adaptation of equation 10.46 that modifies the two-dimensional airfoil data in the tip region for three dimensional effects. The correction stipulates that the axial loading tends to zero at the tip due to pressure equalisation (Shen et al. 2005). The correction modifies the normal, C_n and tangential, C_t , force coefficients in the region of the tip by a further correction factor, F_1 , given in equation 10.47. By applying this further correction factor, pressure equalisation at the tip is ensured.

$$F_1 = \frac{2}{\pi} \cos^{-1}[\exp(-g \frac{B(R-r)}{2r \sin \phi})], \quad (10.47)$$

where the empirical function g , was derived from experimental results and takes the form, $g = e^{[-0.125(B\lambda - 21)]} + 0.1$ (Shen et al. 2005).

The axial and tangential interference factors at the blade section now take the forms of equations 10.48 and 10.49 respectively,

$$a = \frac{2 + Y_1 - \sqrt{4Y_1(1 - F) + Y_1^2}}{2(1 + FY_1)}, \quad (10.48)$$

$$a_t = \frac{1}{(1 - aF)Y_2/(1 - a) - 1}, \quad (10.49)$$

The two factors Y_1 and Y_2 are given by equations 10.50 and 10.51 respectively.

$$Y_1 = \frac{4F \sin^2 \phi}{(\sigma C_n F_1)}. \quad (10.50)$$

$$Y_2 = \frac{4F \sin \phi \cos \phi}{(\sigma C_t F_1)}. \quad (10.51)$$

10.3.3 Corrections for heavy rotor loading

The final correction is for heavily loaded rotors (*i.e.* $a > 0.3$) where momentum theory is no longer valid.

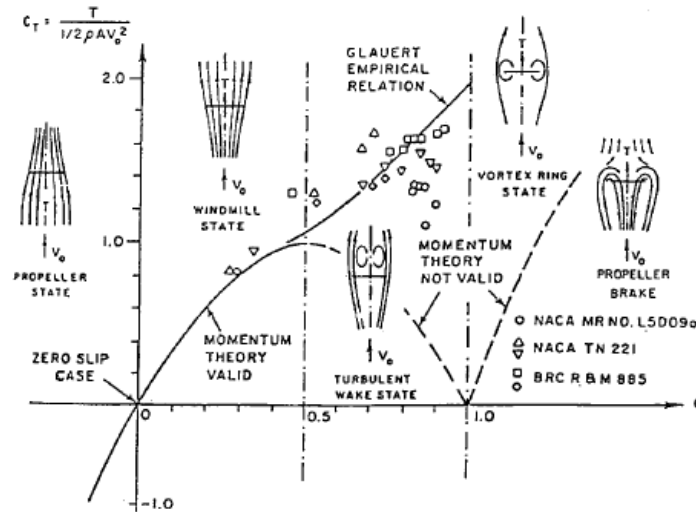


FIGURE 10.4: Momentum theory for wind turbines, with the axial interference factor and the thrust coefficient on the horizontal and vertical axes respectively (Eggleston and Stoddard 1987)

The heavily loaded rotor corrections of Glauert in (Hansen 2008) are modified to incorporate the adaptation of Shen et al. (2005). The corrections for rotor loading are shown in equations 10.53 where a_c is taken as 0.3 (Shen et al. 2005).

$$C_t = 4aF(1 - aF) \quad \text{for } a \leq a_c, \quad (10.52)$$

$$= 4 [a_c^2 F^2 + (1 - 2a_c F)aF] \quad \text{for } a \geq a_c. \quad (10.53)$$

10.3.3.1 BEM code

The BEM method is simple to implement and accurate for a wide range of turbine operating conditions. For this reason, it is the first choice to evaluate the performance of a wind turbine. The BEM method can easily be programmed as an iterative computer program. Such programs can optimise the flow in each annular element based on input parameters. In the absence of a direct force measurement device, a BEM method was used to estimate turbine performance. The BEM method steps are presented next with the relevant equation numbers in brackets;

- 1 Initialize the axial a and tangential a_t interference factors, typically to zero

- 2 Compute the flow angle ϕ
- 3 Compute the local angle of attack, α
- 4 Use a lookup function to determine the lift $C_l(\alpha)$ and drag $C_d(\alpha)$ coefficients
- 5 Compute the normal C_n and tangential C_t force coefficients
- 6 Calculate the Shen et al. (2005) tip loss functions, g, F_1, Y_1, Y_2
- 7 Calculate the axial a and tangential a_t interference factors and difference to the initialised values.
- 8 If a and a_t change more than a specified tolerance, repeat from step 2 until convergence is obtained.
- 9 Apply heavy loading corrections if a is greater than a permissible value, a_c
- 10 Compute the local loads on the blade elements
- 11 Compute bound circulation and other desired flow state properties

References

- R.J. Adrian and J. Westerweel. *Particle image velocimetry*. Cambridge University Press, 2011. pg.
- M. Agelinchaab and M.F. Tachie. PIV study of separated and reattached open channel flow over surface mounted blocks. *Journal of Fluids Engineering*, 130:1–9, 2008.
- B. Akay, D. Micallef, C.S. Ferreira, and G. van Bussel. Stereo PIV experiments on horizontal axis wind turbine rotor model. In *Proceedings of the 46th Symposium of applied aerodynamics, Polytech' Orléans*, 2011.
- Md. Mahbub Alam, Y. Zhou, H.X. Yang, H. Guo, and J.Mi. The ultra-low reynolds number airfoil wake. *Experiments in Fluids*, 48:81–103, 2010.
- P.A. Alfredsson and J.A. Dahlberg. A preliminary wind tunnel study of windmill wake dispersion in various flow conditions. Technical report, The Aeronautical Research Institute of Sweden, 1979. AU-1499, part 7.
- P.A. Alfredsson and J.A. Dahlberg. Measurements of wake interaction effects on the power output from small wind turbine models. Technical report, The Aeronautical Research Institute of Sweden, 1981. HU-2189, part 5.
- K. Ameer, C. Masson, and P.J. Eecen. 2D and 3D numerical simulation of the wind-rotor/nacelle interaction in an atmospheric boundary layer. *Journal of Wind Engineering and Industrial Aerodynamics*, 2011. doi:10.1016/j.jweia.2011.06.002.
- M. Arie, M. Kiya, H. Tamura, M. Kosugi, and K. Takaoka. Flow over rectangular cylinders immersed in a turbulent boundary layer. *Bulletin of the Japan Society of Mechanical Engineers (JSME)*, 18(125):1269–1276, 1975.
- S. Aubrun, G. Espana, S. Loyer, P. Hayden, and P. Hancock. Is the actuator disc concept sufficient to model the far-wake of a wind turbine? *Proceedings of iTi 2010 - Conference on turbulence*, pages 69–70, 2010.
- K.W. Ayotte and D.E. Hughes. Observations of boundary-layer wind-tunnel flow over isolated ridges of varying steepness and roughness. *Boundary Layer Meteorology*, 112:525–556, 2004.

References

- P.W. Bearman and T. Morel. Effect of free stream turbulence on the flow around bluff bodies. *Progress in Aerospace Science*, 20:97–123, 1983.
- A. Bechmann, N.N. Sørensen, J. Berg, J. Mann, and P.-E. Réthoré. The bolund experiment, part ii: blind comparison of microscale flow models. *Boundary-Layer Meteorology*, 141: 245–271, 2011.
- J. Berg, J. Mann, A. Bechmann, M. S. Courtney, and H. E. Jørgensen. The bolund experiment, part i: flow over a steep, three-dimensional hill. *Boundary-layer meteorology*, 141: 219–243, 2011.
- G. Bergeles and N. Athanassiadis. The flow past a surface-mounted obstacle. *Journal of Fluids Engineering*, 105:461–463, 1983.
- G. Berkooz, P. Holmes, and J.L. Lumley. The proper orthogonal decomposition in the analysis of turbulent flows. *Annual Review of Fluid Mechanics*, 25:539–575, 1993.
- R. Betchov. On the curvature and torsion of an isolated vortex filament. *Journal of Fluid Mechanics*, 22(3):471–479, 1965.
- A. Betz. Das maximum der theoretisch möglichen ausnützung des windes durch windmotoren. *Z. Gesamte Turbinenwesen*, 26:307–309, 1920.
- A. Betz. Behaviour of vortex systems. Technical Report NACA TM 713, National Advisory Committee for Aeronautics, 1935.
- M.J. Bhagwat and J.G. Leishman. Measurements of bound and wake circulation on a helicopter rotor. *Journal of Aircraft*, 37(2), 2000.
- M.J. Bhagwat and J.G. Leishman. Generalized viscous vortex model for application to free-vortex wake and aeroacoustic calculations. *Proceedings of the 58th annual forum and technology display of the american helicopter society international*, 2002.
- F. Bingöl, G.C. Larsen, and J. Mann. Wake meandering - an analysis of instantaneous 2d laser measurements. *Journal of Physics: Conference Series*, 75:012059, 2007.
- G.T. Bitsuamlak, T. Stathopoulos, and C. Bedard. Numerical evaluation of wind flow over complex terrain: review. *Journal of Aerospace Engineering*, 17(4):135–145, 2004.
- R.D. Blevins. *Applied fluid dynamics handbook*. Van nostrand reinhold company, New York, 1984.
- H. Bolnot, S. Le Dizés, and T. Leweke. Spatio-temporal development of the pairing instability in helical vortices. *Wake Conference, 8-9 June, Visby, Sweden*, page 12, 2011.

-
- A.J. Bowen and D. Lindley. A wind-tunnel investigation of the wind speed and turbulence characteristics close to the ground over various escarpment shapes. *Boundary-Layer Meteorology*, 12:259–271, 1977.
- P. Bradshaw. The effect of wind-tunnel screens on nominally two-dimensional boundary layers. *Journal of Fluid Mechanics*, 22(4):679–687, 1965.
- P. Bradshaw and F.Y.F. Wong. The reattachment and relaxation of a turbulent shear layer. *Journal of Fluid Mechanics*, 52(1):113 – 135, 1972.
- F.N.M. Brown, editor. *See the wind blow*. University of Notre Dame, 1971.
- T. Burton, D. Sharpe, N. Jenkins, and E. Bossanyi. *Wind Energy Handbook*. John Wiley and Sons, 2001. chapter 3.
- CADDET. The Tjæreborg wind turbines project. Technical report, CADDET Centre for renewable energy, 1998. Technical brochure number 65.
- R. Camussi, M. Felli, F. Pereira, G. Aloisio, and A. Di Marco. Statistical properties of wall pressure fluctuations over a forward-facing step. *Physics of Fluids*, 20:075113–1 075113–13, 2008.
- F. Caradonna. Performance measurement and wake characteristics of a model rotor in axial flight. *Journal of the American Helicopter Society*, 44:101–108, 1999.
- I.P. Castro. Relaxing wakes behind surface-mounted obstacles in rough wall boundary layers. *Journal of Fluid Mechanics*, 93:631–659, 1979.
- I.P. Castro. The stability of laminar symmetric separated wakes. *Journal of Fluid Mechanics*, 532:389–411, 2005.
- I.P. Castro and M. Dianat. Surface flow patterns on rectangular bodies in thick boundary layers. *Journal of Wind Engineering and Industrial Aerodynamics*, 11:107–119, 1983.
- P. Chakraborty, S. Balachandar, and R. Adrian. On the relationships between local vortex identification schemes. *Journal of Fluid Mechanics*, 535:189–214, 2005.
- L.P. Chamorro and F. Porté-Agel. A wind-tunnel investigation of wind-turbine wakes: Boundary-layer turbulence effects. *Boundary-Layer Meteorology*, 132:129–149, 2009.
- A. Chatterjee. An introduction to the proper orthogonal decomposition. *Current Science*, 78 (7):808–817, 2000.
- N.J. Cherry, R. Hillier, and M.E.M.P. Latour. Unsteady measurements in a separated and reattaching flow. *Journal of Fluid Mechanics*, 144:13–46, 1984.
- M.S. Chong, A.E. Perry, and B.J. Cantwell. A general classification of three-dimensional flow fields. *Physics of Fluids A*, 2:765–777, 1990.

References

- G. Comte-Bellot and S. Corrsin. The use of a contraction to improve the isotropy of grid-generated turbulence. *Journal of Fluid Mechanics*, 25:657–682, 1966.
- G.P. Corten, P. Schaak, and T. Hegberg. Velocity profiles measured above a scaled wind farm. Technical report, Energy research centre of the Netherlands, ECN, 2004. ECN-RX-04-123.
- A. Crespo, J. Hernández, and S. Frandsen. Survey of modelling methods for wind turbine wakes and wind farms. *Wind Energy*, 2:1–24, 1999.
- S.C. Crow. Stability theory for a pair of trailing vortices. *AIAA Journal*, 8(12):2172–2179, 1970.
- J. Dandois, E. Garnier, and P. Sagaut. Numerical simulation of active separation control by a synthetic jet. *Journal of Fluid Dynamics*, 574:25–58, 2007.
- V. de Brederode and P. Bradshaw. Three-dimensional flow in nominally two-dimensional separated bubbles. i. flow behind a rear-ward facing step. report 72-19, Imperial College of Science and Technology, 1972.
- W.J. Devenport, M.C. Rife, S.I. Liapis, and G.J. Follin. The structure and development of a wing tip vortex. *Journal of Fluid Mechanics*, 312:67–106, 1996.
- I. Dobrev, B. Maalouf, N. Troldborg, and F. Massouh. Investigation of the wind turbine vortex structure. *14th Int Symp on Applications of Laser Techniques to Fluid Mechanics, Lisbon, Portugal, 07-10 July*, 2008.
- J.K. Eaton and J.P. Johnston. A review of research on subsonic turbulent flow reattachment. *American Institute of Aeronautics and Astronautics Journal*, 19:1093–1100, 1981.
- P.R. Ebert and D.H. Wood. The near wake of a model horizontal-axis wind turbine-i. experimental arrangements and initial results. *Renewable Energy*, 12(3):225–243, 1997.
- P.R. Ebert and D.H. Wood. The near wake of a model horizontal-axis wind turbine-ii. general features of the three-dimensional flowfield. *Renewable Energy*, 18:513–534, 1999.
- P.R. Ebert and D.H. Wood. The near wake of a model horizontal-axis wind turbine. part 3: properties of the tip and hub vortices. *Renewable Energy*, 22:461–472, 2001.
- P.R. Ebert and D.H. Wood. The near wake of a model horizontal-axis wind turbine at runaway. *Renewable Energy*, 25:41–54, 2002.
- D.M. Eggleston and F.S. Stoddard. *Wind turbine engineering design*. Van Nostrand Reinhold, New York, 1987.
- S. Emeis, H.P. Frank, and F. Fiedler. Modification of airflow over an escarpment-results from the hjarde-mål experiment. *Boundary Layer Meteorology*, 74:131–161, 1995.

-
- B.R. Epps and A.H. Techet. An error threshold criterion for singular-value-decomposition modes extracted from piv data. *Experiments in Fluids*, 48:355–367, 2010.
- T.M. Farabee and M.J. Casarella. Measurements of fluctuating wall pressure for separated/reattached boundary layer flows. *Journal of Vibration, Acoustics, Stress, and Reliability in Design*, 108:301–307, 1986.
- M. Felli, F. Di Felice, G. Guj, and R. Camussi. Analysis of the propeller wake evolution by pressure and velocity phase measurements. *Experiments in Fluids*, 41:441–451, 2006.
- M. Felli, R. Camussi, and F. Di Felice. Mechanisms of evolution of the propeller wake in the transition and far fields. *Journal of Fluid Mechanics*, 682:5–53, 2011.
- A. Fouras and J. Soria. Accuracy of out-of-plane vorticity measurements derived from in-plane velocity field data. *Experiments in Fluids*, 25:409–430, 1998.
- A. Fouras, D. Lo Jacono, and K. Hourigan. Target-free stereo PIV: a novel technique with inherent error estimation and improved accuracy. *Experiments in Fluids*, 44:317–329, 2008.
- T.A. Fox. Interference in the wake of two square-section cylinders arranged perpendicular to each other. *Journal of Wind Engineering and Industrial Aerodynamics*, 40:75–92, 1992.
- S. Frandsen and M.L. Thøgersen. Integrated fatigue loading for wind turbines in wind farms by combining ambient turbulence and wakes. *Wind Engineering*, 23(6):327–340, 1999.
- R.E. Froude. *Transactions of the institute of naval architects*, 30:390, 1889.
- W. Froude. *Transactions of the institute of naval architects*, 19:47, 1878.
- I.S. Gartshore. The effects of freestream turbulence on the drag of rectangular two dimensional prism. Technical Report BLWT-4-73, University of Western Ontario, Canada, 1973.
- N. Gasset, G.J. Poitras, Y. Gagnon, and C. Brothers. Study of atmospheric boundary layer flows over a coastal cliff. *Wind Engineering*, 29(1):3–24, 2005.
- Geoscience Australia. Map of operating renewable energy generators in australia. Website, 2010. <http://www.agso.gov.au/renewable/>.
- H. Glauert. *Airplane propellers*. In *Aerodynamic theory*, ed. W.F. Durand. Dover, New York, 1935.
- H. Glauert. *The elements of airfoil and airscrew theory*. Cambridge University Press, London, 1937.
- L. Graftieaux, M. Michard, and N. Grosjean. Combining PIV, POD and vortex identification algorithms for the study of unsteady turbulent swirling flows. *Measurement Science and Technology*, 12:1422–1429, 2001.

References

- I. Grant and E.H. Owens. Confidence interval estimates in piv measurements of turbulent flows. *Applied Optics*, 29:1400–1402, 1990.
- I. Grant and P. Parkin. A dpiv study of the trailing vortex elements from the blades of a horizontal axis wind turbine in yaw. *Experiments in Fluids*, 28:368–376, 2000.
- I. Grant, G.H. Smith, A. Liu, D. Infield, and T. Eich. Particle image velocimetry measurements of the aerodynamics of a wind turbine. *International Congress on Instrumentation in Aerospace Simulation Facilities*, pages 315–320, 1991.
- I. Grant, P. Parkin, and X. Wang. Optical vortex tracking studies of a horizontal axis wind turbine in yaw using laser-sheet, flow visualisation. *Experiments in Fluids*, 23:513–519, 1997.
- I. Grant, M. Mo, X. Pan, P. Parkin, J. Powell, H. Reinecke, K. Shuang, F. Coton, and D. Lee. An experimental and numerical study of the vortex filaments in the wake of an operational, horizontal-axis, wind turbine. *Journal of Wind Engineering and Industrial Aerodynamics*, 85:177–189, 2000.
- S.I. Green, editor. *Fluid Vortices*. Kluwer Academic Publishers, Boston, 1995. pg 1 - 31; 317 - 366; 427 - 463.
- A. Gross, H.F. Fasel, T. Friederich, and M.J. Kloker. Numerical investigation of rotational augmentation for s822 wind turbine airfoil. *Wind Energy*, 15(8):983–1007, 2012.
- B.P. Gupta and R.G. Loewy. Theoretical analysis of the aerodynamic stability of multiple, interdigitated helical vortices. *AIAA Journal*, 12(10):1381–1387, 1974.
- I. Gursul and W. Xie. Origin of vortex wandering over delta wings. *Journal of Aircraft*, 37(2):348–350, 2000.
- W. Haans, T. Sant, G.A.M van Kuik, and G.J.W. van Bussel. Measurement of tip vortex paths in the wake of a hawt under yawed flow conditions. *Journal of Solar Energy Engineering*, 127(4):456–463, 2005.
- W. Haans, T. Sant, G. van Kuik, and G van Bussel. Hawt near-wake aerodynamics, part 1: Axial flow conditions. *Wind Energy*, 11(3):245–264, 2008a.
- W. Haans, G.A.M van Kuik, and G.J.W. van Bussel. The inverse vortex wake model: a measurement analysis tool. *Journal of Solar Energy Engineering*, 130(031009):1–14, 2008b.
- K.S. Hansen, R.J. Barthelmie, L.E. Jensen, and A. Sommer. The impact of turbulence intensity and atmospheric stability on power deficits due to wind turbine wakes at horns rev wind farm. *Wind Energy*, 15:183–196, 2012.
- M.O.L. Hansen, editor. *Aerodynamics of wind turbines*. Earthscan, 2 edition, 2008.

-
- M.O.L. Hansen and J. Johansen. Tip studies using cfd and comparison with tip loss models. *Wind Energy*, 7:343–356, 2004.
- H. Hattori and Y. Nagano. Investigation of turbulent boundary layer over forward-facing step via direct numerical simulation. *International Journal of Heat and Fluid Flow*, 31:284–294, 2010.
- J.T. Heineck, G.K. Yamaguchi, A.J. Wadcock, L. Lourenco, and A.I. Abrego. Application of three-component piv to a hovering rotor wake. *American Helicopter Society 56th Annual Forum, Virginia Beach, Virginia, May 2-4, 2000*.
- A.L. Heyes, R.F. Hones, and D.A.R. Smith. Wandering of wing-tip vortices. In *Proceedings of 12th International Symposium On the Applications of Laser Techniques to Fluid Mechanics, Lisbon, Portugal, 2004*.
- R. Hillier and N.J. Cherry. The effects of stream turbulence on separation bubbles. *Journal of Wind Engineering and Industrial Aerodynamics*, 8:49–58, 1981.
- H.P. Horton. *Laminar separation bubbles in two and three-dimensional incompressible flow*. PhD, University of London, 1968.
- H. Hu, Z. Yang, and P. Sarkar. Dynamic wind loads and wake characteristics of a wind turbine model in an atmospheric boundary layer. *Experiments in Fluids*, 52:12771294, 2012.
- N.E. Huang, Z. Shen, S.R. Long, M.C. Wu, H.H. Shih, Q. Zheng, N-C. Yen, C.C. Tung, and H.H. Liu. The empirical mode decomposition and the hilbert spectrum for nonlinear and non-stationary time series analysis. *Proceedings of the royal society A*, 454:903–995, 1998.
- R.F. Huang and C.H. Lin. Vortex shedding and shear-layer instability of wing at low-reynolds numbers. *AIAA Journal*, 33(8):1398–1403, 1995.
- J.C.R. Hunt, S. Leibovich, and K.J. Richards. Turbulent shear flow over low hills. *Quarterly Journal of the Royal Meteorological Society*, 114:1435–1471, 1988.
- G.V. Iungo, P. Skinner, and G. Buresti. Correction of wandering smoothing effects on static measurements of a wing-tip vortex. *Experiments in Fluids*, 46:435–452, 2009.
- S. Ivanell, J.N. Sørensen, R. Mikkelsen, and D. Henningson. Numerical analysis of the tip and root vortex position in the wake of a wind turbine. *Journal of Physics: Conference Series*, 75:1–8, 2007.
- S. Ivanell, J.N. Sørensen, R. Mikkelsen, and D. Henningson. Analysis of numerically generated wake structures. *Wind Energy*, 12:63–80, 2009.
- S. Ivanell, R. Mikkelsen, J.N. Sørensen, and D. Henningson. Stability analysis of the tip vortices of a wind turbine. *Wind Energy*, 13(8):705–715, 2010.
-

References

- P.S. Jackson and J.C.R. Hunt. Turbulence wind flow over a low hill. *Quarterly Journal of the Royal Meteorological Society*, 101:929–955, 1975.
- E.N. Jacobs and A. Sherman. Airfoil section characteristics as affected by variations of the reynolds number. Technical Report Report No. 586, National advisory committee for aeronautics, 1937.
- D. Lo Jacono, M. Nazarinia, and M. Brons. Experimental vortex breakdown topology in a cylinder with a free surface. *Physics of Fluids*, 21:111704, 2009.
- J. Jaquin, D. Fabre, P. Geffroy, and E. Coustols. The properties of a transport aircraft wake in extended near field: an experimental study. *AIAA Journal*, 1038, 2001.
- J. Jeong and F. Hussain. On the identification of a vortex. *Journal of Fluid Mechanics*, 285: 69–94, 1995.
- W. Johnson. *Helicopter Theory*. Princeton University Press, Princeton, 1980.
- N.E. Joukowsky. Vortex theory of a rowing screw. *Trudy Otdeleniya Fizicheskikh Nauk Obshchestva Lubitelei Estestvoznaniya*, 16(1):1–31, 1912. in Russian.
- M. Kiya and K. Sasaki. Structure of a turbulent separation bubble. *Journal of Fluid Mechanics*, 137:83–113, 1983.
- K. Kondo, M. Tsuchiya, and S. Sanada. Evaluation of effect of micro-topography on design wind velocity. *Journal of Wind Engineering and Industrial Aerodynamics*, 90:1707–1718, 2002.
- J. Kostas, J. Soria, and M.S. Chong. A comparison between snapshot pod analysis of piv velocity and vorticity data. *Experiments in Fluids*, 38:146–160, 2005.
- P-A. Krogstad and M.S. Adaramola. Performance and near wake measurements of a model horizontal axis wind turbine. *Wind Energy*, 2011. DOI: 10.1002/we.502.
- P-A. Krogstad and J.A. Lund. An experimental and numerical study of the performance of a model turbine. *Wind Energy*, pages 443–457, 2012.
- Y. Kubo, M. Miyazaki, and K. Kato. Effects of end plates and blockage of structural member on drag forces. *Journal of Wind Engineering and Industrial Aerodynamics*, 32:329 – 342, 1989.
- P.J. Kunz and I.M. Kroo. Analysis, design, and testing of airfoils for use at ultra-low reynolds numbers. *AIAA Journal*, pages 1–16, 2002.
- T. Kurian and J.H.M. Fransson. Grid-generated turbulence revisited. *Fluid Dynamics Research*, 41:012403, 2009.

-
- J.F. Largeau and V. Moriniere. Wall pressure fluctuations and topology in separated flows over a forward facing step. *Experiments in Fluids*, 42:21–40, 2007.
- G.C. Larsen, H. Aa. Madsen, K. Thomsen, and T.J. Larsen. Wake meandering - a pragmatic approach. *Wind Energy*, 11:377–395, 2008.
- E.M. Laws and J.L. Livesey. Flow through screens. *Annual Review of Fluid Mechanics*, 10: 247–266, 1978.
- D.J.J. Leclercq, M.C. Jacob, A. Louisot, and C. Talotte. Forward-backward facing step pair: Aerodynamic flow, wall pressure and acoustic characterisation. *Proceedings of the 7th AIAA/CEAS Aeroacoustics Conference*, 1249:075113–1 075113–13, 2001.
- H. Levy and G. Forsdyke. The steady motion and stability of a helical vortex. *Proceedings of the Royal Society of London. Series A*, 120(786):670–690, 1928.
- T. Leweke. Monash - flair water channel: Characterisation of flow quality. Internal report, Monash University, 2002.
- T.T. Lim and T.B. Nickels. *Fluid Vortices* ed. S.I. Green. Kluwer Academic Publishers, Boston, 1995. chapter 4.
- C. Lindenburg. Modelling of rotational augmentation based on engineering considerations and measurements. *In proceedings of the European Wind Energy Conference, London, November 22-25.*, 2004.
- P.B.S. Lissaman. Low-reynolds-number airfoils. *Annual Review of Fluid Mechanics*, 15:223–239, 1983.
- M.V. Lowson. Visualization measurements of vortex flows. *Journal of Aircraft*, 28(5):320–327, 1991.
- H.J. Lugt. *The dilemma of defining a vortex, in* Recent developments in theoretical and experimental fluid mechanics: compressible and incompressible flows. Springer, New York, 1979. ed. U. Müller and K.G. Roesner and B. Schmidt.
- J.L. Lumley. The structure of inhomogeneous turbulent flows. *Atmospheric Turbulence and Radio Wave Propagation*, 1987. ed A. Yaglom and V. Tatarski.
- T. Maeda, Y. Kamada, J. Suzuki, and H. Fujioka. Rotor blade sectional performance under yawed inflow. *Journal of Solar Energy Engineering*, 130(031018):1–7, 2008.
- H. Makita. Realization of a large-scale turbulence field in a small wind. *Fluid Dynamics Research*, 8:53–64, 1991.
- J.F. Manwell, J.G. McGowan, and A.L. Rogers. *Wind Energy Explained: Theory, Design and Application*. John Wiley and Sons, Ltd., West Sussex, 2002.
-

References

- C. Masson and A. Smaïli. Numerical study of turbulent flow around a wind turbine nacelle. *Wind Energy*, 9:281–298, 2006.
- E.H. Mast, L.J. Vermeer, and G.J.W. van Bussel. Estimation of the circulation distribution on a rotor blade from detailed near wake velocities. *Wind Energy*, 7:189–209, 2004.
- R. Mathis, A. Lebedev, E. Collin, J. Delville, and J.P. Bonnet. Experimental study of transient forced turbulent separation and reattachment on a bevelled trailing edge. *Experiments in Fluids*, 46:131–146, 2009.
- D. Medici and P.H. Alfredsson. Measurements on a wind turbine wake: 3d effects and bluff body vortex shedding. *Wind Energy*, 9:219–236, 2006.
- D. Medici and P.H. Alfredsson. Measurements behind model wind turbines: Further evidence of wake meandering. *Wind Energy*, 11:211–217, 2008.
- D. Medici, S. Ivanell, J.A. Dahlberg, and P.H. Alfredsson. The upstream flow of a wind turbine: blockage effect. *Wind Energy*, 14:691–697, 2011.
- W.H. Melbourne. Turbulence and the leading edge phenomena. *Journal of Wind Engineering and Industrial Aerodynamics*, 49:45–64, 1993.
- D. Micallef, B. Akay, T. Saint, C.S. Ferreira, and G. van Bussel. Experimental and numerical study of radial flow and its contribution to wake development of a HAWT. In *Proceedings of the European Wind Energy association*, 2011.
- D. Micallef, G. van Bussel, C.S. Ferreira, and T. Sant. An investigation of radial velocities for a horizontal axis wind turbine in axial and yawed flows. *Wind Energy*, 2012. DOI: 10.1002/we.1503.
- R. Mikkelsen, C. Velte, and I. Naumov. Wake measurement using piv on a scaled glauert optimal turbine rotor in a water flume. *Proceedings of the Gotland wake conference*, page 111, 2011.
- B. Montgomerie and J.A. Dahlberg. Vortex system studies on small wind turbines. Technical report, FOI scientific report, 2003. ISRN FOI-R-0936-SE.
- N.G. Mortensen, L. Landberg, I. Troen, and E.L. Petersen. Wind atlas analysis and application program (wa^sp), vol 2, user’s guide. Technical Report Risø-I-666(v.2)(EN), Risø national laboratory, Roskilde, Denmark, 1993.
- W.D. Moss and S. Baker. Re-circulating flows associated with two-dimensional steps. *Aeronautical Quarterly*, August:151–172, 1980.
- T.J. Mueller and J.D. Delaurier. Aerodynamics of small vehicles. *Annual Review of Fluid Mechanics*, 35:89–111, 2003.

-
- K. Nilsson, W.Z. Shen, J.N. Sørensen, and S. Ivanell. Determination of the tip vortex trajectory behind the Mexico rotor. *Wake Conference, 8-9 June, Visby, Sweden*, page 12, 2011.
- T.R. Oke, editor. *Boundary Layer Climates*. Routledge, London, 2 edition, 1987. pg 51 - 58; 182 - 189.
- V.L. Okulov. On the stability of multiple helical vortices. *Journal of Fluid Mechanics*, 521: 319–342, 2004.
- V.L. Okulov and J.N. Sørensen. Stability of helical tip vortices in a rotor far wake. *Journal of Fluid Mechanics*, 576:1–25, 2007.
- P.L. O’Neill, D. Nicolaides, D. Honnery, and J. Soria. Autocorrelation functions and the determination of integral length with reference to experimental and numerical data. *Proceedings of the 15th Australasian Fluid Mechanics conference*, pages 1–4, 2004.
- T. Ota, Y. Asano, and J. Okawa. Reattachment length and transition of the separated flow over blunt flat plates. *Bulletin of the Japan Society of Mechanical Engineers*, 24(192): 941–947, 1981.
- S. Oye. Tjæreborg wind turbines (EBSJERG) geometric and operational data. Technical report, Department of Fluid Mechanics, DTH, DK 2800 Lyngby, 1990. AFM NOTAT VK-184.
- S. Oye. Tjæreborg wind turbines (EBSJERG) first dynamic inflow measurement. Technical report, Department of Fluid Mechanics, DTH, DK 2800 Lyngby, 1991. AFM NOTAT VK-189.
- E.L. Petersen, N.G. Mortensen, L. Landberg, J. Højstrup, and H.P. Frank. Wind power meteorology. Part 1: climate and turbulence. *Wind Energy*, 1:25–45, 1998a.
- E.L. Petersen, N.G. Mortensen, L. Landberg, J. Højstrup, and H.P. Frank. Wind power meteorology. Part 2: siting and models. *Wind Energy*, 1:55–72, 1998b.
- S. Pope. *Turbulent flows*. Cambridge University Press, New York, 2000.
- F. Porté, H. Lu, and Y-T. Wu. A large eddy simulation framework for wind energy applications. *The fifth international symposium on computational wind engineering, CWE2010, Chapel Hill, North Carolina, USA, May 23-27*, 2010.
- M. Raffel, C. Willert, and J. Kompenhans, editors. *Particle image velocimetry—a practical guide*. Springer-Verlag, Heidelberg, 1998. pg 51 - 58; 182 - 189.
- M. Ramasamy, R. Paetzl, and M.J. Bhagwat. Aperiodicity correction for rotor tip vortex measurements. *AHS 67th Annual Forum, Virginia Beach, VA, May 3-5, 2011*, 2011.
- W.J.M. Rankine. Need title. *Transactions of the institute of naval architects*, 6:13, 1865.
-

References

- K. Rokhsaz, S.R. Foster, and L. Scott Miller. Exploratory study of aircraft wake vortex filaments in a water channel. *Journal of Aircraft*, 37(6):1022–1027, 2000.
- C. Roy. *Dynamics and stability of vortices with axial flow*. Phd, Monash University, 2008.
- P.J. Saathoff and W.H. Melbourne. Effects of free-stream turbulence on surface pressure fluctuations in a separation bubble. *Journal of Fluid Mechanics*, 337:1–24, 1997.
- B. Sanderse. Aerodynamics of wind turbine wakes, literature review. Technical Report ECN-E-09-016, The energy research center of the Netherlands, 2009.
- J.G. Schepers and H.Snel. Model experiments in controlled conditions, final report. Technical Report ECN-E-07-042, The energy research center of the Netherlands, 2007.
- F.A. Schraub, S.J. Kline, J. Henry, P.W. Runstadler Jr, and A. Littell. Use of the hydrogen bubbles for quantitative determination of time-dependent velocity fields in low-speed water flows. *Journal of basic engineering*, pages 429–444, 1965.
- M.S. Selig, C.A. Lyon, P. Giguère, C.N. Ninham, and J.J. Guglielmo. *Summary of Low-Speed Airfoil Data, Vol. 2*. SoarTech Publications, Virginia Beach, VA, 1996.
- W.Z. Shen, R.M. Mikkelsen, and J.N. Sørensen. Tip loss corrections for wind turbine computations. *Wind Energy*, 8:457–475, 2005.
- M. Sherry, D. Lo Jacono, and J. Sheridan. An experimental investigation of the recirculation zone formed downstream of a forward facing step. *Journal of Wind Engineering and Industrial Aerodynamics*, 98:888–894, 2010.
- M. Sherry, J. Sheridan, and D. Lo Jacono. The effect of turbulence on flow over a forward facing step. *Journal of Wind Engineering and Industrial Aerodynamics*, 2012. *Under review*.
- J.E. Shigley, C.R. Mischke, and R.G. Budynas, editors. *Mechanical engineering design*. McGraw Hill Higher Education, Boston, 7th edition, 2004.
- S. Shreck, T. Sant, and D. Micallef. Rotational augmentation disparities in the mexico and uae phase vi experiments. *In proceedings of the TORQUE from wind conference, Heraklion, Greece, June 28-30.*, 2010.
- C. Sicot, P. Devinant, T. Laverne, S. Loyer, and J. Hureau. Experimental study of the effect of turbulence on horizontal axis wind turbine aerodynamics. *Wind Energy*, 9:361–370, 2006.
- L. Sirovich. Turbulence and the dynamics of coherent structures. part 1: Coherent structures. *Quarterly applied math*, 45(3):561–571, 1987.
- L. Sirovich and M. Kirby. Low-dimensional procedure for the characterization of human faces. *Journal of the Optical Society of America A*, 4:519–524, 1987.

-
- A.J. Smits and T.T. Lim, editors. *Flow visualization: techniques and examples*. Imperial College Press, 2000. chapter 2,3,6.
- H. Snel. Review of the present status of rotor aerodynamics. *Wind Energy*, 1:46–69, 1998.
- J.N. Sørensen. Aerodynamics aspects of wind energy conversion. *Annual Review of Fluid Mechanics*, 43:427–448, 2011.
- J.N. Sørensen and W.Z. Shen. Numerical modeling of wind turbine wakes. *Journal of Fluids Engineering*, 124:393–399, 2002.
- D.A. Spera, editor. *Wind turbine technology, fundamental concepts of wind turbine engineering*. ASME Press, New York, 1994.
- J. Stack. Experimental investigation of rotor vortex wakes in descent. *Progress in Aerospace Sciences*, 0297, 2004.
- S. Sunada and K. Kawachi. Comparison of wing characteristics at an ultralow reynolds number. *Journal of Aircraft*, 39:331–338, 2002.
- S. Sunada, A. Sakaguchi, and K. Kawachi. Airfoil section characteristics at a low reynolds number. *Journal of Fluids Engineering*, 119:129–135, 1997.
- K.E. Swalwell, J. Sheridan, and W.H. Melbourne. The effect of turbulence intensity on performance of a naca4421 airfoil section. *AIAA Journal*, (AIAA-2004-665):1–10, 2004.
- P.A. Taylor. Turbulent boundary-layer flow over low and moderate slope hills. *Journal of Wind Engineering and Industrial Aerodynamics*, 74-76:25–47, 1998.
- H. Tennekes and J.L. Lumley, editors. *A first course in turbulence*. The Massachusetts Institute of Technology Press, Cambridge, Massachusetts, 1972.
- A Thacker, S. Loyer, and S. Aubrun. Comparison of turbulence length scales assessed with three measurement systems in increasingly complex turbulent flows. *Experimental Thermal and Fluid Science*, 34:638–645, 2010.
- N. Troldborg. *Actuator line modelling of wind turbine wakes*. Phd, Technical University of Denmark, 2008.
- N. Troldborg, J. Sørensen, and R. Mikkelsen. Actuator line simulation of wake of wind turbine operating in turbulent inflow. *Journal of Physics: Conference Series*, 75:012063, 2007.
- N. Troldborg, G.C. Larsen, H.A. Madsen, K.S. Hansen, J.N. Sørensen, and R. Mikkelsen. Numerical simulations of wake interaction between two wind turbines at various inflow conditions. *Wind Energy*, 14:859–876, 2011.
- C. Tropea, A.L. Yarin, and J.F. Foss, editors. *Springer handbook of experimental Fluid Mechanics*. Springer-Verlag, Berlin, 2007. pts. 5.3.2, 24.3;.
-

References

- TSI. Phase doppler particle analyzer (pdpa)/ laser doppler velocimeter (ldv). Technical Report P/N 1990048, TSI Incorporated, 500 Cardigan Road, Shoreview, MN, 55126, USA, 2006.
- B.G. van der Wall and H. Richard. Analysis methodology for 3c-piv data of rotary wing vortices. *Experiments in Fluids*, 40:798–812, 2006.
- B.W. van Oudheusden, F. Scarano, N.P. van Hinsberg, and D.W. Watt. Phase-resolved characterisation of vortex shedding in the near wake of a square-section cylinder at incidence. *Experiments in Fluids*, 39:86–98, 2005.
- F.X. Vandernoot, P. Barricau, and H-C. Boisson. Mean and turbulence measurements of wake vortices. wandering effects. *In Proc. 14th Intl Symp. On the Applications of Laser Techniques to Fluid Mechanics, Lisbon, Portugal*, 2008.
- L.J. Vermeer. A review of wind turbine wake research at tudelft. *American Institute of Aeronautics and Astronautics*, A01-16944, 2001.
- L.J. Vermeer, J.N. Sørensen, and A. Crespo. Wind turbine wake aerodynamics. *Progress in Aerospace Sciences*, 39:467–510, 2003.
- H. Vollmers. Detection of vortices and quantitative evaluation of their main parameters from experimental velocity data. *Measurement Science and Technology*, 12:1199–1207, 2001.
- C.F. vonCarmer, R. Konrath, A. Schroder, and J-C. Monnier. Identification of vortex pairs in aircraft wakes from sectional velocity data. *Experiments in Fluids*, 44:367–380, 2008.
- R. Vonlanthen and P.A. Monkewitz. A new passive turbulence grid with improved isotropy. *In proceedings of the 61st meeting of APS division of fluid dynamics*, 2008.
- R. Vonlanthen and P.A. Monkewitz. A novel tethered-sphere add-on to enhance grid turbulence. *Experiments in Fluids*, 51:579–585, 2011.
- J.H. Walther, M. Guénot, E. Machefaux, J.T. Rasmussen, P. Chatelain, V.L. Okulov, J.N. Sørensen, M. Bergdorf, and P. Koumoutsakos. A numerical study of the stability of helical vortices using vortex methods. *Journal of Physics: Conference Series*, 75(012034), 2007.
- J. Weiss. The dynamics of enstrophy transfer in two- dimensional hydrodynamics. *Physics D*, 48:273–294, 1991.
- J. Whale. *A study of the near wake of a model wind turbine using particle image velocimetry*. PhD, The University of Edinburgh, 1996.
- J. Whale, C.G. Anderson, R. Bareiss, and S. Wagner. An experimental and numerical study of the vortex structure in the wake of a wind turbine. *Journal of Wind Engineering and Industrial Aerodynamics*, 84:1–21, 2000.

- S. Widnall. The stability of a helical vortex filament. *Journal of Fluid Mechanics*, 54(4): 641–663, 1972.
- R.E. Wilson and P.B.S. Lissaman. Applied aerodynamics of wind power machines. Technical report, Oregon State University, 1974. NSF-RA-N-74-113.
- R.E. Wilson, P.B.S. Lissaman, and S.N. Walker. Aerodynamic performance of wind turbines. Technical report, Oregon State University, 1976. NSF/RA-760228.
- Z. Yang, P.Sarkar, and H. Hu. An experimental investigation on the wake characteristics of a wind turbine in an atmospheric boundary layer wind. *29th AIAA applied aerodynamics conference, 27–30 June, Honolulu, Hawaii*, AIAA 2011-3815, 2011.
- S. Yoshida. Performance of downwind turbines in complex terrain. *Wind Engineering*, 30(6): 487–502, 2006.
- F. Zahle and N.N. Sørensen. Characterisation of the unsteady flow in the nacelle region of a modern wind turbine. *Wind Energy*, 14:271–283, 2011.
- F. Zahle, N.N. Sørensen, and J. Johansen. Wind turbine rotor-tower interaction using an incompressible overset grid method. *Wind Energy*, 12(6):594–619, 2009.
- C.X. Zhang. Numerical predictions of turbulent recirculating flows with a $k-\epsilon$ model. *Journal of Wind Engineering and Industrial Aerodynamics*, 51:177–201, 1994.
- W. Zhang, C.D. Markfort, and F. Porté-Agel. Near-wake flow structure downwind of a wind turbine in a turbulent boundary layer. *Experiments in Fluids*, 52:12191235, 2012.
- J. Zhou, R.J. Adrian, S. Balachandar, and T.M. Kendall. Mechanisms for generating coherent packets of hairpin vortices in channel flow. *Journal of Fluid Mechanics*, 387:353–396, 1999.
- Y. Zhou, Md. Mahbub Alam, H.X. Yang, H. Guo, and D.H. Wood. Fluid forces on a very low reynolds number airfoil and their prediction. *International Journal of Heat and Fluid Flow*, 32:329–339, 2011.